

Seaglider observations of biogeochemical variability in the Iberian upwelling system.

A thesis submitted to the
School of Environmental Sciences
of the
University of East Anglia
in partial fulfillment of the requirements for the degree of
Doctor of Philosophy

By
Christopher Walker Brown

Supervised by: Dr Jan Kaiser, Professor Karen Heywood and Dr Carol Robinson

September 2013

© Copyright by CWB 2013

All Rights Reserved

Acknowledgements

The Iberian upwelling system was an interesting region for UEA's first Seaglider deployment. Thanks are due to Des Barton, who helped make the research possible by allowing use of his labs and ship time onboard the RV Mytilus.

Piloting a Seaglider is a 24 hour a day job- it requires constant attention, and if something goes wrong, it will always happen in the middle of the night. For help in watching over the Seaglider, I am indebted to Cedric, Marion and Bastien.

After receiving a huge dataset, I am truly thankful for the help of my three supervisors, Jan Kaiser, Karen Heywood and Carol Robinson. Their input was invaluable.

Finally I would like to thank all of my friends and family for their help and support at my time at the UEA.

Abstract

Seaglider observations of biogeochemical variability in the Iberian upwelling system.

Seasonal upwelling events along the Galician coastline of the North Atlantic furnish the upper watercolumn with nutrients, resulting in strong summer phytoplankton blooms and the sustenance of one of Europe's largest fisheries. The episodic nature of these upwelling events result in considerable challenges studying the region using traditional shipboard observations. This thesis demonstrates an alternative sampling technique, providing high spatial and temporal resolution biogeochemical data through the use of an autonomous underwater glider- the Seaglider.

SG510 "Orca" was outfitted with sensors to measure dissolved oxygen, temperature, salinity, chlorophyll *a* (chl *a*), coloured dissolved organic material (CDOM) and optical backscatter. Deployed for 113 days over summer 2010, Orca completed 17 zonal transects across the shelf, continental slope and open ocean at 42.1° N. Data collected during the campaign was used to assess both the physics of the watercolumn, and the effect these physical processes have on the region's biogeochemistry. As part of this biogeochemical study, a novel attempt at calculating net community production (NCP) was completed using an oxygen inventory technique.

Two major phytoplankton bloom events occurred during the deployment period, with respective peak Chl *a* concentrations of 9.65 and 11.23 mg m⁻³. During these bloom events, NCP varied between (net autotrophic) values of 25 and 123 (±17) mmol m⁻² d⁻¹. Negative values of NCP were only observed twice for 24 and 60 hours respectively, with a maximum heterotrophy of -44 (±17) mmol m⁻² d⁻¹. Overall, the summer season featured a net autotrophic metabolic balance of +27 mmol m⁻² d⁻¹ thus highlighting the importance of the region for net carbon sequestration. Finally, this thesis also demonstrates the success of using autonomous glider platforms for sustained biogeochemical and physical observations within a highly dynamic and challenging operational environment with strong currents and considerable shipping traffic.

CONTENTS

	Page
Acknowledgements	
Abstract	
Seaglider observations of biogeochemical variability	iv
Contents.	vi
List of Tables	
List of figures	
Introduction: Global Carbon cycles and the North Atlantic	1
1.1 The global carbon cycle	1
1.2 Measuring productivity	7
1.3 The transect region	11
1.4 Productivity of the transect region	14
1.5 Gliders and autonomous underwater vehicles	16
1.6 Aims of the thesis	17
Design, flight behavior and sensor calibration of a glider	19
2.1 The Seaglider	19
2.2 Seaglider dives	22
2.3 Seabird Electronics CT cell overview	26
2.4 Seaglider and RV Mytilus CTD data	32
2.5 WetLABS ECO puck	34
The Oxygen Optode	40
3.1 The optode	40
3.2 Oxygen optode calculation technique	43
3.3 Optode data processing	45
3.4 Oxygen concentration calibration with Mytilus data	53
3.5 Conclusions	61
Biogeochemical and physical observations of the transect region.	64
4.1 Introduction	64
4.2 Water masses observed in the region	66
4.3 Observations of Upwelling	68
4.4 MODIS, ERA Interim and Seaglider observations of upwelling	90
4.5 Tracking watermasses using CDOM	91
4.6 Phytoplankton Blooms	97
4.7 Particulate	99
4.8 Conclusions: Comparing the physical and biogeochemical observations of upwelling	105
Estimating productivity using an O₂ watercolumn inventory	113

5.1	Introduction	113
5.2	P _N methodology	114
5.3	Water column rate of change	117
5.4	Physics and air-sea interactions	128
5.5	Bubble fluxes	133
5.6	Conclusions	144
	Unaccounted processes	144
An overview of summer 2012 and final conclusions		148
6.1	Results	148
6.2	Context	151
6.3	Future research	154
References		156
Appendix		163

List of Tables

1.1 List of transects	13
4.1 Physical observations of the transect region	91
4.2 Biogeochemical observations of the transect region	99

List of figures

Chapter One

1.1: The growth of atmospheric CO ₂ growth over the 20 th century.	2
1.2: An overview of the major carbon fluxes between the atmosphere, ocean and oceanic sediment,	3
1.3: Global annual average net primary productivity.	5
1.4: NCP data locations coloured by net autotrophy/ heterotrophy.	10
1.5: Published in vitro and in situ NCP rates.	10
1.6: The transect region.	12
1.7: Plankton carbon budgets	15

Chapter Two

2.1: A comparison of the three main commercialized gliders	20
2.2: A schematic of a Seaglider dive	21
2.3: GEBCO bathymetry	23
2.4: Basic principles of the glider operation.	24
2.5: Seabird Electronics 25 + Sealogger CTD salinity values	29
2.6: Mytilus calibrated CTD cast salinity data.	32
2.7: Seaglider salinity data.	33
2.8: Seaglider chl a, with calibrated CTD fluorimeter chl a concentrations	36
2.9: A comparison matlab gridding techniques	39

Chapter Three

3.1: Aanderaa 4330 optode..	41
3.2 A schematic of an oxygen optode response .	42
3.3 Optode thermistor inaccuracies	46
3.4.Despiking of oxygen data.	47
3.5. Optode mounting position..	49

3.6. Schematic of τ time adjustments.	51
3.7. Uncalibrated downcast oxygen saturation data.	52
3.8. Winkler titrations calibration of RV Mytilus' CTD	53
3.9 RV Mytilus CTD calibration of Seaglider optode	57
3.10 Linear regressions between Seaglider and CTD	58
3.11 SBE43 pseudo θ_{CP} , and the optode θ_{CP} linear regressions	59
3.12 Uncalibrated optode θ_{CP} values comparison	60
3.13 Entire seaglider optode and R.V Mytilus SBE 43 dataset	62
3.14 Sensor drift correction output of the Aanderaa 4330F	63
Chapter Four	
4.1 Hovmoller plots of MODIS Chla and SST concentrations	65
4.2 Theta - S diagram	67
4.3 Upwelling overview for summer 2010	70-86
4.4 A schematic of upwelling in the seaglider transect region.	88
4.5 Theta anomalies for the seventeen transects,	
4.6 0-250 m TS diagrams.	93
4.7 Gridded CDOM concentrations from each of the seventeen transects.	94
4.8 A schematic of on-shelf CDOM	96
4.9 5 m binned oxygen and chl a data from the Seaglider.	98
4.10 Gridded Chl a concentrations	103
4.11 Oxygen relative saturation.	104
4.12 Backscatter compared with oxygen concentrations	106
4.13 Gridded backscatter values for each of the seventeen transects	108
4.14. Backscatter spikes.	110
4.15 Photic zone correlations.	111

Chapter Five

5.1 A schematic of the three main Pn considerations .	116
5.2 Box and whisker plot of 5 m binned oxygen concentrations	119
5.3 The choice of water column bases	121
5.4 Sensitivity of the water column bases	122
5.5 A schematic of the two integration comparison techniques.	125
5.6 Gridding techniques	127
5.7 Air sea gas exchange fluxes.	132
5.8 Bubble fluxes	136
5.9 Upwelling fluxes	
5.10 Ekman diagram	
5.11 Oxygen inventory.	
5.12 Hovmoller of Pn.	142
5.12 Combined oxygen inventory.	143

Chapter six

6.1 Seaglider and MODIS data for summer season	
6.2 Satellite sources of productivity data.	

Introduction: Global Carbon cycles and the North Atlantic

1.1 The global carbon cycle

Solar radiation, the primary source of energy on the surface of the Earth, is not distributed equally across the Earth's surface. Features ranging from the curvature of the surface, the Earth's axial tilt and weather patterns all influence how much solar energy reaches the planet's surface. This imbalance results in the Earth's climatic system, essentially a mechanism to redistribute energy from warm equatorial regions to the cooler poles, via the oceans and atmosphere.

A major physical control on climate results from the ocean's immense heat capacity—three orders of magnitude larger than that of the atmosphere (IPCC AR4, 5.1). The thermohaline circulation system enables regional scale transport of heat via surface currents, thus directly influencing regional climate (IPCC AR4, 5.3.2). The interaction between the atmosphere and oceans is not limited to heat exchange; soluble gases (such as oxygen) readily transfer between the ocean and the atmosphere through the ocean's surface (IPCC AR4, 3.5.6). It is through this gas exchange that the ocean's second major control on global climate occurs, as a major reservoir of carbon. The global carbon cycle describes the flux of carbon between reservoirs found in the biosphere, hydrosphere, atmosphere, pedosphere and lithosphere. Carbon dioxide in the atmosphere has a well documented influence on climate, by absorbing infra-red radiation emitted from the surface— leading to atmospheric heating.

If the global carbon cycle were at steady state, all fluxes *ex* of these reservoirs would equal reciprocal fluxes into the reservoir, resulting in a stable net carbon content. Anthropogenic perturbations to the carbon cycle, such as the net release of carbon from the lithosphere's fossil fuel reservoir, have resulted in an increased flux of carbon into the atmospheric reservoir (IPCC AR4, 7.3.1.1). These perturbations are reflected by an increased CO₂ concentration in the atmosphere, with pre-industrial CO₂ atmospheric concentrations of 280 μmol mol⁻¹ (abbreviated to ppm) rising through the past two centuries to a present day concentration of ~400 ppm (IPCC preliminary AR5 and figure 1.1). The majority of the anthropogenic CO₂ flux comes from three sources; fossil fuel use, cement manufacture and deforestation. The magnitude of the anthropogenic CO₂ emissions over the past two centuries

can be derived from land and industrial records, or more recently from direct measurement of atmospheric CO₂ (Le Quéré et al. 2009). However, lower carbon dioxide concentrations are found in the atmosphere than would be expected considering the anthropogenic CO₂ emissions, with only 43 % of the total CO₂ emissions between 1959 and 2008 remaining in the atmosphere as of 2008 (Le Quéré et al. 2009). It appears that increasing the carbon flux to the atmosphere, thereby increasing the size of the atmospheric reservoir, has resulted in an alteration of the dynamic equilibrium of the carbon cycle. As a result, carbon fluxes from the atmosphere to other reservoirs have increased (IPCC, 7.3.1, figure 1.2).

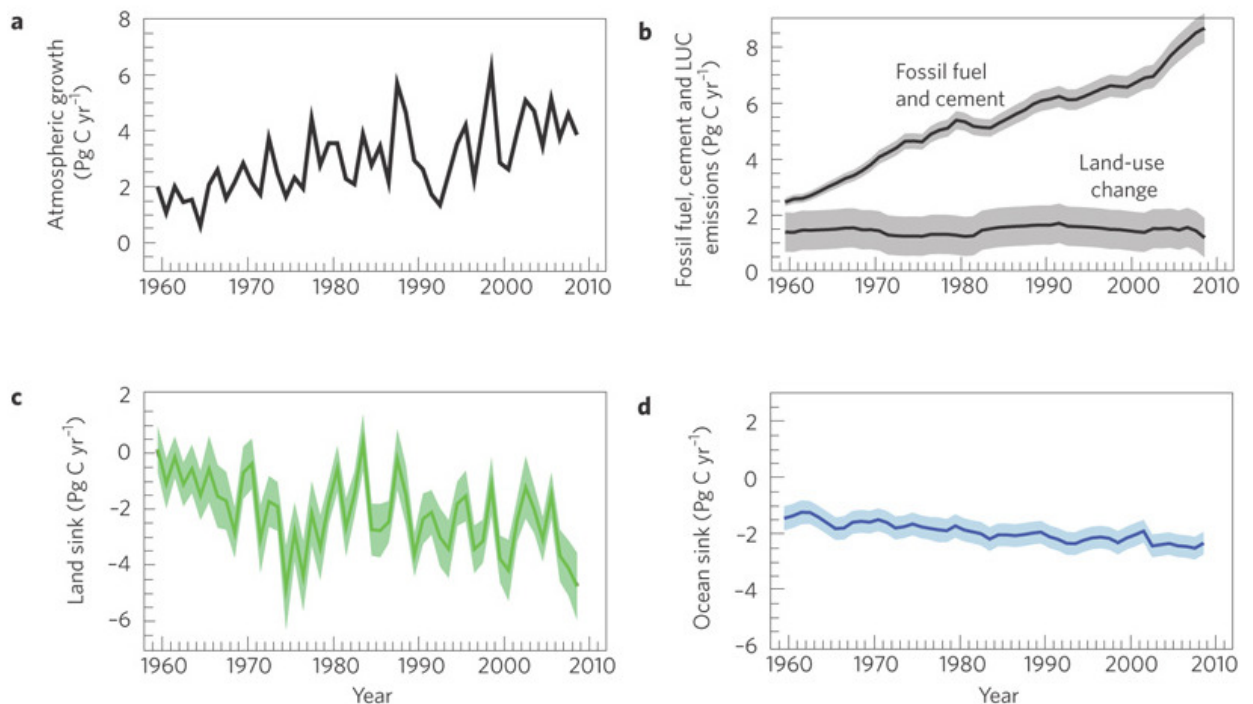


Figure 1.1: a, The atmospheric CO₂ growth rate. b CO₂ emissions from the combustion of fossil fuels, land use change and the manufacture of cement. c, Land CO₂ sink (negative values indicate net uptake). d, Ocean CO₂ sink (negative values indicate net uptake.) Modified from figure 3, Le Quéré et al., 2009.

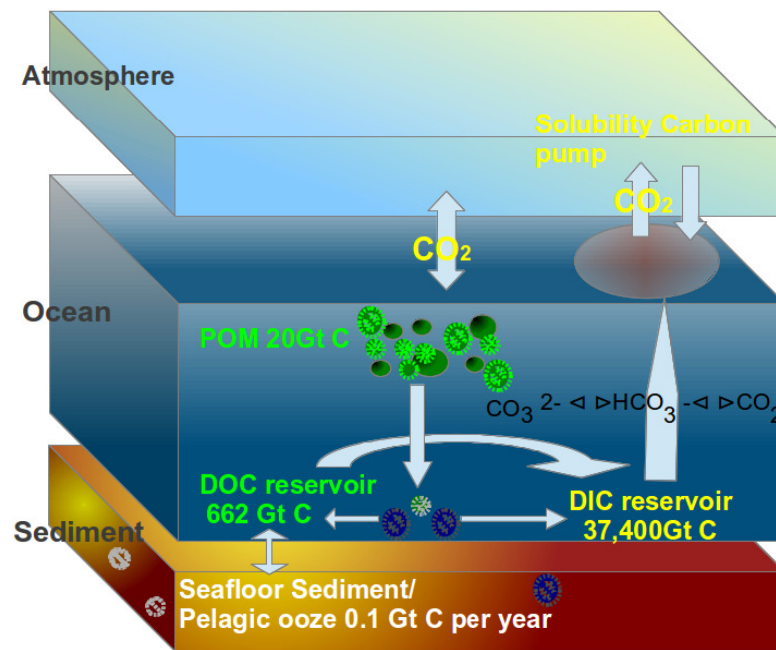


Figure 1.2: An overview of the major carbon fluxes between the atmosphere, ocean and oceanic sediment, including particulate organic matter (POM), dissolved organic carbon (DOC), dissolved inorganic carbon (DIC), and estimated reservoir contents (values are from Jiao et al. 2010).

Through inorganic carbon measurements, Sabine et al. (2004) estimated that the ocean was a sink for 48 % of the total anthropogenic CO_2 produced since the industrial revolution (118 Pg between 1800 to 1994). As anthropogenic CO_2 emissions increase year on year, a lower fraction of the total CO_2 released is being absorbed by the oceans (figure 1.1). At 2008 levels of CO_2 emission, an estimated $2.3 \pm 0.3 \text{ Pg a}^{-1}$ of anthropogenic CO_2 was absorbed by the oceans, out of total emissions of $8.7 \pm 0.5 \text{ Pg a}^{-1}$, only 26 % of total annual emissions (figure 1.1 b and d). Whether this trend continues, or accelerates is of considerable importance to the CO_2 concentration within the atmospheric reservoir and hence climate.

The mechanism behind the transfer of CO_2 between the atmosphere and ocean reservoir includes both physical and biological processes. Physical processes include the cooling of surface waters (thus increasing the concentration of CO_2 the water can hold at saturation), and deep winter convection (thus enabling the transport of cold, CO_2 saturated waters to great depth, and outside of the summer mixed layer, preventing the re-equilibration of this water with the atmosphere, Alkire et al. 2011). The reverse processes, upwelling of

Introduction: Global carbon cycles and the North Atlantic

deep water masses and the warming of the surface layer promote the transfer of CO₂ from the ocean to the atmosphere through ventilation (figure 1.2- the carbon solubility pump). The balance between the two physical processes cannot be considered in isolation as biota, through the biological carbon pump, alters both fluxes (figure 1.2, Gist et al. 2009)

Although the oceans contain only 0.2 % of the total photosynthetic biomass within the biosphere, they are responsible for approximately half of global gross primary productivity- the rate at which autotrophic organisms capture and store energy absorbed from the environment as biomass (Falkowski et al. 2000). Through this primary productivity, a biological pathway is created, removing CO₂ from the atmosphere and transferring it into the ocean (figure 1.2). Therefore, carbon fixed by photosynthetic autotrophs increase the carbon stored within the oceanic biomass reservoir. There are two typical fates for this biological carbon: respiration back to dissolved inorganic carbon (DIC) within the photic zone, or export to the deeper oceans as particulate organic carbon (POC), or dissolved organic carbon (DOC). It is the transfer of DOC or POC from the photic zone to the deep that is referred to as the biological carbon pump (figure 1.2, Falkowski et al. 2000.) The eventual remineralisation of organic carbon from the biological pump or carbon rich sediment increases DIC at depth, which equilibrates with the atmosphere during upwelling and subsequent ventilation of these deep waters. In certain regions of the ocean, the time elapsed between initial carbon fixation, export, remineralisation and ventilation can be on the order of centuries to millennia (Sarnthein et al. 1988). Additionally, a small fraction (estimated at 0.5 Gt C per year by Jiao et al. 2010) of the carbon transported via the biological pump will be deposited as sediment in the deep ocean, and remain isolated from the atmosphere for much longer time-scales (figure 1.2). It is this isolation between carbon in the deep oceanic/ sediment reservoirs and carbon in the atmospheric reservoir combined with the time elapsed between initial photosynthesis and eventual ventilation of deep water that has been postulated as a major medium-term sink of carbon (IPCC 7.3). As an identified sink, the biological pump is both important to the global carbon cycle and a control on atmospheric CO₂ concentrations. The effect that increasing atmospheric CO₂ through the next century has on total carbon transported via the global oceanic biological pump is hotly debated, with no consensus yet reached (Sarmiento et al. 2006, IPCC 7.3.4, Hutchins et al. 2011.) Increased levels of CO₂ could prove beneficial to autotrophs during photosynthesis, or detrimental during frustule formation in certain plankton species (Sarmiento et al. 2006).

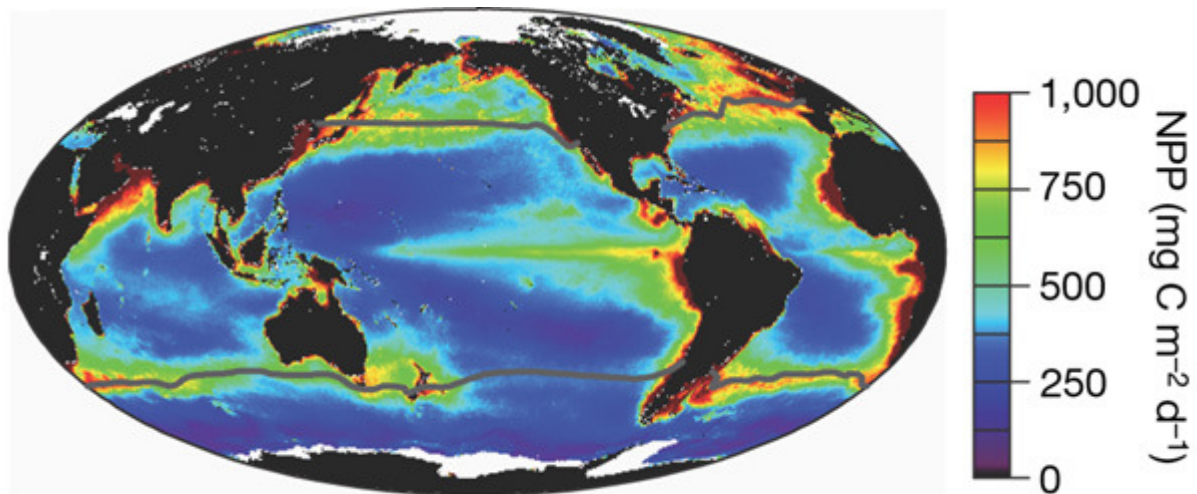


Figure 1.3: Global annual average net primary productivity. Low-latitude, subtropical waters with average surface temperatures over 15 °C are delineated by black contour lines. Modified from figure 1 of Behrenfeld et al. 2006.

Observations of atmospheric O₂ and CO₂ provide strong constraints on total global carbon fluxes, however, estimating regional carbon fluxes resulting from the oceanic biological pump is difficult due to the high temporal and spatial variability of productivity in the oceans (figure 1.3, Pacala et al. 2001; Emerson et al. 1997). Previous work has indicated that the North Atlantic is one of the most important regions in terms of the strength of the biological pump (Robinson et al. 2002). Providing 'Goldilocks' conditions, namely high levels of primary productivity, and CO₂ uptake, combined with plankton assemblages dominated by micro-plankton, the North Atlantic thus provides an efficient carbon export system to the deep (Takahashi et al. 2002). These conditions have proved so effective at promoting a large biological pump, recent estimates suggest that this pump (in addition to other physical CO₂ pumps) has slightly less than a quarter of the total anthropogenic CO₂ emitted since the industrial revolution has been stored in the North Atlantic, a considerable fraction of the 48 % of the missing carbon total (Sabine et al. 2004).

The distribution of CO₂ uptake in the North Atlantic is highly heterogeneous. High levels of productivity occur in the subpolar North Atlantic and the subtropical eastern boundary current (EBC) regions, contrasting with strongly oligotrophic and low productivity

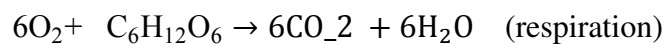
conditions seen in the North Atlantic subtropical gyre/ Sargasso Sea regions (figure 1.3, Takahashi et al. 2002; Morgan-Smith et al. 2013). Much work has been conducted on the productivity of the North Atlantic sub-polar spring bloom (Robinson et al. 2002; Alkire, et al. 2011). In comparison, EBC regions seem comparatively under-sampled. These regions, both in the Atlantic and the rest of the global oceans, are disproportionately important for global oceanic productivity, accounting for approximately 11 % of the total global gross primary productivity, yet covering only 1 % of the total global oceanic surface area (Chavez and Toggweiler, 1995). The reasons behind these high levels of productivity can be explained qualitatively by two features of EBC regions:

1. EBC regions frequently feature a North - South aligned coastline, which, when coupled with equatorward trade winds, allow for net transportation of water (within the Ekman layer) towards the west, resulting in the upwelling of nutrient rich deeper waters along the continental shelf (Ekman. 1902, figure 1.4)
2. EBC regions tend to encompass shelf seas, where terrestrial dust, fluvial inputs of nutrients and intensified diapycnal mixing by tides and internal waves all act to increase photic zone nutrient concentrations (Chavez and Toggweiler, 1995.)

The processes above enable higher and longer-sustained nutrient concentrations in the photic zone resulting in prolonged bloom events and increased levels of productivity within EBC regions (Chavez & Messié 2009). This high productivity has proved beneficial to humans, as 35% of global fish catch is from EBC regions (Kahru et al. 2009). The Portugal EBC within the Iberian North Atlantic is no exception, with the Port of Vigo benefiting from the highly productive ecosystem in the proximal North Atlantic. The Port of Vigo is now one of the largest fishing ports in the world, and home to extensive canning, processing and shellfish farming industries (Lopes et al. 2013).

1.2 Measuring Productivity

Measuring productivity as part of an assessment of the global carbon cycle can be achieved by measuring either CO₂ or O₂; both feature in photosynthesis and (aerobic) respiration:



By measuring the changes in mass balance of either CO₂ or O₂ in a closed system, the mass balance of carbon fixed as biological carbon can be calculated: CO₂ or O₂ are linked by the photosynthetic quotient $r(\text{O}_2 / \text{C})$ (Laws 1991). In the oceans, measuring O₂ is often favoured, as dissolved CO₂ can form one of numerous carbon species (such as carbonic acid, bicarbonate anion and carbonate), collectively known as DIC. In contrast, oxygen remains as dissolved oxygen, making measurement easier.

Productivity is a rather loose term, hence more specific definitions are frequently used: gross primary production (GPP) and net community production (NCP). GPP isolates all respiration (including that done by the autotroph) from photosynthesis, thus calculating the total amount of carbon fixed by the biota. Using in-vitro incubations, GPP can be calculated using isotopically labelled substances and mass spectrometry. One of the first techniques involved spiking the water of an in-vitro phytoplankton culture with ¹⁴C labelled sodium bicarbonate. Photosynthetic biotic metabolism results in the incorporation of carbon from inorganic sources into biomass thus removing ¹⁴C from the in-vitro environment. GPP is derived from the proportion of ¹⁴C in the biomass fraction versus ¹⁴C remaining as inorganic carbon in the seawater (Marra 2009). Other techniques have used oxygen's three stable isotopes, (¹⁶O, ¹⁷O and ¹⁸O). The isotope exchange between CO₂ and H₂O in phytoplankton and terrestrial autotrophs during photosynthesis is a first order control on the δ¹⁸O found in atmospheric CO₂ and photic zone DIC (Hoag 2005). Approximately one third of CO₂ uptaken by autotrophs is assimilated to organic carbon, with the remaining two-thirds released back into the surrounding environment featuring a modified δ¹⁸O CO₂ directly influenced by oxygen fractionation within the autotroph (Hoag 2005). Thus, working backwards, the GPP of the community of autotrophs can be derived from the observed δ¹⁸O

in the environmental CO_2 /DIC combined with knowledge of typical levels of fractionation caused by biotic metabolic processes.

NCP differs from GPP, by accounting for respiration (R) of both autotrophs, and heterotrophs, to produce an estimate of net carbon assimilation within the ecosystem. As NCP includes the net metabolism of all biota within a watercolumn, this process can be described by the balance between photosynthesis and respiration, and hence the net change in DIC or O_2 concentration between the start and end of sampling. Net increase in O_2 (or a decrease in DIC) concentration is described as an autotrophic situation where GPP is higher than R, conversely if R is higher than GPP, net heterotrophy prevails (DIC increases and O_2 decreases). For net heterotrophy to prevail over a longer timescale, a fresh input of POC or DOC is required (Williams et al. 2013). The first attempts at calculating NCP rates in the oceans were made approximately 100 years ago, using in-vitro incubations and measurements of oxygen concentration (Field 1916). Oceanic water samples of a fixed volume were bottled, incubated, and the change in oxygen concentration between the start of the incubation and the end are used to estimate the rate of biological carbon fixation. Bottle incubations still form the basis of many productivity measurements (e.g. Robinson et al. 2002.) Other techniques use in-situ measurements of O_2 / CO_2 to estimate NCP. By accounting for all physical processes that either add to or remove O_2 / CO_2 from the watercolumn (such as gas exchange with the atmosphere), any change in concentration of O_2 / CO_2 between each set of in-situ measurements can be assumed to result from biotic metabolism, and hence represent NCP (Alkire et al. 2011.)

As of 2013, there have been at least 4799 NCP estimates made in the world's oceans, of which 66 % were made in regions outside the oligotrophic gyres (Duarte et al. 2013.) The distribution of NCP measurements is biased towards the North Atlantic, South Atlantic and North Pacific, leaving the Southern Indian, Southern Pacific oceans and highly productive regions such as shelf seas and eastern boundary currents poorly represented (Duarte et al. 2013, figure 1.5.) In-vitro based techniques have been the most commonly used technique to estimate NCP, with 4485 measurements completed, versus 697 for watercolumn integrated samples. There appear to be differences in the NCP values calculated from both techniques (figure 1.6). In-vitro NCP estimates have identified higher individual values of heterotrophy and autotrophy compared to watercolumn integrated samples (figure 1.6). Additionally in-vitro NCP estimates have identified that 40 % of sample sites are heterotrophic, whereas very

few watercolumn integrated studies identify net heterotrophy. Average NCP values indicated net autotrophy on average at 1.2 to 17.5 mmol m⁻³d⁻¹ O₂ for in-vitro and watercolumn integrated techniques respectively (figure 1.6).

Both techniques have their respective problems. A concern for in-vitro samples is that the environment recreated is different to that of the open ocean, hence biological communities in the ocean are not strictly analogous with communities grown in-vitro. Robinson and Williams (2005) reviewed the potential limitations of light/ dark bottle incubations, distinguishing between errors affecting the precision and those that affected the accuracy. As part of the latter, procedural errors (including the omission of light R and the non-linearity in O₂ consumption) and errors of containment (including those pertaining to sample size) were identified. Clearly, any sample excludes part of the natural community, and thus alters both the trophic compartments and interactions. Assuming the universal inverse relationship between size and abundance of organisms (Enquist et al. 1998), and the size-trophic level relationship (Brown 1995), one generalised problem of any bottle incubation is the reduction or removal of grazing pressure over lower trophic levels of the community. In plankton communities, this may lead to an increase in the size of phytoplankton and autotrophic bacterial communities, thus incorrectly representing the dynamics of the natural population (Garcia-Martin et al. 2011).

Watercolumn integration techniques rely on the correct parametrisation of the flux of oxygen via air-sea gas exchange, an inherently difficult calculation due to uncertainties over the effects of waves, bubbles and wind velocity on gas exchange (Nightingale et al 1999.) Additionally, watercolumn inventories require the assumption of a stationary watercolumn with limited advection or diapycnal mixing to ensure that the oxygen signature from surrounding watermasses does not influence the inventory, again an aspect that is difficult to quantify (Alkire et al. 2011.) The selection of the total depth of the watercolumn important to the correct calculation of NCP, too shallow risks the exclusion of some primary productivity, too deep results in the inclusion of aphotic respiration, with both effectively reducing the measured NCP value.

Introduction: Global carbon cycles and the North Atlantic

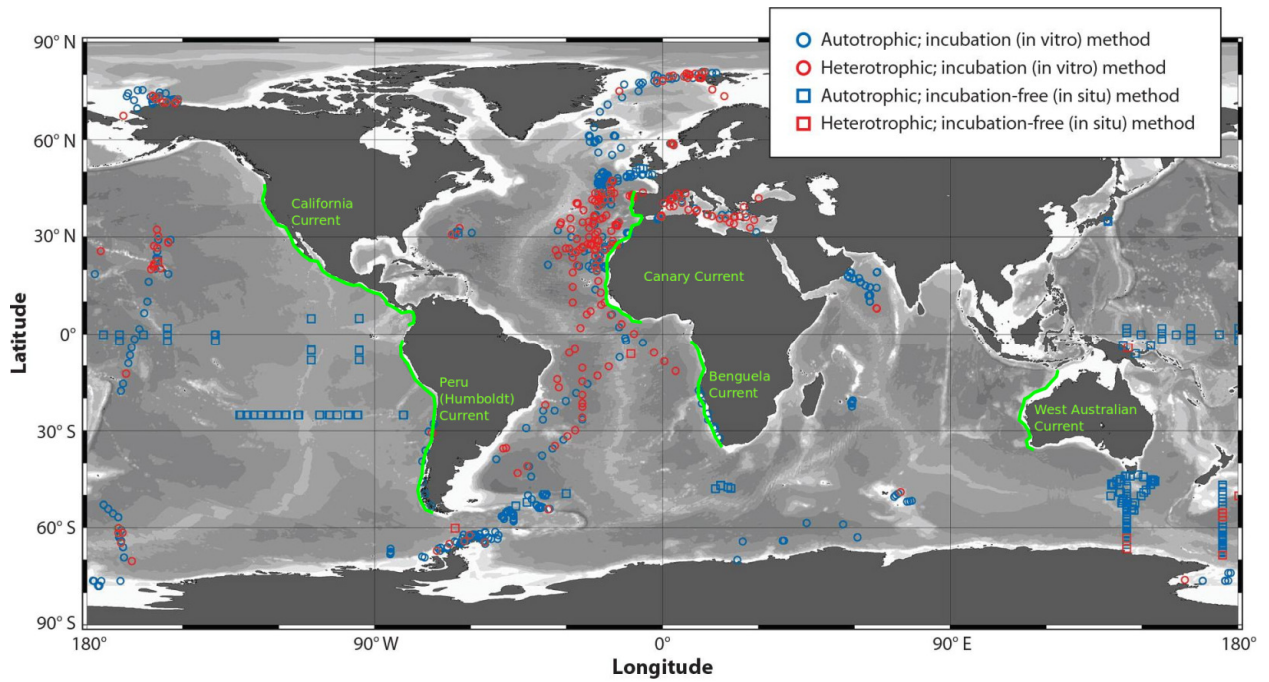


Figure 1.4: NCP data locations coloured by net autotrophy/ heterotrophy. Eastern boundary currents coloured green. Figure modified from figure 3 of Duarte et al. 2013

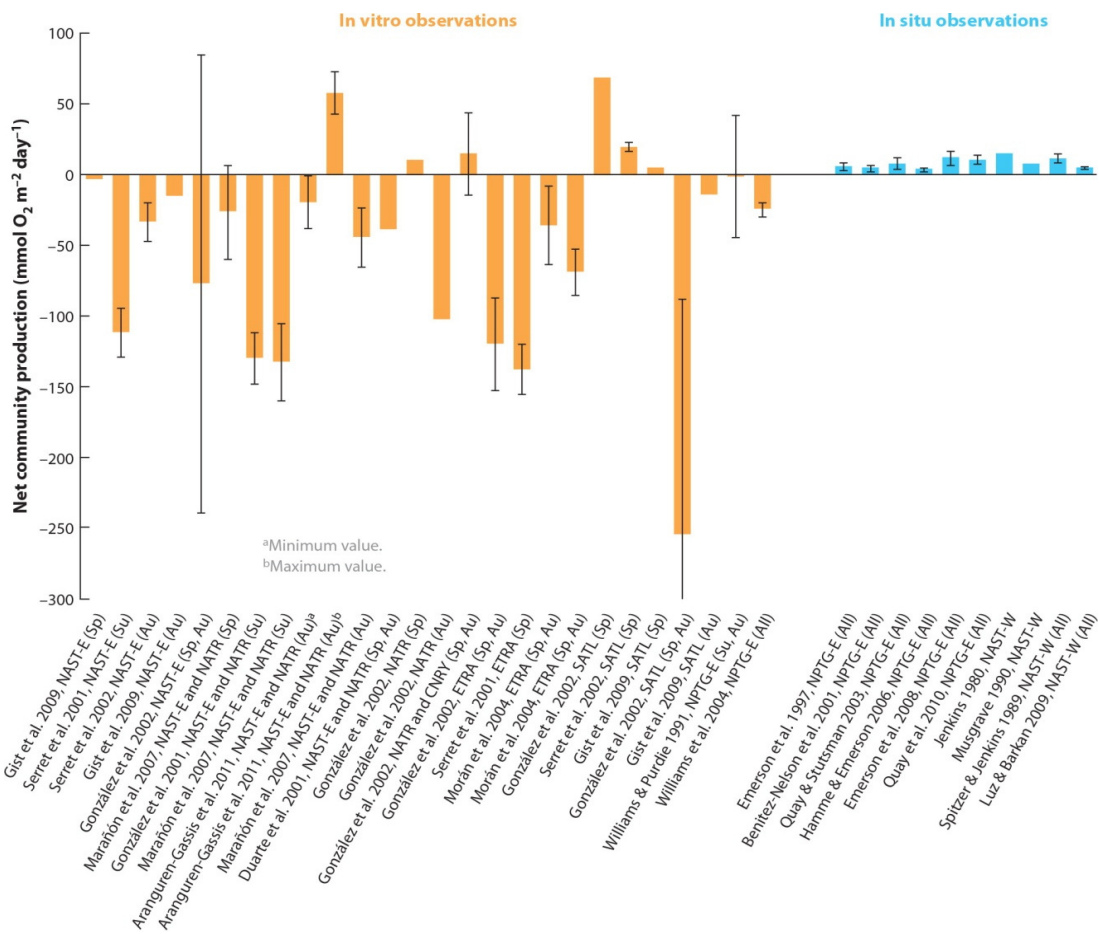


Figure 1.5: Published in vitro and in situ NCP rates for the oligotrophic subtropical gyres in the Atlantic and Pacific. Figure 2. Williams et al. 2013.

Air-sea exchange of carbon ($F_{\text{air-sea}}$) and riverine inputs of carbon (A_{input}) also have to be considered in any NCP mass balance equation:

$$\text{NCP} = \text{GPP} - \text{R} + F_{\text{air-sea}} + A_{\text{input}} \text{ (Duarte et al. 2013)}$$

There has been debate as to whether the higher GPP observed in highly variable shelf seas and EBC regions result in autotrophic NCP values (Borges et al. 2006), or if other environmental factors such as large carbon fluxes from fluvial sources and an efficient grazing community result in heterotrophic NCP values (Smith & Hollibaugh 1993). Although efforts have been made to broadly categorize different EBC/ shelf sea regions into net autotrophic or net heterotrophic using proximity to fluvial carbon sources, localized upwelling conditions and seasonal variability, this is difficult due to a lack of NCP data, hence the net metabolism of these regions is not well constrained (Borges et al. 2006).

1.3 The transect region

The Portugal Current (containing the Iberian Upwelling system), forms the north-eastern boundary of the Sargasso Sea/ North Atlantic subtropical gyre, lying between the meridional Canary Current and the zonal North Atlantic Current (Relvas et al. 2002). Cape São Vicente represents the southern limit of the Iberian upwelling, which is separated from the Mauritanian upwelling by the Gulf of Cádiz. At Cape São Vicente, the coastline abruptly changes from north-south to east-west alignment, forming a boundary between the southern sector of Portugal Current, and the Gulf of Cádiz. To the north, a sharp boundary exists between the Portugal current region and the Bay of Biscay, found north of Viveiro. Between Viveiro in the north and Cape São Vicente in the south, an important feature of the Portugal current region is the near continuous shelf. This shelf, between 10 to 60 km wide, has a shallow gradient until the shelf break (found between 130-250 meters depth, with the Iberian abyssal plain found to the west of the shelf break Barton et al. 2001, figure 1.6). To attempt to quantify the processes occurring within the Portugal current, the Seaglider transect was designed to incorporate both the on-shelf and offshelf areas within at 42.1 °N, an area subject to a large historic dataset completed by the Marine Institute of Vigo (CSIC).

The Seaglider occupied a transect at 42.1 °N, 9.05 to 9.67 °W (figure 1.6, table 1). A total of 17 consecutive transects were completed between yearday 151 (June 2nd 2010) and 223 (August 15th 2010), comprising of almost 1050 individual dives. After the 17 transects

were completed, the Seaglider was instructed to complete one final transect which finished 40 km further west than the previous transects. This was done in order to test the endurance of the platform. Data from this final transect is not included as part of this thesis.

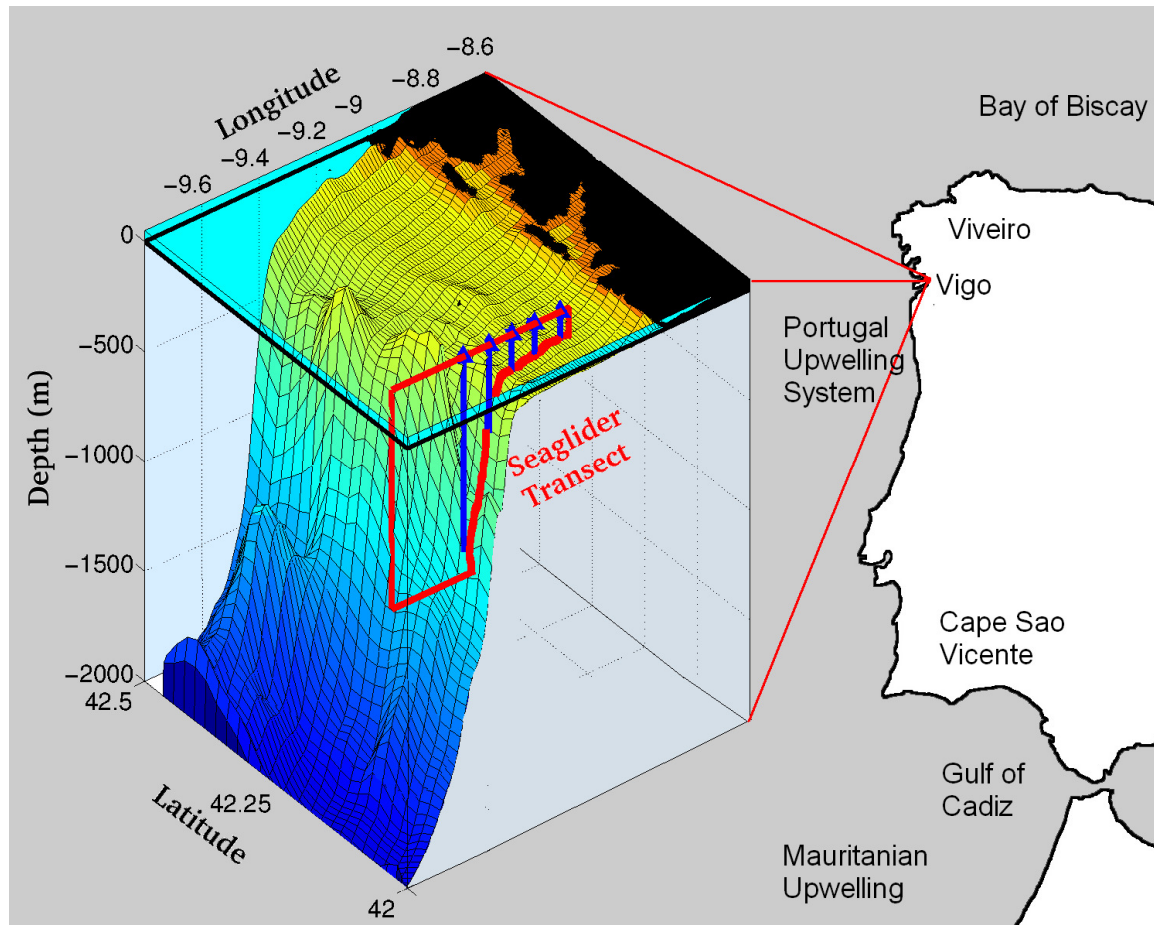


Figure 1.6: The transect region, within the Rias Baixas region. The red lines indicate the transect. A concurrent transect was completed by the Instituto de Investigaciones Marinas de Vigo using the research vessel Mytilus. Her transect is marked by blue lines.

Table 1.1: A list of transects completed by the Seaglider over the course of summer 2010.

Transect	Year Day ST	Year Day END	Dive ST	Dive END	Direction	Longitude ST	Latitude END
1	151	155	1	79	E > W	9.05	9.67
2	155	159	79	138	W > E	9.67	9.04
3	159	162	138	196	E > W	9.04	9.68
4	162	165	196	233	W > E	9.68	9.15
5	165	167	233	271	E > W	9.15	9.67
6	167	171	333	363	W > E	9.67	9.18
7	171	173	363	417	E > W	9.18	9.68
8	173	176	417	486	W > E	9.68	9.05
9	176	181	486	551	E > W	9.05	9.68
10	181	185	551	601	W > E	9.68	9.05
11	185	188	601	657	E > W	9.05	9.68
12	188	191	657	714	W > E	9.68	9.05
13	191	196	714	780	E > W	9.05	9.68
14	196	202	780	833	W > E	9.68	9.05
15	202	206	833	936	E > W	9.05	9.67
16	206	213	936	991	W > E	9.67	9.05
17	213	217	991	1048	E > W	9.05	9.67
Post	217	252	1048	1422	W>E	9.67	9.4

Looking in more detail at the physics involved in the region, the North Atlantic upwelling region shares many characteristics with the other large EBCs (Benguela, California and Humbolt). All four feature slow, broad equatorward flowing currents (forming the eastern boundaries of their respective subtropical gyre), a N-S alignment of coastlines and dominant equatorward wind conditions that prevail for a substantial portion of the year (Relvas et al. 2007). The combination of N-S coastal alignment and equatorward winds result in offshore Ekman transport and a lowering of sea level along the nearshore regions of these currents (hence the upwelling of deep water and resulting high productivity (Relvas et al. 2007)). Geostrophic adjustment in response to this along-shore lowering of sea level results in an alongshore (equatorward) baroclinic jet, transporting nutrient rich upwelled water parallel to the continental margin. The prevalence of northerly, upwelling favourable winds in the Iberian upwelling region varies throughout the year, occurring most frequently between late spring and autumn (Lorenzo et al. 2005). In contrast, during the winter, southerly winds predominate, resulting in the mass transport of water northwards, onshore Ekman transport and hence downwelling (Lorenzo et al. 2005). Although these two regimes are strongly

associated with the aforementioned seasons, the wind forcing observed across the region is highly variable, hence upwelling favourable conditions occasionally occur in the winter, and downwelling in the summer (Barton et al. 2001). Furthermore, the time response of the Iberian upwelling system switching from upwelling to downwelling regimes in response to a change in wind forcing is short, and has been calculated between 24 to 72 hours (Torres & Barton 2007).

The summertime wind forcing over the Iberian upwelling system is hugely variable (on a typical time scale of 10-15 days), which results in repeated switching between upwelling, relaxation and downwelling over a single summer season (Torres & Barton 2007). Under a persistent northerly wind, fully developed upwelling can occur. Fully developed upwelling can be noted by the development of an onshelf front, and the formation of major filament structures. These filaments, which are fast, westward flowing baroclinic jets usually forming in close proximity to capes and other topographically rough features, transport upwelled water from the near shore environment to beyond the front, often extending further than 200 km from the shoreline (Barton et al. 2001, Relvas et al. 2007). These filaments are of great interest, as they export significant volumes of plankton, organic matter and sediment outside of the EBC, and into oligotrophic offshore regions of the North Atlantic. As filaments and high productivity from upwelling occur simultaneously and provide a pathway by which to export new production into the open ocean, these fully developed upwelling events are an important mechanism for off-shelf transport and sedimentation (Arístegui et al. 2006).

Below the surface, a deep, (>150 m) poleward countercurrent has been found in the Iberian Upwelling system over the summer season (Barton et al. 2001, Relvas et al. 2007). This countercurrent acts to compensate the along-coast mass transport produced by the summertime equatorward surface currents, and is responsible for the northwards transport of Mediterranean outflow waters, into the subpolar North Atlantic (Barton et al. 2001, Relvas et al. 2007).

1.4 Productivity of the Transect region

Analysis of chlorophyll and sedimentation has indicated that the Portugal current is a highly productive region (Bode & Varela 1998; Vilas et al. 2005; Tilstone et al. 1999). However, both total phytoplankton carbon and phytoplankton community structure have been shown to be highly dependent on watercolumn physics (discussed above, Cermeño et al. 2006). Fully developed upwelling result in a substantial increase in the population of medium

to large-sized phytoplankton (such as diatoms and flagellates), and a large total mass of phytoplankton carbon (figure 1.8). A relaxed summertime watercolumn features almost half of the total phytoplankton carbon of an upwelling watercolumn, but a similar community composition in terms of phytoplankton size classes (figure 1.8). During wintertime downwelling, the phytoplankton community is generally smaller, featuring more pico and nano phytoplankton, consummate with the less fertile watercolumn found during a downwelling event. The cell size fraction has an important influence on both NCP and export from the photic zone, as smaller cells are more readily remineralised in the euphotic zone, whereas the POC derived from large summer phytoplankton populations is more likely to be exported to the shelf floor, or westwards off shelf (Cermeño et al. 2006)

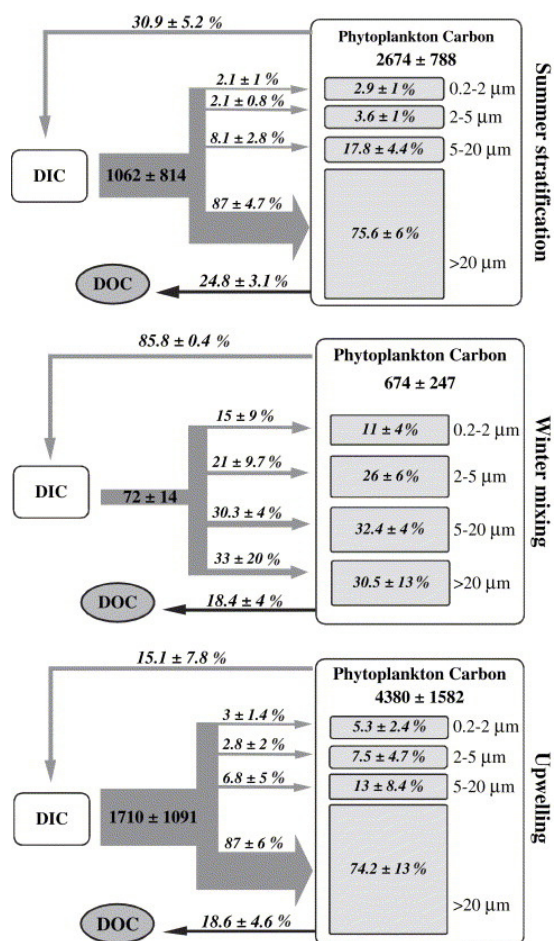


Figure 1.7: Plankton carbon budgets under the three watercolumn regimes, stratification, upwelling and winter mixing. Carbon fluxes are displayed in bold, as mg C m⁻² d⁻¹. Phytoplankton biomass is expressed in mg C m⁻². Italic numbers indicate the relative contribution of any given flow or phytoplankton size fraction to GPP or total phytoplankton carbon. From figure 6, Cermeño et al. 2006.

Studies on NCP in the region are limited (Alvarez-Salgado et al. 2011). One study on the Ria de Vigo found that the region was highly productive, with average PP over the summer season (April- October) between 100-125 $\text{mmol C}^{-2} \text{d}^{-1}$, rising to $> 250 \text{mmol C}^{-2} \text{d}^{-1}$, during upwelling events. High GPP and NCP values were likely to be due to location of the study region on the inner continental shelf, (between 8.95° and 8.8° W). This region is heavily anthropologically influenced by run-off and sewage outflow, and so is unlikely to be representative of either the outer shelf (encompassed by the transect region) or the greater Portugal current region (Alvarez-Salgado et al. 2001.)

1.5 Gliders and autonomous underwater vehicles

Autonomous underwater gliders constitute a new class of oceanography sampling platform. With hydrodynamic wings designed to generate lift, they glide through the water using subtle changes in buoyancy controlled using internal hydraulics. Gliders have proved an invaluable tool in many applications owing to their low operational costs, autonomy and ability to complete long-range, long duration deployments in harsh environments ranging from the Weddell Sea to the North Atlantic (Queste et al. 2012). The attitude of glider flight is controlled by moving a heavy internal mass to promote a change in the glider's centre of gravity. This in turn changes the position of the wings relative to direction of travel, and hence enables the glider to steer by altering the direction that the lift force generated by the wings is applied (Erikson et al. 2001, discussed further in chapter 2.1.) Gliding flight, driven by the difference in density between the glider and surrounding water mass enables the glider to change depth, becoming negatively buoyant on downcasts, and positively buoyant on upcasts.

Gliders travel slowly, a Seaglider's typical velocity is between 10 and 30 cm s^{-1} , making the glider much slower than traditional propeller-driven autonomous underwater vehicles (AUVs). However, the low energy method of propulsion enables mission durations of many months (Erikson et al. 2001), and thus enables the glider to be used for season-long observations of the watercolumn relatively inexpensively compared with other AUVs or research ships. The operational costs of gliders are approximately \$2 per km (including ship time for launch and recovery, telemetry and post-mission refurbishment), allowing a typical glider to be operated for a year for the equivalent cost of 24 hours of ship-time, with the entire glider only costing 2-4 days of ship time (at \$100,000 to \$160,000, Graver 2005.) A range of small, energy efficient sensors has been developed for AUV/ glider based

deployment. These include oxygen optodes, conductivity-temperature cells and fluorometers (Erikson et al. 2001).

Two previous AUV studies of NCP calculated using Jenkins and Goldman's (1985) oxygen inventory technique have been completed prior to this mission (Emerson et al. 2008, Alkire et al. 2011). Both used Lagrangian, (free drifting) PALACE floats or drifters, deployed in a mid oceanic setting. In this thesis, NCP measurements using the oxygen inventory technique are completed using an Eulerian sampling technique. This required the Seaglider to maintain a transect within the EBC region, in a similar way to most ship borne measurements of oxygen inventory NCP (Peng et al. 1987; Jenkins & Goldman 1985). As this technique is not sampling the same watermass, calculating NCP requires the assessment of various factors that potentially influence the oxygen inventory, such as the advection of watermasses within the region. Essentially, the change in oxygen inventory that results from biological processes needs to be separated from any inventory changes caused by physical processes, and this is described in more detail in chapter 5.

1.6 Aims of the thesis

The Seaglider is a relatively novel platform, with few published papers existing at this time. The instruments used on the Seaglider are also relatively novel, with very little in the way of accepted calibration protocol. Therefore, there are two broad themes of this thesis, the processing and collection of data, and observations of upwelling in the transect region during 2010. The first section of this thesis is dedicated to demonstrating a satisfactory technique to calibrate the instruments of the Seaglider, flag data according to its reliability and discuss the performance of the Seaglider over the duration of the mission. Chapter two has a main focus on the mechanical functioning of the Seaglider, as well as the calibration of the Seabird conductivity salinity cell and the WetLABS ECO puck fluorometer/ CDOM/ Backscatter sensor. Chapter three deals with the calibration of the Aanderaa 4330 fast-foil optode. A supplementary section (found within the appendix) discusses the use and performance of a wildlife tracking tag, the Wildlife computers SPOT-5 Argos tag, which was used on some of UEA's Seaglider missions as a failsafe against Seaglider failure. This

section does not directly relate to the Iberian upwelling system, but is potentially useful to users of the Argos system, hence its inclusion within this thesis.

The second half of this thesis concentrates on the results from the study. The results are broadly split into two, the first part is a discussion of the Iberian upwelling system over summertime 2010, including physical observations of the watercolumn, and a qualitative discussion on the upwelling and relaxation processes observed. The response of phytoplankton to these events is discussed with reference to the Seaglider's oxygen, chlorophyll a, backscatter and colour-dissolved organic material measurements.

Seaglider oxygen measurements are used to calculate an estimate of NCP using a novel Seaglider based watercolumn inventory calculation, described in chapter five, with the aim of answering the question: is the Iberian upwelling system a net source or sink of carbon from the atmosphere?

2 Design, flight behavior and sensor calibration of a glider

2.1 The Seaglider

The development of ALACE (Autonomous Lagrangian Circulation Explorer) and PALACE (Profiling ALACE) floats by Davis and Webb during the 1980's laid much of the groundwork required for glider development (Graver 2005). The ALACE floats, and other similar floats termed collectively as 'Argo' floats, can dive from the surface of the ocean, to a preset depth (typically 2 km) and then resurface and automatically transmit data collected during the dive via satellite. These floats are ballasted to be neutrally buoyant in the watercolumn. When the float dives, an external, oil filled rubber bladder is emptied, with the oil pumped inside the pressure hull of the float. This oil transfer acts to decrease the float's overall volume, whilst retaining the floats overall mass, thus increasing the float's density to a point that it becomes negatively buoyant in the water, and sinks. The reverse process, using an electric buoyancy pump to refill the external oil filled bladder, allows the float to attain positive buoyancy, and start to move towards the surface. Once on the surface, the float is able to transmit via the Argos or Iridium satellite datalink systems (Graver 2005).

Henry Stommel's visionary paper "The Slocum Mission" took the concept of the ALACE floats further, suggesting that small, autonomous profiling gliders could, one day, be roaming the world's oceans (Stommel 1989). The key difference between Stommel's hypothesized gliders and the ALACE floats was the ability for the user to steer the gliders via a series of waypoints, rather than simply drifting with the local ocean currents (*as per* ALACE floats). Essentially, whereas an ALACE float is a Lagrangian method of data collection, the glider was Eulerian. These gliders would use the thermal gradient above and below the thermocline as a source of energy to power the buoyancy device (the 'thermal engine'), remaining at sea for many months or years without maintenance. 24 years later, Stommel's ideas have largely come to fruition, and there are indeed many dozens of underwater gliders traversing the world's oceans. Commercialisation of these underwater gliders has seen the replacement of the thermal engine with a simpler electronic buoyancy pump, however, the long mission duration, and ability to control the direction-of-travel of the gliders postulated by Stommel

Design, flight behavior and sensor calibration of a glider

remains. As of 2013, there are three main commercial designs of glider, the University of Washington Seaglider, the Webb Research Slocum glider and the Scripps Spray glider (figure 2.1.) All gliders in figure 2.1 use a buoyancy engine and wings for movement, and the size, maximum operating depth, mass and mission duration of each of the gliders are broadly comparable.



Figure 2.1: A comparison of the three main commercialized gliders, with data from respective developers websites (Slocum- www.webbresearch.com/slocumglider, Seaglider- www.seaglider.washington.edu and Spray- www.spray.ucsd.edu)

Seagliders were developed originally at the Applied Physics Laboratory, University of Washington (UW APL), and subsequently manufactured by iRobot and then Kongsberg under license. One of Stommel's original ideas was that gliders would be portable and easy to handle manually. Seagliders fulfill these criteria, featuring a mass of 52 kg, a length of 1.8 m and a wing-span of 1 m. These relatively modest dimensions enable the deployment and recovery of the vehicle without heavy lifting equipment (figure 2.1, Eriksen et al., 2001).

Seagliders are constructed with a glass reinforced plastic (GRP) fairing around an aluminium pressure hull, with two GRP wings, a polycarbonate rudder and a carbon fibre

Design, flight behavior and sensor calibration of a glider

aerial attached to the fairing. The void between the pressure hull and fairing is filled with seawater. The pressure hull has been engineered to have the same compressibility as seawater, thus ensuring that there is virtually no change in buoyancy as the Seaglider dives or climbs through the water column.

The interior of the pressure hull houses two lithium sulphuryl chloride batteries at 24 V and 10 V. The 24 V-battery powers the motors, the 10 V-battery powers the sensors and electronics assembly. The 24 V-battery weighs 9 kg and is housed within the mass shifter (section 2.2), whilst the smaller 2.6 kg 10 V-battery is housed above the main electronics assembly. This electronics assembly contains the main microprocessor (Motorola MC68332), an electronic compass and the Iridium telecommunications modem. Towards the rear of the pressure hull are housed the LeDuc hydraulic pump, hydraulic fluid reservoir and control valves of the variable buoyancy device (VBD, discussed in section 2.2). An acoustic transducer is mounted at the front of the pressure housing, in the flooded section between the pressure housing and the fairing.

The Seaglider navigates using a combination of a Global Positioning System calculated geolocation (GPS), and compass-enhanced dead reckoning. Communication to the Seaglider during missions is via a two-way data link transmitted through the Iridium satellite system, received whilst the Seaglider is on the surface (figure 2.2, Seaglider positions 'A' and 'G', Eriksen et al., 2001).

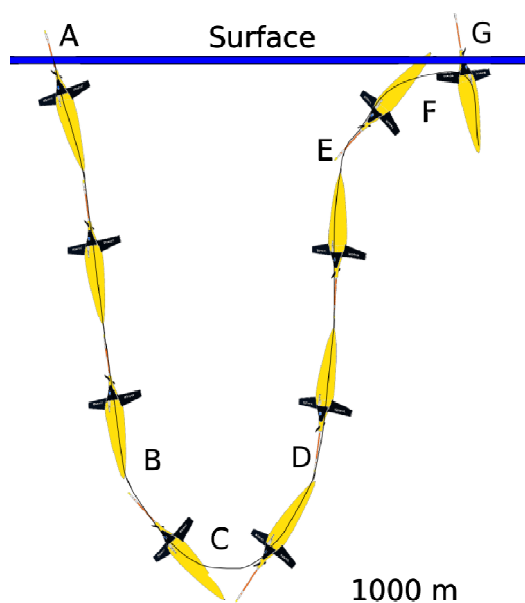


Figure 2.2:

A schematic of a Seaglider dive to 1000 m. Diving positions A-G are discussed in section 2.2.

2.2 Seaglider dives

One of the principal design parameters for the Seaglider was a long mission duration achieved through low motor and instrumentation energy use (Erikson et al. 2001). To achieve this low power consumption, the Seaglider combines a highly hydrodynamically efficient body with an energy saving buoyancy engine (the VBD) for propulsion. In much the same way that ALACE floats control their buoyancy, the VBD pumps hydraulic fluid from inside the pressure hull to a small neoprene bladder mounted in the flooded rear section, with this process increasing the total volume, without altering its total mass. Inflating the external bladder decreases the density of the Seaglider and gives positive buoyancy compared to the surrounding water. By completing the opposite process; transferring the hydraulic fluid from the external bladder into the internal reservoir in the pressure hull, the Seaglider gains a higher density than the surrounding water, and starts sinking.

Looking in more detail at an individual dive, the Seaglider moves in a series of saw-tooth shape dive profiles, driven using changes in vehicle buoyancy and controlled by the Seaglider guidance control (GC) functionality. From position 'A' (figure 2.2), the Seaglider decreases its buoyancy, and starts to sink through the water (B), until it reaches its maximum dive depth (maximum operational depth is 1000 m). At this point (C in the schematic, referred to as 'apogee' throughout this thesis) the Seaglider increases its buoyancy and starts to travel towards the surface (D). Once the Seaglider reaches the surface (E), it moves its aerial above the water surface (F), and starts Iridium communications (G), thus completing a dive-climb cycle.

The default depth of apogee, (C), is 1000 m. However, our Seaglider transect incorporated parts of the Galician continental shelf that were significantly shallower than 1000 m (figure 1.6). To prevent the Seaglider crashing into the seafloor at positions B or C, the apogee depth can be pre-programmed into the Seaglider prior to the dive. Alternatively, a bathymetric map can be loaded into the Seaglider's memory, and used to

Design, flight behavior and sensor calibration of a glider

define apogee. These techniques were found to be unsuitable for this region, due to the inaccuracy of local GEBCO bathymetry data (figure 2.3). Instead, the Seaglider's acoustic transducer was used to range for the Seafloor, and this was used to define the apogee depth. As this is an in-situ acoustic measurement of the Seafloor, we found this method to be more accurate than GEBCO bathymetry.

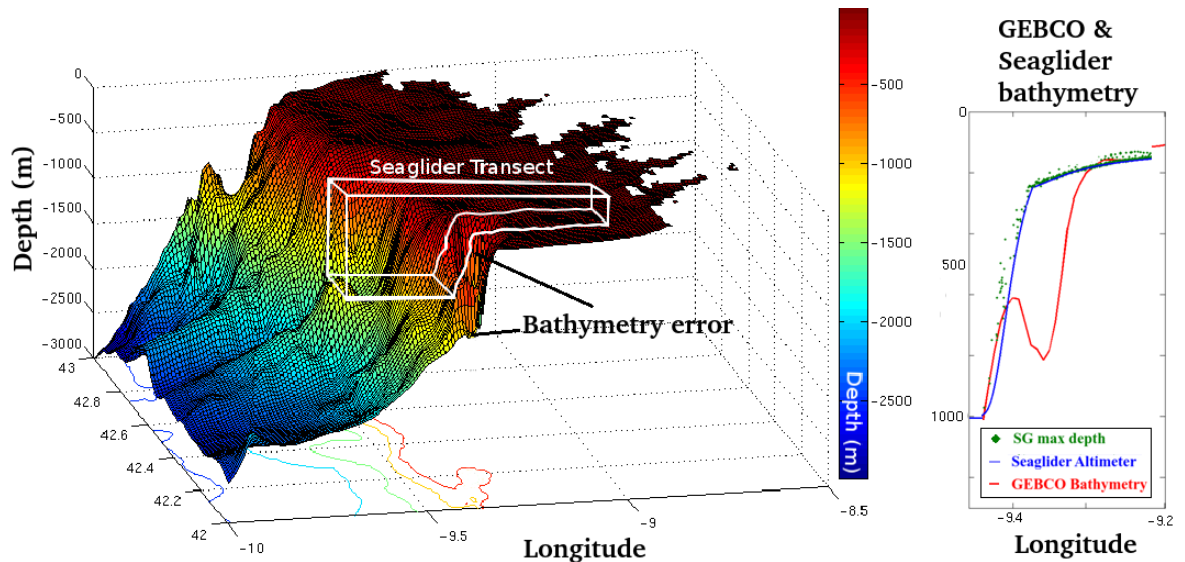


Figure 2.3: GEBCO bathymetry compared with Seaglider depth of apogee, and Seaglider acoustic transducer measured seafloor depth. Note inaccuracies in GEBCO bathymetry at -9.36 W.

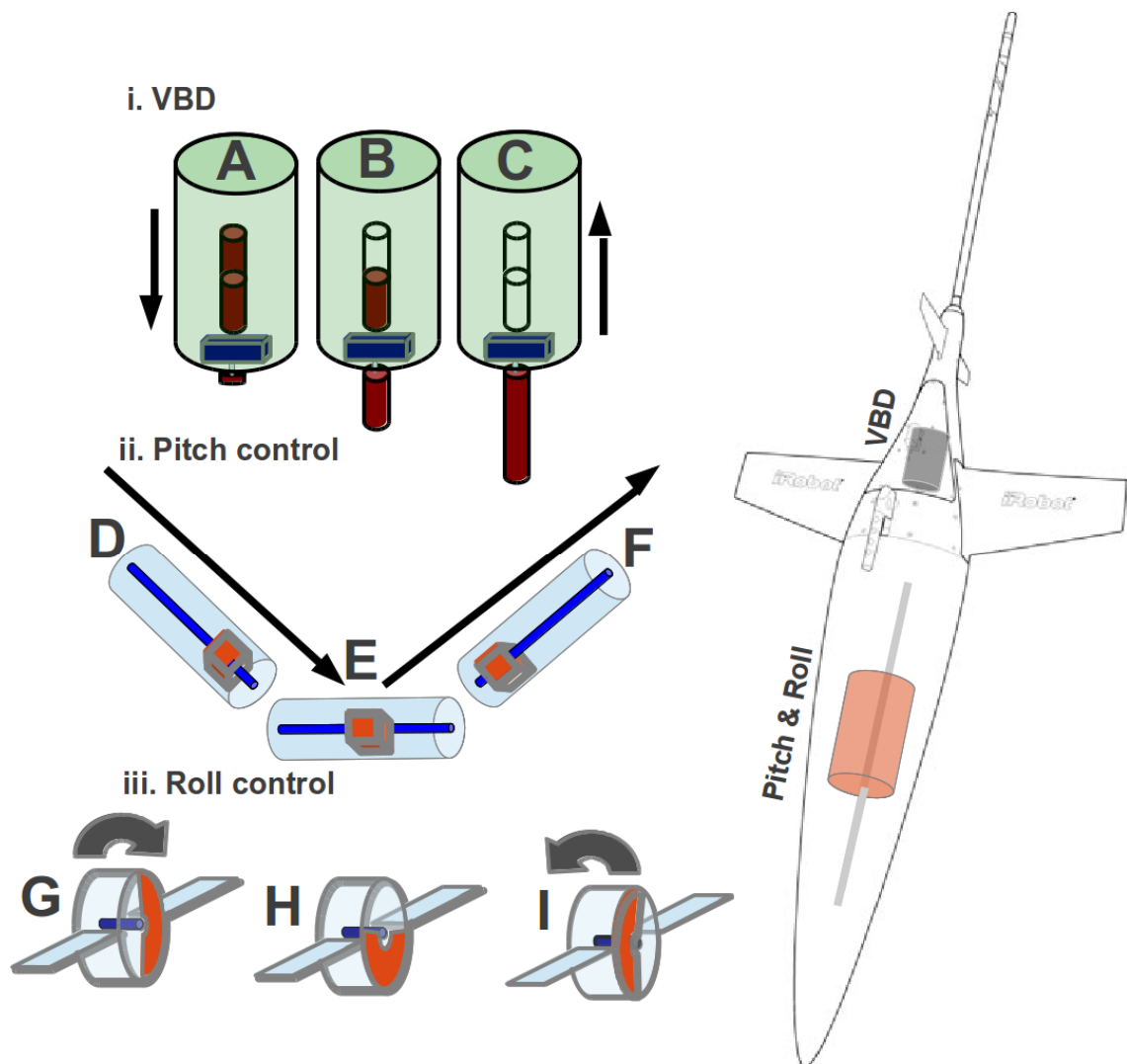


Figure 2.4: Basic principles of the glider operation (Seaglider outline modified from an iRobot engineering diagram).

I. Buoyancy engine or VBD. In situation 'A', the oil-filled external bladder is deflated, resulting in the Seaglider having a higher density than the surrounding water, and the Seaglider moving towards the sea floor. In 'B', there is no density difference between the Seaglider and surrounding water column. In situation 'C' the bladder is completely filled, the Seaglider is less dense than the surrounding water, and hence the Seaglider moves towards the surface.

II. Pitch control. The Seaglider can alter the pitch angle (the angle between the tail of the Seaglider and the nose) by moving its heavy battery pack fore and aft.

III. Roll control. The Seaglider can roll from side to side by rotating the battery pack.

Design, flight behavior and sensor calibration of a glider

As discussed above, the Seaglider's vertical motion is actively controlled by adjusting buoyancy using the VBD; its horizontal motion is achieved using a passive 'gliding' technique. Gliding is achieved using two laterally mounted wings to generate hydrodynamic lift by the use of an aerofoil profile (see Seaglider schematic in figure 2.4). Much like an aerial glider, lift is generated as the Seaglider moves vertically through the water. By careful control of the attitude (the orientation of the aerial-to-nose axis relative to the horizon), the force generated by this lift has a component in the horizontal direction, thus allowing the Seaglider to travel horizontally.

Adjustments to the attitude are completed using both pitch and roll controls (Figure 2.4). Pitch control adjusts the angle of the nose with respect to the horizontal. Sliding the 24 V-battery pack forward within the pressure hull adjusts the centre of gravity, thus pointing the nose downwards (figure 2.4). Roll control is achieved by rotating the heavy central mass within the pressure hull, from side to side. This rotation alters the centre of gravity, thus causing the Seaglider to roll about its nose- aerial axis. The adjustment of roll and pitch adjusts the vector direction of lift forces, and acts to both control the glide angle and to steer the Seaglider.

The control of this gliding motion enables the Seaglider to travel in a saw-toothed glide path, diving at an angle of 15 to 45° from the horizontal to depths ranging between 55 m and 1000 m (during GOPINA). The glide path, vertical velocity and bearing are adjusted using VBD, roll and pitch controlled by the autonomous guidance control (GC) function. GC attempts to achieve user set dive parameters for maximum vertical velocity, heading, maximum depth and latitude and longitude waypoints.

As long mission duration was a key aspect of the GOPINA campaign, much effort was put into minimising power consumption from Seaglider flight. Power consumption during flight has previously been found to exhibit an exponential relationship with vertical velocity (due to increasingly turbulent flow over the Seaglidiers body with increasing velocity, Eriksen et al. 2001), thus requiring more VBD use to maintain the higher speed. For this reason vertical velocities during GOPINA were kept low, with a typical dive-climb cycle completed at approximately 0.1 m s^{-1} .

Design, flight behavior and sensor calibration of a glider

Instrumentation used on the Seaglider has been designed specifically to maximise energy efficiency. The Seaglider deployed on the GOPINA mission featured a Paine Corporation pressure sensor, SBE conductivity temperature cell, Wetlabs ECO puck triplet (measuring chlorophyll *a* and coloured dissolved organic material fluorescence, and 650 nm wavelength light backscatter) and an Aanderaa oxygen optode. Both sensors and main electronics board are programmable to switch between sampling mode and a lower powered 'stand-by mode' at user-defined frequencies. By decreasing the sampling rate of the instruments, average power consumption per dive decreases. This enables mission duration to be increased, albeit at a loss of data spatial resolution. The sampling rate selected for GOPINA reflected this trade-off, with the majority of the mission completed with a 10 s sampling interval of all sensors to a depth of 200 m. Below 200 m, the Wetlabs ECO puck triplet was turned off, and the CT and optode were set to a 20 s-sampling interval. The main electronics board was set to complete GC at an interval of 60 s above 200 m, and 60 s below 200 m. The effects of a lower sampling frequency below 200 m in addition to fewer energy-intensive apogee and surfacing manoeuvres per hour, was a lower power consumption. The glider used an average of 2.1 watts over the course of an 1000 m dive, and 3.6 watts for an < 200 m dive (also see Queste et al. 2012).

2.3 Seabird Electronics CT cell overview

The Seabird Electronics conductivity/temperature (CT) cell is mounted on top of the fairing, towards the aft of the Seaglider. Salinity measurements require accurate measurements of temperature and conductivity; therefore, the output from the CT cell has to be carefully calibrated and corrected to ensure high quality of Seaglider data (Lueck 1990). To achieve the low levels of energy consumption previously discussed, the SBE CT cell does not use an active pumping method to flush the conductivity cell, instead relying on the passive flushing of the conductivity cell generated by the Seaglider's motion through the water column (Figure 2.3). One potential drawback of passive cell flushing is the uncertainty associated with thermal inertial lag. SBE CT thermal inertial lag (as discussed by Lueck (1990)), describes the lag in conductivity measurements resulting from heat stored in the wall of the conductivity cell influencing the temperature

Design, flight behavior and sensor calibration of a glider

properties of a water sample while the instrument moves through a thermal gradient. No sensor can react instantaneously to an environmental change; there is always a lag present in sensor detection. If the environmental rate-of-change is slower than the sensor lag, (e.g. CT sensors mounted on stationary platforms, such as buoys), this lag does not pose an issue. If the CT sensor is mounted on a moving platform, but features a pumped system, thermal inertial lag can be corrected by estimating the heating effect of water flow through the conductivity cell (Lueck 1990). In the Seaglider's unpumped system, water flow through the CT cell is not measured directly. To calculate the correct sensor lag, salinity data from the SBE CT were initially processed from the raw data files using the iRobot/UW APL processing program (which includes SBE's laboratory sensor calibration parameters for the specific CT cell fitted to our Seaglider). The output from these scripts includes T, S and pressure and a timestamp during which this data were collected. T and S and vertical velocity (calculated from the change in pressure/ time) from all of the Seaglider dives are interpolated onto a 0.5 m vertical grid. An arbitrary lag correction of two seconds is then applied to the T and S data. Through small (0.5 second) adjustments to this thermal inertial lag time correction, a series of gridded outputs from up and downcasts featuring different lengths of lag correction was produced. Each pair of up and downcasts with the same lag-correction can be compared by subtracting one from another, and calculating an average root-mean-squared (RMS) value for a complete dive. Repeating this process for a large number of repeat dives, over a sufficiently long timescale to limit noise from short-term watercolumn variability (e.g. internal waves and tides), enables an optimized lag correction to be calculated. (We define this as the time correction that results in the lowest RMS difference between up and downcasts). This technique was used on the entire dataset, providing an estimate of the optimum lag correction based on the up and downcast data from 1300 + dive (Schmidtke et al., in prep, Queste et al. 2012, and discussed further in chapter 3.3).

Seabird Electronics CT cell data quality control and flagging

All salinity data in this chapter are given as thermal inertial lag corrected, practical salinity (as per the UNESCO PSS-78 definition, Knap 1996). Over the course

Design, flight behavior and sensor calibration of a glider

of the Seaglider mission, the CT cell data was checked for accuracy three times, on the 1st of June, 29th June and 30th July 2010, against a co-located CTD rosette transect completed by the research vessel R/V Mytilus, operated by the Institute of Marine Research, Vigo, Spain.

The technique of using calibrated T-S measurements from the R.V. Mytilus, for the in-situ calibration of the Seaglider is dependent on watercolumn variability. The watercolumn within the Iberian upwelling is variable (in terms of T-S properties) in the near surface, owing to a mix of Ria outflow waters, upwelled deep water, and solar heating (figure 2.5, Peliz et al. 2002). However, below the thermocline, the T-S properties become more stable, and are a product from end-member mixing between three water masses (figure 2.5 and Chapter 4.1). Therefore, in-situ calibrations are optimized by the use of water below the thermocline.

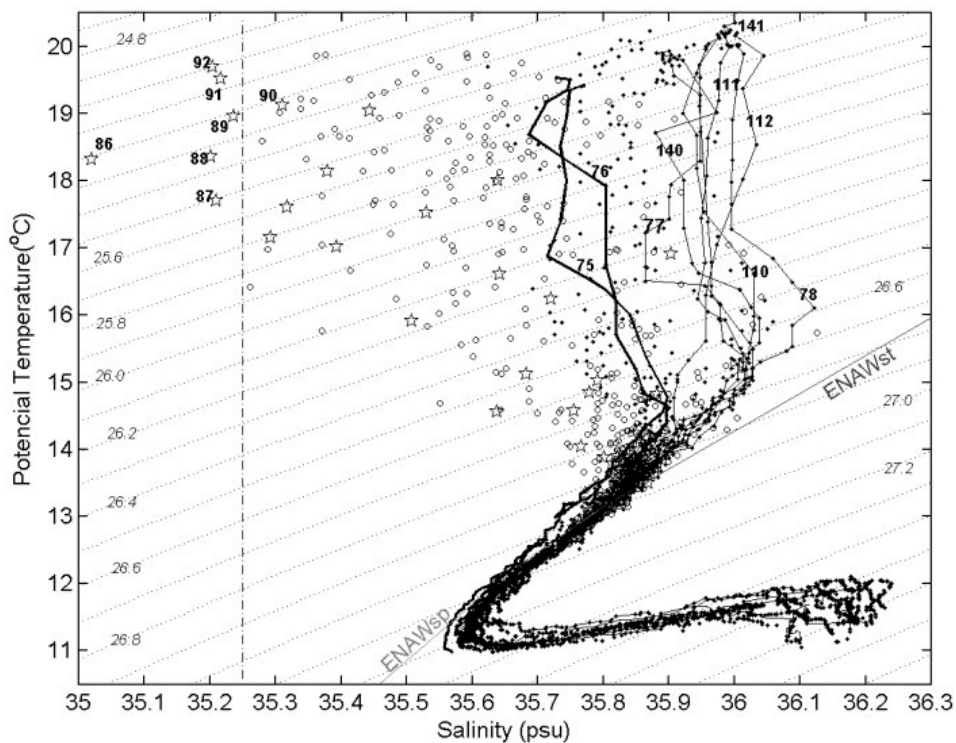


Figure 2.5: T-S diagram to show regional summertime variability within the Iberian upwelling region. Central Water mass curves are represented for ENAWst—Eastern North Atlantic Central Water (subtropical branch) and ENAWsp—Eastern North Atlantic Central Water (subpolar branch). Symbols are as follows: ○—stations over the shelf with less than 150-m; ○ - deep stations with more than 150-m deep; and ★—stations between 8.7–8.9°W. From Peliz et al. 2002

Design, flight behavior and sensor calibration of a glider

The distance between the CTD rosette and the Seaglider was 1800 m, 4000 m and 3300 m, respectively, for the three calibration dates. The Mytilus' rosette was fitted with a pumped Seabird Electronics 25 CTD. All Mytilus CTD data were initially processed using SBE Software Version Seasave V 7. Thermal inertial lag was corrected using this software, and conversion of conductivity, depth, latitude and depth to salinity was completed using the Matlab TEOS-10 toolbox (Feistel 2010). CTD measured salinities agreed to within 0.05 with bottle samples (analysed using a salinometer) taken from the same depths (figure 2.5), and within 0.01 at deeper depths of > 100 m. Thus, CTD salinity values were judged suitable to be used for Seaglider CT cell calibration.

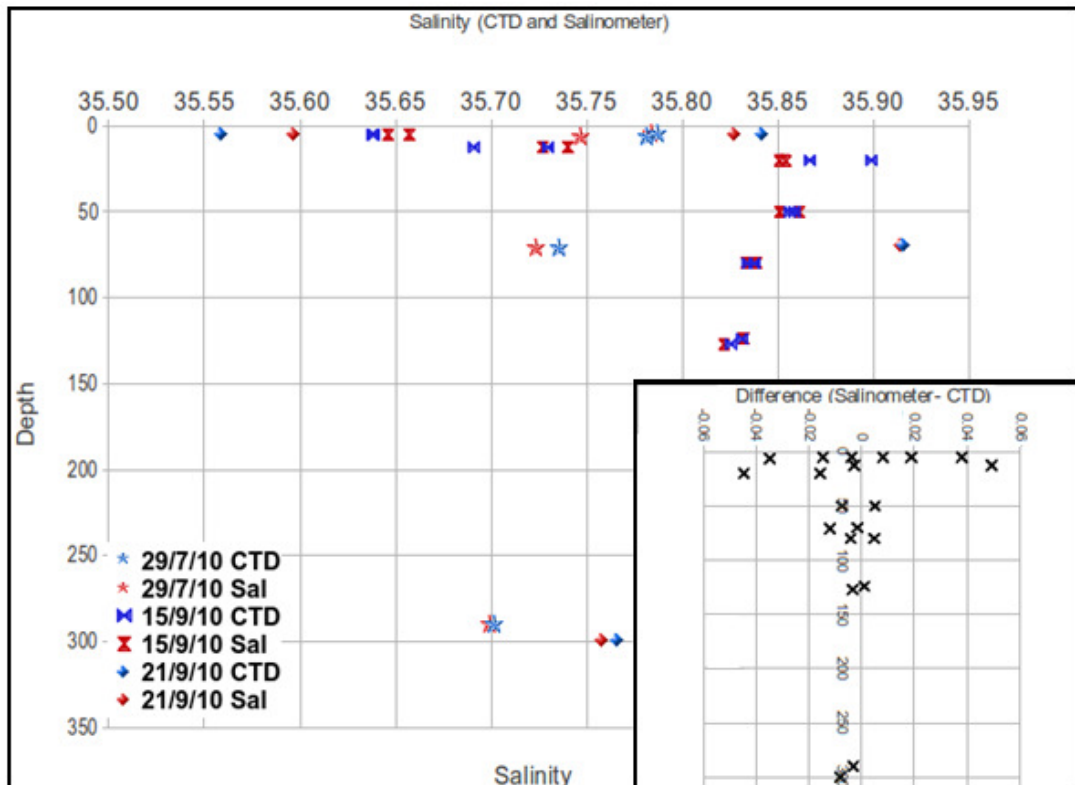


Figure 2.5: Seabird Electronics 25 + Sealogger CTD salinity values with corresponding salinometer-measured salinities from the 29th July, 15th September and 21st September 2010. @CTD refers to salinity measured by the CTD mounted SBE sensor. Sal refers to salinometer measurements from bottle water samples. Inset: Differences in salinity values for each individual sampling point, between salinometer and CTD values.

Salinity Data Analysis (including flagging definitions)

Following the suggested flagging categories (UW-APL flagging instruction manual, 2012), salinity data from the CT cell was flagged as one of five categories:

QC_GOOD – Value is OK, and falls within published historic data

QC_APOGEE- Value falls within historic data and Seaglider vertical velocity is <2 cm/s

QC_OFFSET- Value falls outside historic data in the region

QC_OSAPPLIED- Value falls outside historic data in the region, but shape of TS plot is correct and a linear offset has been applied to bring the data within the range of historic data

QC_BAD- Data is untrustworthy and uncorrectable due to either salinity values falling outside the expected range, or anomalous spikes.

For subsequent chapters, only QC_GOOD and QC_OSAPPLIED data are used. To generate the flagging definitions, all data is first passed through a bandwidth filter of 33 to 36.9 PSU, or 0.5 outside the absolute highest and lowest salinity values of 33.5 to 36.4 PSU observed in the transect region between 42.0 to 43.0° N and 8.1 to 12.5° W (Barton et al., 2001, Alvarez-Salgado et al., 1993, 2001 & 2009). Data falling outside these ranges are flagged as QC_BAD. Occasionally, data output from the T-S sensor features anomalous salinity spikes, defined here as a single salinity data point that is 0.5 higher or lower than the nearest values from the 5 preceding and 5 successive salinity measurements. As the dataset features sub-1 m T-S resolution at all depths for the entire mission, such a large salinity change over a small depth range is treated as a spike and flagged QC_BAD.

As the CT cell is unpumped, the flushing rate of the cell is low in three situations: during the surface manoeuvre, during apogee, and at any time the velocity of the Seaglider with respect to the surrounding water parcel tends towards zero. To identify these potentially incorrect data points, T-S data collected when the vertical velocity of the Seaglider (calculated using measured pressure change / time), falls below 2 cm/s, are flagged as QC_APOGEE (figure 2.5). The flagging of data during these slow velocity periods also removed another source of potential error: water entrained in the void space

between the aluminium pressure hull and the fibreglass fairing could be released into the path of the CT cell, causing anomalous C & T readings (UW-APL flagging instruction manual, 2012).

QC_OFFSET

Previous UEA Seaglider missions conducted in Loch Linnhe, Scotland have indicated that the CT sensor is susceptible to the intake of particulate into the conductivity cell, resulting in both conductivity and salinity offsets. An offset of approximately -1 was observed in the Vigo dataset between dives 366 to 472, with off-shelf salinities at 400-500 m decreasing from 35.75 – 35.85 immediately before the suspected offset event, to 34.70 to 34.79 directly afterwards. This offset event was confirmed as an instrument fault using a salinometer calibrated-CTD cast made by the RV Mytilus within 3 km of the Seaglider during the 30th June, 2010 at 9.38° W (figure 2.5). This was the sole occurrence of any such offset within the entire mission.

In an effort to correct the QC_OFFSET salinities, data from dives 465-467, and T-S data from the 9.38° W CTD cast were interpolated onto a 1 m grid. The mean difference between QC_OFFSET and Mytilus salinity values was found to be 1.051, at a standard deviation of 0.023. The difference between QC_OFFSET data and the CTD cast showed no depth dependence (figure 2.5, a) suggesting that the offsets are correctable by applying an arbitrary offset (of 1.05). After this offset is applied, the data are flagged as having an offset applied to it: QC_OSAPPLIED, to distinguish it from the non-corrected offset data (an example of QC_OSAPPLIED data can be seen in figure 2.5).

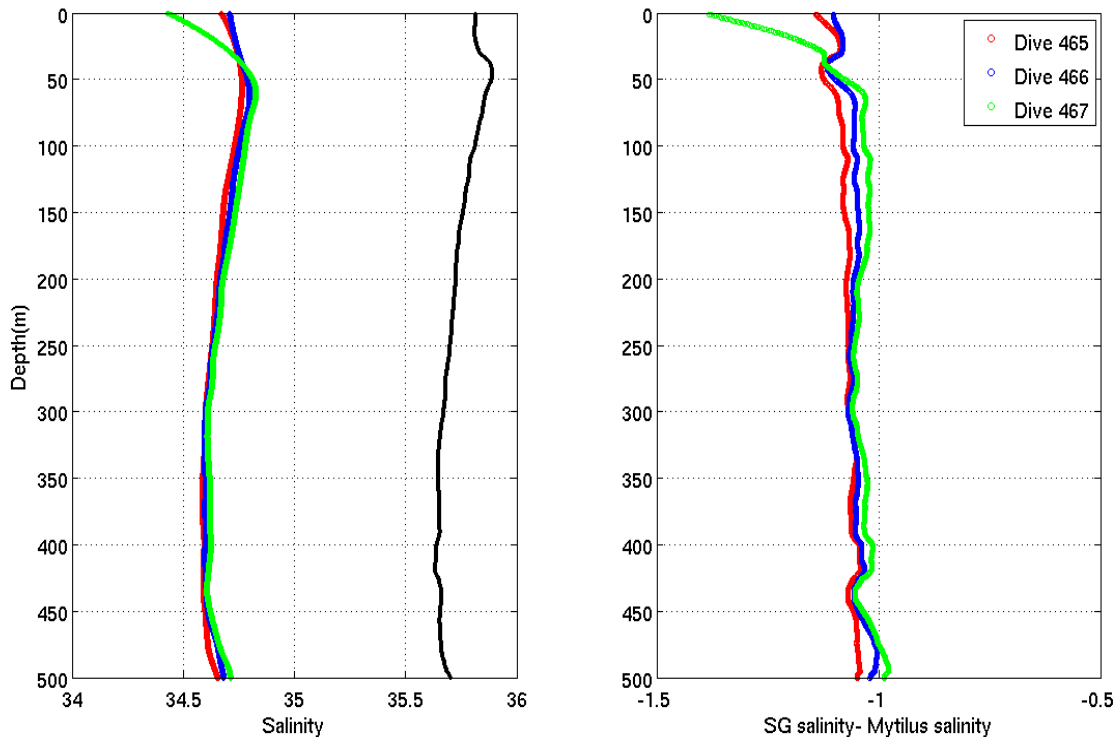


Figure 2.5: Left panel: QC_OFFSET flagged data from the 29th June 2010 collected over dives 465, 466 and 467 plotted with Mytilus calibrated CTD cast salinity data in the same location (black line), with all data interpolated onto the same grid. Right panel: 2 m gridded Mytilus salinity concentrations subtracted from the gridded salinity concentrations from dives 465, 466 and 467.

2.4 Seaglider and co-located RV Mytilus CTD data

The RV Mytilus completed three CTD casts concurrently with the Seaglider sampling campaign (on the 1st of June, 30th of June and the 30th July) that were sufficiently close to the Seaglider for direct calibration. The lag-corrected Seaglider data were found to closely follow the calibrated Mytilus casts. Therefore, no additional correction was applied to the Seaglider salinity data (fig. 2.3).

Design, flight behavior and sensor calibration of a glider

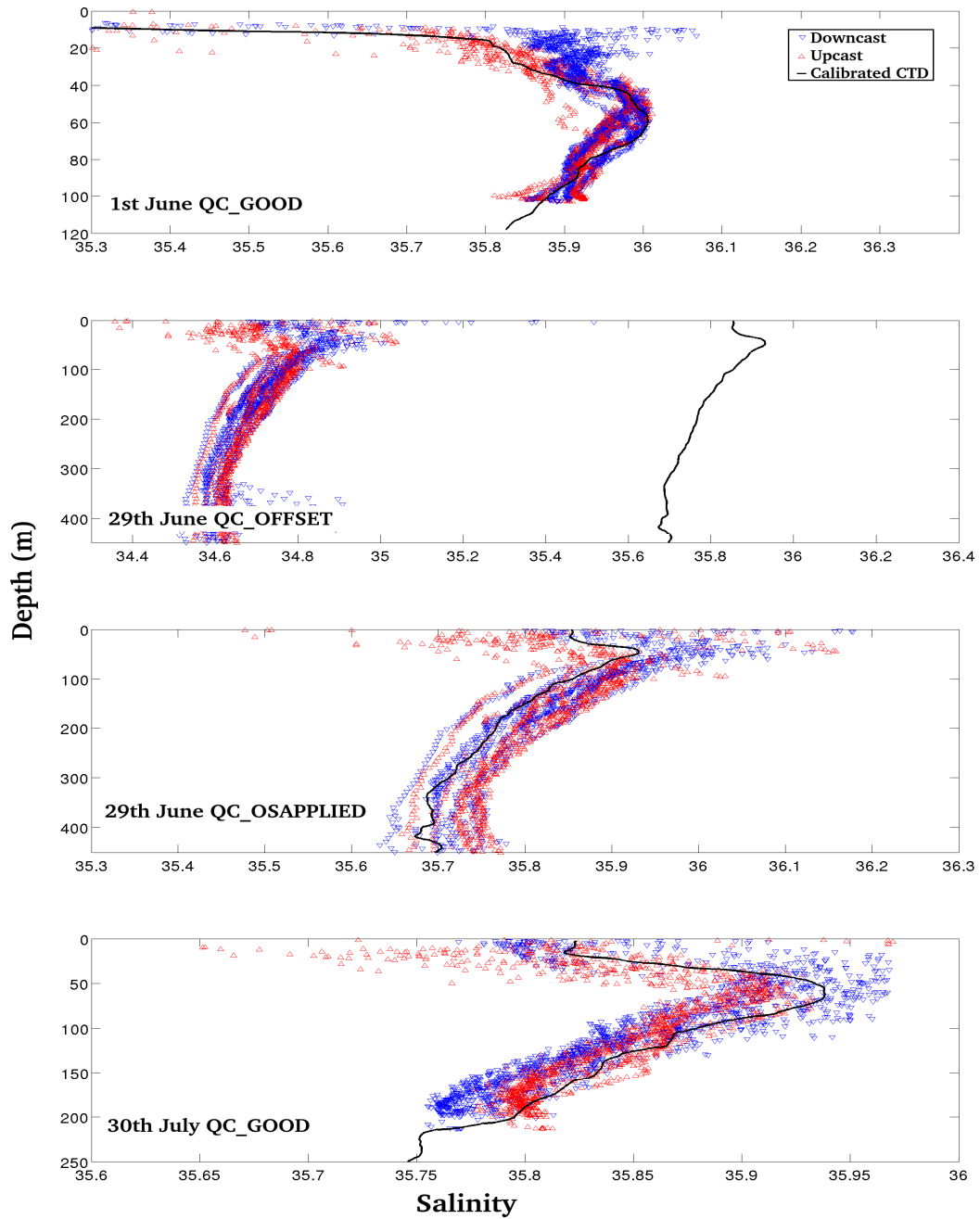


Figure 2.6: Seaglider salinity data for ten dives temporally and spatially nearest 7 casts to the Mytilus CTD cast on the 1st and 29th June and the 30th July, for QC_GOOD, QC_OFFSET and QC_OSAPPLIED data. The black line indicates salinometer-calibrated Mytilus CTD salinity data.

2.5 WetLABS ECO puck

The WetLABS ECO puck measures fluorescence as a proxy for the concentration of chlorophyll *a* (chl *a*), which fluoresces over a range of wavelengths centered around 682 nm (Maxwell 2000). This measurement is achieved using a blue LED to excite the chlorophyll pigment, and a photodiode to detect near-infrared fluorescence featuring wavelengths centred around 700 nm (Maxwell 2000). CDOM is also measured using a similar fluorescence technique, and backscatter is measured using a LED and photodiode both calibrated to the same wavelength of 650 nm (see below). All three are sampled simultaneously within the Wetlabs ECO puck. As the response time of the sensor is very fast (<0.1 S), there is no upstream sensor lag to correct (WetLabs manual). However, a significant source of error results from the single thread processing capabilities of the Seaglider's TT8 processor. As the Seaglider's internal electronics cannot process more than one data stream at once, the sensors are activated sequentially, with the Wetlabs ECO puck sensor recorded to internal memory after the CT cell. The Seaglider processing code assigns a single timestamp to all measurements collected during a sequence, resulting in a considerable delay of 1-5 seconds between the individual time stamp recorded in the Seaglider data, and the actual time when the Wetlabs ECO puck completed the measurement. To correct this, a unique timestamp and depth for all Wetlabs ECO puck data is interpolated to correct for this time delay (described in more detail in chapter 3.3).

Chlorophyll *a*

In the absence of other measurements, chl *a* derived from measurements of fluorescence is often used as a proxy for phytoplankton biomass carbon (Faure et al. 2006). This relies on a static ratio between chl *a* and biomass which is highly dependent on the taxonomy of the community (Frajka-williams 2009). Carbon-to-chlorophyll ratios are affected by photoacclimation, chlorophyll pigment types, phytoplankton size, and the presence of detrital fluorescing pigments as products of decomposition (Cullen 1982). As the dominant taxa in phytoplankton communities have been observed to change between

Design, flight behavior and sensor calibration of a glider

wintertime, summer relaxation and summer upwelling periods, attempting to apply a relationship between chl a and the carbon content of biomass is prone to error in this situation (Lutz et al. 2003; Cermeño et al. 2006). Although we cannot directly use chl a to estimate carbon uptake by phytoplankton, it still remains a useful proxy for bloom strength. Hence, we used the calibrated CTD fluorescence measurements from the co-located Mytilus dataset to calibrate the Seagliders chl a measurements (figure 2.7).

The WetLABS ECO puck is calibrated at the factory using a mono-culture of the phytoplankton *sp Thalassiosira weissflogii*. This calibration is applied to raw output from the sensor, to convert this output into chl a concentrations (in $\mu\text{g/l}$ or mg m^{-3}). This equation, in the form $y = mx + c$, has a dark counts/ blank value (i.e. the intercept, c), and a scale factor (i.e. the gradient, m). It was found that the blank value from the WETlabs factory calibration was marginally too high, as although a blank of 52 was specified within the calibration, the sensor measured 48-49 counts at depths greater than 150 m, in the offshore regions of the transect, (where very low/ zero concentrations of chl a would be expected). Therefore, the value of 48 was assigned as the calibration blank. The scaling factor from the laboratory sensor calibration (of 0.121, or m in the above equation) was now found to provide a very satisfactory fit with the calibrated fluorescence data from the CTD for all 3 co-located casts (figure 2.6). It was decided not to attempt to alter the scaling factor 'm' in the calibration, as no further accuracy would be gained from changing factory calibrations in favour of a CTD cast taken many hundreds of meters away in a highly biogeochemically variable region.

Design, flight behavior and sensor calibration of a glider

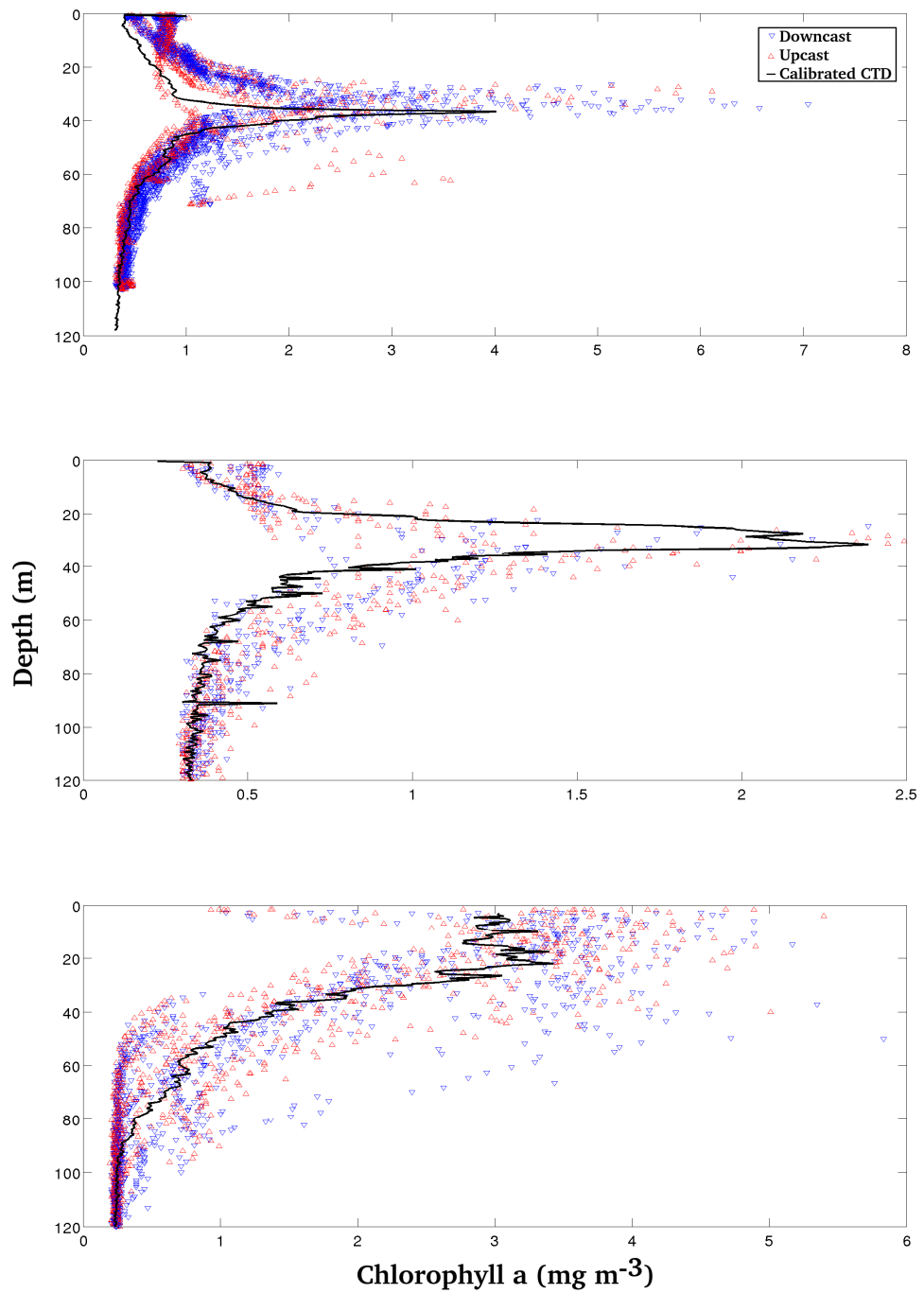


Figure 2.7: Seaglider chl a, with calibrated CTD fluorimeter chl a concentrations for each of the three co-located CTD locations

Backscatter and light transmittance

The WetLABS ECO puck measures water column backscatter, through the emission of a fixed wavelength of light (650 nm during the GOPINA mission) from an LED, and photodiode measurement of identical wavelength light backscattered towards the sensor. These measurements provide a proxy for the light transmittance of the watercolumn, which is conventionally measured with a transmissometer. Although the R.V Mytilus carried a transmissometer, the difference in operation between the two sensors meant that in-situ calibration was not possible. Finally, the ECO puck measures coloured-dissolved organic material (CDOM). The RV Mytilus did not carry a CDOM instrument, thus there is no data to calibrate CDOM. As a result, both backscatter and CDOM retain the calibration constants from laboratory calibrations performed by Wetlabs.

2.6 Part four: Gridding Seaglider data

The geolocation of individual datapoints measured by the Seaglider differ from ship borne CTD data. A ship allows for CTD casts to be completed at a precise surface latitude and longitude. These casts are made vertically (perpendicular to the surface) through the watercolumn and feature a uniform vertical sampling rate. This makes subsequent interpolation of data simple, as the data has consistency between the cast sampling depths and surface geolocations, producing a uniform dataset. The Seaglider offers little control over surface latitude and longitude prior to a dive, the subsequent dive is made at an acute angle to the surface, forming a V- shaped pattern through the watercolumn. The sampling rate of the instruments is a function of time rather than depth, so different Seaglider velocities result in a different vertical spatial sampling rate. This results in a non-uniform dataset. To interpolate this dataset onto a 2D grid using the traditional Matlab linear interpolation techniques based on (`griddata.m` and `triscatterinterp.m`), results in horizontal interpolation artifacts within the gridded output (figure 2.9). These ‘striation’ like features are formed from the interpolation of data between equal depths. Any missing data at a particular depth results in an interpolated

Design, flight behavior and sensor calibration of a glider

result derived from a multiple dive average (and hence a large longitudinal range). To produce a more accurate gridded data output, John D'Errico's `gridfit.m` function was used. This function is based on Sandwell's (1987) technique for interpolating irregularly spaced data (in his example, estimates of sea floor depth) by completing a weighted linear interpolation between geographically neighboring points. This removes the striated pattern seen in the other two gridded techniques.

To test the three gridding techniques, I conducted a root-mean-squared (RMS) calculation between the individual Seaglider datapoints, and the three gridded data products. From this, the smaller the lower the average RMS between gridded product, and actual point data, the better the interpolation. `Gridfit.m` was found to feature substantially lower RMS error than either `griddata.m` or `triscatterinterp.m`, at both fine and course resolution gridding resolutions (figure 2.9).

With the Seagliders temperature, salinity, chlorophyll a, backscatter and CDOM datasets corrected, oxygen from the Aanderaa optode remains. The method of calibrating oxygen is discussed in chapter 3 (below).

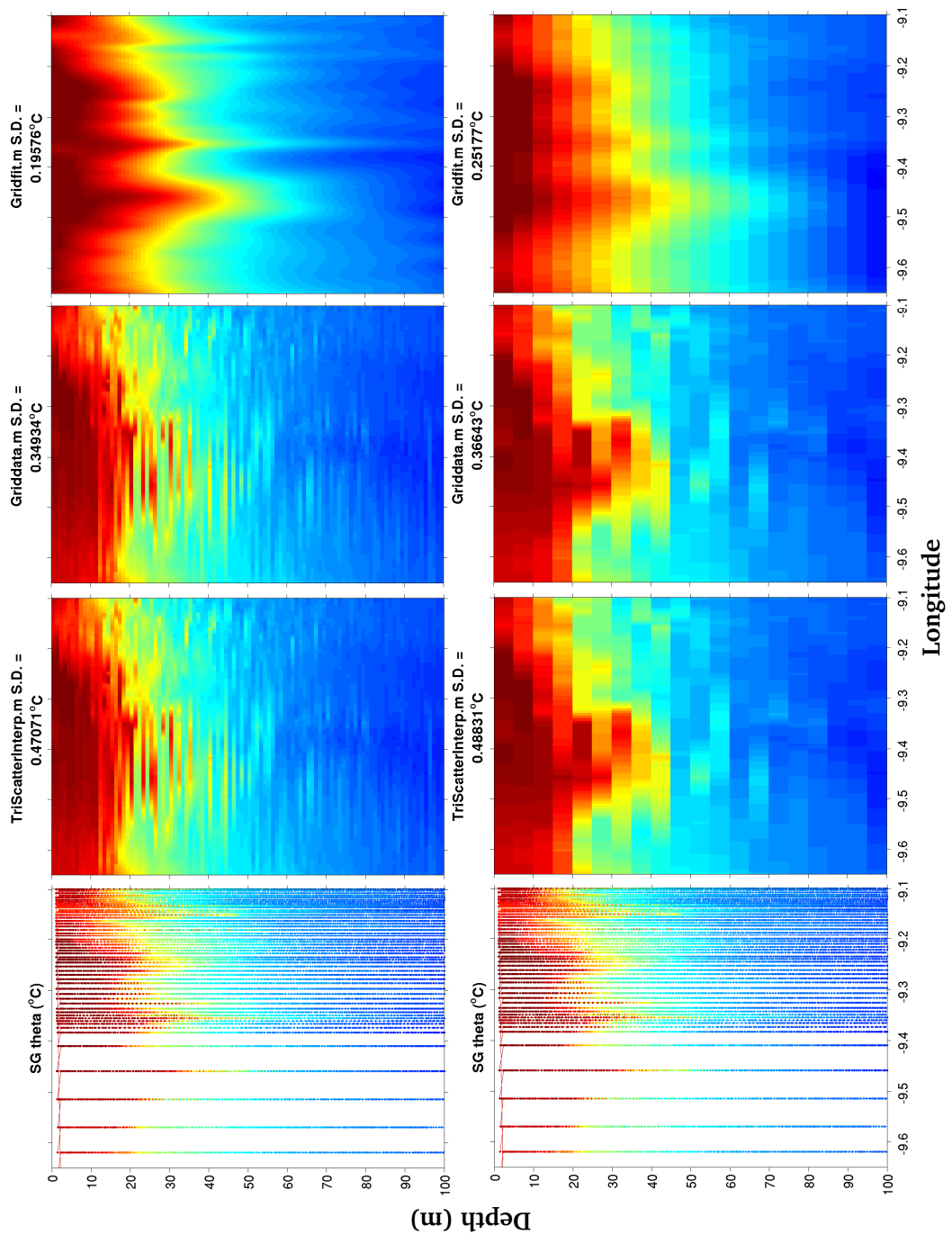


Figure 2.9: A comparison of three different matlab gridding techniques (triscatteredinterp, griddata and gridfit), using QC_Good seaglider potential temperature data. The first three gridded outputs are at ‘fine’ resolution, 1m x 0.001° longitudinal spacing, the second three outputs are at ‘coarse’ resolution, 5m x 0.005° longitude spacing

The Oxygen Optode

3.1 The optode

Measuring dissolved oxygen is typically achieved using one of three methods: using Winkler titrations, electronically using a Clarks type oxygen sensor, or optically using an oxygen optode (Pai et al. 1993; Berntsson et al. 1997; Tengberg et al. 2006). The highest precision is achieved by Winkler titrations (better than $0.2 \text{ } \mu\text{mol kg}^{-1}$), however, this comes at a highest expense and longer sampling time per oxygen sample (Pai et al. 1993, Tengberg et al. 2006). Collecting and pickling water-samples for Winkler titrations is impractical using AUV's, so oxygen concentrations are typically measured using a Clarks type sensor, or an optode (Alkire et al. 2011). Miniaturized versions of both sensors have been produced, and deployed on Seagliders prior to the Vigo mission, and both have produced satisfactory datasets (Briggs et al. 2011). The choice to use an optode for the Seaglider missions stems from the operation of a Clarks type instruments fitted to a Seaglider used by Toby Sherwin's group at the Scottish Association for Marine Science. Here, the Clarks type instrument was found to require frequent recalibration due to poor factory calibration and substantial sensor drift (Sherwin 2009, personal communication).

The Aanderaa 4330F(ast) foil optode fitted to the deployed Seaglider is a small, low power sensor designed to measure dissolved oxygen concentrations in marine and freshwater environments (figure 3.1). The optode measures oxygen based on dynamic fluorescence quenching of a luminophoric platinum porphyrin complex embedded in a polymer sensing foil (Tengberg et al. 2006). This luminophore is excited by blue light pulses from an LED below the foil. Relaxation of the luminophore to its ground state can occur via fluorescence (emission of a longer wavelength photon) or dynamic quenching (collisional energy transfer) by an O_2 molecule. Fluorescence emitted by the sensing foil is therefore inversely related to the oxygen concentration of the water (Tengberg 2006). Total fluorescence can be influenced by factors other than oxygen concentration, such as external light sources. These factors are cancelled out by measuring the lifetime of the fluorescence (rather than its intensity), which is achieved by modulating the blue light

The Oxygen Optode

excitation source to 5 kHz, and measuring the fluorescence decay time between the excitations, a measurement known as the phase angle (Tengberg 2006).



Figure 3.1: Aanderaa 4330 optode. A: sensing foil with protective polymer covering, B: thermocouple.

The relationship between decay time and dissolved oxygen concentration is described by the Stern-Volmer equation:

$$O_2 = \frac{1}{K_{SV}} \left\{ \frac{\tau_0}{\tau} \right\} - 1$$

where τ = decay time, τ_0 = decay time in the absence of oxygen, and K_{SV} = Stern-Volmer constant. The phase angle measured by the optode is directly proportional to the decay time of this fluorescence, τ (Tengberg et al., 2006). τ is reported as the raw phase output from the Aanderaa optode (see equation above).

The sensing foil of the optode is mechanically protected by a layer of gas permeable polymer (figure 3.1), which prevents biofilms and particulate matter from inhibiting the light pathway between the sensor foil, and the photo diodes/ light sources. There are two types of polymer protection foil types available from Aanderaa, fast response and slow response. The optode used on this deployment used the 'fast' foil type, with the fundamental difference between the two foils being the thickness of the gas-

The Oxygen Optode

permeable polymer protective coating. The fast foil type has a thinner protective coating, resulting in speedier gas diffusion across this protective membrane with the trade-off of increased noise in environments with strong UV light, i.e. near the surface on a bright day (Aanderaa manual, 2009).

The rate of oxygen diffusion across the optode sensing foil is a first order control on the response time of the optode. The effect of a change in oxygen concentration on the measured optode signal is described schematically in Figure 3.2. Here, the oxygen concentration increases instantaneously from X to $Y \mu\text{mol kg}^{-1}$ at time T_0 . Prior to T_0 , the optode signal is stable. Between T_0 and T_R there is no change in measured optode oxygen concentration measurement. This is due to the time taken for oxygen to diffuse over the gas-permeable polymer protective coating- the initial response time of the optode. The oxygen measurement from the optode then increases until the porphyrin-oxygen complexation approaches equilibrium at the new $Y \mu\text{mol kg}^{-1}$ oxygen concentration. The time $(T_{100} - T_0)$ required to reach this new equilibrium is the full optode foil lag.

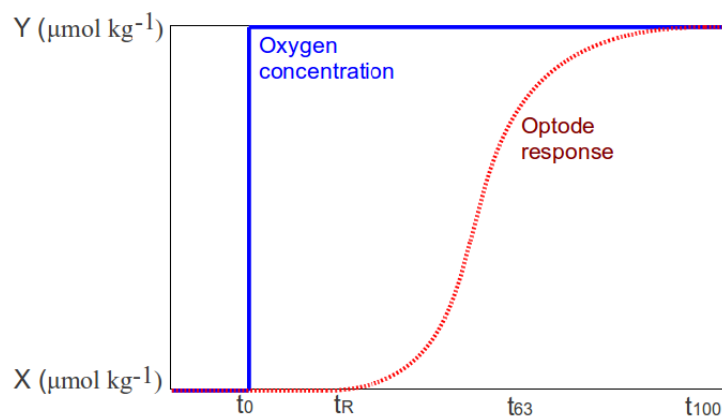


Figure 3.2 A schematic of an oxygen concentration increase from X to $X+1$, with corresponding response from the optode (blue dotted line). The optode has no response to the increased oxygen concentration between T_0 and T_R . The optode approaches the correct oxygen concentration at T_{100} .

The Oxygen Optode

As the optode response curve is a cubic function (figure 3.2), defining the exact point at which T100 is reached is difficult. One method of comparison is to calculate the time taken to reach T63- 63 % or within one sigma unit of the correct oxygen concentration at T100. The optode time lag to reach T63 was measured at 10, 12 and 12-14 s by Tengberg et al. (2006), Körtzinger et al., (2008) and Uchida et al. (2008) respectively. This compares to optode foil T63 lags of >30 s for slow foils (Anderaa 2009). Taking a midpoint of these fast foil lag estimates, 12 s, an optode mounted on a Seaglider maintaining a typical vertical velocity of 10 cm s^{-1} would therefore travel a vertical distance of 120 cm from time T0 to time T63. As oxygen concentration measurements are made on both the up and down casts, this optode foil lag results in hysteresis in the watercolumn above the oxycline, and hence requires correction.

3.2 Oxygen optode calculation technique

The oxygen concentration of the water is calculated from the raw phase angle, calibrated Seaglider temperature, salinity and pressure measurements. These use the methodology in the Aanderaa manual, in combination with the pressure correction calculated by Uchida et al. (2008). Optode processing, including this foil pressure correction is completed in six stages, as detailed below.

The Oxygen Optode

$$[1] \quad \theta CP = \phi_0 + \phi_1 \cdot \theta_{\text{DifferentialPhase}}$$

Where θCP = Calibrated phase angle, ϕ_0 = Phase coefficient 1, ϕ_1 = Phase coefficient 2,
 $\theta_{\text{DifferentialPhase}}$ = Raw phase angle as measured by the optode

$$[2] \quad \Delta_{\text{PartialPressure}} = \epsilon_{A0} \cdot t^{T0} \cdot \theta CP^{P0} + \epsilon_{A1} \cdot t^{T1} \cdot \theta CP^{P1} + \epsilon_{A2} \cdot t^{T2} \cdot \theta CP^{P2} + \epsilon_{A3} \cdot t^{T3} \cdot \theta CP^{P3} + \epsilon_{A4} \cdot t^{T4} \cdot \theta CP^{P4} \\ + \epsilon_{A5} \cdot t^{T5} \cdot \theta CP^{P5} + \epsilon_{A6} \cdot t^{T6} \cdot \theta CP^{P6} + \epsilon_{A7} \cdot t^{T7} \cdot \theta CP^{P7} + \epsilon_{A8} \cdot t^{T8} \cdot \theta CP^{P8} + \epsilon_{A9} \cdot t^{T9} \cdot \theta CP^{P9} \\ + \epsilon_{A10} \cdot t^{T10} \cdot \theta CP^{P10} + \epsilon_{A11} \cdot t^{T11} \cdot \theta CP^{P11} + \epsilon_{A12} \cdot t^{T12} \cdot \theta CP^{P12} + \epsilon_{A13} \cdot t^{T13} \cdot \theta CP^{P13} + \epsilon_{B0} \cdot t^{T14} \cdot \theta CP^{P14} \\ + \epsilon_{B1} \cdot t^{T15} \cdot \theta CP^{P15} + \epsilon_{B2} \cdot t^{T16} \cdot \theta CP^{P16} + \epsilon_{B3} \cdot t^{T17} \cdot \theta CP^{P17} + \epsilon_{B4} \cdot t^{T18} \cdot \theta CP^{P18} + \epsilon_{B5} \cdot t^{T19} \cdot \theta CP^{P19} + \epsilon_{B6} \cdot t^{T20} \cdot \theta CP^{P20}$$

Where ϵ_A = Foil coefficients A0 – A13, ϵ_B = Foil coefficients
 B0 – B6, t = temperature (°C), T0 – T20 and P0 – P20 = Foil monomial degrees

$$[3] \quad \%O_{2\text{saturation}} = \frac{(\Delta_{\text{PartialPressure}} \cdot 100)}{(1013.25 \text{ hPa} \cdot 0.20946)}$$

where 0.20946 is the fraction of the oxygen component of dry air

$$[4] \quad O_2 \text{ concentration (}\mu\text{M)} = \frac{(C^x \cdot 44.614 \cdot \%O_{2\text{saturation}})}{100} P^x$$

Where

$$[5] \quad \ln(C^x) = A_0 + A_1 T_S + A_2 T_S^2 + A_3 T_S^3 + A_4 T_S^4 + A_5 T_S^5 + S (B_0 + B_1 T + B_3^3) + C_{0S}^2$$

$$[6] \quad P^x = (1 + P_{\text{comp}} \cdot P / 1000)$$

Using the 11 polynomial coefficients calculated by Garcia and Gordon (1992):

$$A_0 = 2.00856 \quad A_1 = 3.22400 \quad A_2 = 3.99063 \quad A_3 = 4.80299 \quad A_4 = 9.78188 e^{-1} \quad A_5 = 1.71069$$

$$B_0 = -6.24097 e^{-3} \quad B_1 = -6.93498 e^{-3} \quad B_2 = -6.90358 e^{-3} \quad B_3 = -4.29155 e^{-3} \quad C_0 = -3.11680 e^{-7}$$

and P_{comp} is the foil compression compensation coefficient of 0.032, and P is ambient pressure (dbar), following Uchida et al., 2008.

1. Raw phase angle (calculated within the optode from the difference between the phase obtained between blue excitation light and the fluorescence emitted from the luminophore) is first converted into calibrated phase angle (θCP in this chapter, or 'Calphase' in Aanderaa literature), by applying two phase coefficients (provided as part of the Aanderaa factory calibration) to the raw phase angle readings.

The Oxygen Optode

2. From θ_{CP} , the partial pressure of oxygen is calculated using a two dimensional, 20-term polynomial, using the polynomial coefficients A_0 to A_{13} and B_0 to B_6 foil temperature coefficients $T1$ to $T20$ and $P0$ to $P20$ (with these coefficients calculated by batch foil calibration by Aanderaa)
3. Oxygen saturation is calculated using a standard air pressure (1013.25 hPa at sea level), and mole fraction of O_2 in dry atmospheric air (0.20946)
4. Finally, the fully salinity, pressure and temperature corrected oxygen concentration can be calculated using [5] C^X , the oxygen solubility of saline waters at the in-situ temperatures and salinities as described by Garcia and Gordon (1992). A pressure compensation (p^*) is also calculated, as the response of the foil decreases with increasing ambient pressure at a rate of 3.2 % per 1000 dbar (Uchida et al., 2008).

3.3 Optode data processing

The Aanderaa 4330F is able to internally process the raw phase angle, to produce an estimate of oxygen concentration in ml/l. This is completed using stages 1,2,3, and 4 (above), with temperature correction completed using data from the inbuilt thermistor on the optode (figure 3.1). However, the optode does not have the capability to measure either pressure or salinity, both of which influence optode estimates of oxygen concentration, and hence the optode is unable to complete the correction stages 5 and 6 (Tengberg et al., 2005). Oxygen concentrations used in subsequent sections are calculated using all six stages described above, rather than using the optode generated oxygen concentration. Both salinity and temperature measurements used in this calculation are from the SBE CT cell on the Seaglider (with optode thermistor temperatures discarded). This is due to thermistor values being found to exhibit both time delay and miscalibration (figure 3.3). This time delay can be observed in the large differences between the Seaglider CT (see chapter 2) measured temperature, and the optode thermistor measured temperatures taken from the same timestamp, as seen in figure 3.3. Median optode thermistor temperatures, and calibrated CT temperatures are not identical, with the optode measuring 0.04 °C lower than the Seaglider's CT

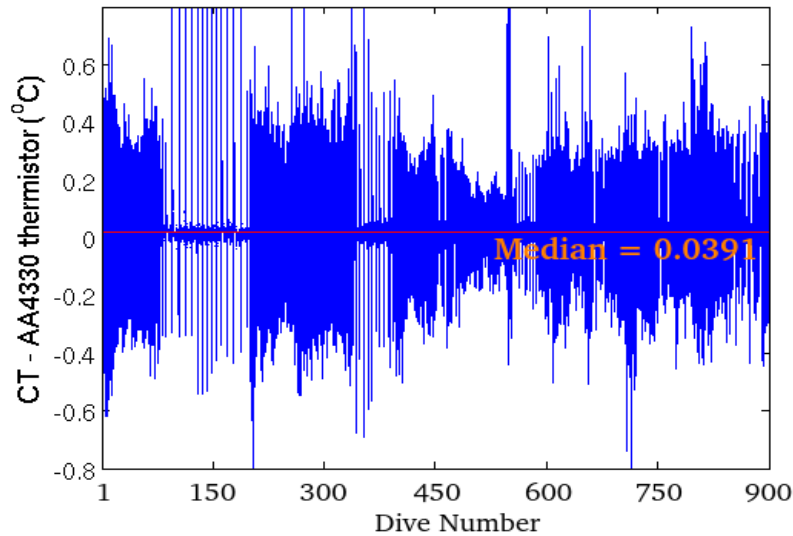


Figure 3.3 Optode thermistor temperatures subtracted from calibrated Seaglider CT cell temperatures recorded on the same timestamp. If the two sensors were recording the same temperature, there would be a single line at $Y=0$. Although the median difference between the two is small, clear differences in output of up to ± 0.8 °C can be seen. The smaller differences seen for example at dives 79-100 and 320 - 350 are due to an increased number of measurements made at depths below the thermocline, as the Seaglider completed 1000 m dives in the deeper water off-shelf.

Despiking optode data

At this point, the oxygen concentrations processed using the six steps above, and using the corrected TS data should broadly represent the oxygen concentration of the watercolumn. As oxygen inventory NCP calculations were made using the data, additional effort was made to ensure that the oxygen dataset was as accurate as possible. To do this, oxygen data have to be despiked, have the correct instrument lag applied (to account for the processes discussed in section 3.1) and the optode calibrated with in-situ oxygen samples from Winkler titrations.

The Oxygen Optode

θ CP angle values of 30° to 40° correspond to oxygen concentrations of 110 to 380 $\mu\text{mol kg}^{-1}$ (at a salinity of 35 and temperature of 14°C) using the unique foil constants supplied with the optode. Any values outside these θ CP angles can be considered to be anomalous (R.V Mytilus summer 2010 observations within the region did not identify any oxygen concentrations outside this range), and thus are removed (figure 3.4, panel A). However, spikes still exist after this filtering, with these spikes clearly visible for the first 70 dives in figure 3.4, curve A. To remove these spikes, each value of θ CP is subtracted individually from the 5 previous and 5 successive θ CP values, providing ten values:

$$[7] \text{ Difference} = \theta\text{CP}(n) - \theta\text{CP}(n-5 \text{ to } n+5),$$

where $n = \text{datapoint number}$

The RMS of these 10 differences is taken and recorded for all datapoints for the first 1050 dives, and the size of the 99th percentile spike is recorded. All θ CP values featuring an associated RMS above this 99th percentile value are flagged as being anomalous, and removed from all further oxygen calculations (see figure 3.4):

$$[8] \text{ Spike Flag} = (99^{\text{th}} \text{ Percentile threshold} < \text{RMS Difference})$$

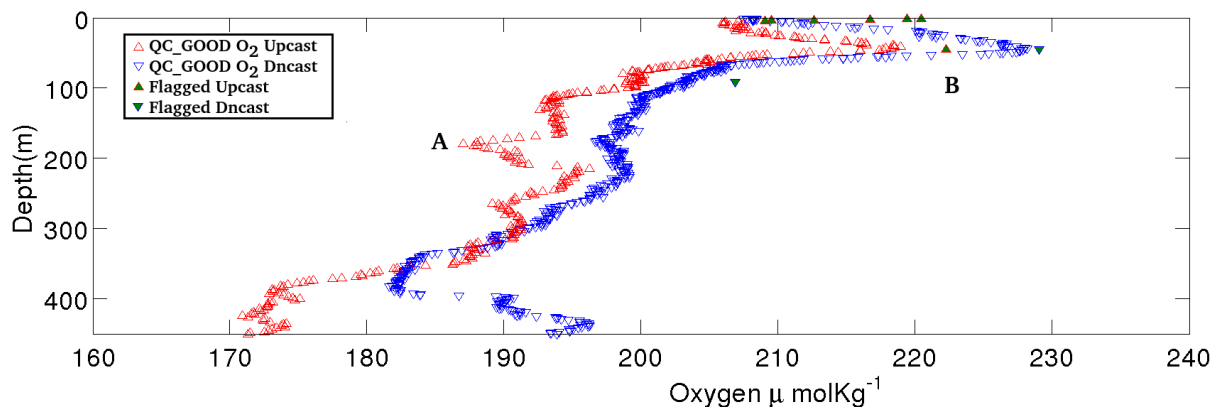


Figure 3.4. QC_GOOD oxygen values after removing outlying θ CP values of $<30^\circ$ and $>40^\circ$. 95th percentile spikes as calculated from a rolling ten consecutive data point technique, as described in the text [equations 7 & 8], are shaded in green. This technique allows water-column variability to be preserved, such as the feature at A, but removes outliers, such as those at the surface and oxycline at B. Note, θ CP has been converted into oxygen concentrations to ease comprehension in this plot.

The Oxygen Optode

This technique was found to remove both out-of-range oxygen data, caused by the optode being bleached by sunlight in the upper 10 m of the watercolumn, resulting in anomalous spikes in the data (figure 3.4 B). Whilst structure within the watercolumn such as the deviation labeled A in figure 3.4, are not filtered out as spike. This technique results in the removal of approximately 3.8% of the total oxygen data.

Single thread processor timestamp delay

The time delay between the optode sampling, and the timestamp is corrected using the UEA Seaglider toolbox function `gt_sg_adjust_sensor_timings.m` (Schmidtko et al. in prep). The TT8 processor fitted to the Seaglider's logic board was originally chosen for energy efficiency, albeit at the expense of processor speed (Eriksen et al. 2001). As the processor is of single thread architecture, it is only able to process a single stream of data, thus data from the Seagliders sensors and recording to memory must be completed sequentially. Data from the T-S sensor is recorded first, followed by data from the WetLABS ECO puck, and finally the optode. Unfortunately, completing this sequential processing can take 5 to 8 seconds, so the single timestamp and depth assigned to a group of sensor readings results in the optode data being recorded to an earlier timestamp than the actual point of measurement, potentially resulting in hysteresis. Prior to completing any correction for foil lag, it is important to produce a correct timestamp and depth value for the optodes measurement. This is completed by interpolating the timestamp and depths onto a 0.5 s grid, and assigning a new interpolated timestamp and depth from this grid to each optode measurement depending the time delay caused by the sequential processing of the TT8.

The Oxygen Optode



Figure 3.5. Optode mounting position. The optode (blue cylinder) is mounted towards the back of the Seaglider, 25 cm behind the CT cell (grey protrusion).

Optode positional timestamp delay

A final potential source of error in optode data arises from the mounting of the optode 25 cm behind the CT cell and pressure sensor (figure 3.5). Assuming a typical angle of flight of 30° , and the Seaglider maintaining a typical vertical velocity of 10 cm s^{-1} , a parcel of water will take 1.25 s to travel between the CT cell and the optode. As the timestamp is the same for all of the instruments, and is optimised for the positioning of the CT cell, this slight delay will lead to hysteresis even if the optode has an instantaneous response time. To review, there are three main issues that could cause optode sensor lag:

1. Oxygen diffusion across the foil membrane
2. TT8 timestamp error
3. Positioning of the optode behind the CT cell, with the timestamp optimized for the position of the CT cell.

Rather than try to deal with each of these issues separately, the overall net lag resulting from issues 1+2+3 was corrected. To complete this, despiked θ_{CP} values for the downcast and upcast were gridded onto a 0.015 kg m^{-3} density grid. The choice of a

The Oxygen Optode

density grid resulted from observations that raw oxygen concentrations measured on the same isopycnal surface had a lower variance than oxygen concentrations measured on the same depth (z-depth) surface. As this lag correction attempts to find an optimized lag correction value (τ) to limit the RMS difference between consecutive up and down casts, minimizing this source of noise is beneficial.

Different τ values from 0 to +60 seconds were applied to the optode θ_{CP} measurements, by adjusting the timestamp on optode measurements with respect to the timestamp on depth measurements. The schematics in figure 3.6 further explain this. Here, uncorrected optode data (i.e. no τ adjustment, $\tau = 0$ s) are shown as yellow dots. By comparing oxygen concentrations on downcasts with subsequent upcasts for $\tau = 0$ s the effect of the response time for the optode foil (figure 3.2) results in an offset between the two profiles, where the downcast oxycline features are observed at a shallower depth than in the upcast. A τ offset effectively adjusts the vertical location of individual optode measurements, so increasing τ in a positive direction 'shifts' oxygen values on the downcast to shallower depths/isopycnal surface, and on the upcast to deeper depths/isopycnal surfaces (shown by the red arrows in figure 3.6). The larger the size of positive τ , the larger the vertical displacement of the optode measurements.

By applying the correct τ offset, the up and downcast oxycline features align (Figure 3.6), By applying too large τ values, the downcast oxycline features are plotted at a shallower depth than the upcast features. Therefore, by calculating the RMS between the up and down casts for a sufficiently large number of dives, in an environment with no large net loss or gain of oxygen concentration allows an optimized τ value to be calculated, and hysteresis between up and downcast removed.

The Oxygen Optode

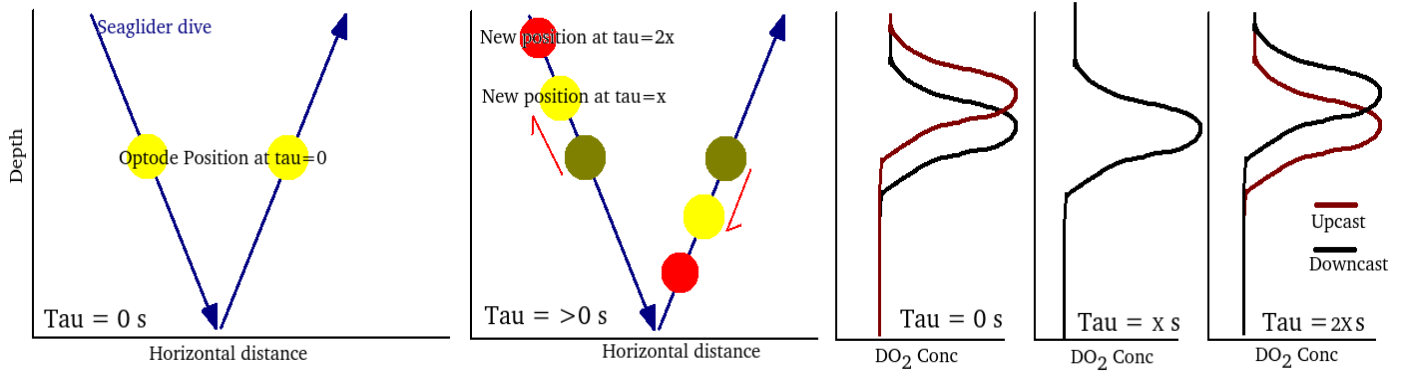


Figure 3.6. Schematic of the effects of increasing τ time adjustment, with respects to the water mass that the optode is measuring, if the optode foil response time was x seconds, oxygen concentration in a horizontally homogeneous watermass would feature no hysteresis between up and down casts for the $\tau=x$ position, but considerable hysteresis in the 0 s and $2X \tau$ values.

Excluding photic zone noise

The optode data, prior to lag correction, shows a high variability in the near surface, and a lower variability at depth, below the oxycline. This can be seen in figure 3.7; here oxygen concentrations along isopycnal surfaces are plotted for the first 1000 dives. Isopycnal surfaces that were closer to the surface, such as the 1026.5 kg m^{-3} surface, show a large variation compared to deeper isopycnals, such as the 1027 or 1028 kg m^{-3} isopycnal surfaces. To remove noise caused by photic zone biotic metabolism, all the lag correction uses oxygen measurements below the 1027 kg m^{-3} isopycnal,

A range of τ values

A range of different τ timestamp delay values from 0 to 60 seconds were applied to the optode data, and the corresponding RMS differences between up and down casts calculated for each τ value calculated. The optimum τ (the value that results in the lowest total RMS difference between up and down casts) for each dive is plotted in figure 3.8.

The Oxygen Optode

Here, different values of τ form a Gaussian distribution centred around 34 s- the optimum τ value to reduce RMS differences between up and down casts. There was no discernible temporal trend in optimal individual optimal values of τ , between the start and end of the Seaglider mission, suggesting that the optimum value of 34 s can be applied to all data from the start of the mission to the end.

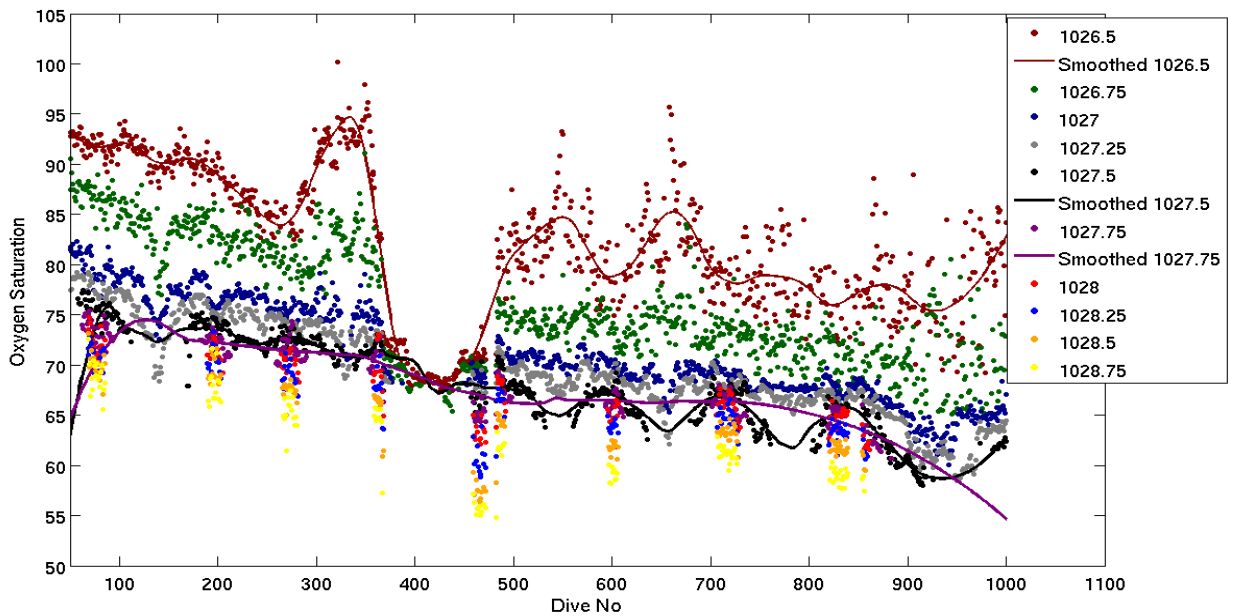


Figure 3.7. Uncalibrated downcast oxygen saturation data plotted for the first 1000 dives at isopycnals from 1026.5 to 1028.75 kg m^{-3} . Low (water-mass) density oxygen values (1026.5 and 1026.75 kg m^{-3}) were subject to a very high degree of variability caused by near surface processes such as phytoplankton bloom patchiness.

The Oxygen Optode

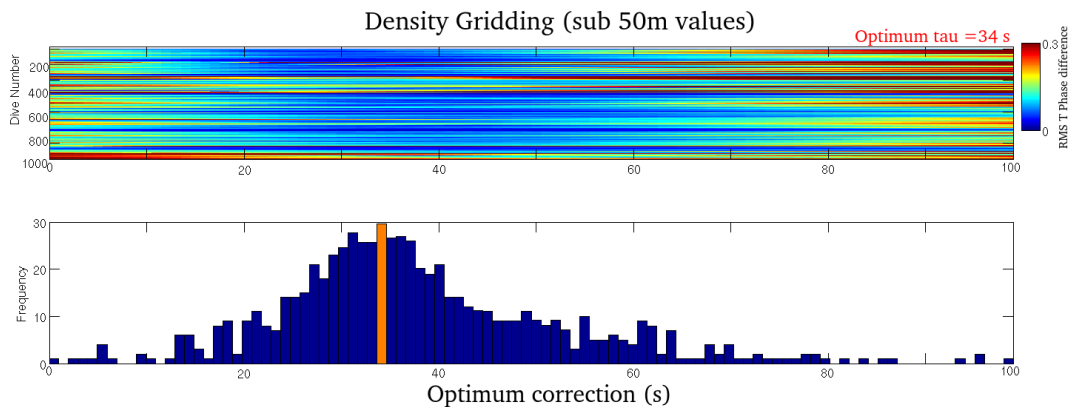


Figure 3.8

A: Median RMS difference between θ_{CP} values interpolated onto a density grid for consecutive up and down casts for first 100 dives, with different τ lag times applied to the sensor. The lower the RMS difference, the more closely aligned the up and down casts.

B: Frequency density of optimum lag times for the first 800 dives, indicating that a τ of 34 seconds provides the best fit

C: The optimal τ lag times for each individual dive.

3.4 Oxygen concentration calibration with *Mytilus* data

With the correction of sensor lag issues, checking the calibration of the instrument can be completed. Although many studies have indicated that the data output from the Aanderaa optode is stable over extended (> 1 month) deployments (e.g. Tengberg et al., 2006, Hydes et al., 2009), to ensure that the optode is functioning correctly, in-situ calibration of the optode against external oxygen measurements is required (Uchida et al., 2008).

To perform this calibration requires a second dissolved oxygen dataset. One possible calibration technique requires the removal of the optode from the Seaglider, and verification of optode output by testing water samples with a known oxygen content

The Oxygen Optode

(derived from Winkler titrations- essentially how the optode is calibrated by Aanderaa before being shipped to the end user, Aanderaa manual, 2009). This is not possible with the Seaglider mid-mission, as the Seaglider would have to be removed from the water, disassembled, and undergo instrument testing back in the UEA's laboratories, before being relaunched back into the North Atlantic. For this reason, the Seaglider's optode was calibrated in-situ at sea, using a similar technique to other University of Washington AUV deployments (Frajka-Williams 2009, Alkire et al. 2011). Over the course of the Seaglider mission, the optode was calibrated in situ three times, on the 1st June, 29th June and 29th July 2010, using a co-located CTD/rosette transect completed by the research vessel *Mytilus*. The *Mytilus*' rosette was fitted with a Seabird Electronics SBE43 Clark type oxygen sensor. To ensure that the SBE43 was correctly calibrated, oxygen Winkler samples were taken, and compared with the SBE43 readings (fig. 3.9). A linear regression correction was subsequently applied to the SBE43 oxygen values, and this calibrated SBE43 oxygen output was used to calibrate the Seaglider optode.

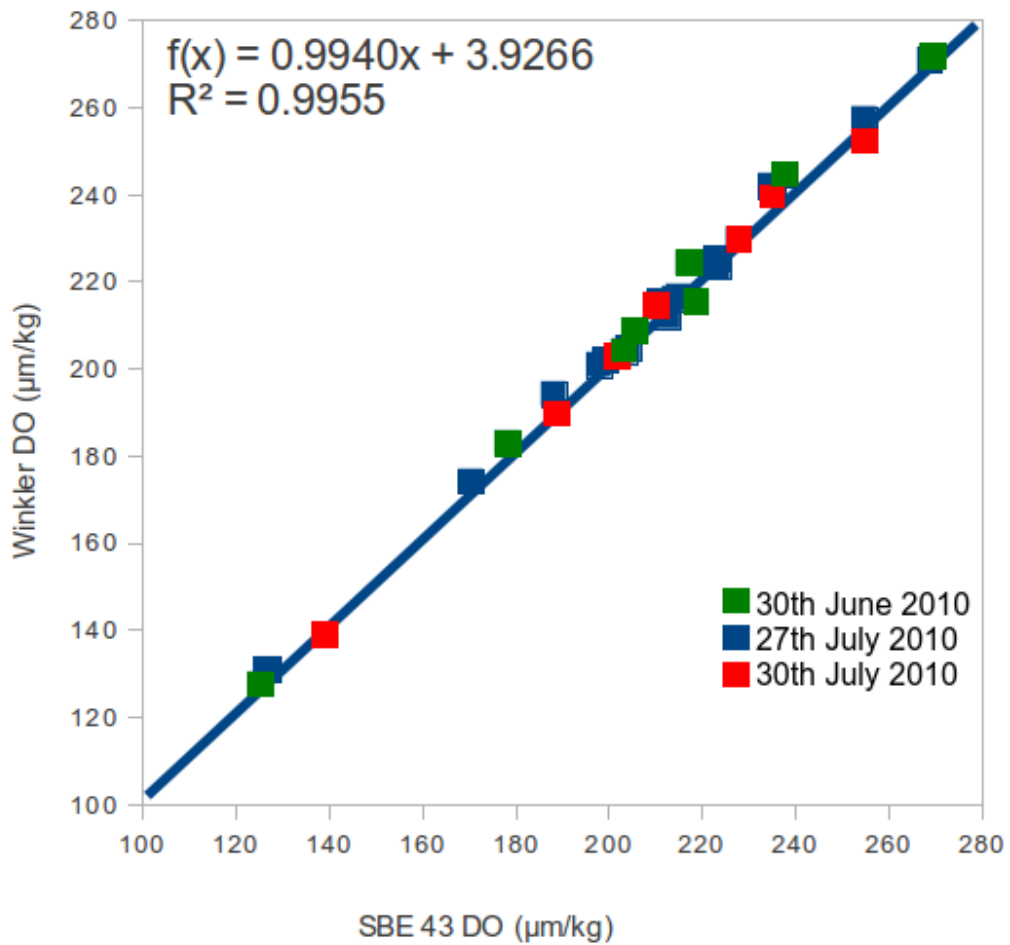


Figure 3.9 Uncalibrated SBE43 oxygen concentrations plotted against Winkler titrations for RV Mytilus cruises on the 29th June, 27th July and 29th July 2010, made in the Seaglider transect region. The linear fit equation was applied to the uncalibrated SBE43 data for all CTD casts, providing the calibrated data source for subsequent Seaglider optode comparisons. The oxygen values from the SBE43 remained stable for all three Winkler calibrations, so all three calibration dates were used to produce this combined calibration of the SBE43.

Using the optode calibration technique described by Frajka-Williams (2009), the Seaglider was calibrated in-situ, using the ship-borne oxygen (SBE43) values. Completing in-situ calibration using the corrected SBE43 values, against the Seaglider optode is more problematic than the in-situ calibration from Winkler bottle sample

The Oxygen Optode

against SBE43, as the Seaglider and rosette mounted SBE43 are not in close proximity to each other. The distances between the two instruments were:

1st June- at a separation of 1800 m

29th June at a separation of 3300 m

29th July 2010 at a separation of 4000 m.

The conversion between calibrated phase angle and oxygen concentration varies depending on foil coefficients for the particular batch of luminophoric foil that the optode is fitted with (described in further detail in section 3.2). To calibrate θ_{CP} on a target optode using data from a calibrated instrument requires the back calculation of a 'pseudo' θ_{CP} value from oxygen concentrations measured by the calibrated instrument, using the foil coefficients from the target optode (Uchida et al., 2008). Using this method, any technique for measuring oxygen (eg Winkler, optode, Clark-type electro-potentiometer) can be used as the source of oxygen data used to calibrate the optode.

Oxygen concentrations from the calibrated SBE43 were back calculated using equations 1-6 in reverse order, from oxygen concentration to calibrated pseudo θ_{CP} . These SBE43 pseudo θ_{CP} , and the optode θ_{CP} (fully corrected for all response-related time lags) were then gridded onto the same 0.015 kg m^{-3} density surfaces for dives 3,4 & 5 on the 1st June 2010, dives 466, 467 and 468 for June 29th 2010, and 870, 871 and 872 for July 29th 2010. By comparing the correct SBE43 pseudo θ_{CP} with the optode θ_{CP} interpolated onto the same density surfaces enables a linear regression between the two to be calculated for each of the calibration dates (figure 3.10), with this regression representing the calibration required to correct the optode data. Once this regression has been applied to the optode θ_{CP} data, the oxygen concentration from the optode can be calculated using equations 1 to 6, to produce a calibrated optode oxygen dataset. To complete quality control on this optode oxygen data, the optode and SBE43 oxygen values is plotted against density (panel c), depth (panel d), and subtracted from each other (SBE43- optode oxygen), and then plotted against density in panel B. Optode oxygen data after calibration closely follows SBE43 oxygen data on all calibration dates. To further highlight the effect calibration has on optode data, original, uncalibrated optode oxygen concentrations are plotted as green crosses in panel d.

The Oxygen Optode

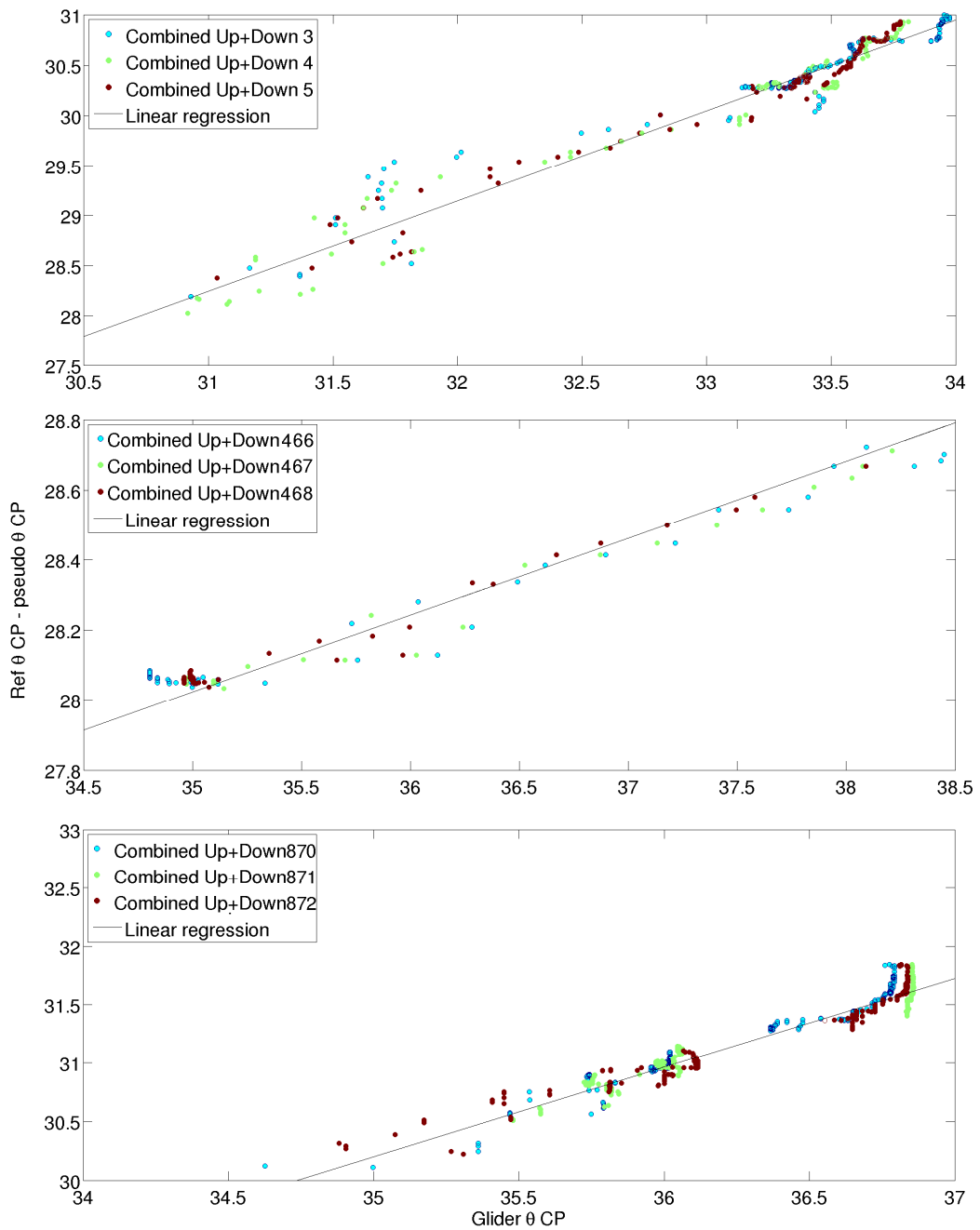
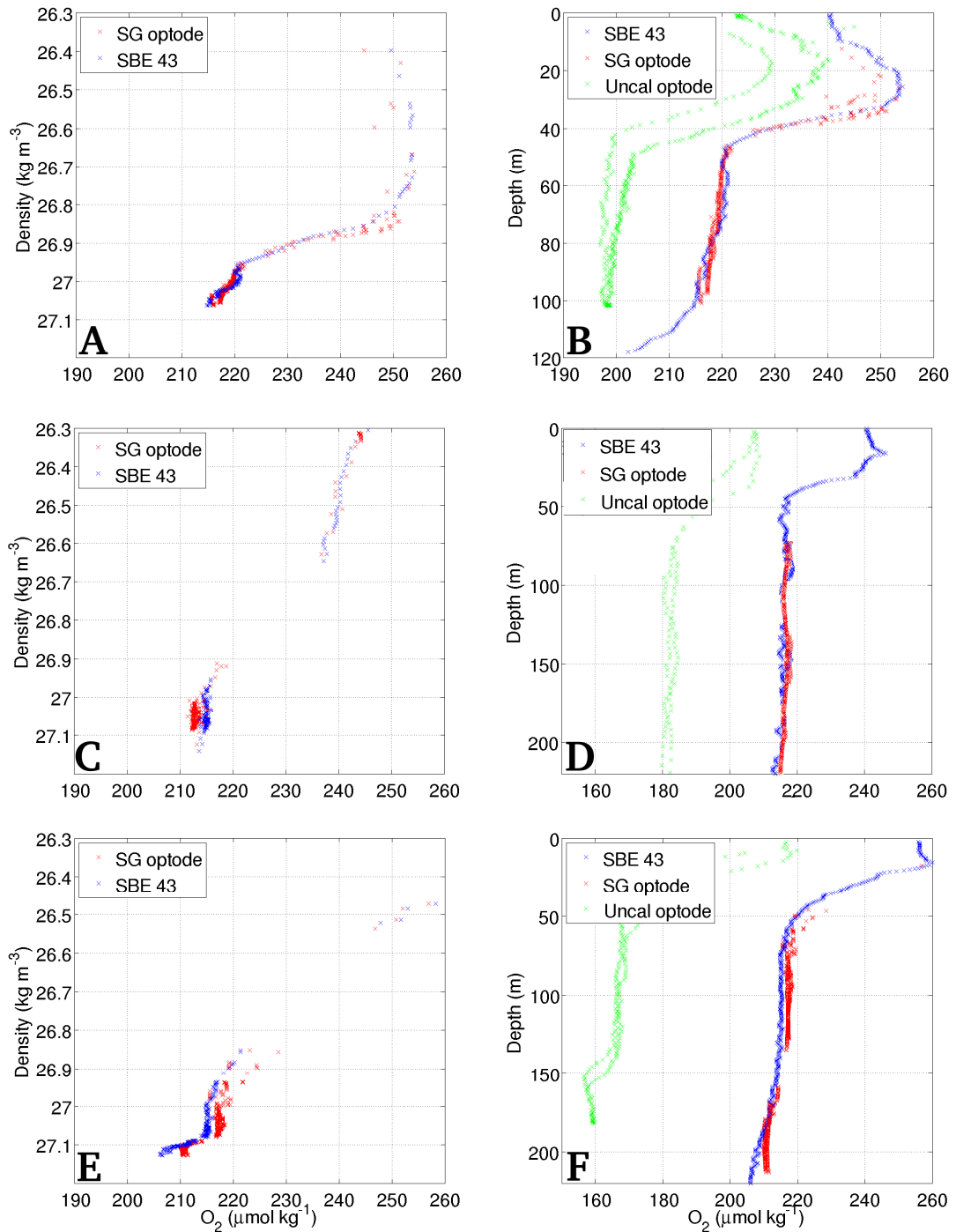


Figure 3.10 Top: 1st June 2010 optode calibration, using dives 3,4 & 5, Middle: 29th June 2010 optode calibration, using dives 466,467 & 468, Bottom: 29th July 2010 optode calibration using dives 870, 871 & 872.

The Oxygen Optode



Figures 3.11

A test of the linear regressions, with **A** and **B** relating to the 1st June calibration, **C** and **D** relating to 29th June and **E** and **F** relating to 29th July calibrations.

The Oxygen Optode

The three SBE43 pseudo θ_{CP} , and the optode θ_{CP} linear regressions from June 1st, June 29th and July 29th are plotted in figure 3.10. To test these regressions, both the 'correct' oxygen from the calibrated Mytilus CTD cast, and the 'corrected' Seaglider optode data is plotted against density and depth (figure 3.11). Here, there is good agreement between the two data sources, therefore suggesting that the calibration has been successful.

The linear regressions show a drift between each of these calibration dates, with decreasing θ_{CP} values with increasing time. This manifests itself in uncalibrated optode oxygen data showing erroneously decreasing oxygen concentrations with increasing time, described here as optode foil drift. Therefore, to calibrate the entire optode oxygen dataset using these three linear regressions requires a description of how the linear regressions change (drift) with respect to time.

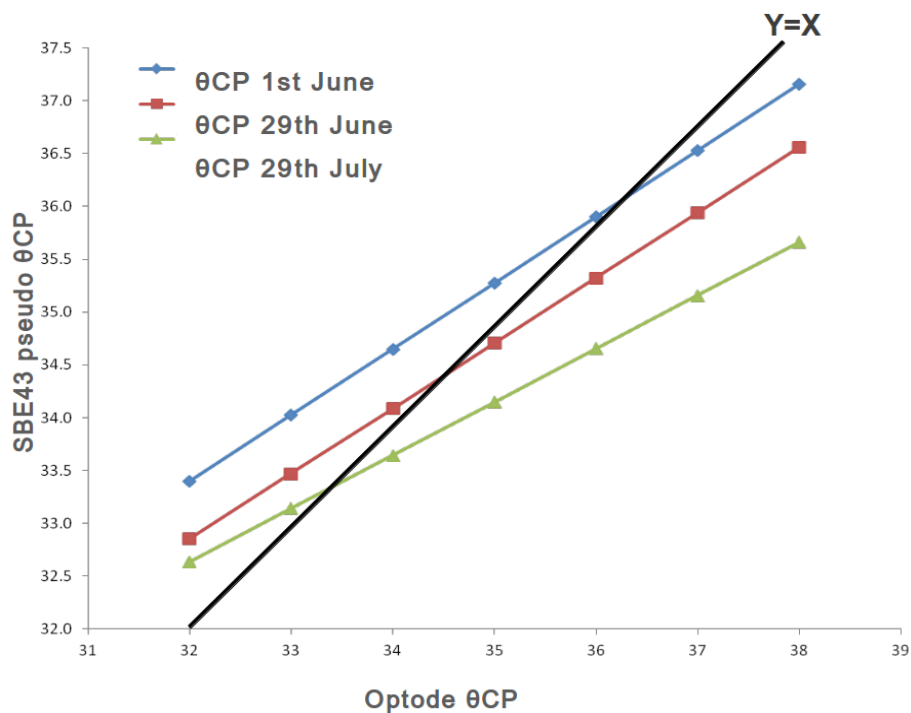


Figure 3.12 SBE43 pseudo θ_{CP} , and the optode θ_{CP} linear regressions for 1st June, 29th June and 29th July

The Oxygen Optode

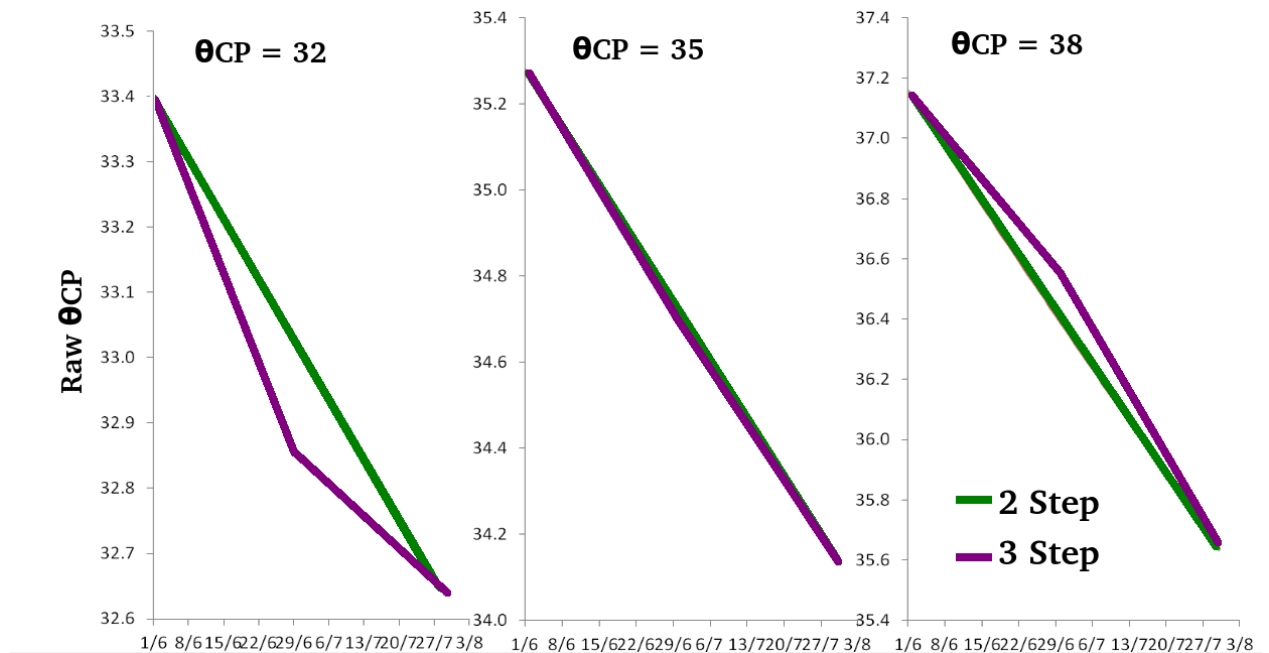


Figure 3.13 Uncalibrated optode θ_{CP} values that equate to calibrated θ_{CP} values of 32, 35 and 38, between the 1st June, 29th June and 29th July 2010,

Optode calibration and optode drift can be corrected by applying both the linear regression equation from the 1st of June to all θ_{CP} data (to calibrate the optode's θ_{CP}), and a time dependent θ_{CP} correction that removes the optode foil drift (to ensure that all θ_{CP} values are equivalent to optode θ_{CP} values June 1st). Deriving the time dependant optode foil drift correction can be completed either by a two point calibration, assuming a linear drift occurs between 1st of June and the 29th July (figure 3.13 green line). Alternatively, a three point calibration can be completed, assuming a linear drift occurs between the 1st of June to the 29th June, and then second definition of linear drift occurs between 29th June to the 29th July (figure 3.13, purple line). As there is little difference between the two techniques at θ_{CP} values between 32 and 38 where 98.45% of all mission θ_{CP} values fall, I have assumed that the foil drift is linear with respect to time, and hence chosen the two point calibration.

3.5 Conclusions

Data from the optode processed solely using factory calibrations, and corrections for pressure, salinity and temperature indicated some hysteresis between up and down casts (figure 3.2), and optode sensor foil drift (figure 3.13). Both of these features can be seen in the large variability of optode measured oxygen concentrations below the oxycline in figure 3.16 A, that do not exist in oxygen data measured by the SBE 43. Therefore, to remove these erroneous features, corrections and calibration made to the Seaglider's Aanderaa 4330F optode data were made, broadly falling into two categories:

1. Optode sensing foil lag and Seaglider timestamp corrections
2. Optode oxygen calibration and optode foil drift correction.

Correcting lag and timestamp errors was first completed by removing the Seaglider timestamp errors caused by the Seagliders TT8 processor applying a single timestamp to all data from all instruments. Issues with the mounting of the optode further back from the CT cell, and time lag due to the response time from the optode sensing foil where dealt with together, by attempting to minimise the differences in optode θ_{CP} measurements between up and downcast for a large, representative sample of dives (200 to 800), thus producing an optimised τ time correction.

Optode calibration and foil drift correction were completed using 3 co-located CTD casts made by the RV Mytilus on the 1st June, 29th June and 29th July 2010. Here Winkler calibrated SBE43 oxygen measurements were converted into pseudo θ_{CP} values using the unique foil coefficients for the Seagliders optode. The optode θ_{CP} , and SBE43 pseudo θ_{CP} were then gridded onto identical isopycnal surfaces, and optode θ_{CP} calibrated from the linear regression between the two. This calibration was found to be effective, with calibrated oxygen concentrations from the Seaglider's optode closely mirroring calibrated SBE43 oxygen calibrations.

Foil drift correction was completed by calculating the change in θ_{CP} values with respect to advancing time. This time component was added to the calibrated θ_{CP} values from the 1st of June, to calibrate the entire Seaglider oxygen dataset. The effects of these corrections can be seen in figure 3.14 B and 3.15, where the Seaglider optode data closely resembles both the SBE 43 and winkler titration data.

The Oxygen Optode

At this point oxygen, temperature, salinity, chl a, backscatter and CDOM from the Seagliders mission have all been calibrated, and where possible compared with in-situ data. This completed dataset can be used to assess the biogeochemistry of the region in the following chapters.

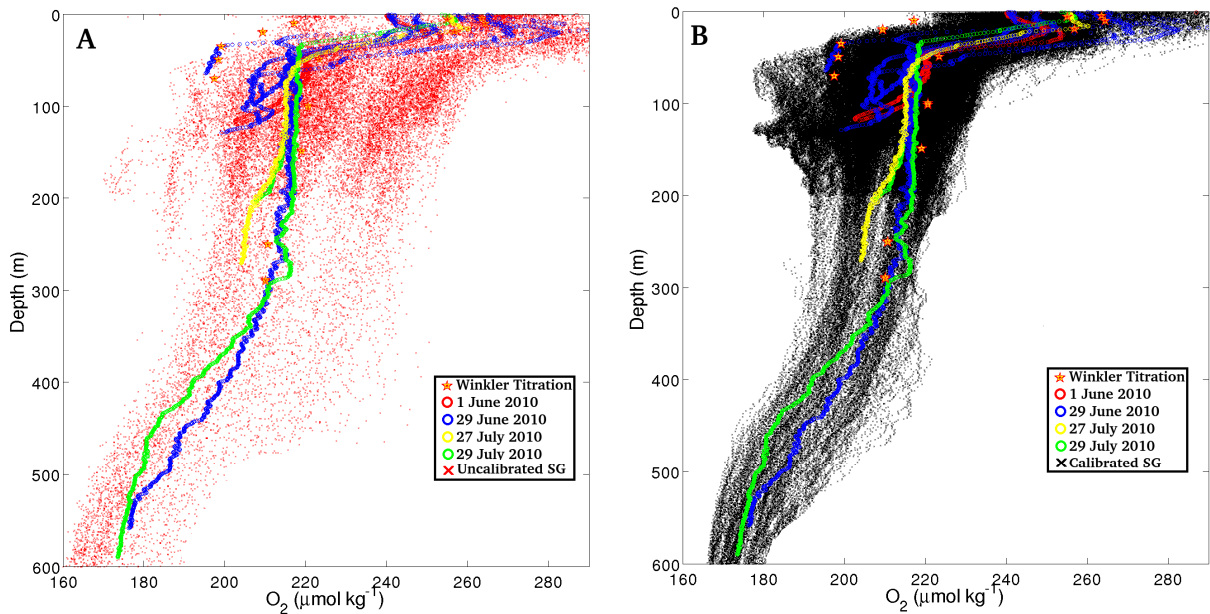


Figure 3.14 All QC_GOOD seaglider optode data (red or black crosses) and R.V Mytilus SBE 43 (coloured circles) and winkler titration (red stars) data collected during summer (June-August 2010). Panel A shows optode data with salinity, pressure and temperature corrections, using the standard Aanderaa factory calibrations, but with no time or foil lag corrections, or cross calibration with the Mytilus dataset. Panel B shows optode data with all corrections, and calibration against the RV Mytilus data

The Oxygen Optode

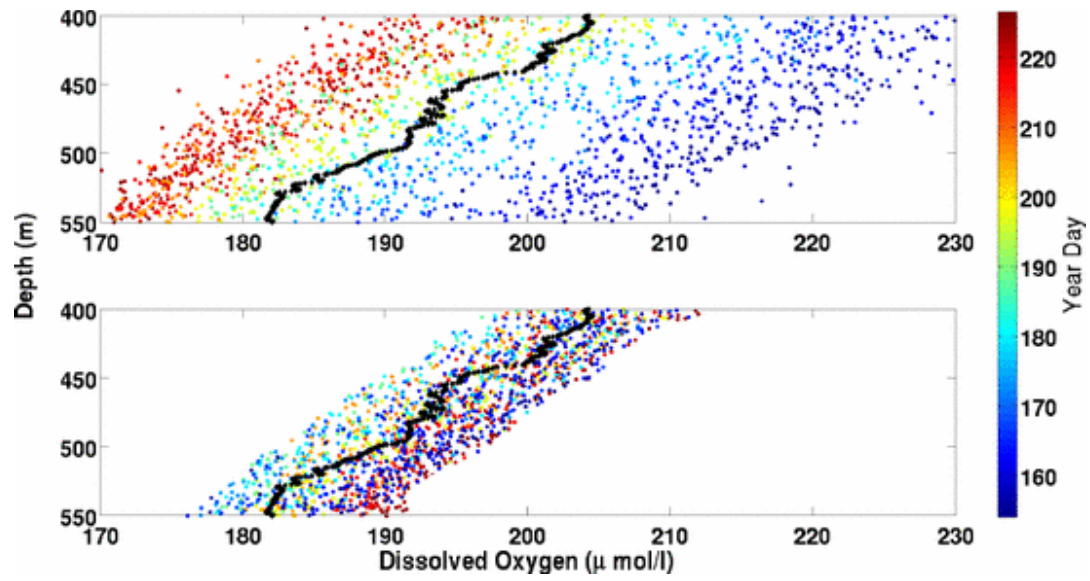


Figure 3.15 Pre (top) and post (bottom) sensor drift correction output of the Aanderaa 4330F. A net time-dependent shift is visible indicating gradual sensor drift throughout the mission. The black line represents the colocated Mytilus CTD.

Biogeochemical and physical observations of the transect region.

4.1 Introduction

The Seaglider transect samples a highly productive region, with the upwelling regime of the watercolumn shown to be the first order control on phytoplankton bloom dynamics within the Iberian upwelling system (Piedracoda et al. 2008; Moncoiffe et al. 2012). As discussed in chapter 1, upwelling strength is moderated by the regional surface wind forcing, with variability in wind forcing causing repeated switching between upwelling, relaxation and downwelling over a single summer season (Torres & Barton 2007). Fully developed upwelling has been observed to considerably (~ 50%) increase total biomass carbon, and chl a concentrations, compared to periods of watercolumn relaxation within the same season (Gago et al. 2011; Cermeño et al. 2006). The physical and biological variability resulting from changes in upwelling regime can be observed in MODIS chl a and sea surface temperature (SST) data from the transect region (42.1 N, 9.05 to 9.67 W). Here, a lowering of SST can be used as a proxy for upwelling, as cooler, deep water is brought towards the surface (Barton et al. 2001, figure 4.1). There is a repeated pattern of SST fluctuating between cooler (14-15 °C) and warmer (17- 18 °C) temperatures (e.g. in 2010, year days (YD) 150 to 155 shows warmer SST, with YD 165-170 showing cooler SST), highlighting periods of upwelling and relaxation. Demonstrating this connection between upwelling and phytoplankton bloom dynamics, periods of upwelling also feature higher chl a concentrations. This can be observed both qualitatively, by the alignment of high chl a and low SST events in figure 4.1, but also quantitatively on a seasonal timescale, with lower-than-average SST seasons featuring higher-than-average chl a concentrations (such as 2006, 2010 and 2011).

MODIS data, by virtue of being a satellite product, is restricted to observations of the sea surface, or the optical depth of the property being measured (Behrenfeld & Falkowski 1997). To understand watercolumn processes below the surface layer requires the collection of ship-bourne, mooring or Seaglider data.

Biogeochemical and physical observations of the transect region

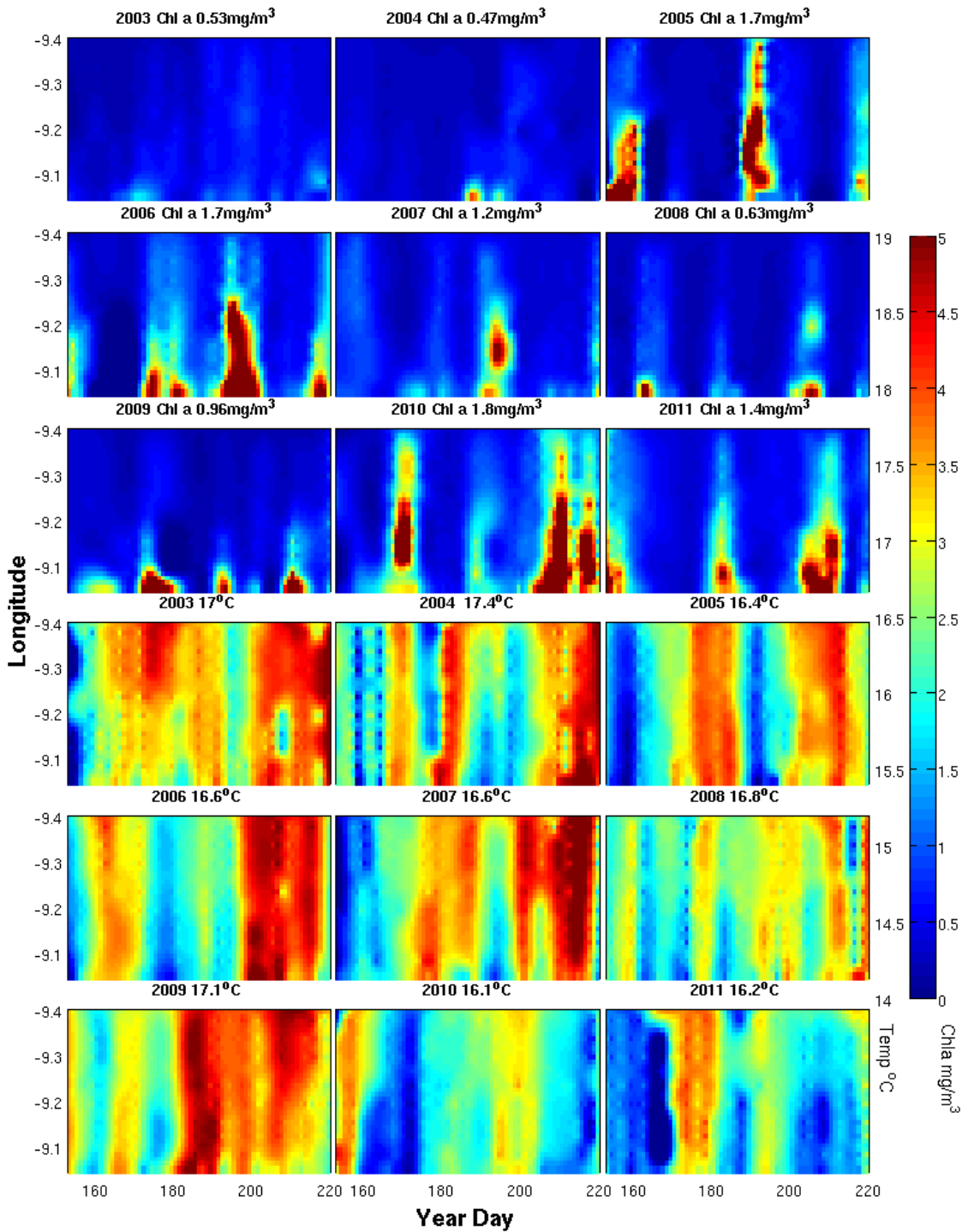


Figure 4.1 Hovmoller plots of MODIS Chla and SST concentrations for the transect region (42.1 N, 9.05 to 9.67 W) between 2003 and 2011), with seasonal average values above each plot. The Seaglider mission was conducted in 2010.

4.2 Water masses observed in the region

As the biogeochemistry and physical processes of the region are strongly intertwined, an understanding of the physical processes within the watercolumn is required before any assessment of the biology can be made. One method of doing this is to examine the watermasses observed in the region using Seaglider collected temperature and salinity data. Over the course of summer 2010, three main water-masses were observed between the surface and 1000 m on the Iberian continental shelf, shelf slope, and open ocean within the Seaglider transect. Both the depths and temperature/ salinity properties observed by the Seaglider were consistent with those in the literature (Fiuza et al. 1994, Barton et al. 2001). The deepest water-mass is modified Mediterranean outflow water (MMOW). Typically found below 550 to 600 m, MMOW is identified from overlying water-masses by a slight increase (0.4 ± 0.1 °C) in water temperature, and an increase in salinity from 35.65 ± 0.05 to 36.2 ± 0.05 (fig 4.2). MMOW originates from the mixing of Mediterranean outflow waters and North Atlantic central water at the Espartel sill, west of the Strait of Gibraltar (figure 1.6). This water is exported as a poleward counter current, flowing in close proximity to the Iberian continental slope towards the transect site (Wesson 1994, Barton et al. 2002). Eastern-North Atlantic Central water (ENACW) that overlies MMOW consists of two water masses of different origins (Fiuza et al. 1994). The deeper and typically denser of the two water masses is ENACW of subpolar origin (ENACWP), formed in regions north of 46 °N (identified by temperatures of 10-12.2 °C and salinities of 35.40 to 35.66 (Fiuza et al. 1994)). ENACWP dominates ENACW in the Bay of Biscay, and forms the core of the northern limb of the Portugal current, which is transported southwards as part of the EBC (Barton et al. 2001). The lower density ENACW of subtropical origin (ENACWT) identified by temperature properties of 13.13-18.50 °C and salinities of 35.8-36.75 (Fiuza et al. 1994), originates from subtropical North Atlantic, and is formed along the Azores front at 35 °N. ENACWT has previously been described as the dominant surface watermass along the Iberian upwelling region south of 43 °N (Alvarez et al 2005). The two ENACW water masses convergence within the Iberian upwelling region between 42 and 44 °N, where ENACWT meets ENACWP transported southwards (Rios et al., 1992). This convergence

Biogeochemical and physical observations of the transect region

was seen over the transect region (at 42.1 °N), with both limbs of ENACW observed in all transects.

Over the course of the Seaglider mission, ENACWP was found to exist between a maximum depth of 600-550 m to a minimum depth of 250 to 180 m. ENACWT was typically observed between a lower depth of 250-180 m, and featured a highly variable upper limit of 70-20 m depending on upwelling and mixing processes (fig 4.4 and 4.5). Finally, the last water mass is 'surface water', a highly variable mix of ENACWT and low density, brackish and warm Rìa-outflow waters. This surface water has a large range of T-S properties, dependant on the relative proportions of ENACWT and Rìa-outflow waters it contains (Arístegui et al. 2006).

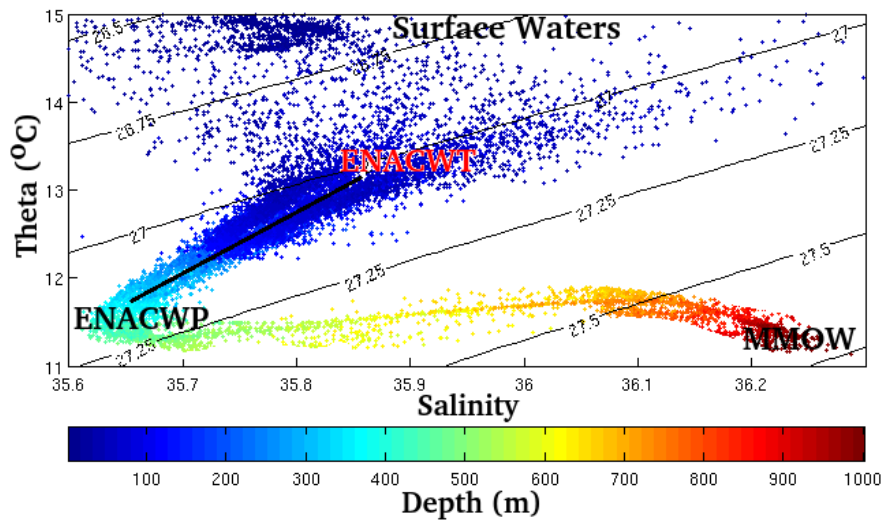


Figure 4.2 Theta - S plot for entire mission, with individual points coloured by depth, black lines indicate isopycnals. Four water masses can be observed, as MMOW at depths greater than 550 m, ENACWP at depths of 550 to 250 m, ENACWT at depths of 250 to 70 m and a highly variable Rìa outflow/ENACWT mix between 80 m and the surface.

4.3 Observations of Upwelling

Upwelling regimes can be identified through the use of an upwelling index (figure 4.3). The NOAA (National Oceanic and Atmospheric Administration) FNMOC (Fleet numerical meteorology and oceanographic center) upwelling index (UI) is forced using FNMOC observational wind fields in combination with an Ekman upwelling model designed for EBC continental boundary regions (NOAA 2013). This UI provides an estimate of the westward surface water advection in units of cubic metres/ 100 m of coastline. Assuming geostrophy, this is equal to the upwelling rate, (and hence high positive UI indicates strong upwelling). Data from summer 2010 indicates that there were two major upwelling events, one between YD 160 and 175, and a second from YD 203 onwards. There was an additional, short lived upwelling peak at YD 186, but this did not feature the same longevity of the other two events.

There were two periods of downwelling, at YD159 and 192 to 196, but these events were small in magnitude, and short lived. Average UI indicated net upwelling for the Seaglider observation period at $981 \text{ m}^3 \text{ 100 m d}^{-1}$ (figure 4.3).

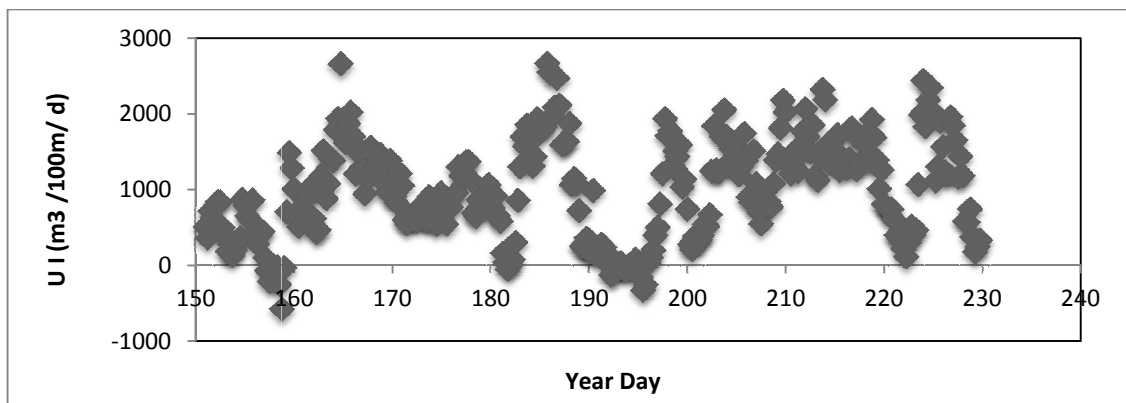


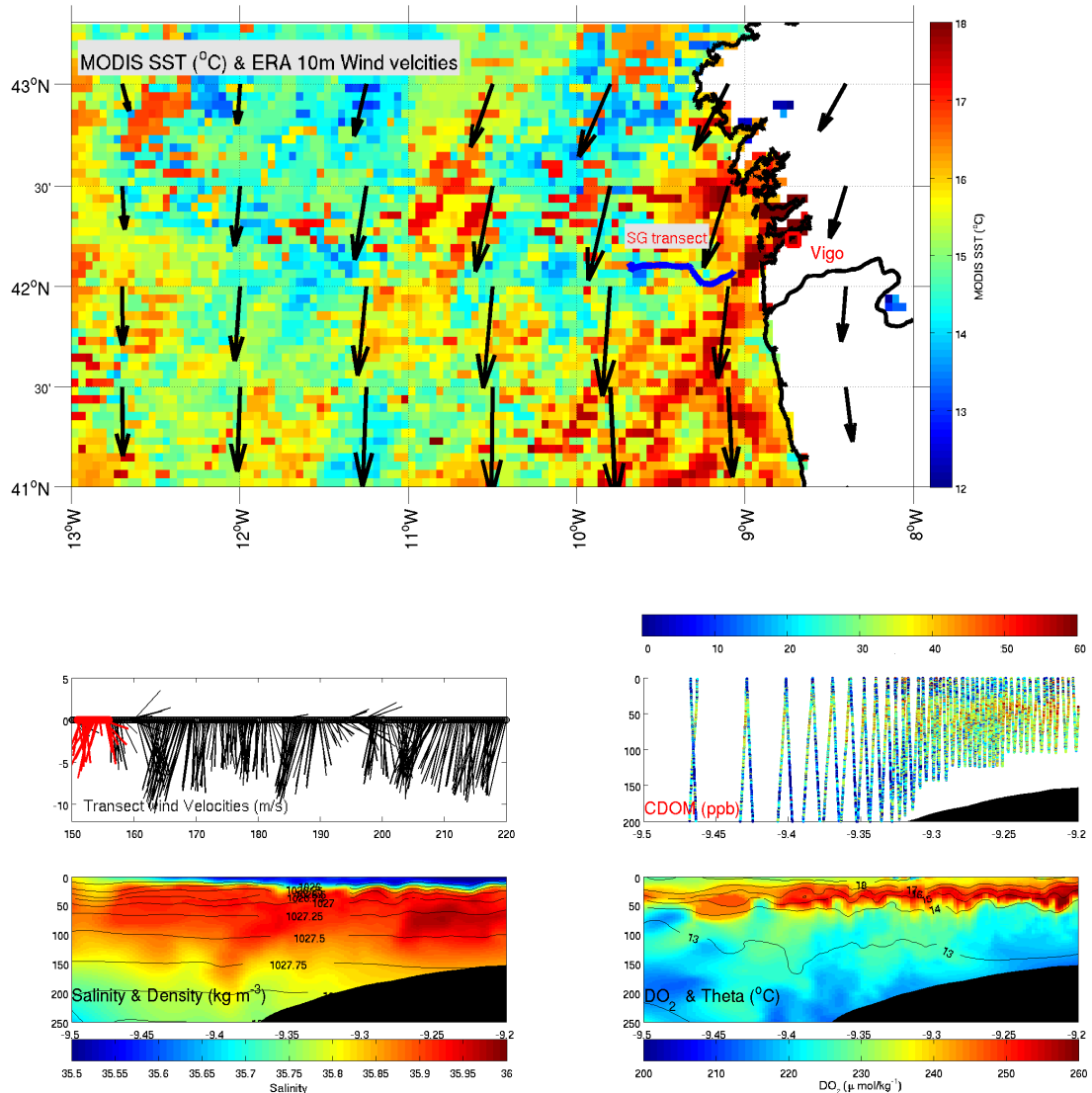
Figure 4.3 Upwelling index for summer 2010, from NOAA/FNMOC modeled output.

Biogeochemical and physical observations of the transect region

Although UI data provides a useful synoptic overview of upwelling events over 2010, Seaglider, MODIS (Moderate resolution imaging spectroradiometer) and ERA (ECMWF reanalysis) interim wind velocities are required to investigate the biogeochemical variability resulting from these upwelling events.

The Seaglider transects that feature upwelling or relaxation are defined in table 4.1, and are depicted graphically over the next seventeen pages. To produce a MODIS/ERA wind product that is directly comparable to the Seaglider data product, daily level 3 gridded MODIS Aqua SST data and ERA interim wind velocities were merged over the range of YD for each transect. For example, transect one was completed between the 2nd and 8th of June, YD151 to YD157. Therefore, daily MODIS Aqua SST from YD 151, 152, 153, 154, 155, 156 and 157 were downloaded, and an arithmetic mean of each grid point was taken, producing a single matrix of average SST over the dates of the Seaglider transect, which was subsequently used to plot SST. An identical technique was used for the ERA Interim wind velocity data, shown as arrows overlaying the SST. This processed MODIS and ERA interim data is plotted, along with Seaglider data over the next seventeen pages.

Biogeochemical and physical observations of the transect region

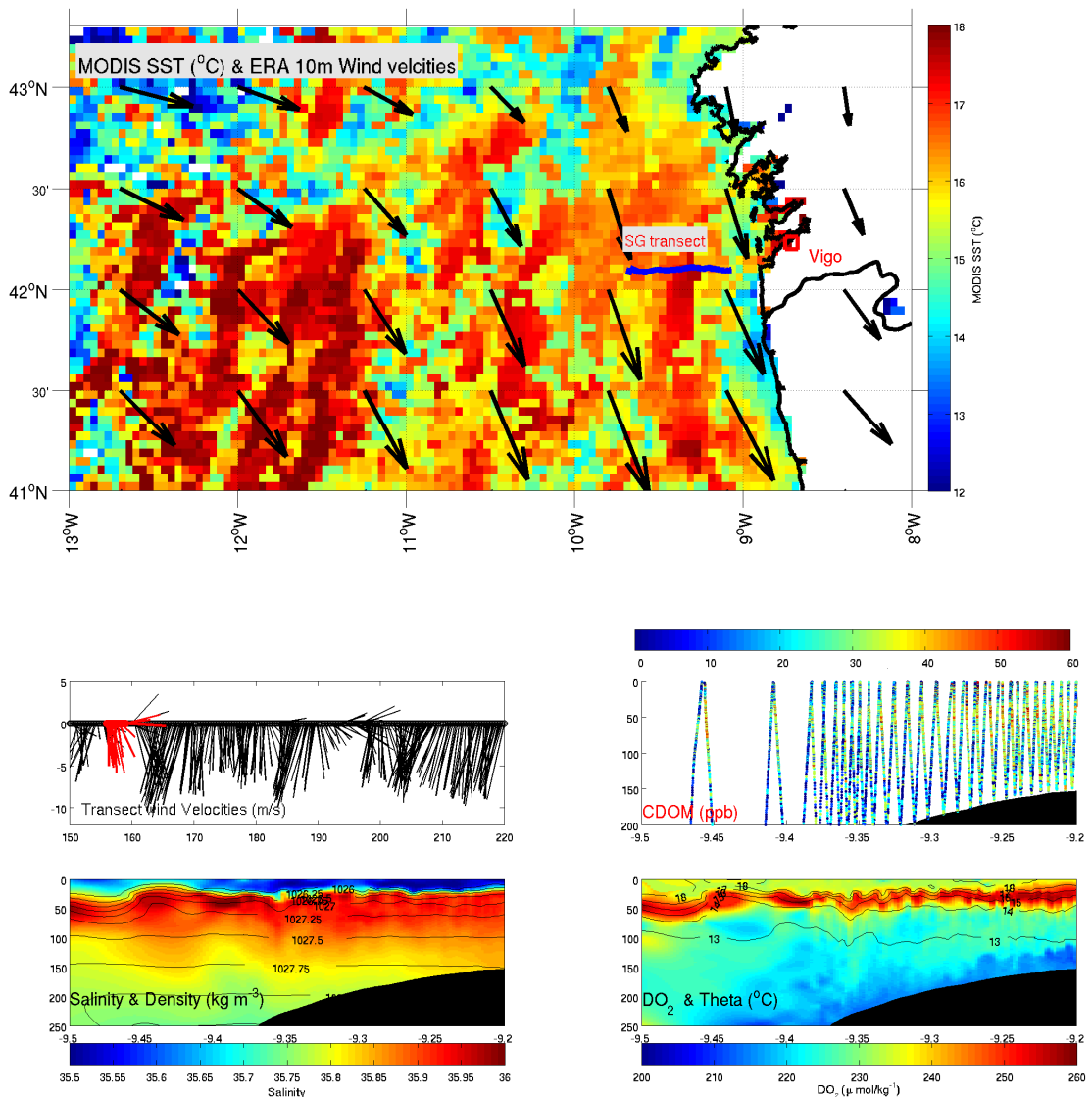


Transect 1

Seaglider transect: east to west. Conditions: Non upwelling & highly stratified. Wind stress: <6 m/s NNE to NW

A stratified and stable water column above 100m persisted from transects one to three, identified by the large range in temperature seen above the thermocline, the presence of a low density and salinity, high temperature Ria outflow water (seen above 20m east of 9.4 °W), and high MODIS SST temperatures close to the shoreline. Surface winds were weak, and variable in direction, suggesting that stratification/ limited upwelling occurred during these first three transects.

Biogeochemical and physical observations of the transect region



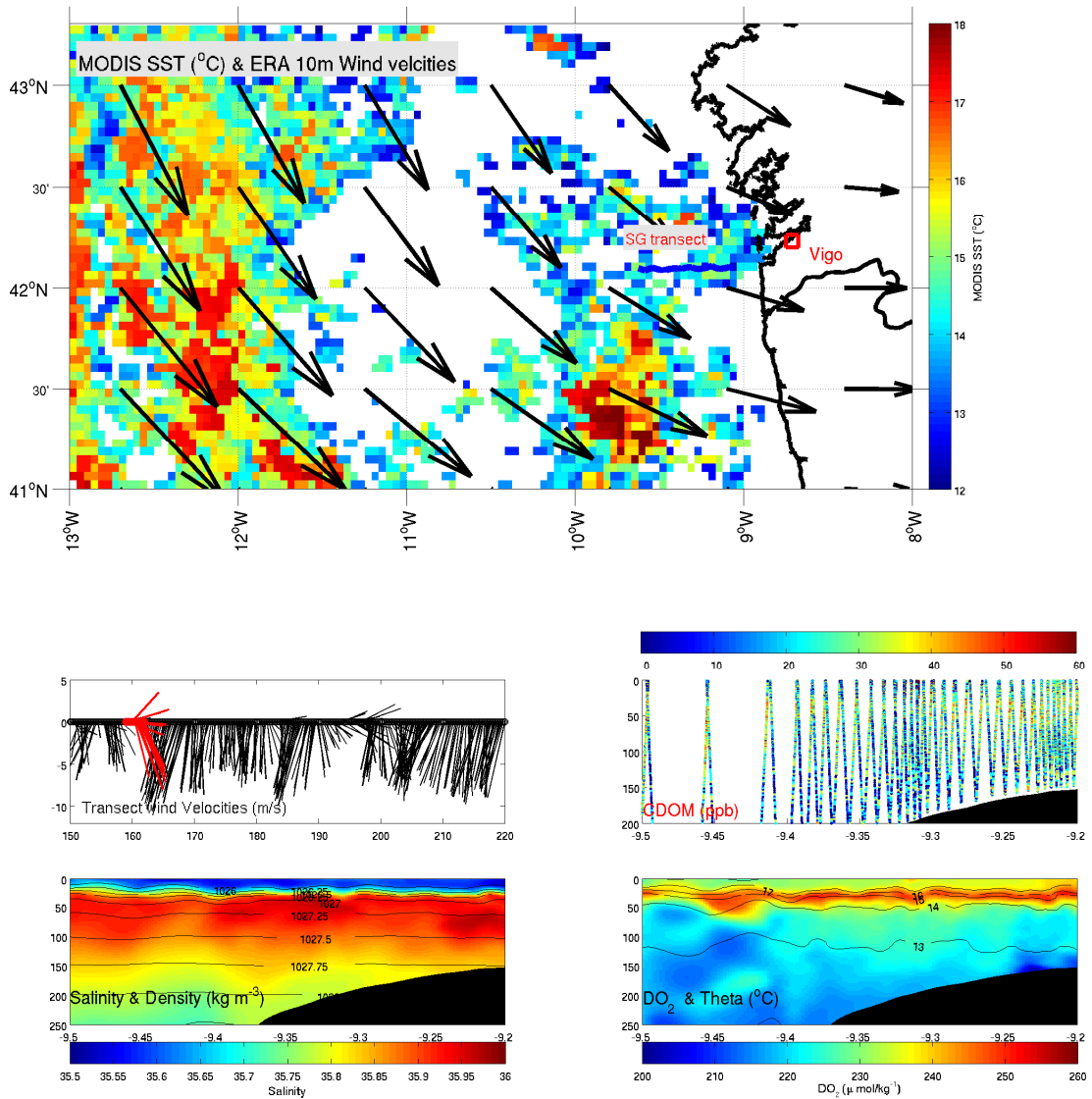
Transect 2

Seaglider transect: west to east. Conditions: Non upwelling & highly stratified.

Wind stress: <6 m/s NNW to NW

Continuing on from transect one, transect two was also highly stratified, featuring very warm <20m temperatures, weak surface winds, and little difference in MODIS SST data between the near shore and off shore temperatures, again suggesting limited upwelling.

Biogeochemical and physical observations of the transect region

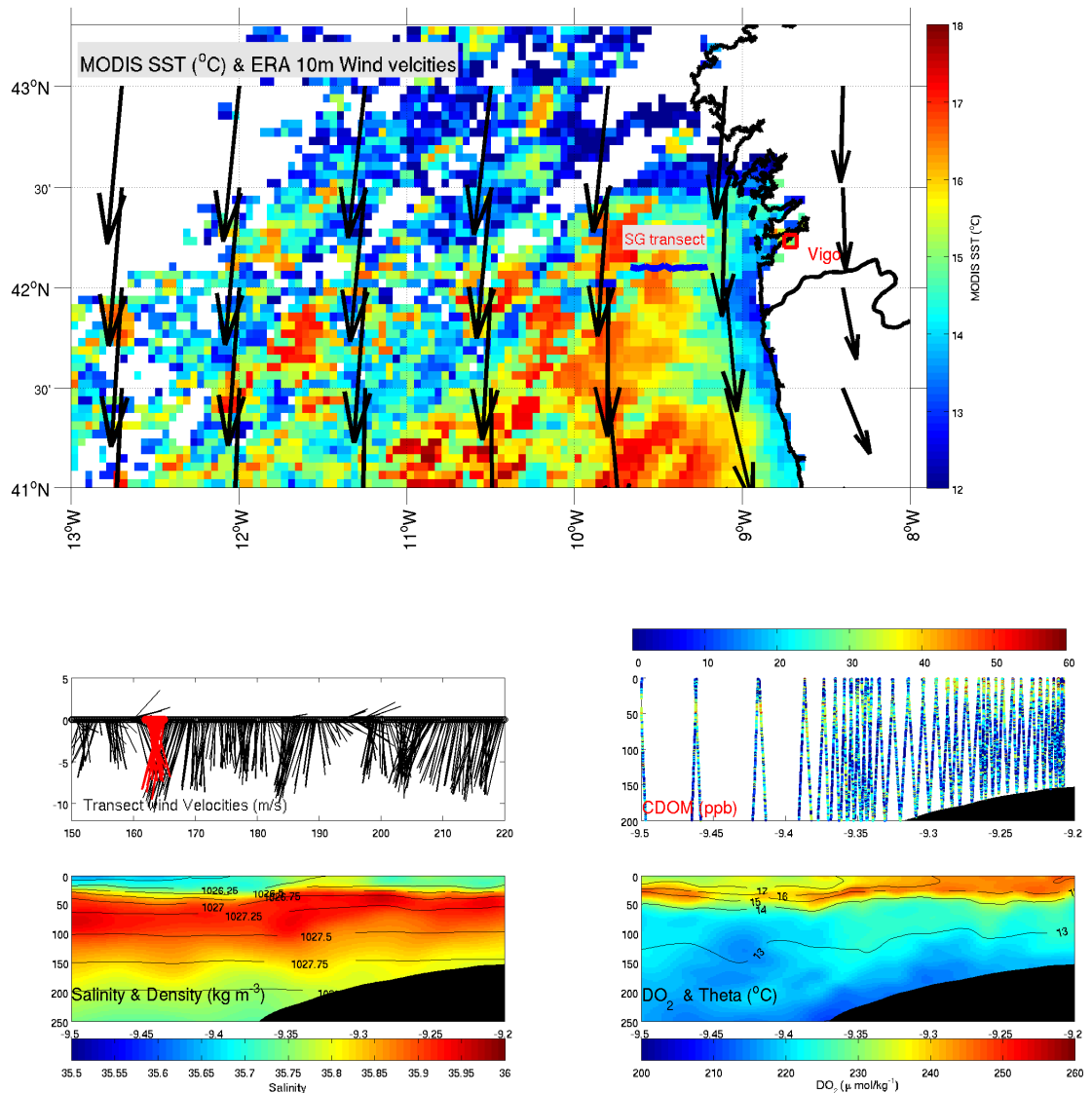


Transect 3

Seaglider transect: east to west. Conditions: Non upwelling & highly stratified. Wind stress: <8 m/s NNW to W

The final stratified transect before upwelling occurs, transect three again features high near surface water column temperatures. Surface winds for this period became stronger (up to 8 m/s vs <6 m/s for the first two transects), but were orientated in a westerly direction for the first two days of the transect. This increased wind stress resulted in a deepening of the mixed layer depth (as seen by the mixing of warmer surface waters deeper into the water column), but limited upwelling (as seen by the similar near shelf and off shelf MODIS SST data).

Biogeochemical and physical observations of the transect region

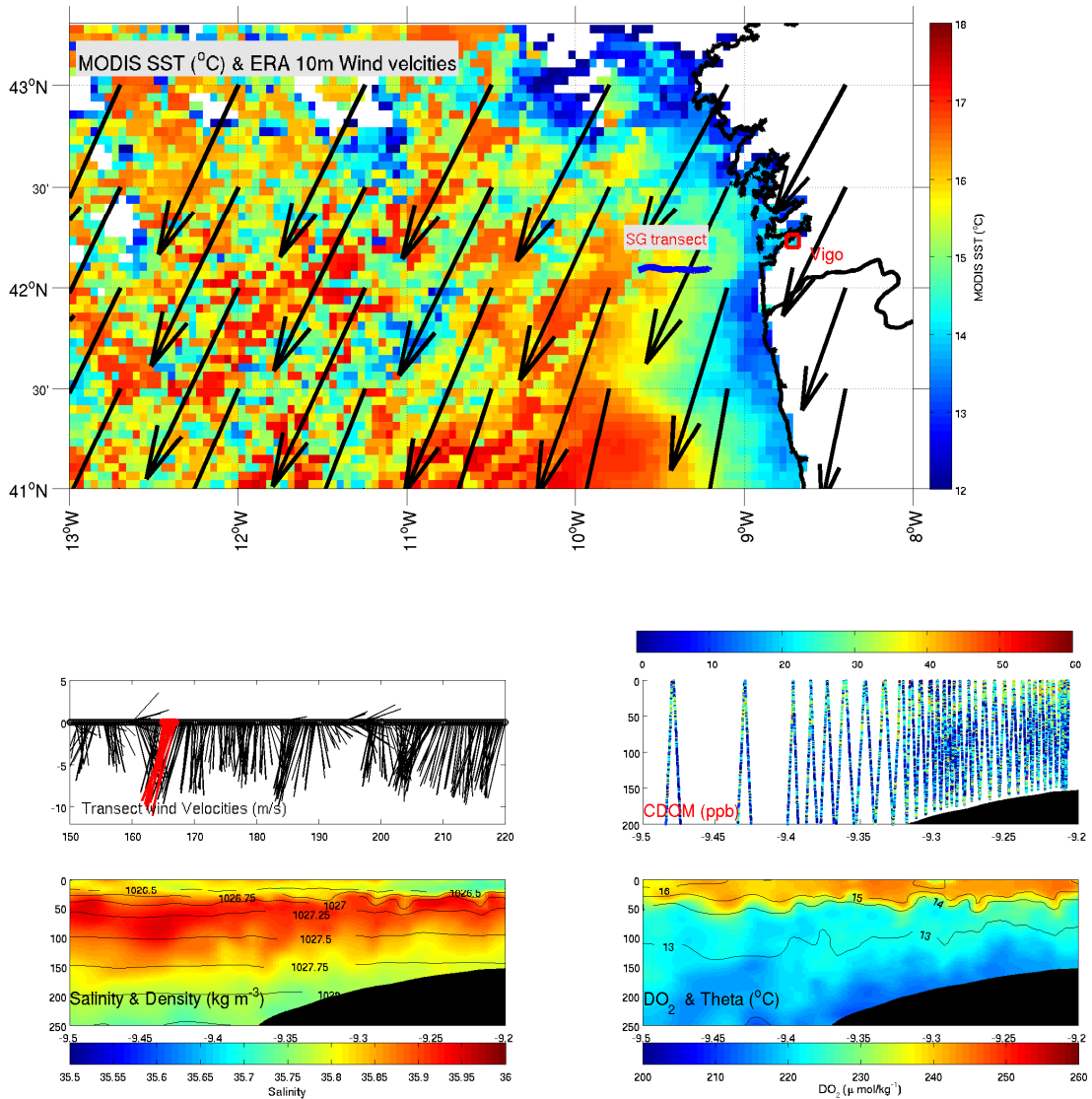


Transect 4

Seaglider transect: west to east. Conditions: Initiation of upwelling, with strongest upwelling towards the east of transect. Wind stress: <10 m/s NNE to N

Wind stresses during transect four were from a northerly direction, and increased in strength compared to the previous three transects. These northerly winds allowed for the first sustained period of upwelling, with colder SST's seen across the wider region in the MODIS dataset. Seaglider data showed a large decrease in surface water temperatures towards the east of the transect, with a 1.5 °C decrease in temperature of the top 20m of the water column east of 9.32 °W. The increased strength of the upwelling on the east of the transect is also seen in MODIS SST, with lower temperatures east of 9.25 °W.

Biogeochemical and physical observations of the transect region

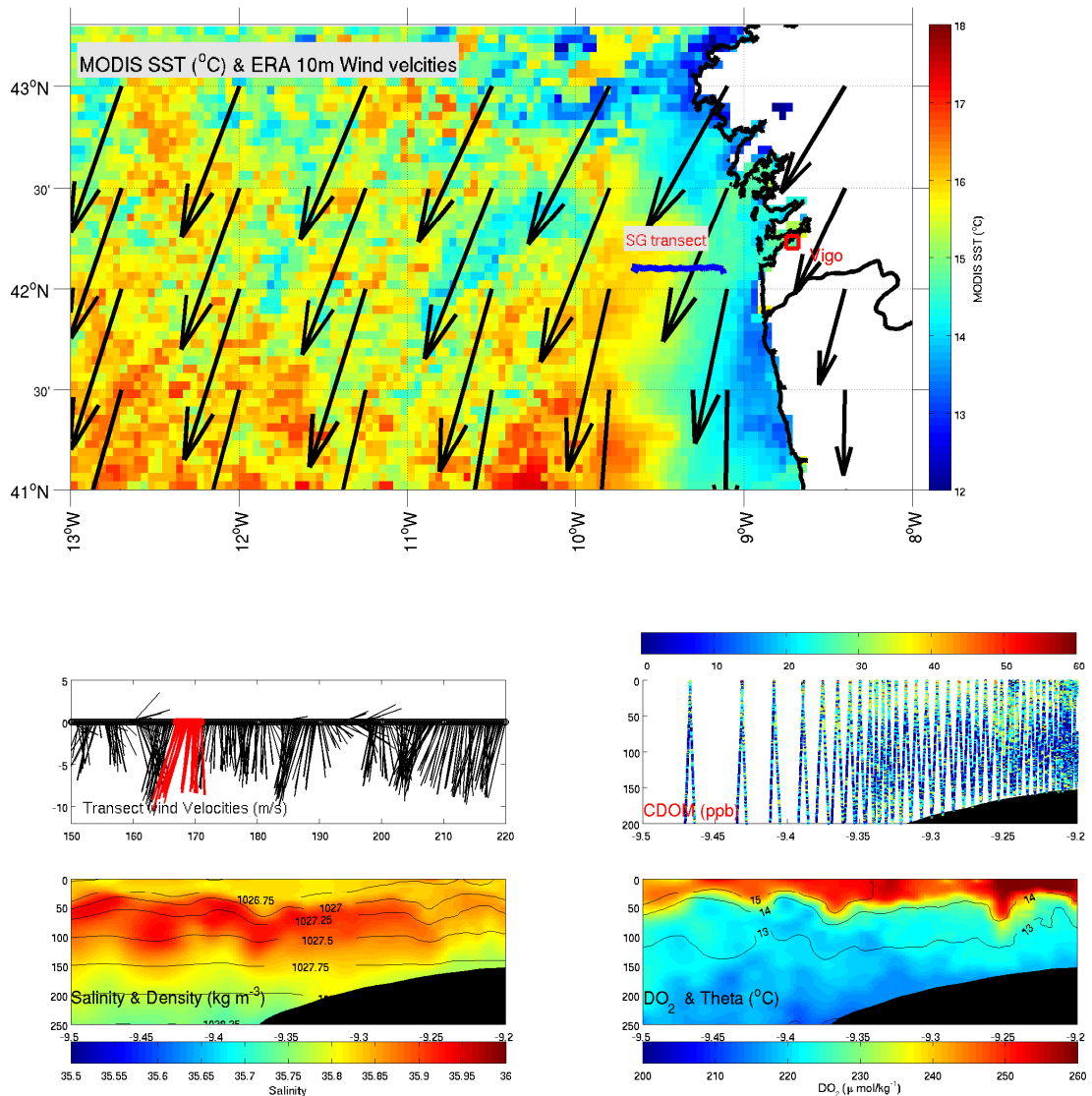


Transect 5

Seaglider transect: east to west. Conditions: Strong upwelling across the Transect. Wind stress: 11 to 13m/s NNE

The strongest wind-stresses for the entire mission occurred during transect five. Resulting upwelling of deeper water masses is seen both across the full extent of the Seaglider transect, and also across the region by colder near shore water seen in MODIS SST. The stratified structure of the water-column is greatly reduced during this time period, with maximum near surface temperatures observed by the seaglider at 15-16 °C. Eastern North Atlantic Central water of sub-polar origin (ENACWP) starts to be advected onto the shelf, as seen by the appearance of 12 °C water between -9.35 and -9.27 °W in locations close to the sea floor.

Biogeochemical and physical observations of the transect region



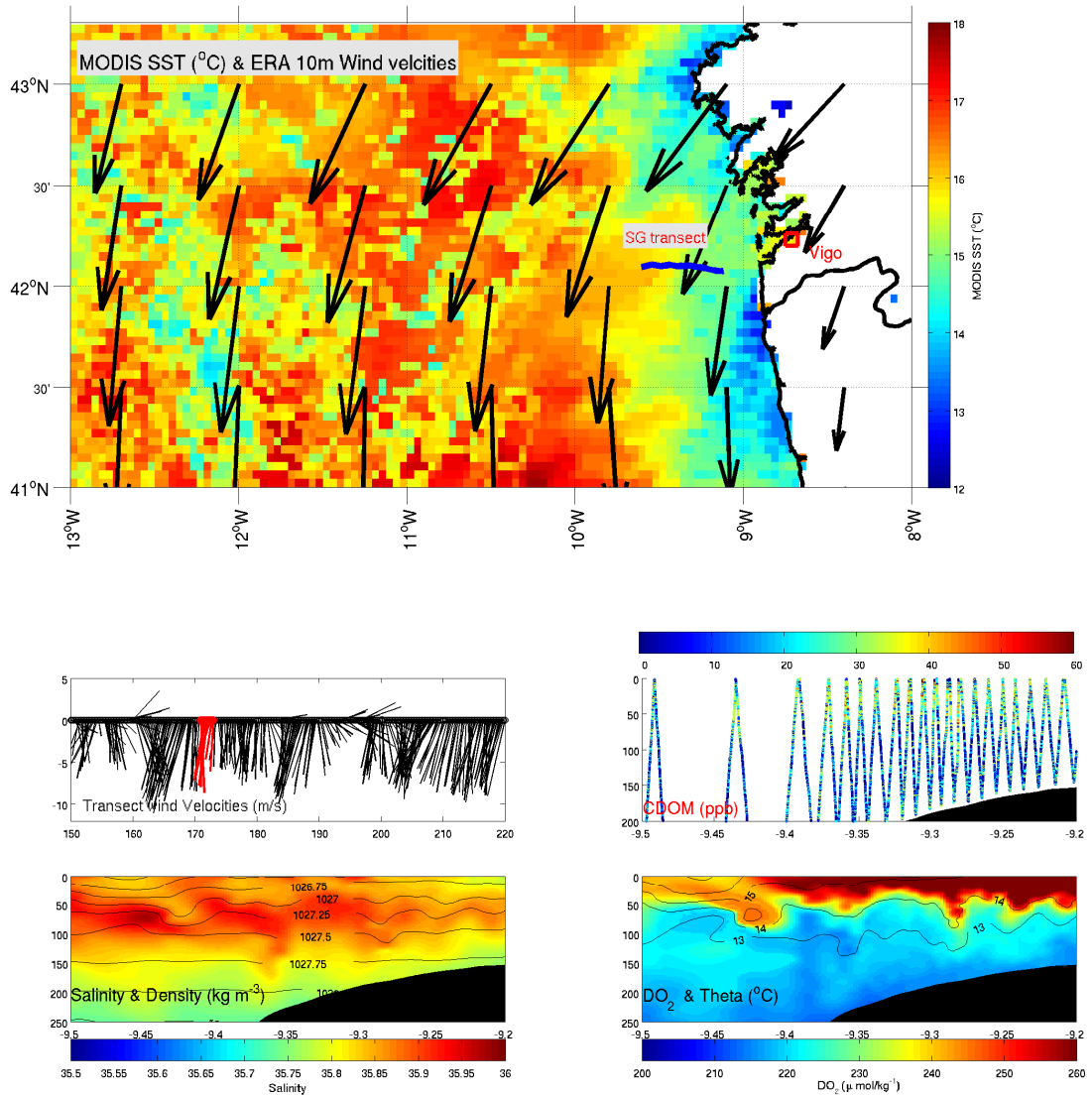
Transect 6

Seaglider transect: west to east. Conditions: Strong upwelling focused towards east of transect

Wind stress: 9 to 13m/s N NNE

The continuation of strong northerly winds maintain the strong upwelling seen during transect five. Seaglider temperature data indicates that the upwelling is strongest in the east of the transect. ENACWP continues to be advected onto the shelf, reaching -9.2 ° W, reaching a depth of 160 m . MODIS SST shows a further decrease in SST from transect 5, with the possible development of filament at 43 °N.

Biogeochemical and physical observations of the transect region

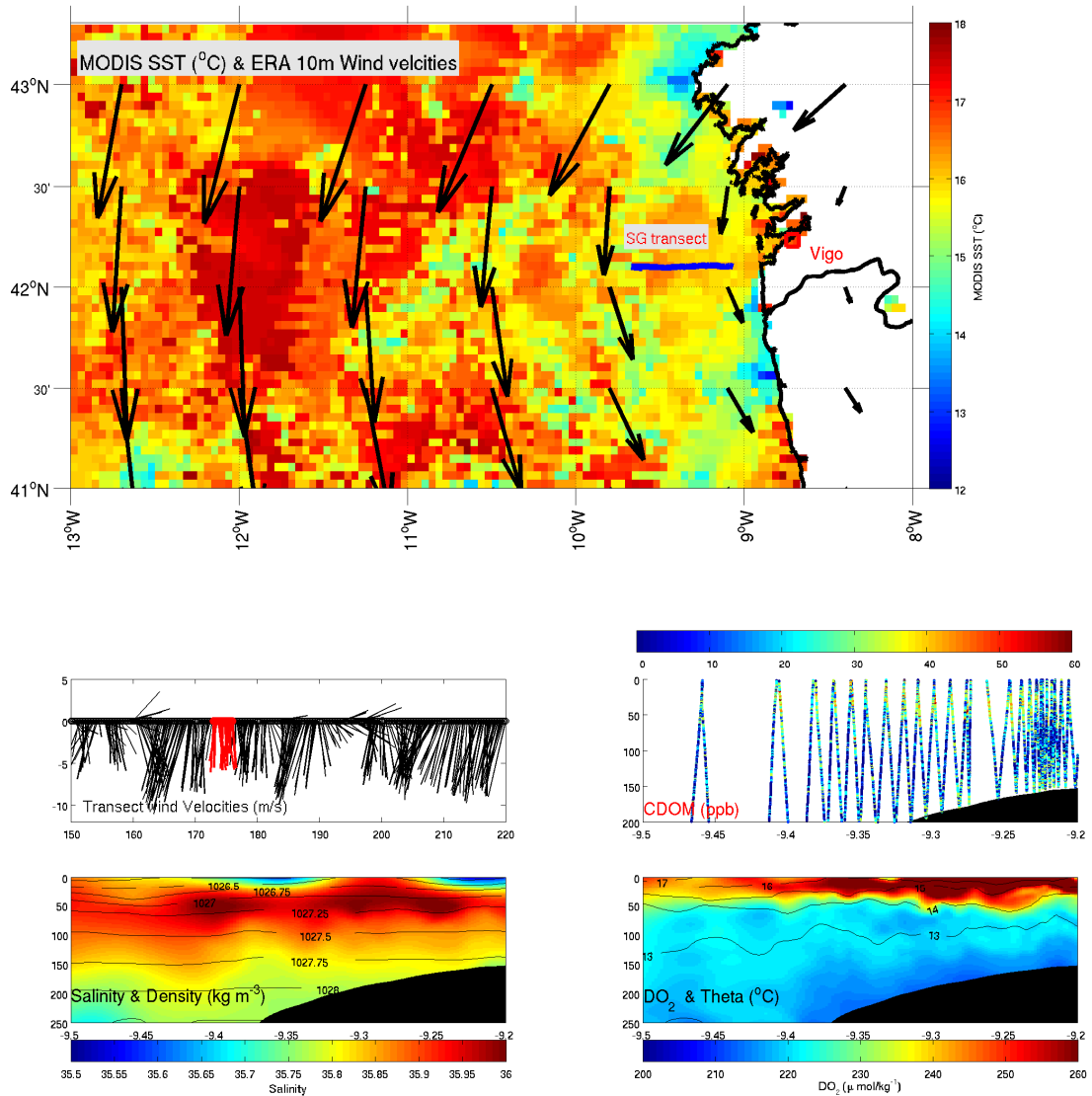


Transect 7

Seaglider transect: east to west. Conditions: Weakening upwelling focused towards east of transect. Wind stress: 8 to 9m/s N

Wind stress during this transect reduces in strength, with wind direction remaining Northerly. Upwelling strength also appear to be reduced, as MODIS SST shows a general warming across the region compared to the previous transect. The filament observed in the previous transect has extended to 11 ° W.

Biogeochemical and physical observations of the transect region

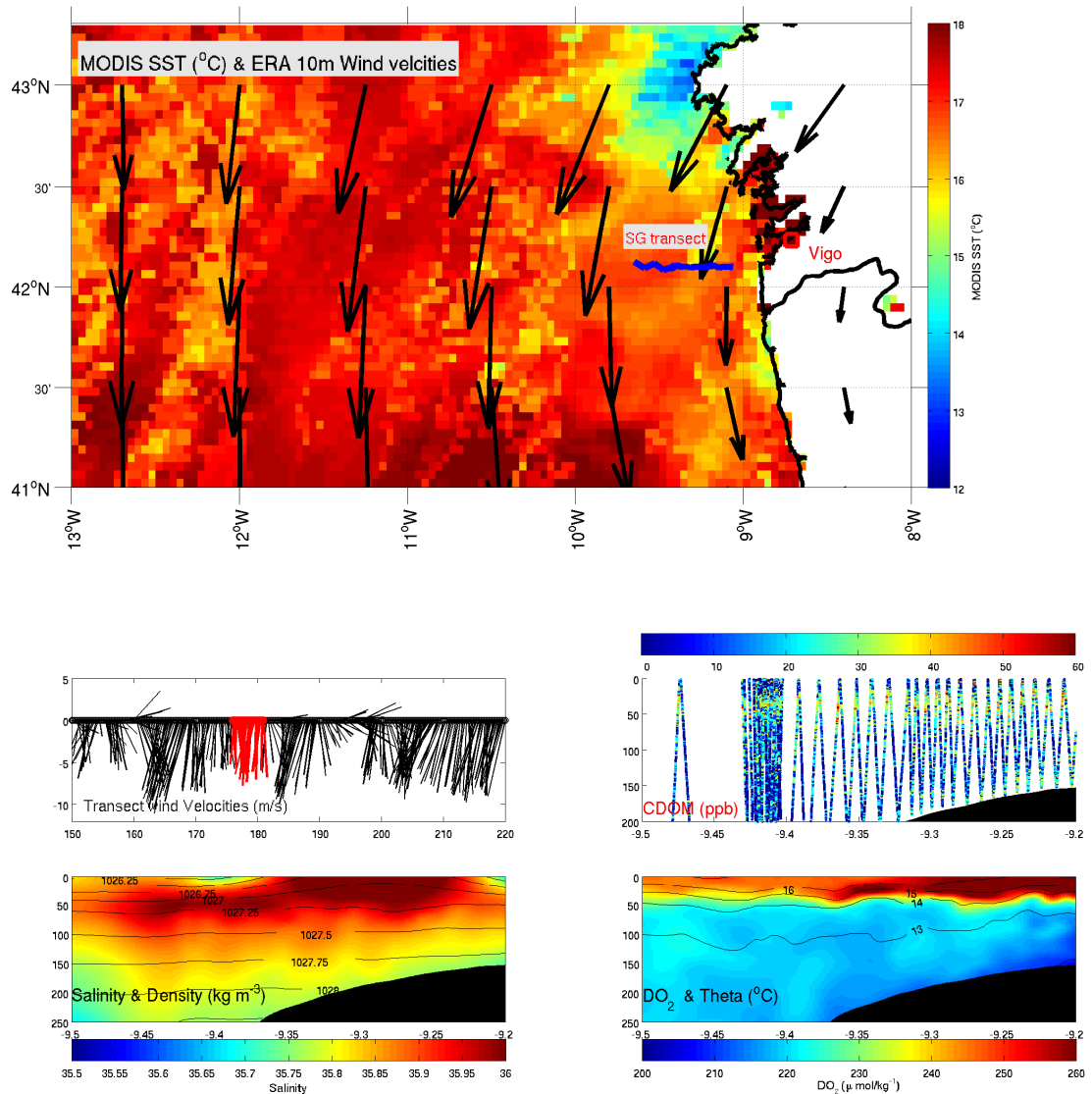


Transect 8

Seaglider transect: west to east. Conditions: start of restratification. Wind stress: 5 to 7m/s N

Transect eight marks the initiation of the second period of water-column stratification for the entire Seaglider transect. Further reductions in wind-stress occur during transect eight, with maximum velocities of only 7 m/s. Both MODIS and Seaglider data indicate that the sea surface continues warming, as per transect seven, with the fastest temperature increases occurring west of -9.4 °W. The filament structure has become less prominent as seen in MODIS SST during this transect.

Biogeochemical and physical observations of the transect region

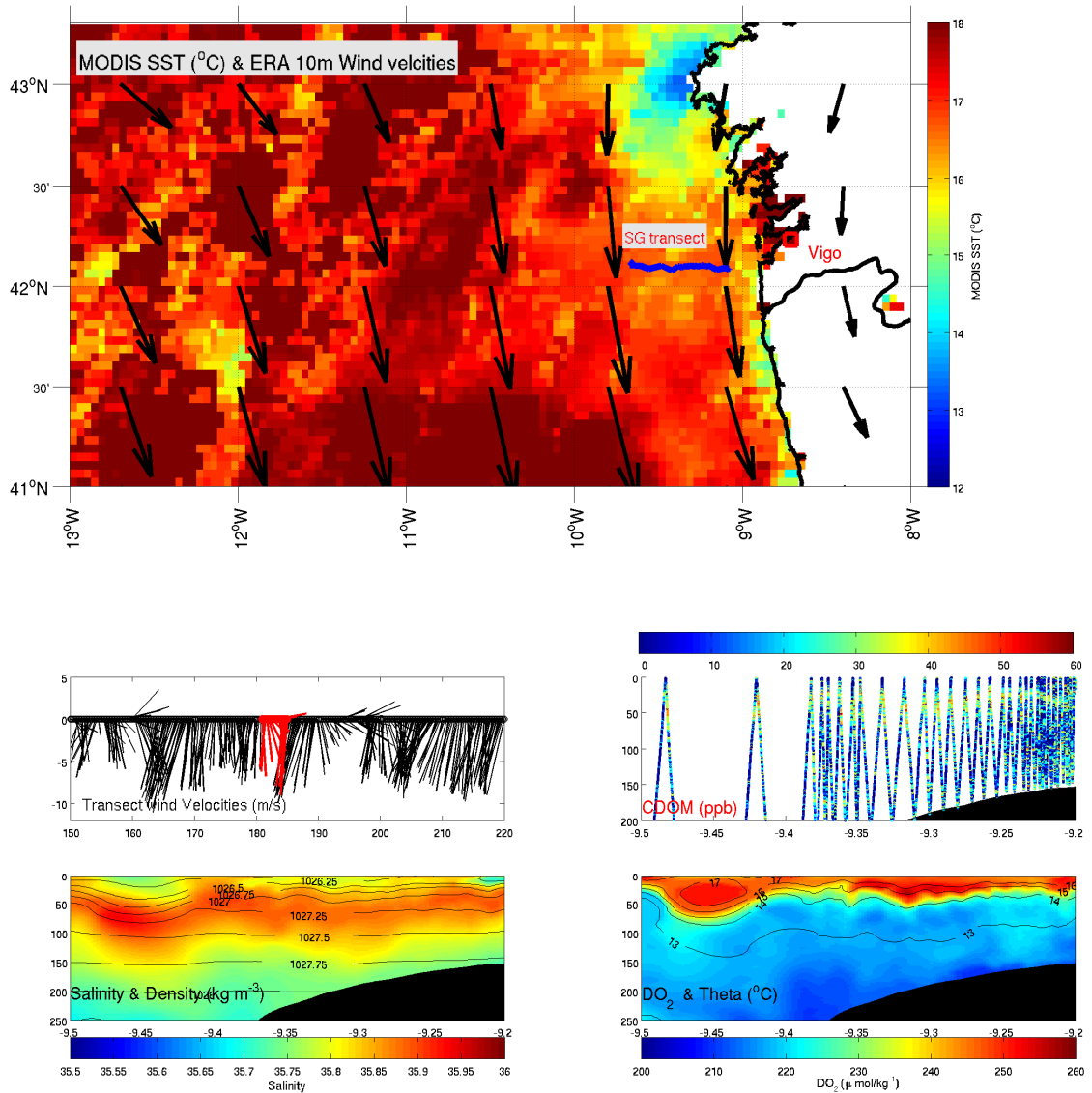


Transect 9

Seaglider transect: East to West. Conditions: restratification. Wind stress: 5 to 8m/s N

Much the same as transect eight, transect nine sees the both the continued restratification and increasing surface temperatures of the water-column. MODIS SST have increased across the entire region by 1-2 °C compared to the previous transect.

Biogeochemical and physical observations of the transect region



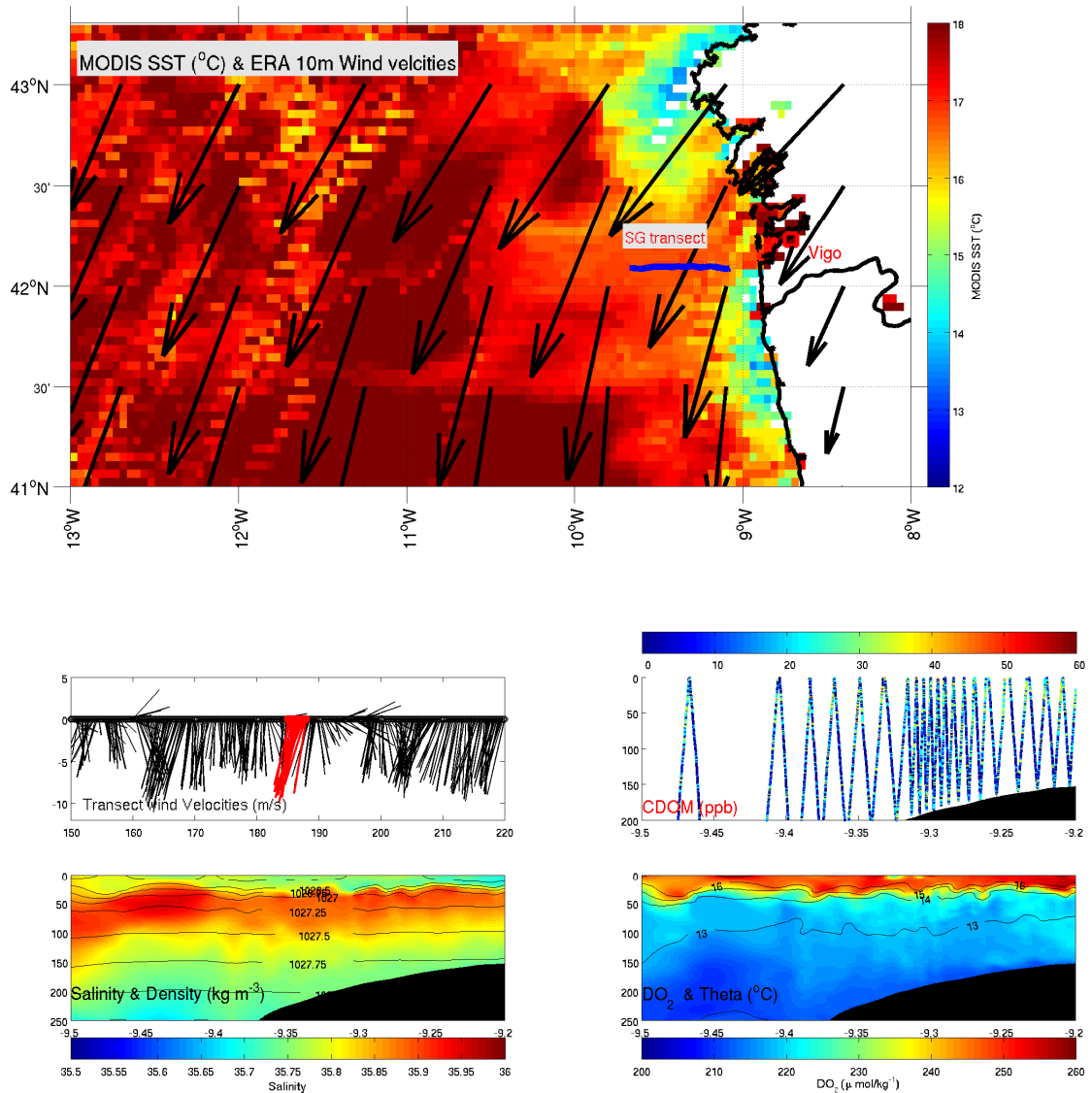
Transect 10

Seaglider transect: west to east. Conditions: Non upwelling & highly

Stratified. Wind stress: 5 to 7m/s N to W

The second restratification period continues through transect ten, with weak and highly variable surface winds, and further upper water column heating.

Biogeochemical and physical observations of the transect region

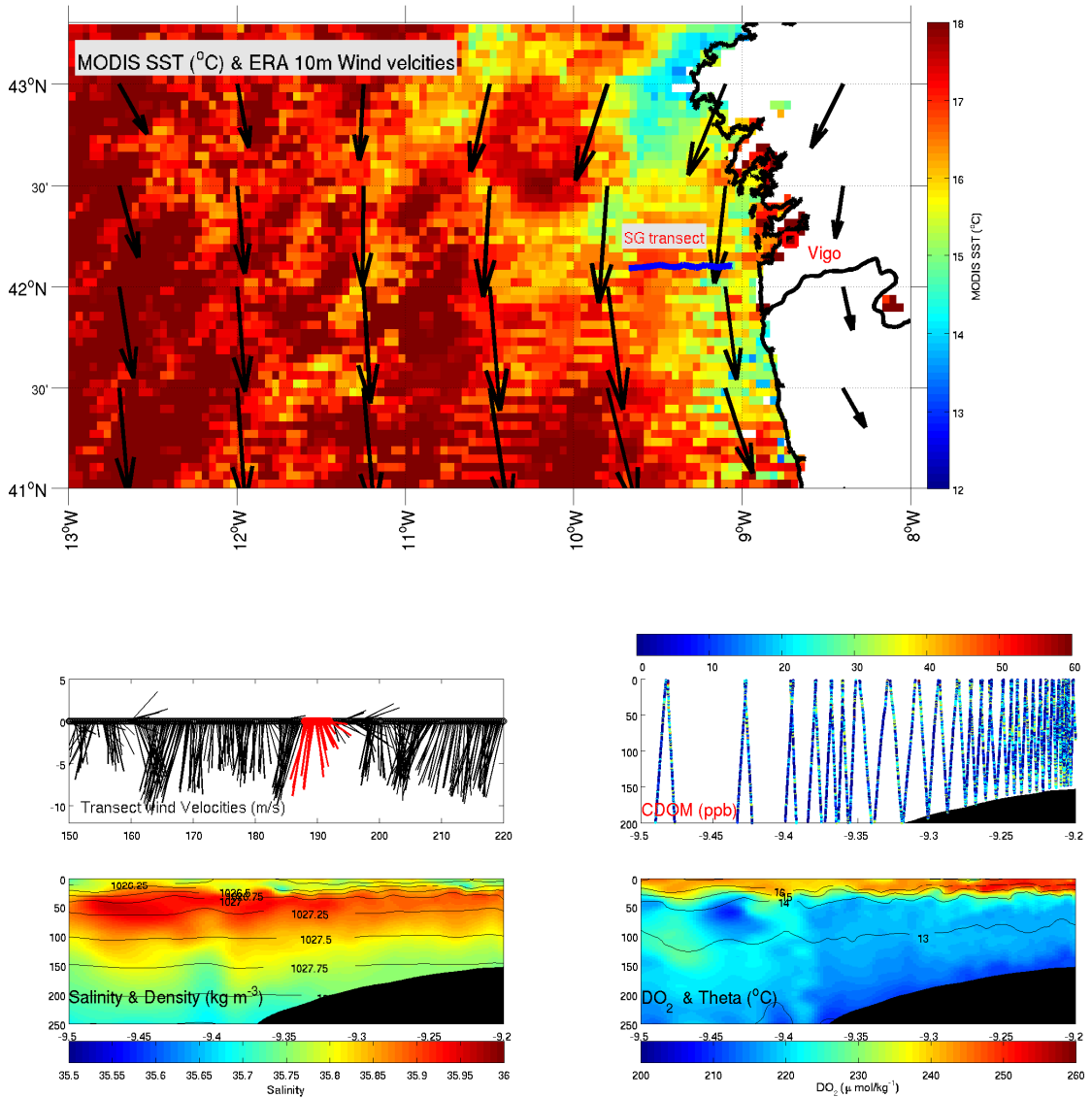


Transect 11

Seaglider transect: east to west. Conditions: Initiation of upwelling. Wind stress: 8 to 11m/s NNE

Transect eleven sees the initiation of a second upwelling event. Wind stress for the transect becomes NNE in direction, and also increases in velocity, providing suitable conditions for Ekman suction. Near shore MODIS SST data shows a reduction in temperature, and top 20m Seaglider data for this transect also indicates that upper water column temperatures have decreased by 1 °C compared to the previous transect.

Biogeochemical and physical observations of the transect region



Transect 12

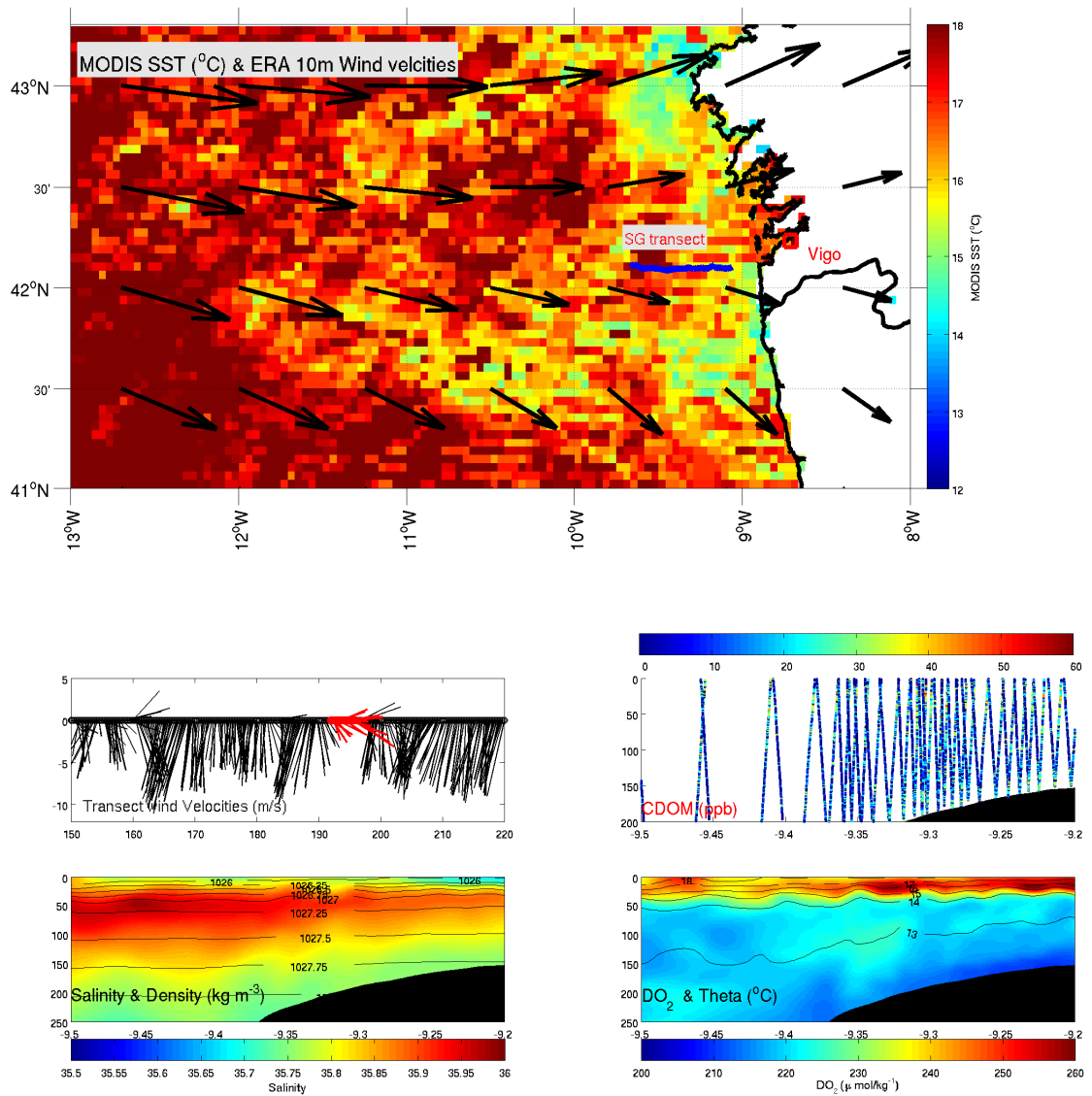
Seaglider transect: west to east. Conditions: Ending of second upwelling

Period. Wind stress: 4to 11m/s NNE to NW

Transect twelve sees the initiation of the third period of stratification. After day 187 wind-stresses fluctuate greatly during this transect, both in velocity and direction.

This can be seen in the Seaglider temperature plot, with the western section (sampled first during the course of this transect) of the Seaglider transect showing strong upwelling of ENACWP at -9.4 °W, and then restratification of water towards the east of the transect.

Biogeochemical and physical observations of the transect region

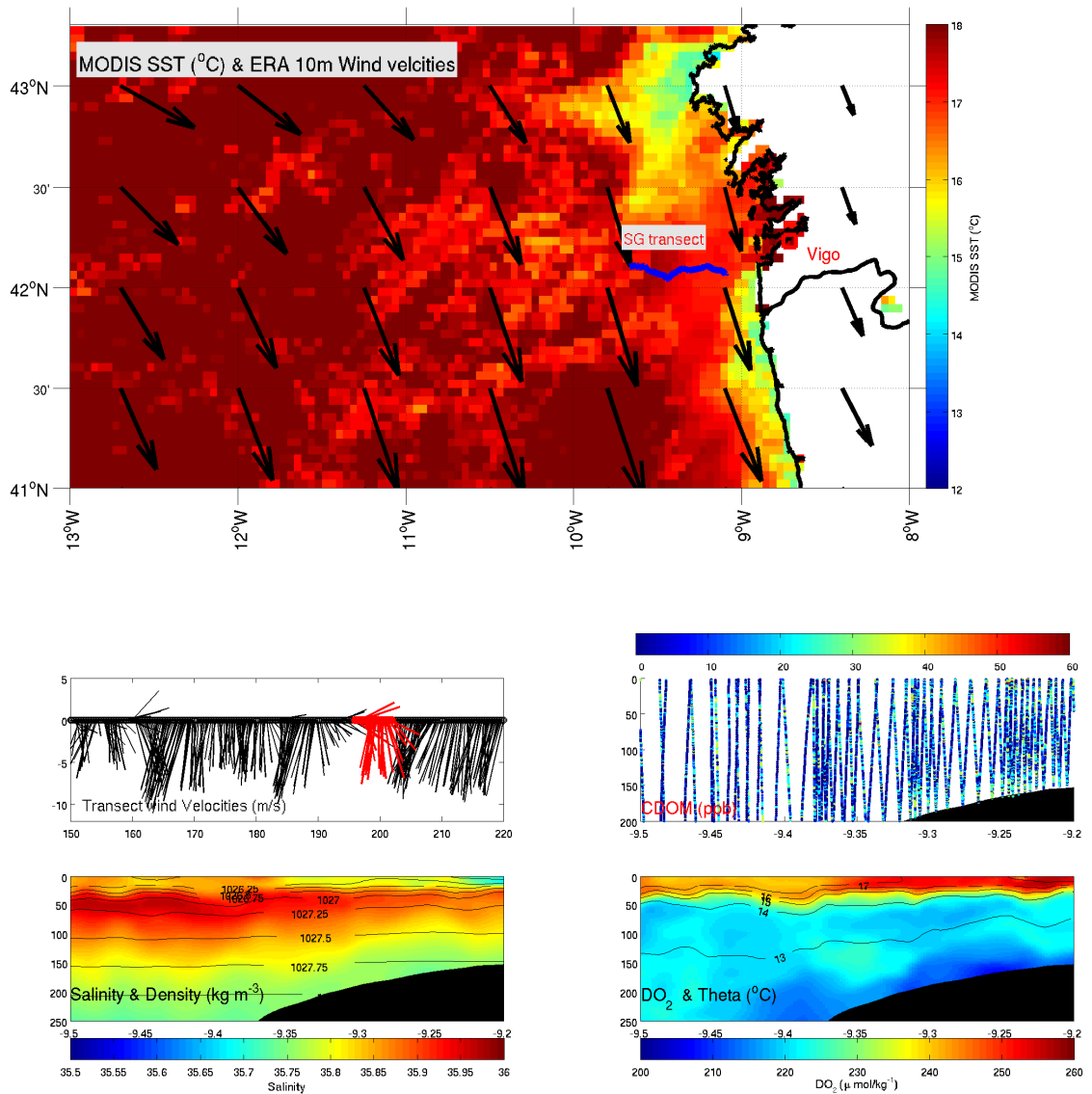


Transect 13

Seaglider transect: east to west. Conditions: Restratification. Wind stress: 4to 6m/s NW to SSW

Restratification continues strongly during transect thirteen. Wind stresses become light, and generally from a westerly direction. Increased cloud cover results in poor MODIS SST coverage, but a general trend of increasing near-shore sea surface temperatures are seen.

Biogeochemical and physical observations of the transect region

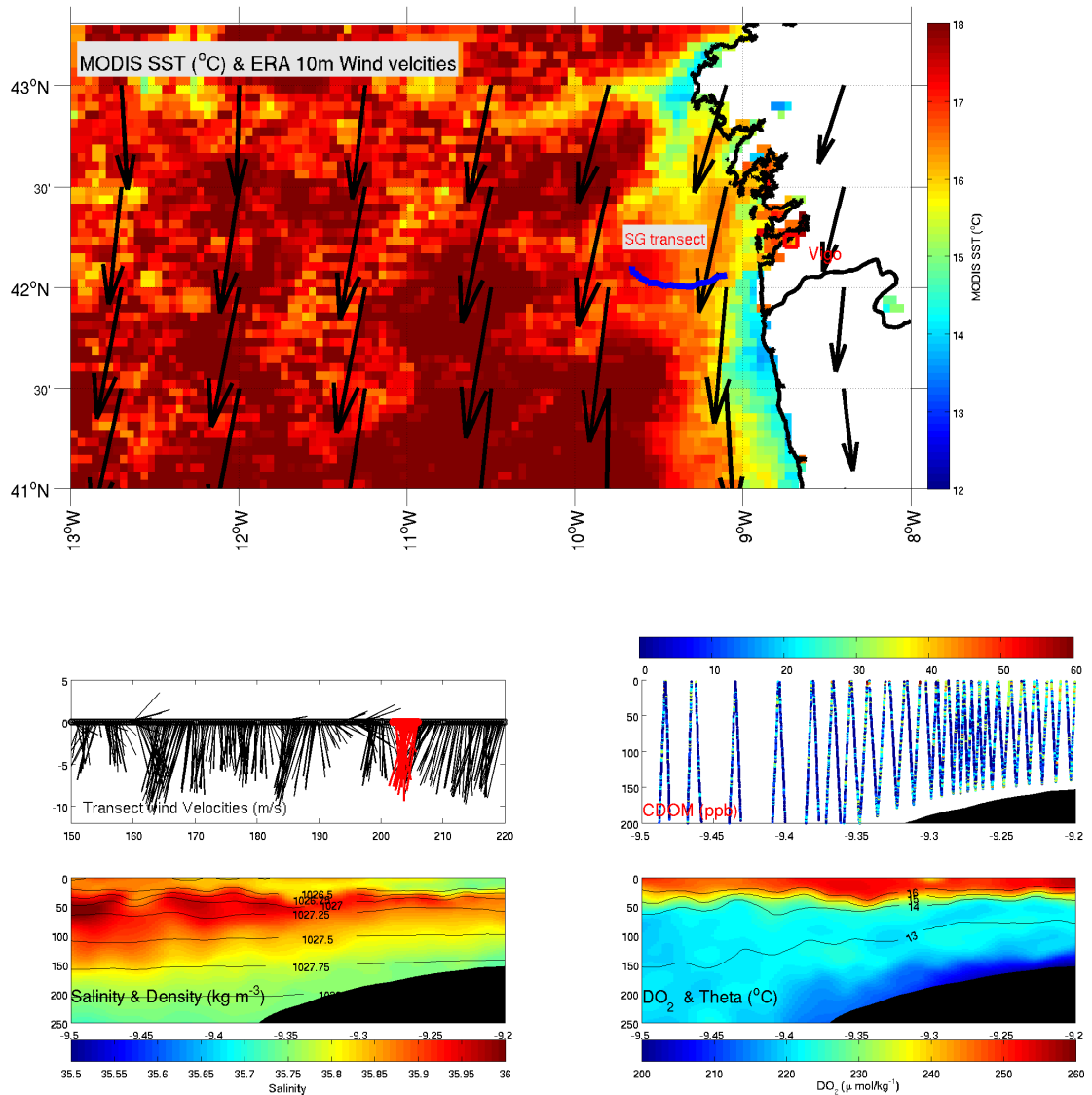


Transect 14

Seaglider transect: west to east. Conditions: Restratification with a region of localised on shelf upwelling. Wind stress: 4to 11m/s N to SW

Highly variable wind conditions continue. through the first two days of transect 14, but then switch to a more consistent Northerly direction. This change to upwelling favourable wind - stresses can be seen in the Seaglider temperature data between -9.3 and -9.2 °W, where the stable stratification seen during transect thirteen begins to break down.

Biogeochemical and physical observations of the transect region



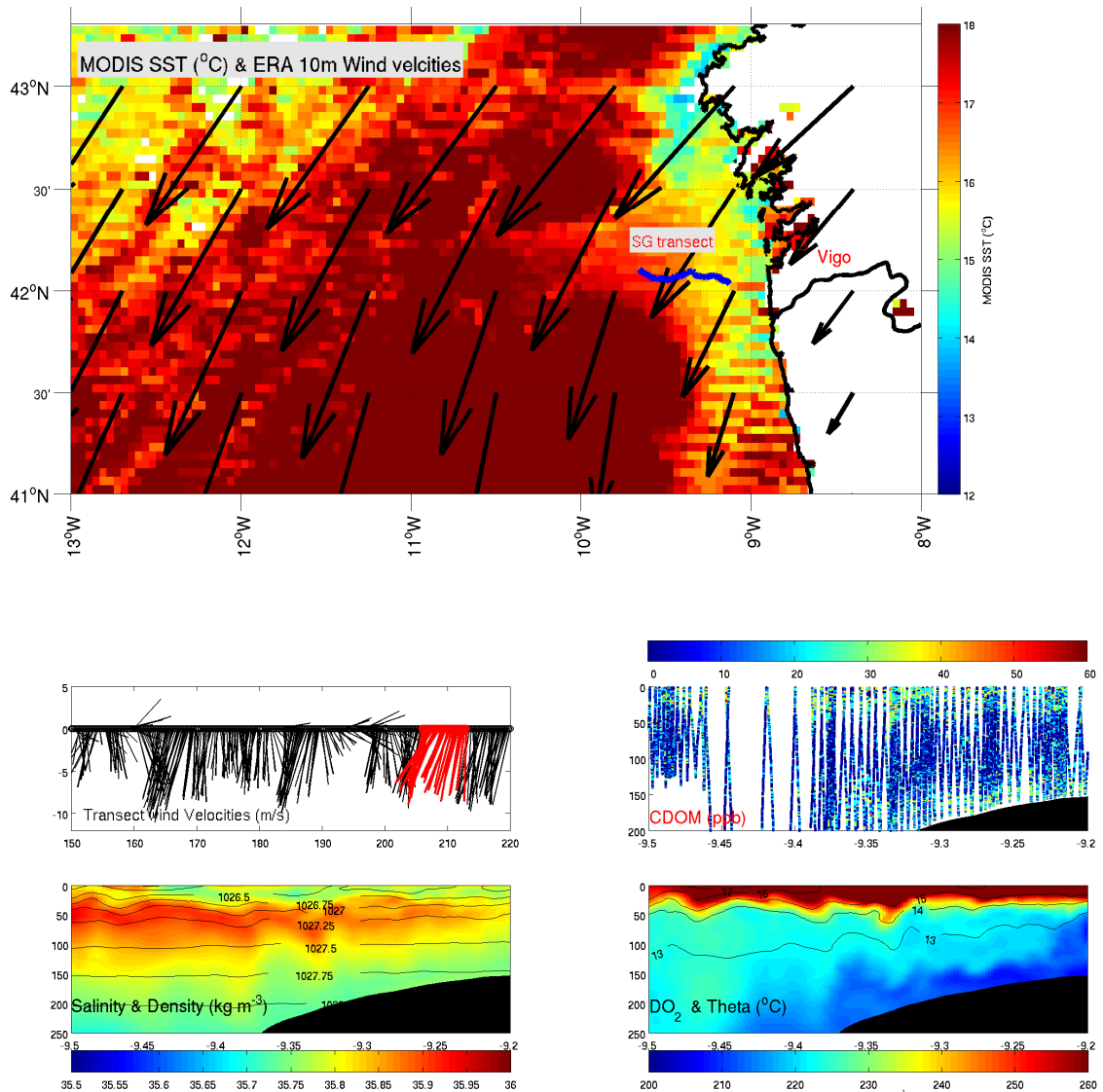
Transect 15

Seaglider transect: east to west

Conditions: Upwelling

Wind stress: 8 to 11 m/s NNE to NNW. Wind conditions favourable for upwelling continue across the entire transect during transect fifteen. Northerly wind velocities are lower than those estimated during the first upwelling period, but are sustained from the end of transect 14 through until after transect 17. This allows for upwelling to continue unabated for these transects.

Biogeochemical and physical observations of the transect region



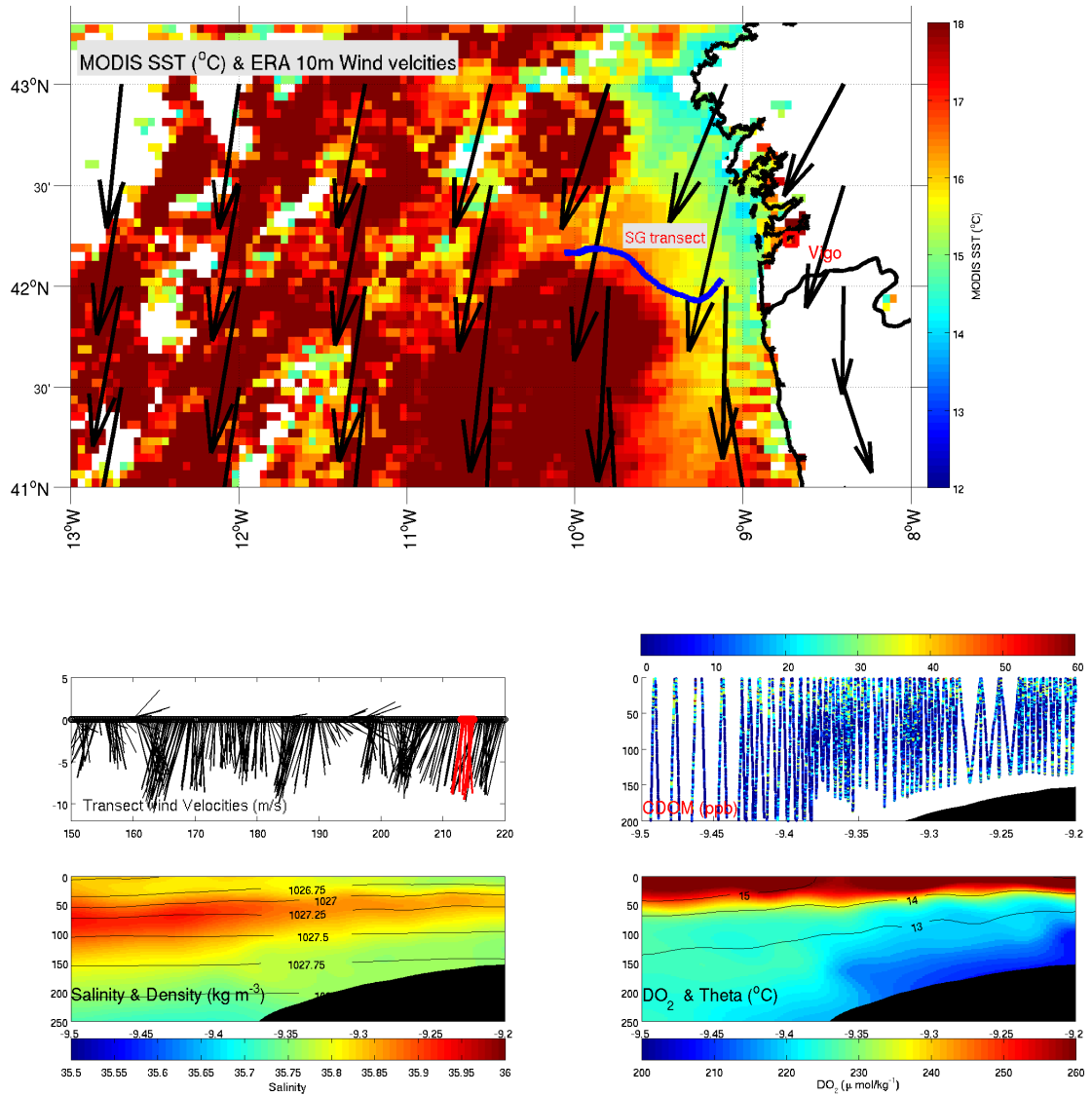
Transect 16

Seaglider transect: west to east. Conditions: Strong upwelling. Wind stress: 9 to 11m/s NNE

Strong NNE winds continue through transect sixteen, and promote strong upwelling, that can be seen in both Seaglider temperature data, and MODIS SST data. Seaglider observed top 20m watercolumn temperatures are upto 4 °C lower than transect fourteen, and ENACWP water is once again advected up onto the shelf.

This upwelling also promotes the largest SST differences between the on-shelf and offshelf regions seen during summer 2010, with a gradient of 3 °C observed across the Seaglider transect, and 7 °C observed in the MODIS SST. The formation of jets and eddies are also highly visible in the MODIS SST data.

Biogeochemical and physical observations of the transect region



Transect 17

Seaglider transect: east to west. Conditions: Strong upwelling. Wind stress: 9 to 11m/s NNE

The third consecutive transect featuring strong NNE winds and strong upwelling, upper 20m water-column temperatures for transect seventeen are the lowest measured during the mission. Offshore advection of the surface waters also becomes stronger, with the Seaglider only taking two days (as opposed to 3 to 5 days) to complete an east-west transect. Upwelling is strongest in the east of the transect, with the depth of the 14 °C isotherms at 60m in the West of the transect, and 5m in the east. MODIS observations indicate that a filament is forming in the North of the region.

1. Overview-

To the east of the shelf break front (i.e. the on-shelf region), both the magnitude of temperature anomalies and the vertical movement of isothermal surfaces are greater for all transects, and become especially strong during upwelling (fig 4.4, and T4- 7, and 15-17) Therefore, it appears that upwelling (or at least the presence of upwelled water) is strongest over the shelf, east of the shelf break front. The largest changes in salinity between transects are seen offshore (e.g. figure 4.4, T13 and 14). As salinity is a pseudo conservative tracer, and the offshore region during T13 and 14 does not show indications of upwelling, these differences in salinity must be caused by horizontal advection of saltier water from outside the transect region. Therefore, it appears that horizontal advection is greatest offshore within the Seaglider transect, an observation that is consistent with other studies of shelf break fronts (Gawarkiewicz & Chapman 1992; Falkowski et al. 1988).

The TS properties observed between 20-200 m either side of this front change during the mission. The offshore watermass during transects 1,2 and 3 is cooler and fresher than the onshelf watermass (figure 4.4 and 4.5). Therefore, the offshore water is dominated by almost pure ENACWP, contrasting the warmer and more saline (ENACWT influenced) water found onshelf at the start of the Seaglider mission (figure 4.2). Transects 13, 14 and 15 show a reversal of this situation, with a warmer, saltier watermass offshore, and a cooler, fresher (ENACWP influenced) watermass onshelf. It could be hypothesized that Ekman transport is the mechanism that promotes this exchange of watermasses (figure 4.3). Water featuring ENACWP signatures is advected eastwards over the shelf break (as shown by the low temperature, low salinity water ENACWP water in close proximity to the sea floor over the shelf during T 6, 7, 16 and 17, figure 4.4). As Ekman transport exports near surface water towards the west, there is a gradual replacement of shelf residing ENACWT (exported in the Ekman current) by upwelled deep water on the shelf.

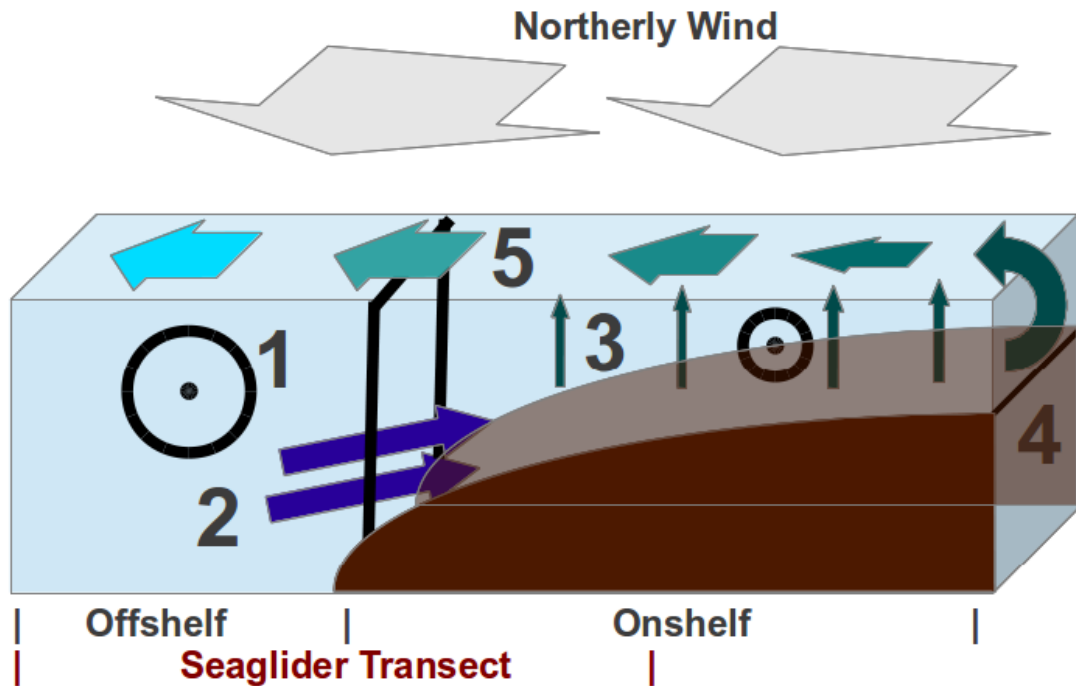


Figure 4.4 A schematic of upwelling in the seaglider transect region.

- 1 The EBC flows southwards, at a faster velocity offshelf than onshelf (Gawarkiewicz & Chapman 1992)
- 2 During upwelling periods, the surface Ekman current is directed offshore, and water is advected up and over the shelf break
- 3 Upwelling of deep water can be observed on-shelf by temperature anomalies, and isopycnal shoaling. Average watercolumn vertical velocities are highest at the on shelf front.
- 4 Upwelling exists further east of the Seaglider transect, forming the surface Ekman current that flows through the transect region
- 5 A shelf break front is formed, where offshelf water is dominated by the EBC, and onshelf water is dominated by upwelling.

Biogeochemical and physical observations of the transect region

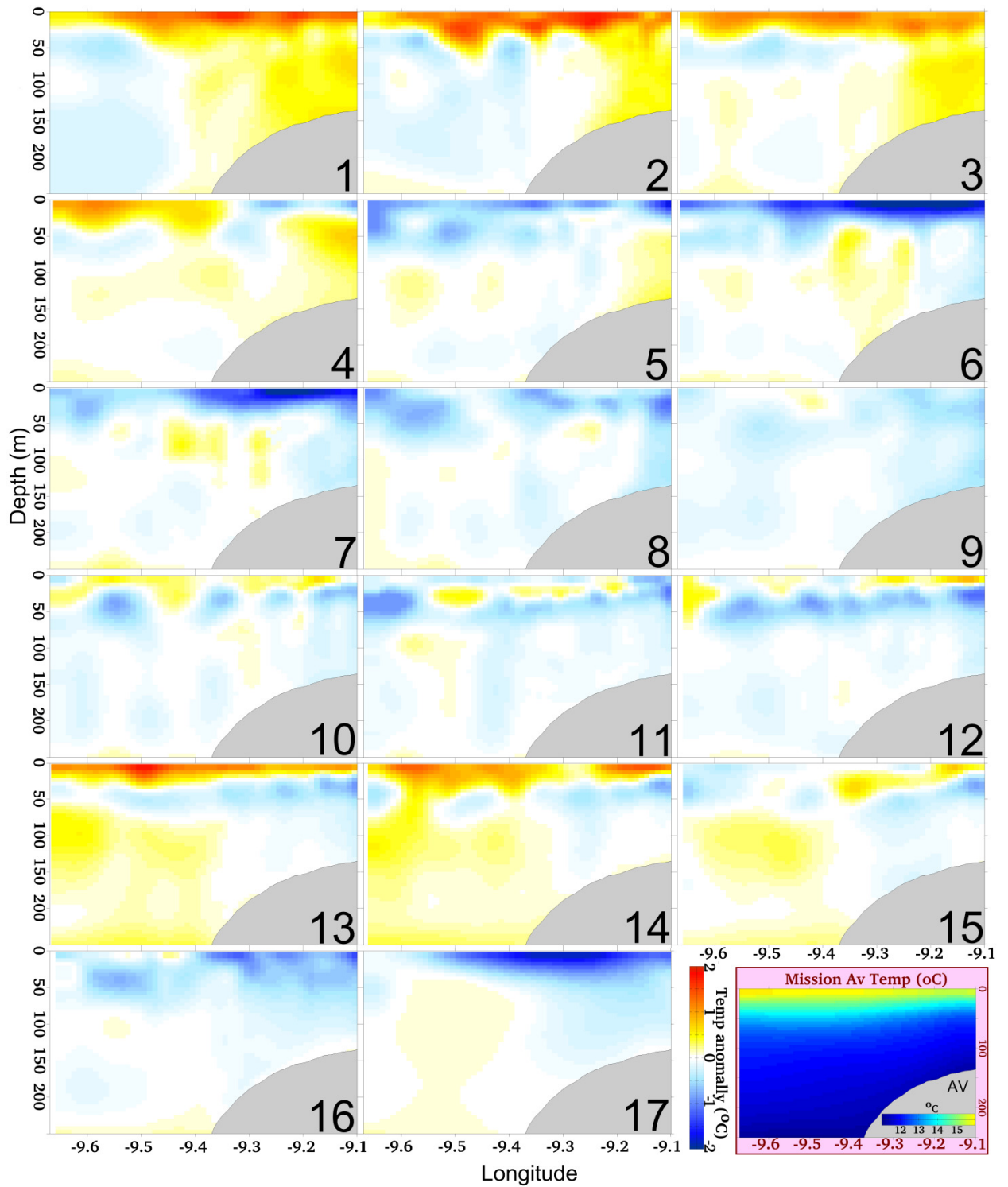


Figure 4.5 Temperature anomalies for the seventeen transects, with mission average theta plotted in panel 18 (note the different colour scale).

Biogeochemical and physical observations of the transect region

4.4 MODIS, ERA Interim and Seaglider observations of upwelling

The MODIS SST/ ERA interim wind data confirms some of the watercolumn features seen in the Seaglider data. Transects 1, 2, 3, 12, 13 and 14 all have light ($5-8 \text{ ms}^{-1}$), variable winds in a northerly to westerly direction (table 4.1). Transects featuring these weak winds also feature high, homogeneous MODIS SST values (figure 4.6 and table 4.1), and high 0-30 m watercolumn temperatures within the transect region (figure 4.4.) This confirms that the watercolumn was in a state of relaxation at these times. In contrast, transects 5, 6, 15, 16 and 17 featured strong northerly to north easterly winds, and a marked lowering of SST along the continental shelf region- a feature associated with upwelling (table 4.1). A filament structure that evolves into a mesoscale eddy is also observed during transects 16 and 17, between $43 - 42.3^\circ\text{N}$, $11 - 8.9^\circ\text{W}$, again suggesting that fully developed upwelling was occurring during these transects. A second, smaller cold water feature is seen during transect 6, at 42.8°N , $10- 9^\circ\text{W}$, that could also be a filament associated with upwelling. Therefore, observations of upwelling are seen in MODIS SST, and Seaglider near surface temperature anomalies between transects 4 and 7, and 15 to 17. Strong winds and filament development were also observed during these transects- features that are usually associated with fully developed upwelling (Relvas 2002) . Between these upwelling events, the watercolumn was in a state of relaxation. The lack of strong southerly winds, required to initiate onshore Ekman transport and hence downwelling, suggests that there were no periods over summer 2010 that featured a downwelling watercolumn. Coupled to this, there is no evidence in the Seaglider observations of a subducting watercolumn, such as the vertical elongation of isopycnal surfaces (main figures.)

Table 4.1: Observations of the transect region from MODIS, Seaglider and ERA Interim data. ‘Upwelling conditions’ were determined from the Seaglider dataset. Note the highest windspeeds, lowest temperatures and highest chl a correspond to an upwelling transect as determined from the Seaglider data.

Transect	YD	Direction of transect	Wind speed (m s-1)	Upwelling Conditions	MODIS SST (Shelf)	MODIS SST (Offslf)	MODIS Chla (Shelf)	MODIS Chla (Offslf)
T1	151-155	E-W	5	Stratified	16.3	16.2	0.3	0.1
T2	155-159	W-E	5.8	Stratified	16.4	16.3	0.3	0.1
T3	159-162	E-W	6.3	Stratified	16.5	16.4	No	Data
T4	162-165	W-E	9.8	Upwelling	15.8	15.9	1.2	0.5
T5	165-167	E-W	12.5	Full Upwl	14.3	15.5	2.3	0.7
T6	167-171	W-E	11.8	Full Upwl	14.8	15.8	6.3	2.4
T7	171-173	E-W	8.6	Upwelling	15.2	15.9	4.2	2.7
T8	173-176	W-E	6.2	Stratified	15.6	16.3	1.2	1.5
T9	176-181	E-W	6.7	Stratified	16.1	16.4	0.6	0.3
T10	181-185	W-E	6.4	Stratified	15.9	16.8	0.7	0.7
T11	185-188	E-W	9.1	Upwelling	15	16.4	1.7	0.2
T12	188-191	W-E	10.2	Stratified	14.7	16.2	2.3	0.9
T13	191-196	E-W	5.4	Stratified	16.6	17.5	1.6	0.9
T14	196-202	W-E	6.5	Stratified	17	17.8	1.4	0.5
T15	202-206	E-W	10.1	Upwelling	16.2	17.5	2.5	1.7
T16	206-213	W-E	10.2	Full Upwl	15.2	16.3	6.1	3.2
T17	213-217	E-W	11.2	Full Upwl	15	15.9	6.1	3.3

4.5 Tracking watermasses using CDOM

Dissolved organic carbon (DOC) constitutes one of the major pools of organic carbon in the oceans (662 Gt C, figure 1.2), and is an important carbon store in the global biosphere, with DOC comparable in size to terrestrial fixed carbon (Kowalczyk et al. 2003). The chemical constituents of DOC are a highly variable mixture of organic carbon compounds, derived from biological or petrochemical sources, and featuring an environmental persistence from less than a second to hundreds of years (Kowalczyk et al., 2003). DOC can be broadly split into two groups depending on the molecule's ability to absorb electromagnetic radiation from the visible light spectrum. DOC that absorbs solar radiation strongly at 300 to 800 nm is of particular biogeochemical interest as it directly affects the turbidity of the watercolumn, photic zone depth and satellite imagery

Biogeochemical and physical observations of the transect region

products of the surface ocean (Kowalczyk et al. 2003). Due to the strong absorption of light in the visible spectrum, this material is often referred to as Gelbstoff ('yellow substance'), humic matter or coloured dissolved organic matter (CDOM) (Kowalczyk et al., 2003). Generated from the decomposition of large organic molecules, CDOM is often used as a tracer for both fluvial outflow, and phytoplankton bloom remineralisation. Although a potentially useful tracer, there have been no large scale studies of CDOM in the Iberian upwelling system.

The long residence time of certain CDOM fractions within the water-column is due to its chemical inertness within the ocean and the difficulty of biological catabolisation. The eventual removal of this highly recalcitrant CDOM from the water-column can occur either through photodegradation caused by the absorption of ultraviolet light by the molecule (leading to bleaching), or respiration by heterotrophic bacteria (Vodacek et al. 1997).

The Seaglider-measured CDOM concentrations, which, although highly patchy, showed interesting structure, with high CDOM concentrations in the upper water column, and lower CDOM concentration in deep waters. An example of this can be seen in figure 4.6. Note the low CDOM in ENACWP water, and increasing CDOM in ENACWT near surface water.

Biogeochemical and physical observations of the transect region

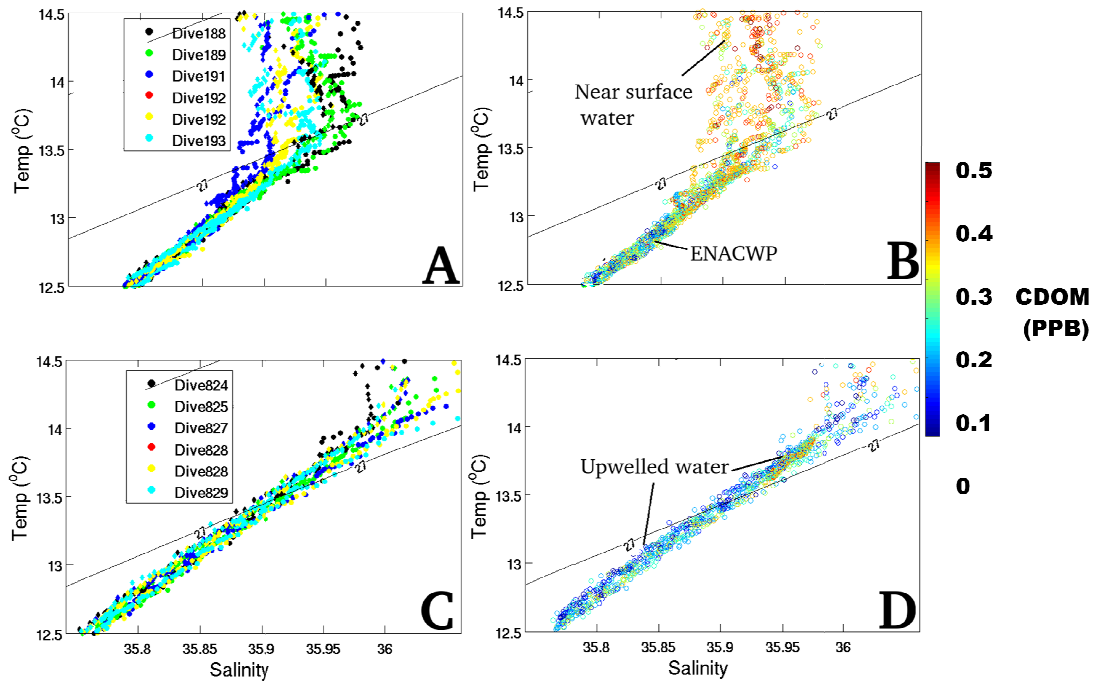


Figure 4.6 0-250 m TS diagrams for six consecutive dives coloured by dive number (A,C), with the same TS plot coloured by CDOM concentrations (B,D).

A: TS diagram from transect three, a transect featuring a relaxed watercolumn.

B: TS diagram from transect three, with points coloured by CDOM concentration.

C: TS diagram from transect sixteen, a transect featuring fully developed upwelling.

D: TS diagram from transect sixteen, with points coloured by CDOM concentration.

Biogeochemical and physical observations of the transect region

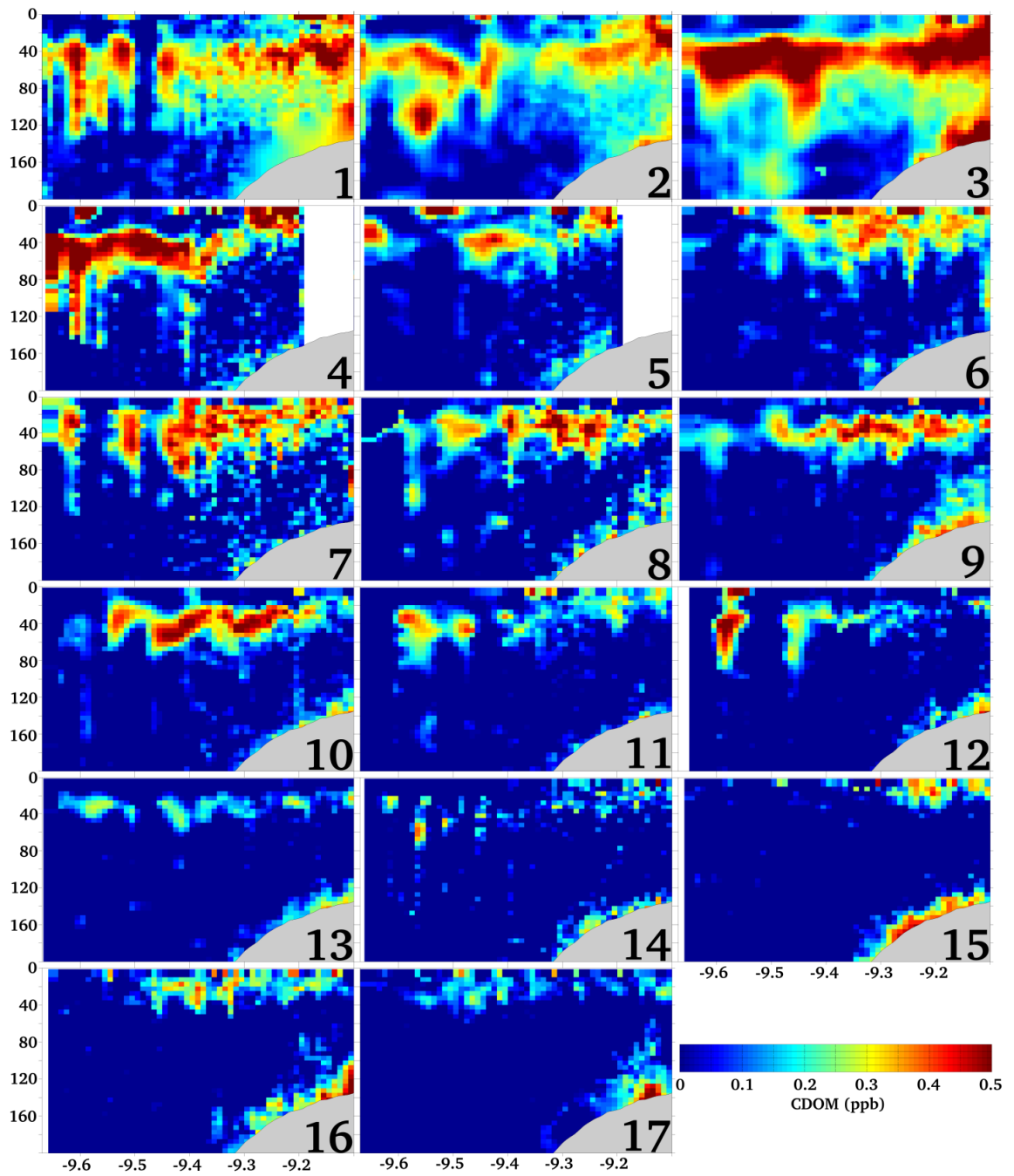


Figure 4.7 Gridded CDOM concentrations from each of the seventeen transects. Note- the Wetlabs ECO-Puck was turned off below 200 m, therefore these plots extend to 200 m, rather than 250 m in figure 4.3.

Biogeochemical and physical observations of the transect region

CDOM concentrations were highest between 0 and 100 m, and in the near shelf floor regions, and lowest in the off-shelf deep water (figure 4.7). Determining conclusively whether elevated CDOM levels result from fluvial inputs, sediment re-suspension or the decomposition products of phytoplankton is impossible without further research, however, the largest phytoplankton blooms (as seen in chl a and oxygen concentrations-figures 4.10 and 4.11) do not correspond with the highest CDOM concentrations, therefore, strong blooms do not necessarily result in high concurrent CDOM concentrations. The highest CDOM concentrations in transects four to seventeen are observed at two depth ranges; between 0 m and 60 m (i.e. within the photic zone), and in locations in close proximity to the continental shelf. Elevated CDOM concentrations in the photic zone of productive shelf regions have been frequently observed before, with both high fluvial and plankton derived CDOM (Steinberg et al., 2004). Increased CDOM concentrations observed close to the sea-floor have been attributed to bottom sediment resuspension events, caused by tides, currents or wave action (Boss et al., 2004.)

The first three transects featured the highest concentrations of CDOM observed during the mission, with high CDOM concentrations at all depths. These transects, as previously discussed, featured a relaxed water-column (Transects 1,2 and 3, table 4.). Through transects four to seventeen, high CDOM concentrations were only observed in regions where CDOM is produced (the near shelf and photic zone, figure 4.8, D), with low CDOM concentrations between these regions. The regions that featured cooler temperature anomalies (i.e. upwelled deep water) in figure 4.3, also feature lower CDOM concentrations in figure 5.7 (transects 16 and 17). Assuming that the majority of the CDOM found in the transect region have a longer residence time than the period for individual upwelling cycles, a possible hypothesis is that high CDOM values indicate shelf derived water (figure 4.8 A & B). Here, riverine outflow water, phytoplankton derived sources and re-suspended shelf floor sediment sources of CDOM are able to accumulate, and result in a high watercolumn CDOM concentration (figure 4.8 A). Low CDOM values indicate 'clean' upwelled ENACWP, which has an inherently low CDOM concentration due to its isolation from major CDOM sources (figure 4.8 C & D). Differentiating between shelf and upwelled ENACWP from offshelf sources is highly useful within this transect, as previous studies on the region have found that the

Biogeochemical and physical observations of the transect region

upwelling of nutrient rich deepwater promotes the largest phytoplankton blooms, as opposed to the recirculation of on-shelf waters. (eg Alvarez-Salgado et al., 2008). Therefore transects with low CDOM concentrations outside of the two CDOM source regions (photic zone and near shelf) contain more offshore ENACWP, and hence are more likely to result in a strong bloom during upwelling.

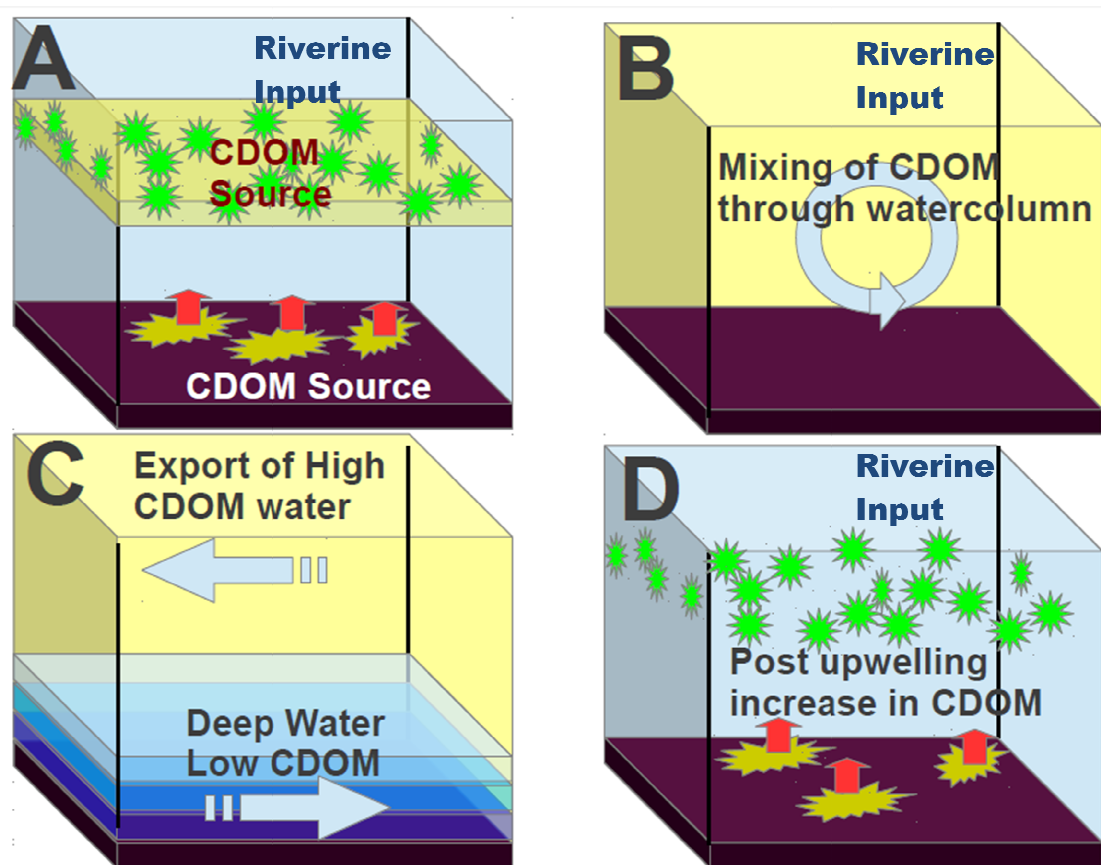


Figure 4.8 A schematic of on-shelf CDOM

A: CDOM originates from three main sources, phytoplankton decomposition, re-suspension of particulate and riverine sources.

B: If the watercolumn is in relaxation, CDOM is mixed through the watercolumn.

C: When the period of relaxation ends, upwelling results in the export of near surface water (high CDOM concentration), and the import of deep (low CDOM concentration) water.

D: The upwelled water promotes a phytoplankton bloom, and the watercolumn is reset to 'A'.

Summary for part one:

1. Two dominant regimes occurred in the transect region over summer 2010, an upwelling regime, and a stratified regime, with the strength of the northerly wind clearly acting as the first order control on which regime was prevalent at a particular moment in time. Southerly winds were not dominant for any of the transects. Hence, the downwelling regime (commonly associated with wintertime, rarely with summer) was not observed (table 4.1).
2. A combination of ENACW and Ria outflow water dominate the upper water-column above depths of 150 m (transects 1-17.) At depths of 250 to 150 m we found that NACWT was dominant over the shelf during the first three transects, and then subsequently replaced with colder, less salty water.
3. MODIS based observations of filament formation (transect 5,6,16 and 17) , suggest that there were two fully developed upwelling events. General effects of upwelling (T,S and SST) were visible both in MODIS SST, and Seaglider watercolumn observations of temperatures and salinities for both of these events.
4. A shelf break front was observed in Seaglider data between -9.4 and -9.2 °W. East of this, strong upwelling was observed, west of this, advection of non-local watermasses was observed.

Part two: Phytoplankton blooms and export

With watercolumn upwelling, relaxation and the presence of a shelf break front identified, biogeochemistry can be put in context with physical observations. Initially, as PP requires light mediated photosynthesis, the depth that light penetrates to within the watercolumn has to be approximated (Serret et al. 2009). Identifying the depth of the photic and aphotic zone is usually achieved using a photosynthetically active radiation (PAR) sensor. Although the Seaglider was not fitted with a PAR sensor, one was fitted to the RV Mytilus's CTD. Average PAR for each of the three collocated transects was between 70 and 82 m within the transect region (figure 4.9). Seaglider biogeochemical

Biogeochemical and physical observations of the transect region

data confirmed this. By binning all oxygen, potential temperature and chl a data recorded by the Seaglider into 5 m bins, little change was observed between average chl a/ oxygen concentrations at 85 m and 90- 110 m, suggesting limited phytoplankton activity below 85 m, and confirming the PAR measurements. Therefore, using these observations as the base of the photic zone four different environments can be defined:

1. The photic zone (0-85 m), on shelf and east of the shelf break front
2. The photic zone (0-85 m), off shelf and west of the shelf break front
3. The aphotic zone (> 85m), on shelf and east of the shelf break front
4. The aphotic zone (> 85 m), off shelf and west of the shelf break front.

By binning Seaglider observations from each transect into one of these four bins, table 4.2 has been produced.

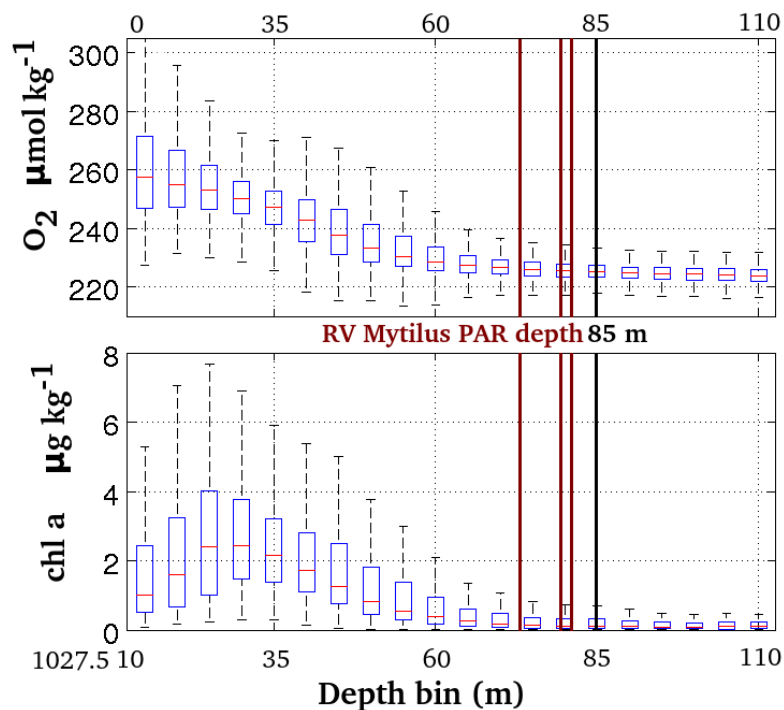


Figure 4.9 5 m binned oxygen and chl a data from the Seaglider, with the depth of RV Mytilus measured PAR plotted as red lines.

Biogeochemical and physical observations of the transect region

Table 4.2 0-85 m and 85- 200 m average values for all variables measured by the Seaglider both onshelf (east of 9.35 °W), and offshelf (west of 9.35 °W)

Oxygen ($\mu\text{mol kg}^{-1}$)		Chlorophyll a (mg m^{-3})							
Transect	YearDay	OffS	OnS	OffS	OnS	OffS	OnS	OffS	OnS
		0-85	0-85	85-200	85-200	0-85	85	85-200	85-200
T1	151-155	228.8	236.2	213	204.5	0.69	0.87	0	0
T2	155-159	227.5	233.6	211.3	205.5	0.68	0.93	0	0
T3	159-162	225.8	231.3	212.9	204.6	0.53	0.8	0	0
T4	162-165	227.9	237.5	215.3	220.9	0.54	0.75	0	0
T5	165-167	227.2	234.9	214.7	218	0.62	0.35	0	0
T6	167-171	229.4	241.4	214.9	216.7	0.89	2.21	0	0
T7	171-173	233.7	244.4	217.4	215.5	1.06	2.39	0	0
T8	173-176	232.3	247.1	215.9	210.6	0.72	1.29	0	0.08
T9	176-181	232.5	246.2	217.7	208.4	0.58	0.93	0	0
T10	181-185	230.8	235.1	216	212.7	0.55	0.72	0	0
T11	185-188	231.8	235.8	215.7	215	0.82	0.91	0	0
T12	188-191	229.1	236.9	215.9	210.4	0.71	1.01	0	0
T13	191-196	234.3	239.8	219.2	210.9	0.75	1.07	0	0.13
T14	196-202	234.7	239.8	221.2	217.7	0.85	1.08	0.01	0.15
T15	202-206	236.5	239.7	223	213.5	1.18	1.19	0	0
T16	206-213	240.3	242.7	223.6	213.2	1.17	1.35	0	0
T17	213-217	248.2	245	223.8	207.1	1.57	1.92	0	0.01
Potential temperature ($^{\circ}\text{C}$)		Salinity							
T1	151-155	15.08	15	12.98	12.93	35.85	35.82	35.87	35.85
T2	155-159	15.18	15.01	12.75	12.73	36.09	35.88	35.81	35.77
T3	159-162	14.94	14.79	12.97	13.16	35.67	35.77	35.82	35.81
T4	162-165	14.94	14.66	12.9	13.15	35.94	35.71	35.86	35.89
T5	165-167	14.31	14.27	12.8	12.97	35.64	36.03	35.77	35.78
T6	167-171	14.19	13.73	12.83	12.99	35.8	35.77	35.85	35.86
T7	171-173	14.37	13.75	12.81	13	35.63	35.78	35.89	36.05
T8	173-176	14.31	13.98	12.77	12.93	35.36	35.86	35.85	35.56
T9	176-181	14.62	14.05	12.79	12.99	35.29	35.71	35.87	35.39
T10	181-185	14.59	14.2	12.88	13.07	35.7	35.76	35.81	35.81
T11	185-188	14.52	14.09	12.83	13	35.58	35.69	35.79	35.79
T12	188-191	14.48	14.07	12.79	12.97	35.67	35.67	35.81	35.81
T13	191-196	14.95	14.31	13.03	12.97	36.15	35.76	35.92	35.94
T14	196-202	15.03	14.45	13.06	13.29	35.65	35.76	35.82	35.82
T15	202-206	14.57	14.29	12.93	13.13	35.83	35.8	35.85	35.86
T16	206-213	14.45	13.82	12.81	12.98	36.03	35.7	35.88	35.91
T17	213-217	14.41	13.74	12.87	13.05	35.65	35.62	35.81	35.82
Backscatter ($\mu\beta$ (θc)m^{-1} sr^{-1})		CDOM (ppb)							
T1	151-155	1.886	2.185	1.324	1.181	1	1.36	0.43	0.76
T2	155-159	1.98	2.471	1.483	2.921	0.99	1.17	0.43	0.69
T3	159-162	1.971	2.362	1.212	2.92	0.94	1.12	0.48	0.82
T4	162-165	2.042	2.619	1.119	2.832	0.92	0.85	0.48	0.48
T5	165-167	2.066	2.233	0.99	2.912	0.57	0.44	0.3	0.39
T6	167-171	2.445	3.188	1.097	3.562	0.58	0.63	0.33	0.39
T7	171-173	2.598	3.301	1.104	3.656	0.6	0.63	0.24	0.38
T8	173-176	2.356	3.439	1.016	4.525	0.62	0.65	0.27	0.51
T9	176-181	1.933	2.938	1.266	4.312	0.65	0.76	0.29	0.51
T10	181-185	1.71	2.735	1.363	3.6	0.59	0.62	0.29	0.64
T11	185-188	2.324	2.137	1.35	2.93	0.55	0.5	0.32	0.51
T12	188-191	2.331	2.388	0.963	3.506	0.54	0.54	0.28	0.57
T13	191-196	2.499	2.591	0.969	3.225	0.5	0.56	0.3	0.6
T14	196-202	2.574	2.708	1.006	2.425	0.54	0.51	0.21	0.53
T15	202-206	2.881	2.752	1.137	2.021	0.43	0.49	0.23	0.6
T16	206-213	2.635	3.23	1.14	4.598	0.5	0.55	0.22	0.69
T17	213-217	2.771	3.04	0.991	5.698	0.5	0.5	0.29	0.74

4.6 Phytoplankton Blooms

Photosynthetic proxies are frequently used to quantify bloom dynamics (Boyd et al. 2000). One method uses measurements of the fluorescence of the ubiquitous photosynthetic pigment chl a (Falkowski and Kiefer 1985). The strength of fluorescence signal is not a simple linear function of plankton cell density or even photosynthetic activity, but varies greatly depending on a vast array of different variables, from species type to environmental conditions (Falkowski and Kiefer 1985). However, measurements of chl a can provide useful insight into the location and strength of phytoplankton blooms. From table 4.2, the largest concentrations of photic zone chl a were observed during T6,7,16 and 17- during the main upwelling events. Areas to the east of the shelf break front featured the highest average concentrations of chl a, with maximums at T7 (2.39 mg m⁻³) and T17 (1.92 mg m⁻³). Maximum offshore chl a concentrations were lower, at 1.06 and 1.57 mg m⁻³ during T7 and T17. During periods of watercolumn relaxation average chl a concentrations were approximately half the size of upwelling values, at 0.35-1.08 mg m⁻³ onshelf, and 0.54- 0.85 mg m⁻³ offshore. The smaller upwelling event during T11 did not increase chl a concentrations markedly above typical concentrations during relaxation (table 4.2).

The distribution of chl a can be visualized by gridding output using the same method as figures 4.3 and 4.4 (figure 4.9). Very low/ negligible concentrations of Chl a were observed below 80 m for the entire mission, suggesting that our photic zone definition is satisfactory, and chl a measured by the instrument represented living phytoplankton (or at least recently living), rather than resuspended detrital material from the shelf floor (figure 4.9). Chlorophyll maxima remained between 0-40 m for the entire mission, with deep chlorophyll maxima (DCM) only seen during relaxation events (T1-3, 12-14) at depths of 20-30 m.

Gridded oxygen concentrations

Dissolved oxygen can be used to determine photosynthetic activity (Alkire et al. 2011). As oxygenic photosynthesis hydrolyses water (releasing oxygen), an increase in environmental oxygen concentration (in a closed, non respiring system) can be used to infer photosynthetic activity. The North Atlantic is not a closed system, and estimates of the various physical and biogeochemical oxygen fluxes afflicting this open system are discussed further in chapter five. However, discounting these fluxes, and using increased oxygen concentrations as a proxy for photosynthetic activity, structure can be seen (4.11).

The highest average oxygen concentrations within the upper 85 m of the watercolumn were observed at T8 on shelf ($247.1 \mu\text{mol kg}^{-1}$), and T17 offshelf ($248.2 \mu\text{mol kg}^{-1}$). As upwelling started during T4 and T15, a lag is apparent between the initiation of upwelling, and peak watercolumn chl a (2-3 transects later- equating to 5-9 days) and peak oxygen concentration (3-4 transects later- equating to 9-12 days). Peak oxygen concentrations were located at 0- 40 m depth throughout the mission, and shared a similar structure to peak chl a concentrations, (albeit lagged by one transect, figure 4.10 and 4.11). This structure varies considerably between stratified and upwelling transects. Stratified transects feature a well defined DCM, and lower surface chl a and oxygen concentrations. During upwelling events both oxygen and chl a concentrations were vertically homogenous through the upper photic zone between 0 and 25-40 m, with the highest concentrations east of the shelf break front (eg T6,7,8,17).

The interpretation of average oxygen concentrations require care, as upwelled water has a lower oxygen concentration than photic zone water. Assuming that upwelling events result in the transport of near surface water to the west via Ekman transport, and this water is replaced with upwelled deep water, a net loss of oxygen from the photic zone watercolumn will occur. The oxygen concentration of aphotic, offhshelf water varies between 211.3 to $223.8 \mu\text{mol kg}^{-1}$ between T1 and T17. Assuming upwelled water originates from this region, upwelled water is depleted in oxygen by approximately $20 \mu\text{mol kg}^{-1}$ compared to photic zone shelf water (table 4.2). Therefore oxygen released by the initial stages of a phytoplankton bloom will be offset by a net loss of watercolumn oxygen via the upwelling of deep water. When upwelling stops, but the bloom is fully

Biogeochemical and physical observations of the transect region

developed, all oxygen produced by the bloom will remain in-situ, resulting in a greater increase in the watercolumn oxygen inventory- as seen during T8 onshelf- this is discussed further in chapter five. Aphotic onshelf oxygen concentrations increase during the initiation of upwelling (eg T4-5 T11), and decrease during late bloom and post bloom transects (T7-10, T12, T17). As aphotic offshelf water has 5-10 $\mu\text{mol kg}^{-1}$ higher oxygen concentrations, the transport of deep water onshelf would have the effect of increasing the average on-shelf oxygen concentration. A deoxygenated nepheloid layer is a feature of the continental shelf in this region (van Weering et al. 2002). From qualitative observations, upwelling appears to be diluting this layer, and post bloom export strengthening it, perhaps by supplying carbon to the shelf floor (figure 4.11). These post bloom export events can be seen more clearly using the Seagliders backscatter channel, as described in the next section.

Biogeochemical and physical observations of the transect region

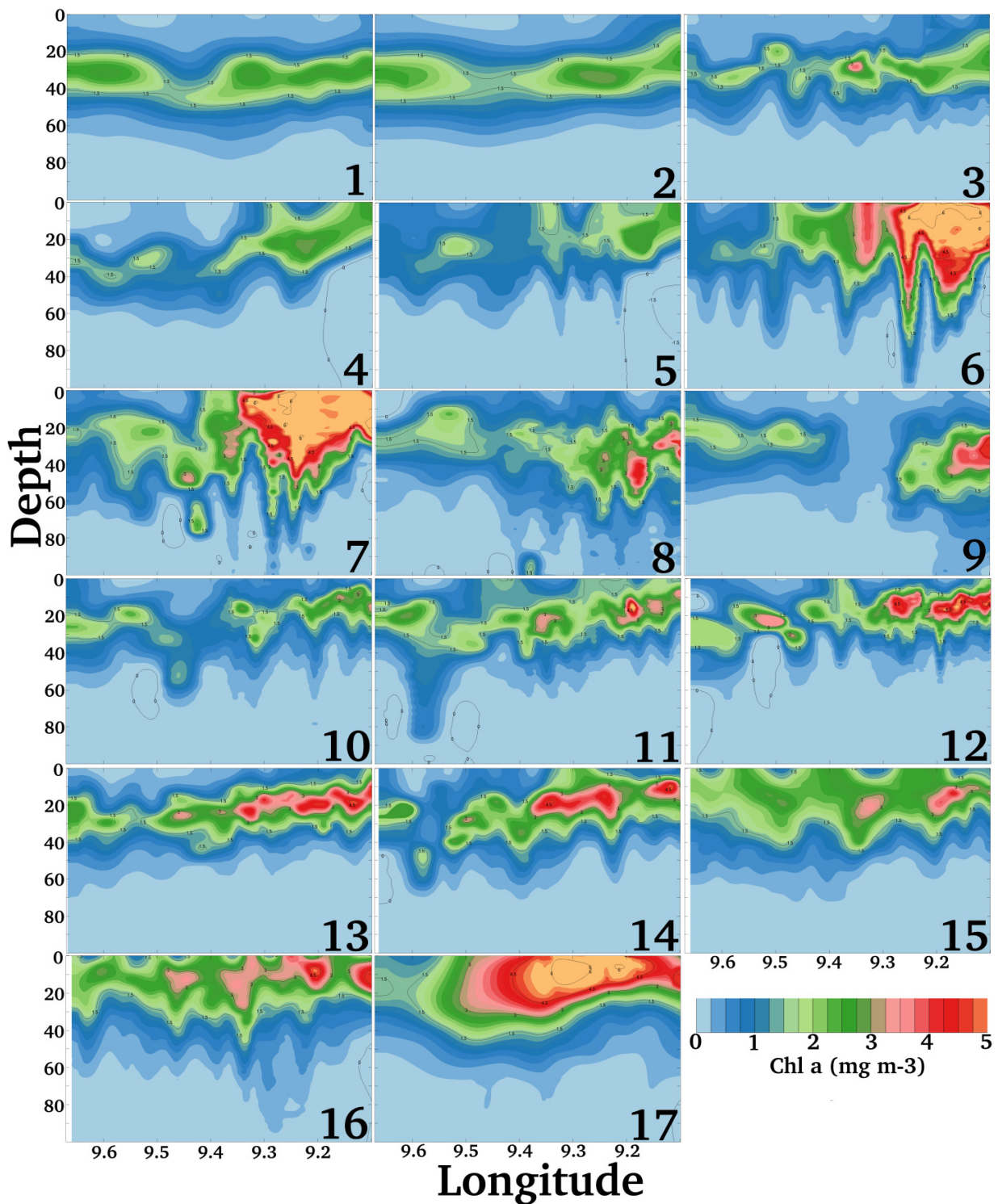


Figure 4.10 Gridded Oxygen concentrations for each of the seventeen Seaglider transects

Biogeochemical and physical observations of the transect region

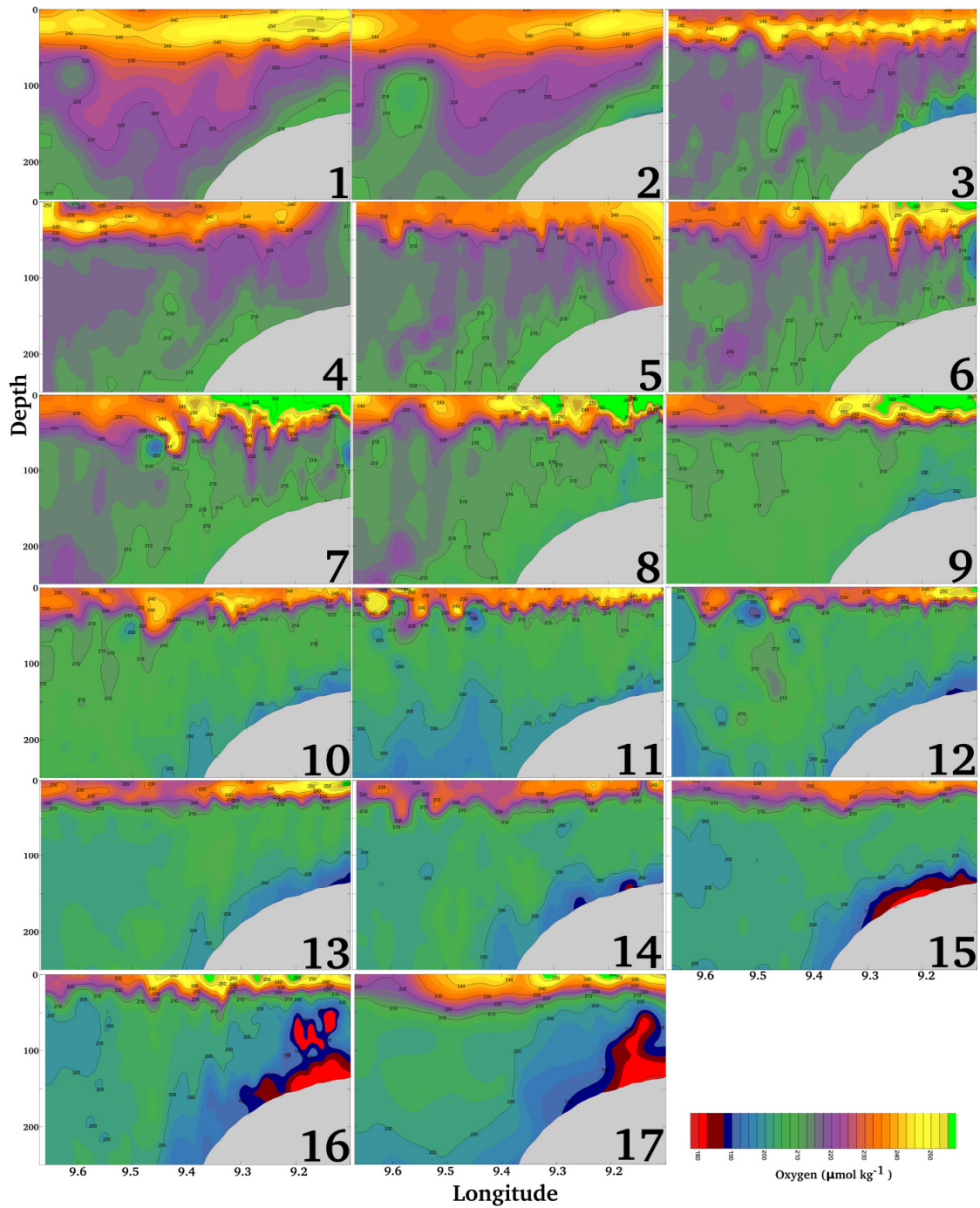


Figure 4.11 Gridded oxygen concentrations for each of the seventeen Seaglider transects.

4.6 Particulate

Oceanic carbon export via sinking aggregated particulate (marine snow) plays an important role in marine biogeochemical cycles by transporting organic carbon from the photic zone to the deep ocean (Nowald et al. 2006). With EBCs responsible for 37-50% of total oceanographic primary productivity, identifying the final destination of this material is vital for carbon export estimation (Joint et al. 2001).

Observations of primary production detritus export in other EBC regions have found high offshore export with ~81% of annual PP being advected offshore in the coastal upwelling region of Monterey Bay, and >50% in the Mauritanian upwelling region (Castro et al. 2000). Previous studies between 42-43 °N have also suggested that a major component of primary productivity is exported off shelf, during upwelling events through offshore currents and filaments (Barton et al. 2001, Alvarez-Salgado et al. 2008). The variable summer season phytoplankton blooms occurring across the transect region are dominated by medium to large-sized plankton taxa (Morán et al. 2004). The decay of these blooms is often followed by the formation of large pulses of POC, including fresh phytoplankton aggregates, that rapidly sink to the seafloor of the Iberian shelf, at rates of upto 400 m/day (Eppley et al. 1967). The production of marine snow in the upper water column is highly dependent on the concentration, relative movement, and stickiness of particles (Briggs et al. 2010). The transport of aggregates and carbon to the shelf and deep ocean depends in turn on their sinking speed and the rate of mid watercolumn respiration whilst sinking (Turner. 2002). Seagliders have successfully been used to study this cycle, and provide an estimate of the aggregation carbon flux in the ocean, using the backscatter channel on the Wetlabs ECO-Puck to estimate POC concentrations, and marine snow densities (Cetinić et al. 2012; Briggs et al. 2011).

Initially focusing on backscatter measurements (figure 4.8), the backscatter values for each of the transects displayed expected maximum values between 0-50 m, closely resembling the vertical distribution of Chl a (figure 4.12). The bloom events during T6-7 and 16-17 are visible in high backscatter values in the same locations as peak Chl a (figure 4.13). Below the deep chlorophyll maximum, backscatter values decreased to a

Biogeochemical and physical observations of the transect region

watercolumn minimum at 75-100 m. Below this, backscatter values then increased towards the shelf floor suggesting that the same process of internal wave and current mediated re-suspension of particulate matter is being observed along the Seaglider transect, as observed by Álvarez-Salgado (2001) in the Ria de Vigo, and suggested in Seaglider observed high CDOM and low oxygen concentrations. This can be seen by comparing oxygen saturation and backscatter values (figure 4.12). High (95 % +) oxygen saturations combined with Chl a values (2 mg m^{-3} +) are labelled 'A' in figure 4.12. These bloom conditions also feature a moderately high backscatter value.

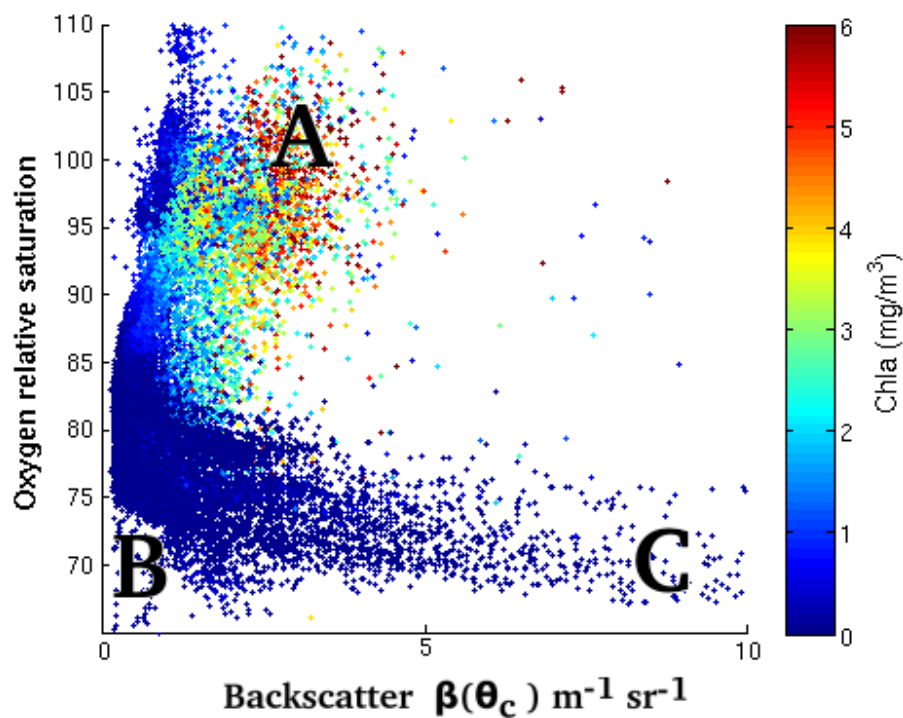


Figure 4.12 Oxygen relative saturation and backscatter scaled output plotted, and coloured by chlorophyll a concentrations.

Biogeochemical and physical observations of the transect region

High oxygen and Chl a concentrations indicate that a phytoplankton bloom is occurring. Moderate backscatter values suggest that there is a large amount of particulate associated with the blooms. Low relative oxygen saturations feature universally low Chl a concentrations (figure 4.12). However, backscatter values vary considerably at these lower oxygen saturations (points B and C.) The low backscatter low oxygen situation appears to happen off-shelf, whereas the high backscatter low oxygen situation appears to happen on-shelf (as seen in the oxygen and backscatter plots figure 4.11 and 4.14)

Oxygen concentrations in the near shelf floor environments are also much lower than observed in ENACWT/ ENACWP water masses, with concentrations of 190-210 $\mu\text{mol kg}^{-1}$ in near shelf waters, compared to 210-220 $\mu\text{mol kg}^{-1}$ in off shelf waters at similar depths (table 4.2). The sediment in the region has been identified as being carbon rich, with pelagic sediment sampled off the Rias Baixas containing a typical organic matter content of greater than 6% (López-Jamar et al. 1992). Local studies of nutrient distributions in the Iberian upwelling have also shown intense organic matter remineralization (eg Prego and Bao, 1997; Álvarez-Salgado et al., 1997). Therefore, oxygen depleted near-shelf waters as observed by the Seaglider are likely to be a result of the oxidation of a combination of fresh marine snow and the carbon rich resuspended sediment. This near shelf floor resuspension and remineralisation of POC (as seen by reduced oxygen concentrations and increased backscatter measurements) is likely to be the source of the high CDOM signal (chapter 4, part one). As the diatom rich particulate previously observed in the region has sinking rates more than two orders of magnitude higher than the strongest upwelling observed in the region (400 m/day vs 1-3 m/day peak upwelling velocity), the movement of particulate can be viewed as a POC export mechanism from the surface to the deep- the high sinking rates would prevent the entrainment of POC from the deep to the photic zone during upwelling.

Biogeochemical and physical observations of the transect region

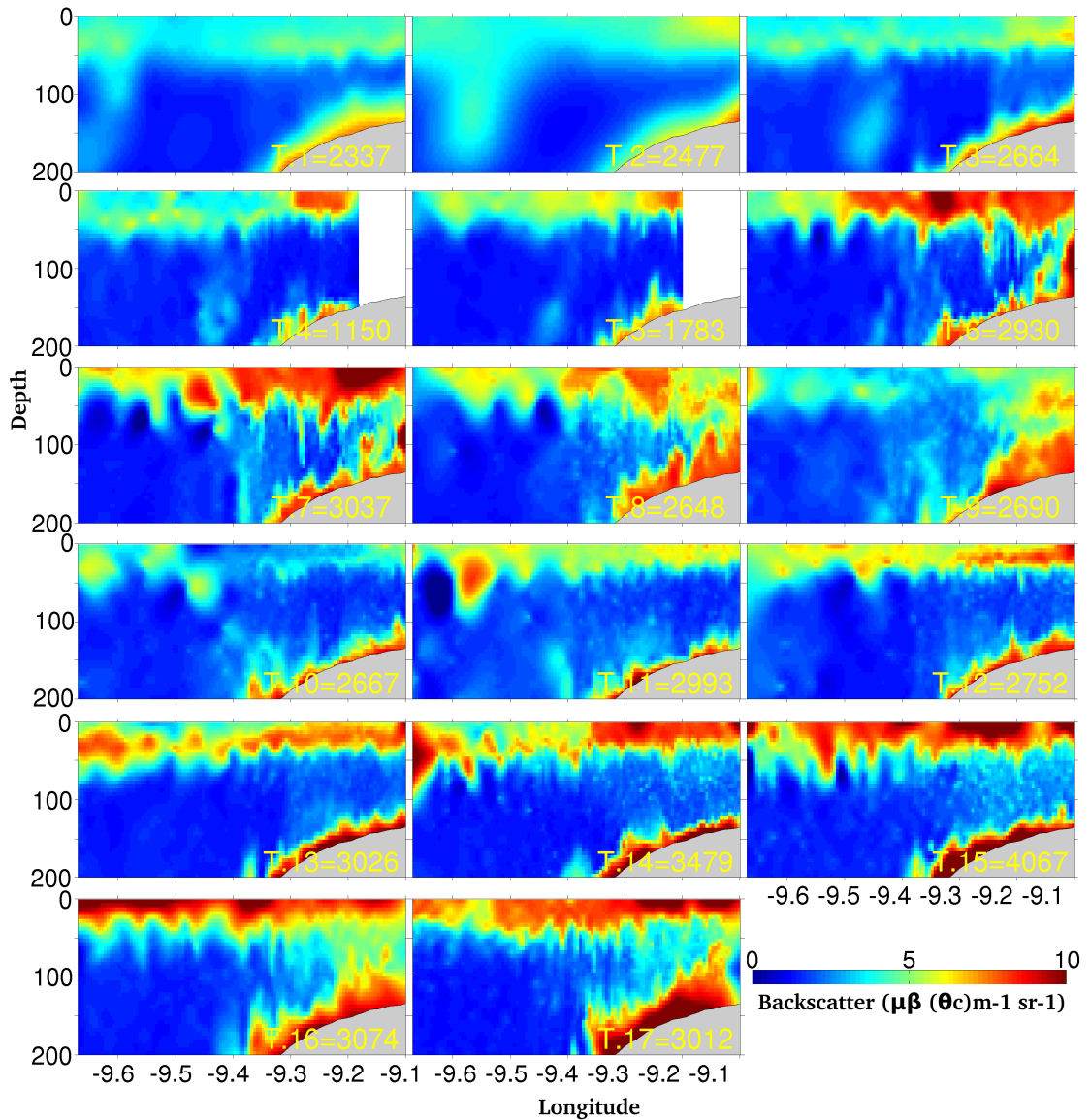


Figure 4.13 Gridded backscatter values for each of the seventeen Seaglider transects, with average backscatter measurements in yellow text.

At this point, high levels of phytoplankton activity and particulate in the photic zone, and high levels of particulate and low oxygen concentrations on the shelf floor have been identified. Shelf break fronts are suspected to form a barrier preventing POC export offshelf to the deep (Gawarkiewicz & Chapman 1992). As the Seaglider data features multiple repeat transects across this front, particulate can be tracked on its journey

Biogeochemical and physical observations of the transect region

through the watercolumn, from the photic zone to the aphotic zone, and its final deposition location identified.

Where is particulate deposited?

To attempt to gauge the transfer of particulate from the photic zone to the aphotic zone, the Brigg's backscatter spike technique was used. To overcome fast particulate sinking rates, the raw backscatter data were processed using the backscatter spike analysis technique invented by Briggs (2010). Using raw backscatter data, spikes were isolated by subtracting a moving 6-dive averaged (3 previous dives + 3 subsequent dives) backscatter signal from each individual datapoint. The resulting dataset contained occasional large spike signals (large increases in measured backscatter compared to the 6-dive averaged value) resulting from a piece of POC/ marine snow drifting in-front of the sensors detection window. Any spike signal that was above the 95th percentile spike signal for the entire mission was flagged as a backscatter spike. This flagged spike data was then binned into 2 m bins, where the total number of spikes/ total number of observations made per bin resulted in a 'spikiness' index. From this dataset, we observe high levels of backscatter spikes over the continental shelf. These regions of high spikiness are at their peak on the post-bloom transects 6-9 and 16-17, and are east of the shelf break front, or within the upper 40 m of the watercolumn (figure 4.14). During relaxation, neither the oxygen minima, or regions with high spikiness appear to be advected westwards to any degree, instead forming directly underneath the preceding phytoplankton bloom (figure 4.11, 4.12 and 4.13). Only during the last major upwelling event, were spikes observed west of the shelf break front. However, these spikes were concentrated in the photic zone, in the upper 50 m, so are likely to relate to the bloom observed during these transects, rather than export.

Biogeochemical and physical observations of the transect region

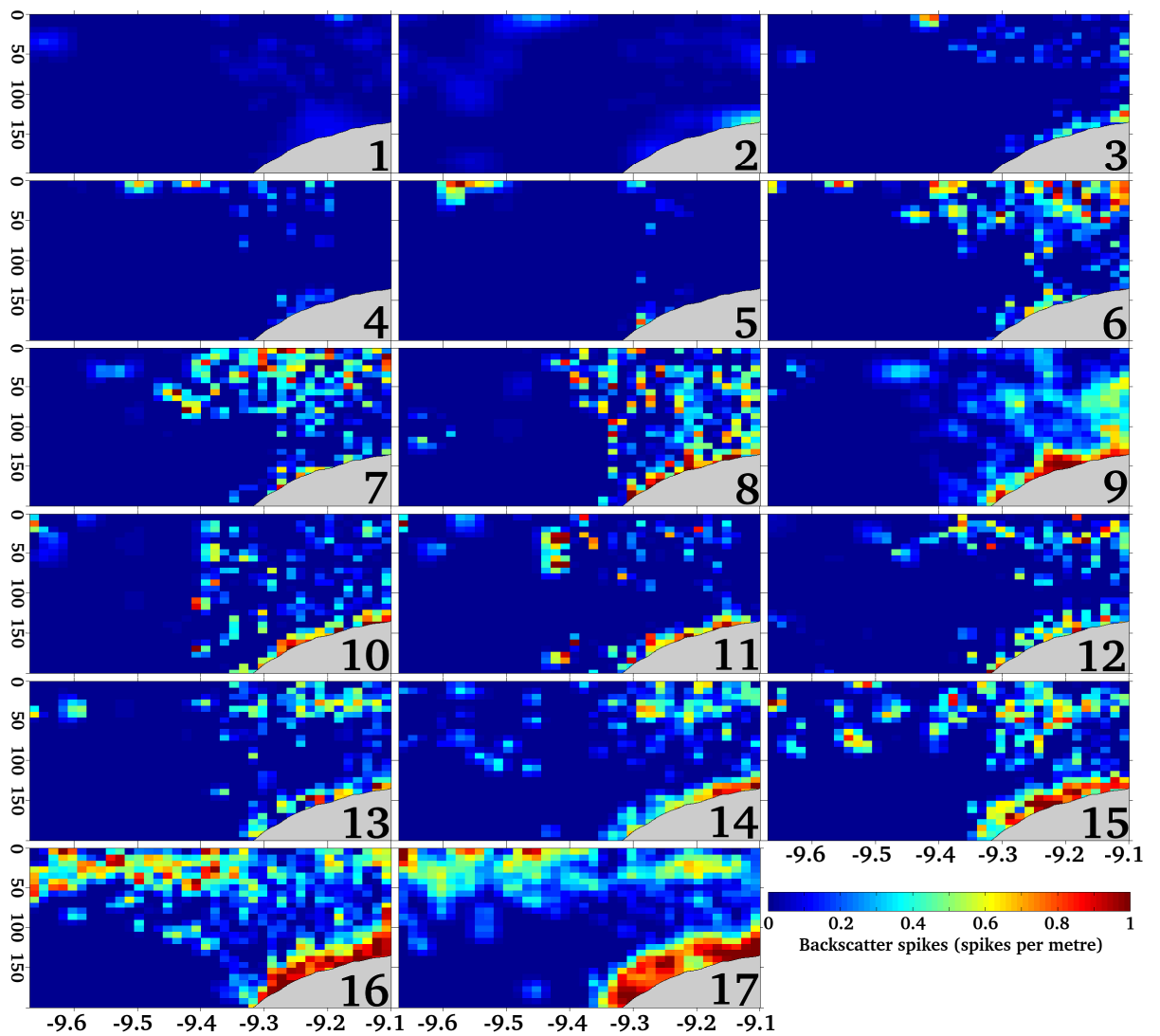


Figure 4.14. Backscatter spikes plotted for each of the 17 transects. Note the high backscatter spikiness east of the shelf break front.

4.7 Conclusions: Comparing the physical and biogeochemical observations of upwelling

Summer 2010 featured two periods of fully developed upwelling, as discussed in part one of this chapter. These upwelling events resulted in phytoplankton blooms, increased photic zone oxygen concentrations and particulate (as observed via backscatter.) The largest blooms occurred east of the shelf break front (4.11, 4.12, 4.13). The presence of both the continental shelf break front, as well as the correlation between upwelling and phytoplankton blooms have been observed before (e.g. Peliz et al. 2002, Barton et al. 2001). The Seaglider data indicates that the front persists throughout the season, and if anything, is stronger and more defined during relaxation, (rather than upwelling, figure 4.4). In the presence of the strong Ekman dynamics (resulting from upwelling favourable winds), the advection of deeper water (eastwards) onto the shelf and Ekman layer water (westwards, off the shelf) appear to result in mid water column mixing, and thus acts to lessen the temperature contrast across the front at depths below 30 m, weakening the front at the shelf break. However, near surface (0-30 m) temperatures during upwelling feature a stronger temperature gradient than during relaxation (as a result of cool, recently upwelled water transported in the Ekman layer).

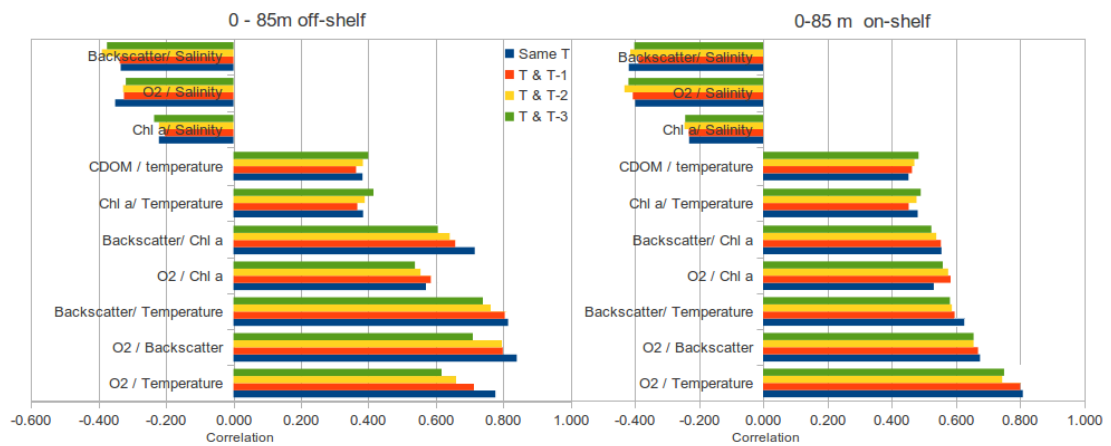


Figure 4.15 Photoc zone correlations between the Seaglider measurements over the seventeen transects.

The mixing and export of shelf water can be assessed using CDOM, as upwelled ENACWP has a low CDOM signal, whilst photic zone water has a high CDOM signal

Biogeochemical and physical observations of the transect region

resulting from phytoplanktonic activities, fluvial inputs and resuspended shelf sediments, with high levels of CDOM east of the shelf break front corresponding with low concentrations of phytoplankton, and hence by association, low nutrient concentrations.

Backscatter, Chl a and oxygen are all useful tracers to assess phytoplankton bloom dynamics, and the export of POC *ex-photic* zone (figures 4.11, 4.12, 4.14). The watercolumn can be split into two vertical 'boxes'- the photic zone and the aphotic zone, and two horizontal boxes- east of the shelf break front, and west of the shelf break front. In the photic zone, oxygen, chl a and backscatter were all strongly correlated with each other (figure 4.15), and weakly inversely correlated with salinity- indicating that low salinity associated with the low salinity endmember watermass- ENACWP results in stronger blooms. Bloom dynamics and productivity are explored in more detail in chapter five.

Estimating productivity using an O₂ watercolumn inventory

5.1 Introduction

The net metabolic state of the oceans (i.e., balance between photosynthesis and respiration of all marine biota), is important for O₂ and CO₂ air-sea exchange. As the vast majority of autotrophic and heterotrophic metabolic systems rely on the reduction of carbon dioxide into carbohydrate, and the oxidation of carbohydrate to carbon dioxide, measurements of the net flux of either oxygen or carbon dioxide can be used to infer net metabolism (Mouriño-Carballido & Anderson 2009). Direct measurement of the metabolism of all organisms within an ocean region is impossible. Instead, bottle incubations using various tracers or biogeochemical and biological in-situ techniques can be used to approximate this metabolism. One such technique, integrated watercolumn oxygen-inventory net community production (see chapter 1), uses measurements of the rate-of-change of watercolumn oxygen concentration to infer the net metabolism (abbreviated to NCP) of all biota present within the water-column. This method has proven successful in a number of different ocean environments, ranging from the tropical gyres to sub-polar seas (Alkire et al. 2011; Riser & Johnson 2008a; Stanley et al. 2010). The categorisation of oceanic regions according to net metabolic states (using NCP) over seasonal and annual cycles is an expanding field, with much focus on whether regions, such as the oligotrophic gyres, are net autotrophic or heterotrophic (Williams et al. 2013). Through this categorisation, the relative global importance of different oceanic regions for O₂/CO₂ fluxes can be estimated, with the eventual aim to improve the estimate of the total global magnitude of the CO₂ flux between the atmosphere and the oceans (Williams et al. 2013).

There are relatively few studies measuring net metabolic state of temperate and sub-tropical shelf seas and EBCs, with data that exists indicating a wide variation in NCP values. Although no studies within the transect region have been completed, the Ria de Vigo has been researched. Arbones et al (2009) measured average summertime NCP of 400 mmol O₂ m⁻² d⁻¹ over July 2004- more than four times higher than NCP rates recorded throughout the rest of the year. High variability has also been identified within

Estimating productivity using a watercolumn inventory technique

the Ria de Vigo, with peak summertime NCP measured at $2000 \text{ O}_2 \text{ m}^{-2} \text{ d}^{-1}$ during July, but a monthly average value of only $533 \text{ O}_2 \text{ m}^{-2} \text{ d}^{-1}$ (Cermenó et al. 2006). Thus, the Ria region appears to have the hallmarks of a highly productive, highly variable region with a strong net autotrophic NCP signature. In contrast, summertime NCP values offshore, within the Atlantic subtropical gyre, were found to be near trophic balance, at $15 \text{ O}_2 \text{ m}^{-2} \text{ d}^{-1}$ (Serret et al. 2001). As the transect region is positioned between these two environments, the nutrient rich Ria outflow region, and the oligotrophic subtropical gyre, it would be expected that NCP rates would fall between these two endmembers.

Making a representative measure of net metabolic state in such a variable region is also challenging, and would be heavily biased by the dynamics of regional upwelling when that measurement was made (measurements made during fully developed upwelling would overestimate NCP, whilst measurements during relaxation would underestimate NCP if subsequently scaled for the entire summer period). Previous studies have identified high year-round primary productivity (P_p) values in the majority of subtropical shelf seas and EBC regions (Borges et al. 2006).

5.2 NCP methodology

There are various methods of measuring NCP. One method used is bottle incubations- the incubation of photic zone water samples under light conditions that approximate those in the photic zone (Bender et al. 1987). A second method compares oxygen concentrations with those of argon and estimates of air-sea gas exchange. In a close system, the dissolved concentrations of the two gases should be similar excluding the effects of metabolism. In an open system the following need to be considered:

1. NCP.
2. The rate of air-sea gas exchange between the mixed layer water-column dissolved-gas inventory and the atmosphere, assuming the mixed layer and atmosphere are not at equilibrium.
3. Mixing with watermasses containing differing concentrations of both gases.

By removing the influences of 2 and 3, higher or lower than expected oxygen concentration with respect to argon concentration can be used to calculate NCP (Bender

Estimating productivity using a watercolumn inventory technique

et al. 1987). Both of these methods involve direct water-sampling, requiring a research ship, rosette, laboratory equipment and considerable expense. Effectively this limits the number of measurements that can be made, and as a result, the spatial and temporal resolution of NCP data.

An alternative method (oxygen inventory) uses the rate of change of oxygen concentration within the watercolumn to calculate NCP. This method has been completed using oxygen measurements from either ship based CTD/ Winkler titrations or via Lagrangian floats (e.g. Argo/ PALACE floats, Riser and Johnson 2008, Alkire et al. 2011.) The use of ship based oxygen data to calculate NCP has similar limitations to the water sample based NCP measurements- expense and poor resolution. Lagrangian float based measurements overcome the expense and resolution issues mentioned above, with multiple dive- climb cycles being completed at a comparatively low cost (Riser and Johnson 2008). These floats are only able to control their vertical travel, moving with the current horizontally (resulting in no control over the location of the unit after release). Operating in a watercolumn with either no current, or an equal unidirectional current at all depths, Lagrangian floats offer substantial advantages over Eulerian techniques- namely the elimination of uncertainty owing to the advection of water masses with differing oxygen properties into the sample region. EBCs lack homogeneity in their current fields, with huge variations in both speed and direction observed within the transect region (Barton et al. 2001). Therefore, any 'Lagrangian' profiling technique used in such an area would require similar corrections for watermass advection as per an Eulerian technique. Thus, NCP measurements using the oxygen inventory technique via Seaglider oxygen measurements potentially combine the advantages of Lagrangian floats and Eulerian ship-based CTD transects; affordable high resolution measurements on a defined transect.

Calculating NCP using a Seaglider requires the assessment of various factors that potentially influence the oxygen inventory. The change in oxygen inventory that results from biological processes needs to be separated from any inventory changes caused by physical processes (figure 5.1). The following sub sections describe the measurements and calculations that are used to calculate NCP over the course of the Seaglider missions.

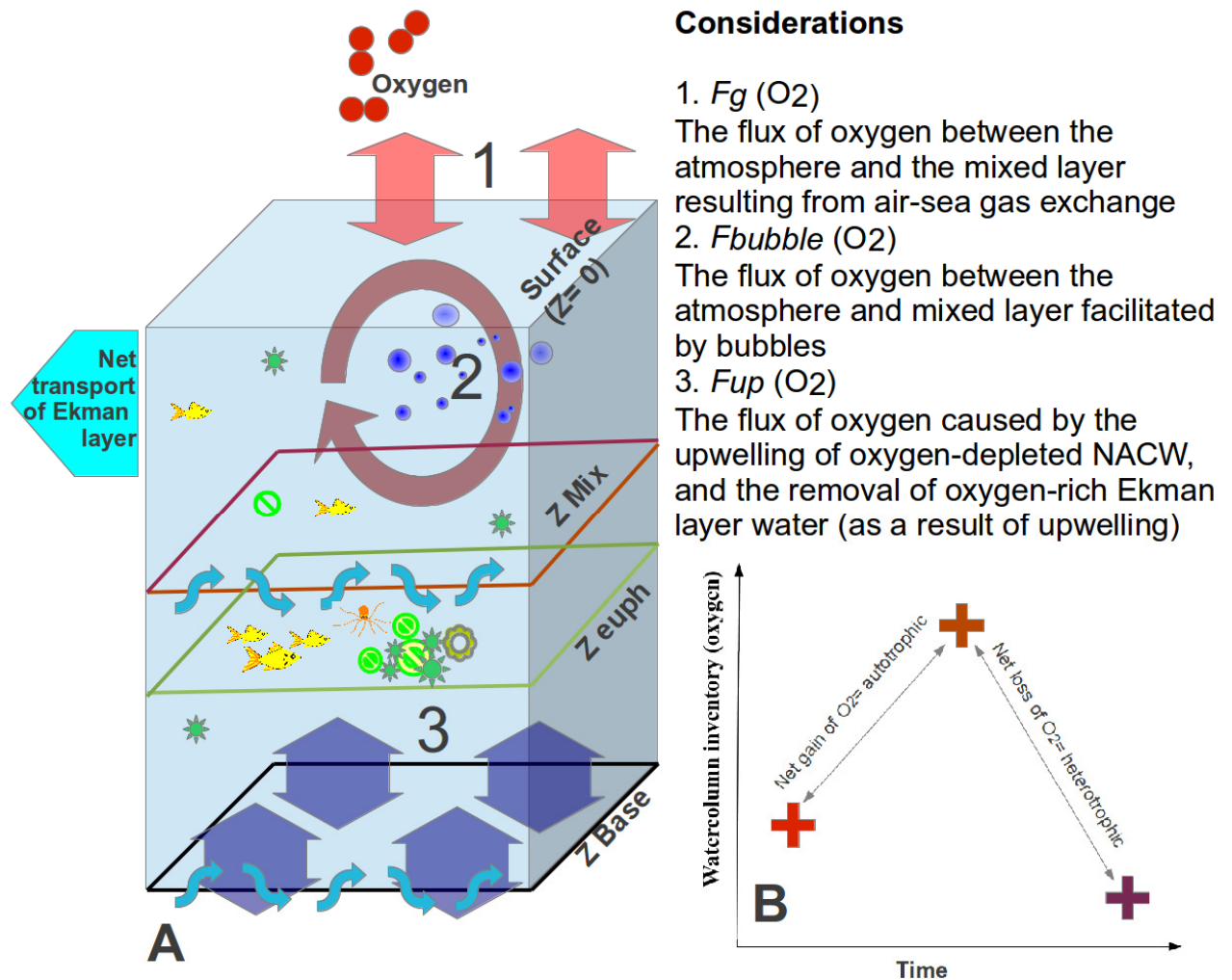


Figure 5.1 A: A schematic of the three main considerations ($F_g[O_2]$, upwelling $F_{up}[O_2]$, and bubble fluxes $F_{bub}[O_2]$) that are included in the Seaglider NCP calculation. The calculation of $F_g[O_2]$, $F_{up}[O_2]$ and $F_{bub}[O_2]$ is discussed below, in addition to the water-column base and surface values .

B: By calculating individual water column oxygen inventories at various locations along the Seagliders transects, transects with the same geolocation can be identified (the water columns colour in shades of red). The physical fluxes $F_g[O_2]$, $F_{up}[O_2]$ and $F_{bub}[O_2]$ that occur between one transect and the next can also be calculated (discussed in text.)

C: By combining physical and water column inventory change calculations, the net change in oxygen content of the watercolumn can be calculated.

5.3 Water column rate of change

The calculation of NCP from Seaglider data is a multiple stage process, with two main components: watercolumn oxygen inventory rate of change caused by biology and oxygen change resulting from physical processes within the watercolumn. These processes are namely the dilution of the oxygen content of the watercolumn by the upwelling of oxygen-depleted ENACWP waters, air-sea interactions and fluxes due to bubbles (figure 5.1.) Initially, the following issues will be addressed:

1. Defining the surface and z-base depth of the oxygen integrated water-column, with two alternatives, a fixed Z -depth and a fixed isopycnal surface (figure 5.1 A)
2. Mathematical definition of oxygen integrated water column
3. Methods of comparing water- column variations in oxygen between each of the seventeen Seaglider transects in order to calculate an oxygen inventory rate of change (figure 5.1 B & C.)

The Seaglider made 17 longitudinal transects between 9.05 and 9.67° W, at a 'fixed' latitude of 42.1° N between yeardays 151 and 220 (with the longitudinal geolocation of the Seaglider plotted in figure 5.5 A). Assuming a stationary water-column and no latitudinal variation of the Seaglidiers path, 17 repeat observations of the water-column at the same geolocation were made over the course of the mission. The watercolumn however was not stationary, westward (offshelf) Ekman transport of water during upwelling has been identified in the Seaglider transects (section 4.2). Eastward (onshelf) advection of deep water also been identified- by increased on-shelf aphotic zone oxygen concentrations during upwelling events (section 4.3.) In addition to these E-W and W-E currents, the meridional EBC (Portugal current) flows slowly N-S across the transect (Barton et al. 2001). As this is not a Lagrangian study, the Seaglider will effectively remain stationary as watermasses sampled flow by, over the course of the season potentially causing a source of uncertainty. This uncertainty is discussed at the end of this chapter.

Estimating productivity using a watercolumn inventory technique

Integrated water column

By integrating the oxygen content of the water-column from the surface ($Z = 0$ m) to a defined Z depth base (labeled ' Z base', figure 5.1), the total oxygen inventory of the water column can be calculated (equation 1). Comparing oxygen inventories from the same geolocation measured on different transects and thus different times (transect number is represented by 'n' in all equations) enables an oxygen inventory change with respect to time to be calculated (equation 2)

$$[1] \quad I(O_2) = \int_{Z=0m}^{Zbase} C(O_2) \cdot \rho dZ$$
$$[2] \quad \frac{\Delta I(O_2)}{\Delta t} = \frac{[I(O_2)Q_{n+1}] - [I(O_2)Q_n]}{tQ_{n+1} - tQ_n}$$

where

$I(O_2)$ is the integrated watercolumn oxygen inventory ($mmolO_2m^2$)

$Z = 0m$,

$Zbase$ defines the top and bottom of the watercolumn (m)

t is sampling timestamp (yearday)

$C(O_2)$ is the oxygen concentration ($\mu molO_2kg^{-1}$)

ρ is the average density of the water – column (kgm^{-3})

Q_n is the transect number,

Significant effort was made during the mission to ensure that the Seaglider remained on a constant latitude of 42.1° N. This was broadly achieved, bar one episode of poor piloting during the first transect that resulted in the Seaglider being steered slightly towards the south. These small variations in latitude are ignored in the calculation, and a constant value of 42.1° N assumed. The possible errors relating to this assumption are discussed in section 5.6.

The Seaglider was piloted using five way points, between 9.05 and 9.67° W. By using five rather than two way points ensured that latitudinal drift during the transect was minimised. Between these way-points, the Seaglider functions autonomously, surfacing and diving to reach each way point. This results in longitudinally non-uniform sampling

Estimating productivity using a watercolumn inventory technique

of the transect. To enable direct comparison of water column oxygen content from one transect to the next, all wind-speed, upwelling, and water column inventory data were interpolated using Matlab function `interp1.m` onto a uniform longitudinal grid of 100 m (the approximate Seaglider sampling rate of the watercolumn in the on-shelf region of the transect). Using this gridded oxygen data, oxygen inventories were calculated for each of the seventeen transects, and the rate of oxygen inventory change between the transects at identical longitudes calculated. To do this, a definition of Z base was needed (figure 5.1 A). There are two main considerations when defining Z base for the water column oxygen inventory- finding a depth or isopycnal surface that is deeper than all primary productivity, but shallow enough to exclude respiration in the aphotic zone- an issue discussed in chapter 4.3. To locate a satisfactory Z depth/ isopycnal, oxygen, chl a and temperature values for the entire Seaglider mission were binned into 5 m vertical bins and 0.01 kg m^{-3} isopycnal surface bins (figures 5.2 a,b,c and 5.2 d,e,f respectively) The high variability in oxygen and temperature within the photic zone can be seen by the large range between the 5th and 95th percentiles in Z depth bins 20, 25 and 30 m (figure 5.2 a & f) and density bins 1026.5 to 1027 kg m^{-3} (figure 5.2 a & c). This variability decreases from the 55 m and 1027.1 kg m^{-3} bins and deeper, and is highly uniform between ~65 m to 100 m and $> 1027.1 \text{ kg m}^{-3}$ (with homogeneous oxygen concentrations of $\sim 225 \mu\text{mol kg}^{-1}$ and temperature of $\sim 13^\circ \text{C}$.) The low oxygen and chl a variability below 55 m and $> 1027.1 \text{ kg m}^{-3}$ suggests that little/no primary productivity is occurring at these depths/ isopycnal surfaces. The uniform temperature below 85 m and $> 1027.4 \text{ kg m}^{-3}$ fits with the description of an upwelled North Atlantic intermediate water (chapter 4.3, Barton et al. 2001), suggesting that this water mass originates from depth, and hence has been excluded from the photic zone. Finally, there is very little chl a below 85 m and $> 1027.4 \text{ kg m}^{-3}$ (figure 5.2 b & c.) Therefore, the most conservative estimates, 85 m and 1027.4 kg m^{-3} were chosen as the ' Z base' definition for the oxygen water column inventory, with the homogeneity of the watercolumn with respect oxygen, chl a and temperature directly above and below these depths/ isopycnal surfaces visible in the raw data (figure 5.3 h,i & j.)

Estimating productivity using a watercolumn inventory technique

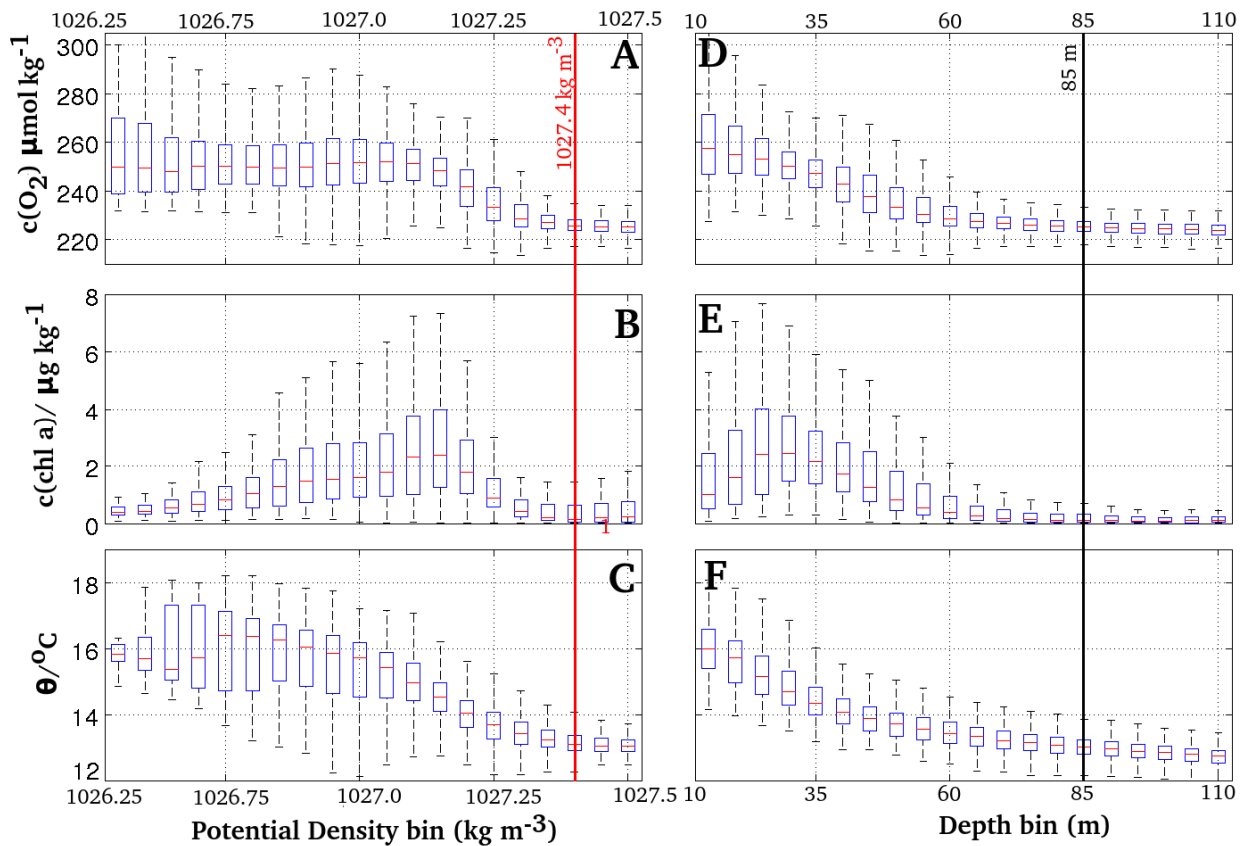


Figure 5.2 Depth: Box and whisker plot of 5 m binned oxygen concentrations (panel A), temperature (panel B), and chlorophyll a concentrations (panel C) for all Seaglider dives between 1 to 1050. The lower blue line indicates the 5th percentile value, the upper blue line indicates the 95th percentile value. The median is represented by the red line, and the highest and lowest outlier values are depicted by the black lines.

Density: Box and whisker plot of 0.1 kg m^{-3} binned isopycnal-surface oxygen concentrations (panel D), temperature (panel E), and chlorophyll a concentrations (panel F) for all Seaglider dives between 1 to 1050. Again, the lower blue line indicates the 5th percentile value, the upper blue line indicates the 95th percentile value. The median is represented by the red line, and the highest and lowest outlier values are depicted by the black lines.

Estimating productivity using a watercolumn inventory technique

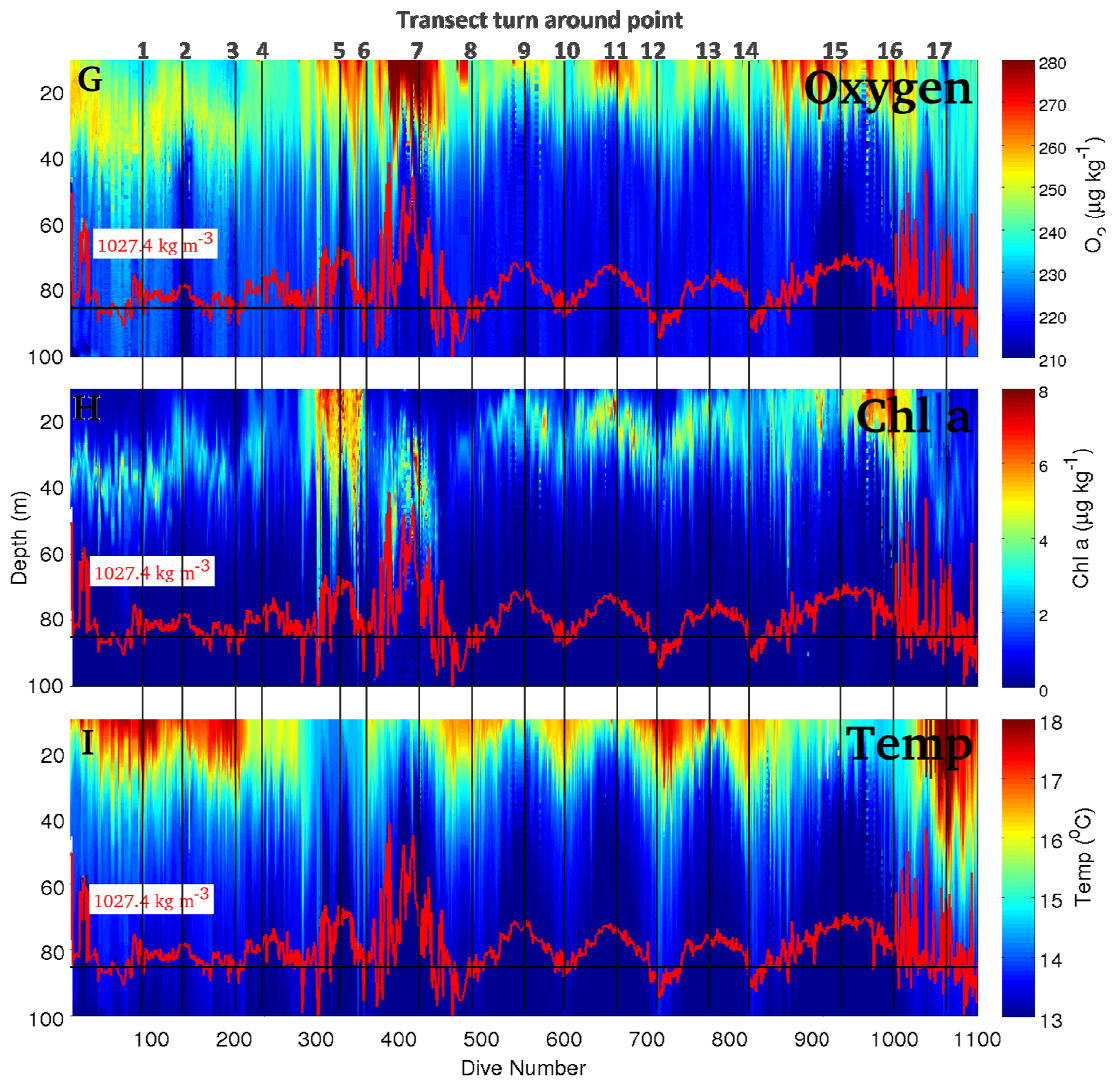


Figure 5.3 Raw data: The choice of 85 m (black line) and 1027.4 kg m^{-3} water column bases ensure that these bases are within a homogeneous and non-productive section of the watercolumn with respect oxygen, chl a and temperature. This suggests that the watercolumn base is deeper than the photic zone, and hence deep enough to ensure all NCP values > 0 occur above this depth/ isopycnal surface.

Estimating productivity using a watercolumn inventory technique

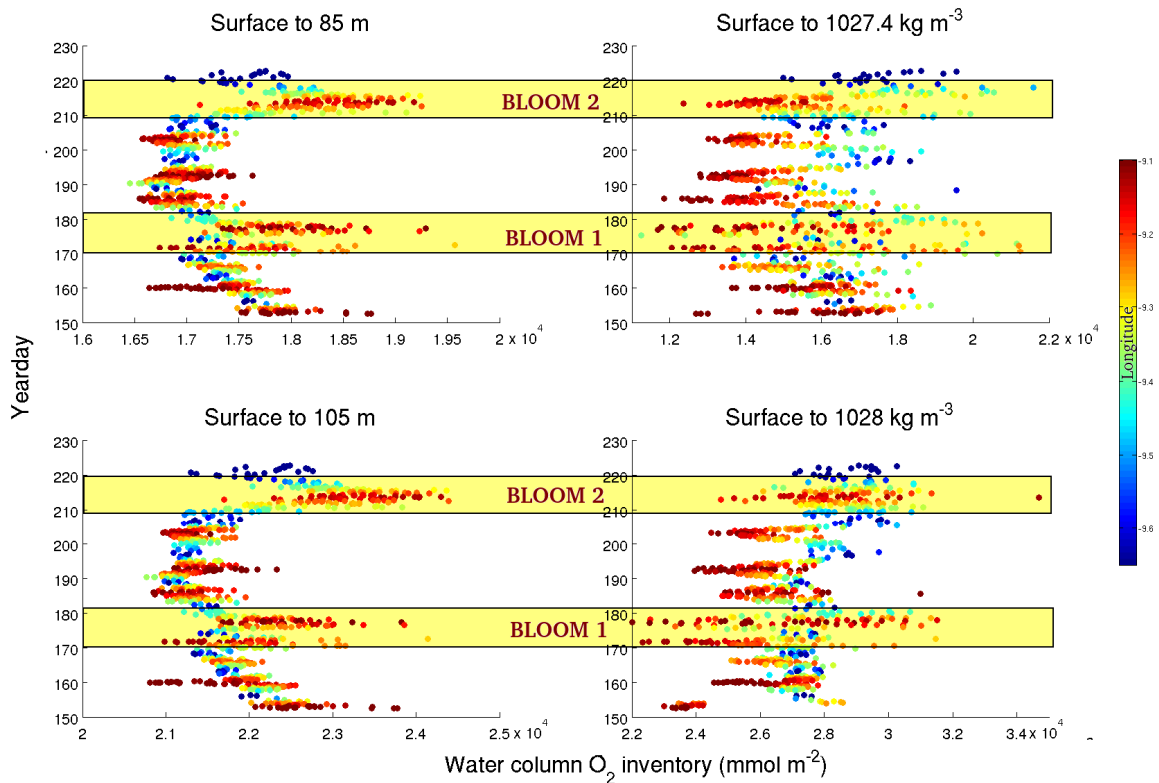


Figure 5.4 Using the 85 m and 1027.4 kg m^{-3} water column bases, $I(\text{O}_2)$ using equation (1) has been calculated. To check the sensitivity of this calculation to different watercolumn bases, 105 m and 1028 kg m^{-3} water column bases were also tested. As the differences, when adjusted for integrated depth, are small between the two watercolumn bases (85 vs 105 m, or 1027.4 vs 1028 kg m^{-3}), the choice of 85 m and 1027.4 kg m^{-3} appears satisfactory. The yellow boxes highlight the main bloom events as described in chapter 4.3. The colour of the individual points relate to the longitude of the water-column, highlighting a general trend of higher water-column oxygen content towards the (on-shelf) east of the transect (red dots) than the west, off-shelf section of the transect (blue dots.)

Isopycnal versus fixed Z-depth watercolumn base

The Iberian upwelling system experiences sporadic summer season upwelling (chapter 1.4.) The upwelling of deep water masses, and westward advection of the Ekman layer would result in a change in the oxygen inventory if the two water masses have a different oxygen concentration. One method of minimising the effects of upwelling on the oxygen inventory is to use an isopycnal as the lower limit 'Z base' of the integrated water column, as (ignoring diapycnal mixing, or heating/cooling of the watercolumn) the isopycnal surface will be transported upwards during upwelling (this method is used by Alkire et al. 2011). This method prevents deep water from entering the bottom of the integrated water-column, however, it is unable to account for the change in watercolumn oxygen inventory caused by the advection of the (typically oxygen-rich) Ekman layer. The effects of this loss of oxygenated Ekman layer water is highlighted by the rapid shoaling of the 1026.4 kg m^{-3} isopycnal surface, as seen in figure 5.2 G. The oxygen concentration at the isopycnal remains at between 220 and 230 during this upwelling event, indicating that there is little mixing of oxygenated near-surface waters or phytoplankton (as indicated by chlorophyll a concentrations) across this isopycnal surface (figure 5.2 F, as the oxygen concentrations are similar to those at 85 m- figure 5.2 G). However, the water-column integrated oxygen values show a net loss of oxygen from the watercolumn during upwelling/ bloom conditions (figure 5.4.) The comparable plots calculated using the 85 m watercolumn base show a net increase in water-column oxygen-inventory (as would be expected in a bloom event.) Looking at the precise data, between dives 387 and 399 the depth of the 1027.4 kg m^{-3} isopycnal surface rises 41 m (from 82 m to 41 m). To maintain watercolumn oxygen inventory the oxygen concentration of the watercolumn (i.e. from the surface to isopycnal floor) during dive 399 would have to be double that of dive 387. The average oxygen concentration observed in the top 85 m of the watercolumn for dive 387 was $239 \mu\text{mol kg}^{-1}$, therefore an average oxygen concentration during dive 399 of $478 \mu\text{mol kg}^{-1}$ would be required to maintain the watercolumn inventory, which is much higher than any oxygen concentration measured during the mission. It is for this reason all calculations in

Estimating productivity using a watercolumn inventory technique

strongly upwelling regions require an estimate of oxygen concentration dilution by upwelling, and hence the choice to use a fixed Z-depth as the base of the integrated watercolumn combined with an estimate of F_{up} - the upwelling velocity in $m d^{-1}$, multiplied by the difference in oxygen concentration between the mixed layer and water at 85 m (figure 5.1 A.)

A sensitivity test was conducted using different definitions of z-base. It was found that choosing a deeper fixed Z-base watercolumn floor had the effect of increasing the total water-column inventory, but had little impact on the amplitude of the water-column inventory variability through time, as shown by the nearly identical shape of watercolumn inventories for the 85 and 105 m Z-depth watercolumns (figure 5.4.) This is confirmed by selecting a shallower definition of z-base, at 55 m; again although the overall inventory size is smaller than the 85 and 105 m z depths (as would be expected, as there is a smaller volume of water integrated for 55 m), the inherent variability of the inventory is similar to both 85 and 105 z depth definitions, and all three are strongly correlated (table 5.1). Therefore, the choice of z-depth appears to have limited effect on the overall calculation of NCP, therefore to maintain consistency with chapter 4, and integrate over the entire photic zone depth, the depth of 85 m was chosen for our calculation.

Table 5.1 A comparison of the oxygen inventory calculated using z depths of 55, 85 and 105 m.

Z depths	55 m	85 m	105 m
Average Inventory	13,690	17,320	21,910
Maximum	15,910	19,600	24,200
Minimum	12,570	16,390	20,940
R ² 55 m	-	0.987	0.979
R ² 85 m	0.987	-	0.987
R ² 105 m	0.979	0.987	-

Oxygen inventory rate-of-change

Initially, using $I(O_2)$ calculated for the 85 m water-column base definition (equation (1)), the oxygen inventory rate-of-change can be calculated (equation 2). As previously discussed, the Seaglider completed 17 longitudinal transects, so there are a total of 17 individual measurements of the water column at each longitudinal point.

Calculating oxygen rate of change can be achieved in one of two ways:

Technique 1: Calculate rate of change using consecutive transects, i.e. transects n and $n+1$, as shown by the red lines in figure 5.5. The timestamp for the data resulting from technique is equidistant from each of the two transects, this is calculated by $\frac{1}{2}(n+1 - n) + n$. If the time taken for the Seaglider to complete transects n and $n+1$ is identical, this timestamp will be a single date for each transect pair- as seen by the green line in technique one.

Technique 2: Use consecutive transects that are in the same direction, (eastward transects and westward transects are paired together) i.e. transects Q and Q_{n+2} . Again, the timestamp for the resulting data will be equidistant between the transects, and as a result will have a variable date across the longitude, as seen by the green line in technique two.

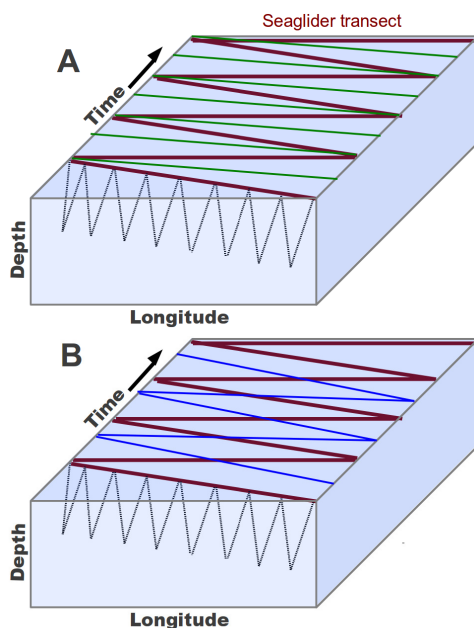


Figure 5.5 A. A schematic of the two integration comparison techniques. The Seaglider path is highlighted in red.

A Technique one compares transect Q with transect $Q+1$, and interpolates the missing data between the two transects by a simple arithmetic average. The time-stamp of this arithmetic average falls on the green lines.

B Technique two compares transect Q with transect $Q+2$, and interpolates the missing data between the two transects by a simple arithmetic average. The time-stamp of this arithmetic average falls on the blue lines.

Estimating productivity using a watercolumn inventory technique

Both methods were tested using the Seaglider I(O₂) data, as seen in figure 5.6. Although both datasets look similar, there are a few noticeable differences. The principle advantages of both techniques can be summarised as:

Technique One:

Uniform timestamp for each transect makes subsequent interpolation of data more straightforward (as shown in figure 5.5)

16 sets of ΔI values can be calculated compared to 15 for technique 2.

Technique Two:

A (more) equal amount of time has elapsed between measurements, so errors in oxygen measurements at the Seaglider turn around points are not magnified by the short elapsed time.

A smoother and less noisy dataset compared with technique one.

The anomalous high and low values at the east and west ends of the transects that are present from technique one are not present in technique two. These anomalies appear to result from the short elapsed time between Q_n and Q_{n+1} magnifying uncertainties in the Seaglidgers oxygen measurements.

The lower noise levels and the lack of anomalous values at the furthest east and west points suggest that technique two is more suitable for the dataset, thus it is this technique that is used to calculate $\Delta I(O_2) / \Delta t$ - the rate of change in the oxygen inventory. A sensitivity test was completed using both techniques using Seaglider data (figure 5.6). Here, the shorter time taken between sampling for technique one can be seen in 5.6C (here the range in time is between 0 days and 13 days), and the more uniform time taken between samples for technique two can be seen in figure 5.6 A (here the time range is between 5 and 13 days). The oxygen inventory rate of change calculated using the first technique (5.6 D) is far more 'spiky' and variable than using the second technique (5.6 B), especially in the far east and west regions of the transect. This is due to calculating oxygen rate of change using a comparatively short time between water-sampling, thus magnifying any error in measurements. It is for this reason, we use technique two for NCP calculations.

Estimating productivity using a watercolumn inventory technique

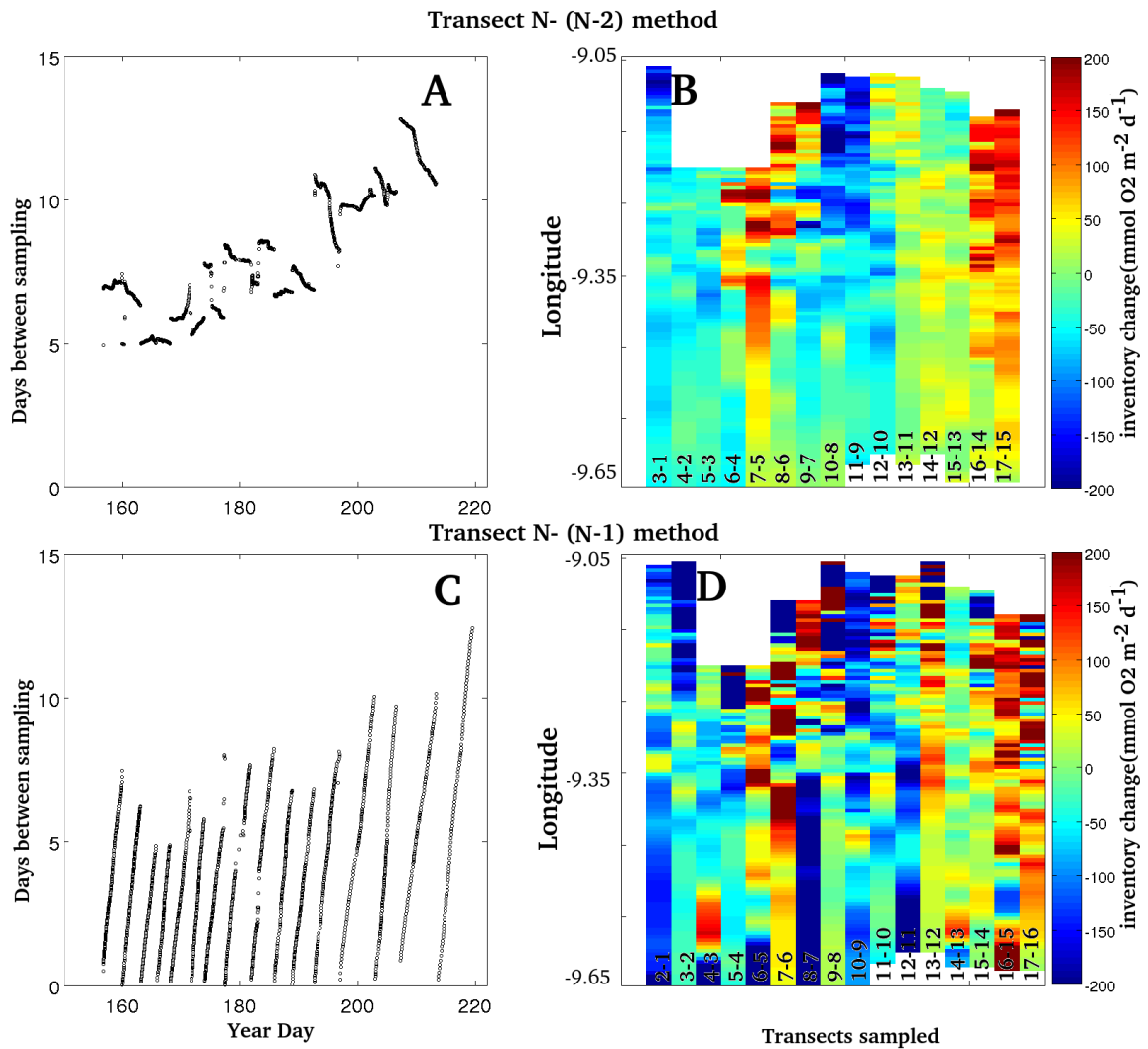


Figure 5.6

A: Time taken between resampling the same watercolumn, with this method this is between 5 and 13 days. **B:** Water-column integrated oxygen rate of change, calculated using technique two, and using 85 m as the base of the water-column.

Technique 1 C: Time taken between resampling the same watercolumn, with this method this is between 0 and 13 days. The sudden switches are due to the Seaglider turning around at the end of each transect, so the comparable watercolumn is separated by less than one day. **D** Water-column integrated oxygen rate of change, calculated using technique one, and using 85 m as the base of the water-column. Note the higher level of noise in panel D compared to panel B.

Estimating productivity using a watercolumn inventory technique

5.4 Physics and air-sea interactions

Now a satisfactory methodology has been identified to calculate $\Delta I(\text{O}_2)/\Delta t$, the physical influences on oxygen concentrations within the watercolumn are left to be calculated.

These include:

1. the flux of oxygen caused by upwelling/ downwelling [F_{up}]
2. the flux of oxygen caused by air-sea interaction [F_{g}]
3. the flux of oxygen caused resulting from bubble dynamics [F_{bub}]

In a closed system, such as a bottle, $\Delta I(\text{O}_2)/\Delta t$ would exclusively describe NCP (equation 2, and figure 5.6 D). However, the North Atlantic is an open system as there is oxygen transfer between the ocean and atmosphere, in addition to the upwelling of deep, low-oxygen water masses (Alkire et al. 2011.) Thus additional oxygen fluxes need to be considered (as shown in figure 5.1). Ekman transport and the corresponding $F_{\text{up}}(\text{O}_2)$, bubble flux $F_{\text{bub}}(\text{O}_2)$ and air sea gas exchange $F_{\text{g}}(\text{O}_2)$ parametrizations all require accurate wind speed (Emerson et al., 2008). Six hourly European Reanalysis (ERA T255 gridded product at ~ 0.75 degree resolution) Interim 10 m wind velocity data from the European Centre for Medium-Range Weather Forecasts (ECMWF) were used for all calculations. As a single wind datapoint covers the entire transect region at T255 resolution, this single datapoint is used to represent the average wind for each 6 hour time bin.

The integrated water-column may be divided into two regions- the mixed layer (0 m to the MLD) and the pycnocline (MLD to 85 m.) The mixed layer contains the air-sea interface where all air-sea gas exchanges and bubble mediated gas fluxes occur. The MLD was calculated using a 0.03 kg m^{-3} density threshold technique (de Boyer Montégut 2004). All calculations for $F_{\text{g}}(\text{O}_2)$, $F_{\text{bub}}(\text{O}_2)$ and $F_{\text{up}}(\text{O}_2)$ use mean temperature, salinity and oxygen concentrations in the ML. Below the mixed layer, the 'pycnocline region' extends from the MLD to the base of the water-column (defined here as 85 m). As this pycnocline region is separated from the air-sea interface by the mixed layer, it is

Estimating productivity using a watercolumn inventory technique

excluded from ($F_g(O_2)$), and thus only used in the oxygen inventory calculations (figure 5.1 A).

Upwelled water- the assumption

To calculate $F_{up}(O_2)$, the following assumptions are made:

During upwelling, all water originates at depths greater than 85 m and is upwelled with no lateral advection of water from depths less than 85 m.

This assumption appears reasonable, as the coastline to the North and South of the transect region is orientated at a similar angle as the transect region (chapter one).

Therefore, under the forcing of a northerly wind, (to maintain geostrophy), the advection of water from the north, south (or indeed East) is unlikely to occur. If it was to occur, there would be a reduction in the F_{up} term, as water above 85 m displayed a higher oxygen concentration at all points throughout the mission (see chapter four), hence the dilution of the mixed layer oxygen inventory would be lower.

Water transported in the Ekman layer has the same oxygen concentration as the ML. As both the Ekman layer depth, and the mixed layer are both ultimately derived from the surface wind forcing, and change in Ekman depth is also likely to be followed by an increase in the ML this appears a reasonable assumption. The velocity of the Ekman layer also decreases as a function of depth (Ekman 1924), hence if the Ekman layer extended below the mixed layer, it would have an increasingly small influence on oxygen inventories with increasing depth.

The upwelling velocity is the same as the velocity of the horizontal advection of the Ekman layer, and other processes (such as evaporation) are negligible.

Although processes such as evaporation, and the influx of Ria outflow water may influence the oxygen inventory, it would be difficult to quantify this flux as part of the upwelling system and the flux is likely to be small due to the climate of the region.

From these assumptions, we can construct the following equation, describing F_{UP} :

$$[3] \quad F_{up}[O_2] = C(O_2(UW)) - C(O_2(ML)) \cdot (W/\rho).$$

where F_{up} is the flux of oxygen resulting from upwelling upwelled water ($mmolm^{-2}day^{-1}$).

where $C(O_2(UW))$ is the oxygen concentration of the upwelled water ($\mu molkg^{-1}$).

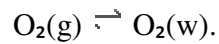
$C(O_2(ML))$ is the oxygen concentration of the mixed layer ($\mu molkg^{-1}$).

W is the upwelling velocity ($m d^{-1}$), and ρ is the density of the ML (kgm^{-3}).

Estimating productivity using a watercolumn inventory technique

Air- sea gas exchange.

The physical process of gas exchange across the air-sea interface can be described in its simplest form by:



Thermodynamic equilibrium is reached when the chemical potential (or fugacity) of oxygen is equal in both air and sea phases, i.e. the sea water is oxygen saturated with respect to the partial pressure of oxygen of the atmosphere. In a static system, oxygen exchange between the two fluids can be calculated using Fick's first law of diffusion coefficients, as described by Liss and Slater (1974), where both the thickness of the boundary layers and diffusion coefficients of the oxygen molecules are estimated. Oxygen has a relatively low solubility in water, compared with many other atmospheric trace gases (e.g. methanol, Kan et al. 2010). This low solubility results in the water transfer coefficient (k_w) being orders of magnitude smaller than k_a , the air transfer coefficient, allowing k_a to be ignored for air-sea gas exchanges (Schwartzbach et al. 1993). Therefore, the flux of oxygen (F_g) can be written as:

In the ocean, k_w is not constant, but varies depending on the physics of the air-sea boundary layer, especially with the windspeed and temperature of the air-sea interface (which is approximated to the temperature of the mixed layer in this parametrisation figure 5.8 A). The calculation of k_w uses the Schmidt number (a ratio of kinematic viscosity over the molecular diffusion coefficient calculated for oxygen from laboratory experiments by Wanninkhov et al. 1992), and a parametrization based on windspeed by Nightingale et al. (2000), the results of which are plotted in figure 5.7 C. k_w combined with C_w and C_{wi} (figure 5.7 B), allows $F_g(\text{O}_2)$ to be calculated:

Estimating productivity using a watercolumn inventory technique

$$[5] \quad Sc = \frac{\nu}{D(O_2)},$$

Where Sc is the Schmidt number, ν the kinematic viscosity of a fluid and D_c is molecular diffusion coefficient.

K_w ($mday^{-1}$), is parametrized as a function of wind speed:

$$[6] \quad k_w = (0.222(U_{10m})^2 + 0.333U_{10m}) \cdot \left(\frac{Sc}{660}\right)^{-0.5},$$

Where U_{10m} = Wind speed at 10m height.
thus F_g ($molO_2m^{-2}d^{-1}$) is expressed by

$$[7] \quad F_g = (Sc \cdot k_w) \cdot (C(O_2(ML)) - C(O_2(Sat))) \cdot \rho,$$

where O_{2sat} is calculated using the TEOS – 10 Matlab toolbox.

There is a time interval of up to 11 days between the measurement of the O_2 inventory during transect n , and then subsequently on transect $n+2$. The wind speeds during the mission were variable (figure 5.3 A), so the range of wind speeds, and hence k_w (equation 6) values will vary between transects n and $n+2$. The 2000 k_w parametrization scales to the square of wind speed (Nightingale et al. 2000). Therefore, inaccuracies would be introduced by using a simple arithmetic mean of the wind speeds observed during Δt to calculate k_w . For this reason, a weighted average of k_w is required.

To calculate a weighted mean wind speed, requires an estimate of the fraction of the mixed layer turned over by wind stress per unit time, following Reuer (2007). This technique relies on estimates of Z_{mix} and windspeed at the same temporal resolution. Although wind speed data for this transect are available at 6 hour resolution, the data are at a resolution of $0.75^\circ \times 0.75^\circ$, otherwise known as TL255 (therefore, there is one wind datapoint covering the entire transect.) To enable calculations, the Seaglider measurements of MLD, O_2 and density over time were also gridded (using linear interpolation) to this temporal (6 hour) and spatial (TL255) resolution. It is from this coarsely gridded Seaglider data and ERA wind speed data an estimate of $F_g(O_2)$ is calculated (figure 5.7 C). Calculated values of $F_g(O_2)$ during the mission show that the flux was not in one direction, instead varying from a net air into sea flux between

Estimating productivity using a watercolumn inventory technique

yeardays (YD) 160 and 171, and again on YD 213 (figure 5.3 C), with these events driven by the undersaturated ML (figure 5.7 B). As the ML remained supersaturated for the majority of the mission, the average $F_g(O_2)$ was positive, with oxygen outgassing from the ocean to the atmosphere (figure 5.7 C).

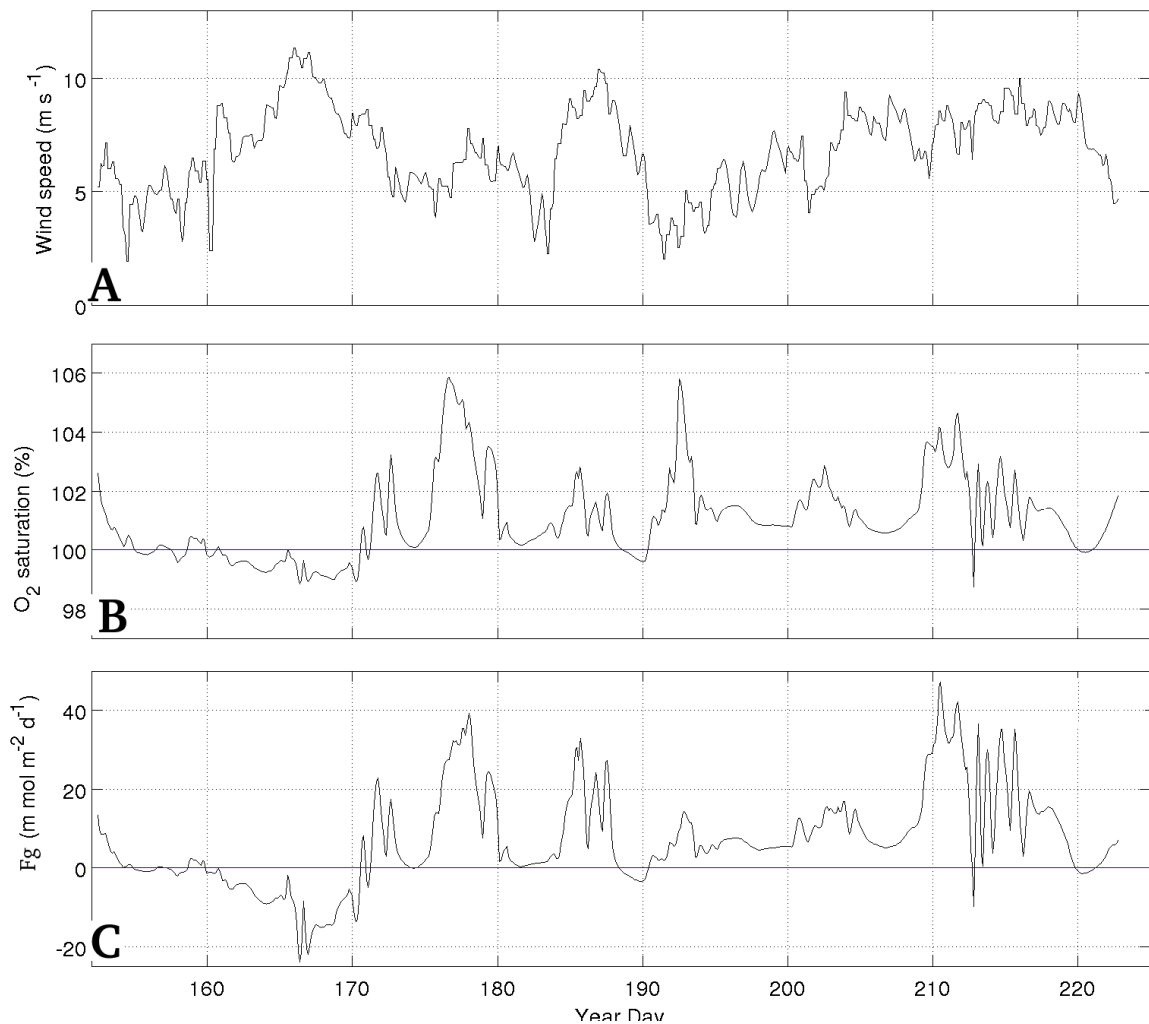


Figure 5.7. A: six hourly ERA interim 10 m windspeed data from ECMWF . **B:** The relative oxygen saturation of the ML was calculated using the TEOS-10 oxygen saturation function, and mixed layer oxygen concentration. **C:** F_g is calculated using equation (7). As part of this calculation, k_w is estimated using Nightingale's parametrisation based on six hourly ERA interim 10 m wind velocity data from ECMWF and Oxygen saturation concentration from the mixed layer (Nightingale et al. 1999).

5.5 Bubble fluxes

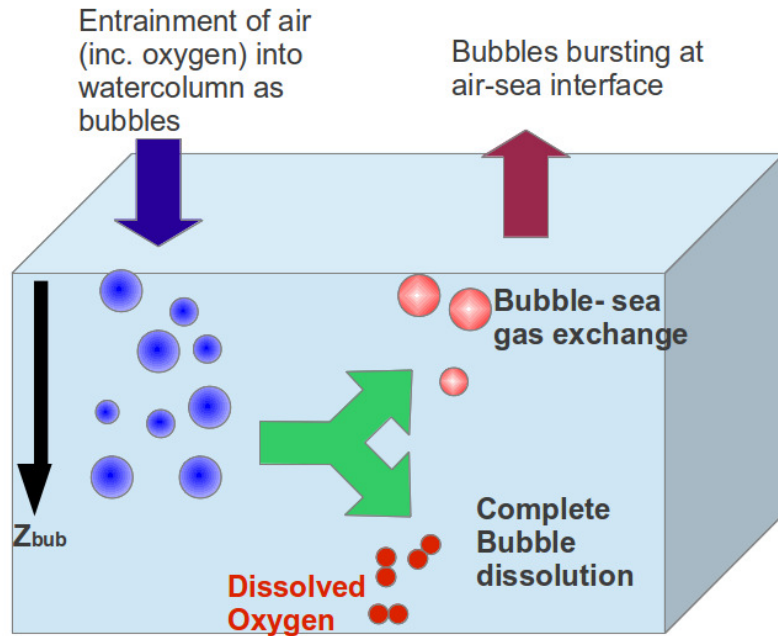


Figure 5.8 A schematic of the two different bubble fluxes (F_{bub}), Bubble-sea gas exchange, where bubbles are injected, exchange gases, and are released to the atmosphere, and total bubble dissolution, where the bubble dissolves completely.

In addition to $F_g(\text{O}_2)$, gas exchange between the atmosphere and the surface ocean can occur via the entrainment of bubbles into the water column by processes such as breaking waves. Bubble flux, $F_{\text{bub}}(\text{O}_2)$ can be considered as two components: bubble exchange and bubble dissolution/ injection (figure 5.8). Bubble dissolution results in the entire gaseous contents of the bubble dissolving into the water column, thus increasing oxygen concentration of the water column irrespective of the relative oxygen saturation of the water column (Woolfe et al. 1991.) Bubble exchange involves a bubble being entrained into the watercolumn, completing air-sea gas exchange, and re-entering the atmosphere with a modified gas content via the sea surface (figure 5.8). This process

Estimating productivity using a watercolumn inventory technique

effectively acts to accelerate the rate at which the water column reaches equilibrium with the air, a parallel process to $F_g(O_2)$ (Woolfe et al. 1991).

Calculating bubble flux is a complex process, with the following main factors influencing $F_{bub}(O_2)$:

-Number and size of bubble generated

The first order control on bubble flux is the total number of bubbles. The size of the bubbles control the split between the two bubble fluxes- smaller bubbles are more likely to dissolve completely, larger bubbles undergo bubble exchange (Woolfe et al. 1991.)

-Depth to which bubbles sink

The deeper the bubble sinks, the longer it will be held under the water- and the higher pressure of the contents, so both the fraction of bubbles completely dissolving and the velocity of the bubble-sea gas flux will increase (see equation 9, and 5.4 C)

-Fraction of bubbles that dissolve completely

Bubbles that dissolve completely contribute their entire gas contents to the watercolumn. Therefore, assuming the same total oxygen content of bubbles, the higher the relative fraction of bubble dissolving completely, the higher the net increase in water column oxygen.

-Relative ML oxygen saturation

Strong oxygen under and super saturations in the ML will increase the magnitude of F_{bub} , especially the flux caused by bubble exchange flux (Stanley et al. 2009).

Estimating productivity using a watercolumn inventory technique

Calculating $F_{\text{bub}}(\text{O}_2)$

The bubble flux (Stanley et al. 2009) parametrisation uses the Graham et al. (2004) parametrisation of the average depth of bubble depression (the depth to which bubbles are forced down into the water column), based on windspeed:

$$[9] \quad Z_{\text{bub}} = (0.15 \cdot U_{10m} - 0.55)$$

Where Z_{bub} is the depth (m) to which the bubble is depressed

z_{bub} , values are plotted in figure 5.9C. The full bubble flux parametrization is as follows:

$$[10] \quad F_{(\text{Bub})} = A_p \cdot \left(\frac{U_{10m}}{\text{ms}^{-1}} - 2.27 \right)^3 \alpha \left(\frac{D_i}{D_0} \right)^{0.5} \frac{(X_i P_{\text{atm}})}{RT} \left(1 + \frac{(\rho g Z_{\text{bub}})}{P_{\text{atm}}} - \frac{C_w}{C_{wi}} \right).$$

where,

$$A_p = 2.3 \times 10^{-3} \text{ s}^2 \text{ m}^{-2},$$

α is the Ostwald solubility coefficient of oxygen (dimensionless),

D_i is the diffusivity coefficient of oxygen,

D_0 is a normalization factor equal to 1, included to simplify the units of D_i to $\text{m}^2 \text{ s}^{-1}$,

X_i is the mole fraction of oxygen in dry air,

P_{atm} is the atmospheric pressure of dry air (Pa),

R is the gas constant ($8.31 \text{ m}^3 \text{ Pa mol}^{-1} \text{ K}^{-1}$),

T is the temperature of the ML (K),

Bubble fluxes were found to be substantially smaller than $F_g(\text{O}_2)$ (figure 5.7 C), and predominantly in an air to ocean direction, Thus, although the bubble fluxes were a minor component in the total NCP calculation, to not include an estimate of bubble fluxes in the oxygen inventory calculation would result in an overestimation of NCP, especially during times of high wind velocities (figure 5.9 D), when the wind speed component in equations 10 result in a high $F_{\text{bub}}(\text{O}_2)$.

Estimating productivity using a watercolumn inventory technique

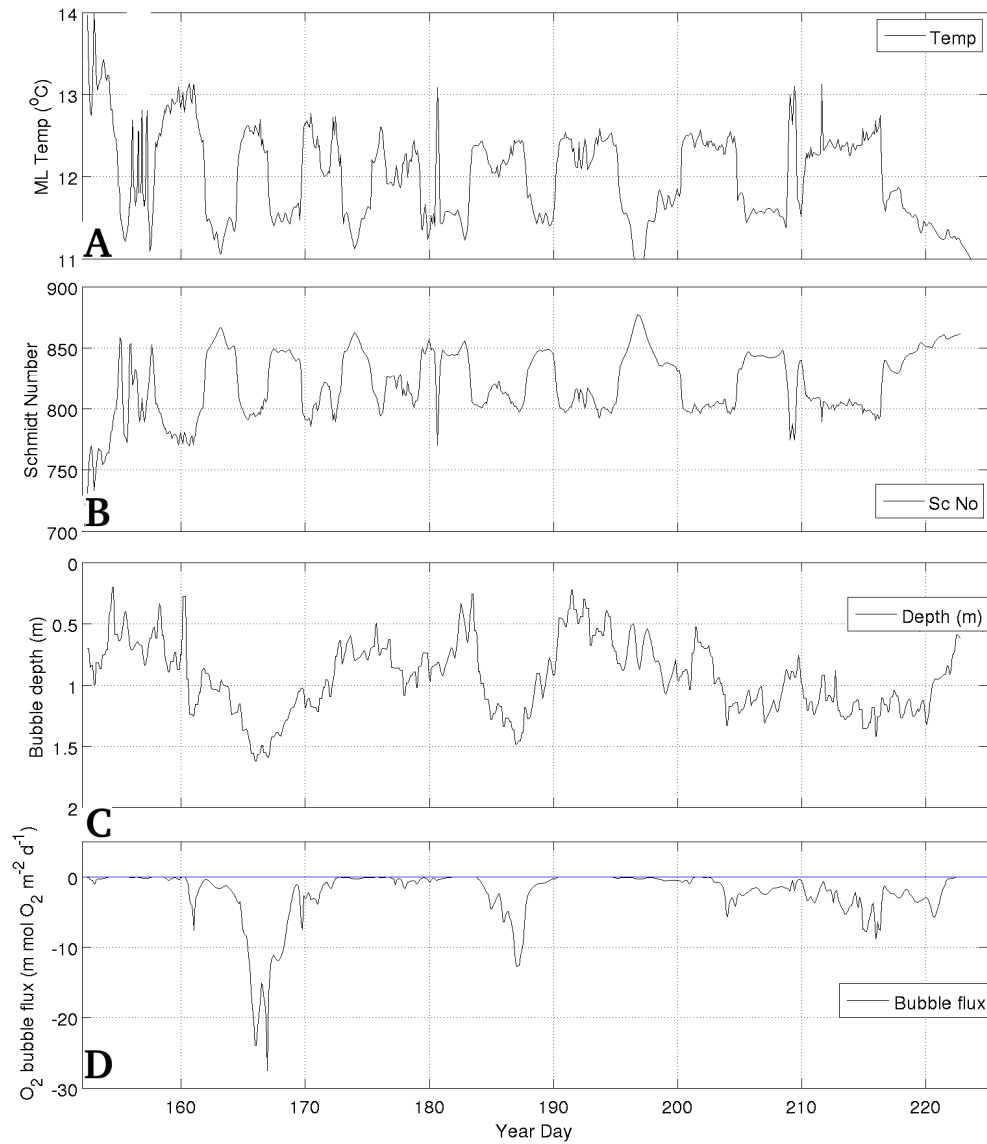


Figure 5.9 A: The mixed layer temperature , B: The mixed layer Schmidt number, used as part of both $F_g(O_2)$ and $F_{bub}(O_2)$. , C: The depth to which the bubble sinking into the water column by wave action, as calculated using equation (9), D: The total $F_{bub}(O_2)$, as calculated using equation (10).

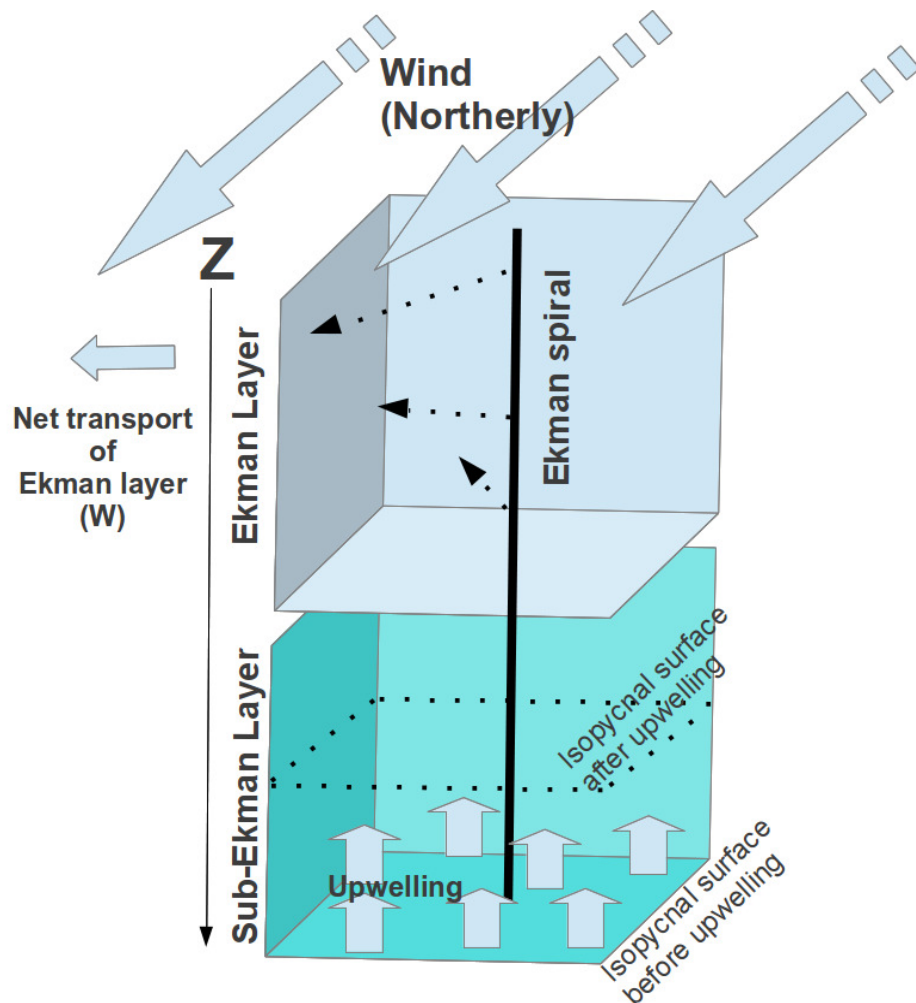


Figure 5.10: A schematic of the Iberian upwelling system. The following assumptions are made:

During upwelling, all water originates in the NACW water mass, at depths greater than 85 m and is upwelled vertically, with no lateral advection of water from depths less than 85 m. The Ekman Layer is entirely within the ML, thus water transported in the Ekman layer has the same oxygen concentration of the ML. The upwelling velocity is the same as the velocity of the horizontal advection of the Ekman layer, and other processes (such as evaporation) are negligible.

Estimating productivity using a watercolumn inventory technique

Typical oxygen concentrations within the ML were substantially higher (20 -80 $\mu\text{mol kg}^{-1}$) than oxygen concentrations in the upwelled NACW water-mass directly underlying the photic zone (chapter 4.2). Assuming the observed upwelling in the watercolumn conforms to traditional Ekman transport (figure 5.10), there will be a loss of oxygen from the water column. (Essentially Ekman transport exports oxygen supersaturated ML water towards the west, which is replaced by oxygen undersaturated ENACWP water from below, resulting in a net loss of oxygen within the water-column, see equation (3). Previous methods of minimising this net loss of oxygen from the integrated water-column inventory was to use a deep isopycnal surface, rather than a fixed z-depth to define the bottom of the water column (Alkire et al. 2011). However, this has been found ineffective in our sample region (as discussed above), A second method to account for this loss of oxygen from the water column inventory is use a fixed z depth as the base of the water-column. By estimating the rate of upwelling within the water column in meters per day, and multiplying this by the difference between oxygen concentration within the ML and the upwelled NACW water mass, an upwelling mediated oxygen flux can be calculated.

The calculation of upwelling was completed using the Ekman upwelling calculation detailed by Sverdrup et al. (1942):

$$[11] \bar{u}DL = wLx$$

$$[12] \bar{u}D = \frac{\tau}{(\rho f)} = \text{net transport of Ekman layer} (\text{m}^2\text{s}^{-1})$$

$$[13] w (\text{m s}^{-1}) = \frac{\tau}{\rho} f x$$

$$[14] W_{(24\text{hrs})} = w \cdot (86400)$$

where \bar{u} is net transport of Ekman layer (towards the west in this example)

D is the Ekman depth

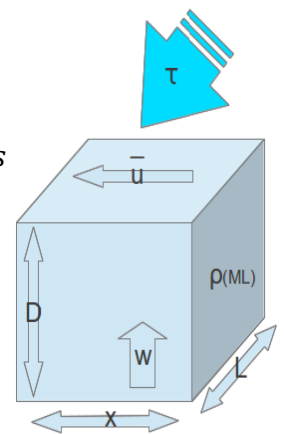
τ is the wind stress, calculated from the $U_{10\text{m}}$ wind speed

f is the coriolis parameter, ρ is density of the water column

x is the width of the continental shelf (52 km)

W is the velocity of upwelling

as depicted in the schematic to the right.



Estimating productivity using a watercolumn inventory technique

$$\bar{u}DL = wLx$$

$$\bar{u}D = \frac{\tau}{(\rho f)} = \text{net transport of Ekman layer (m}^2\text{s}^{-1}\text{)}$$

$$w(\text{ms}^{-1}) = \frac{\tau}{\rho} fx$$

$$W_{(24\text{hrs})} = w \cdot (86400)$$

where \bar{u} is net transport of Ekman layer (towards the west in this example)

D is the Ekman depth

τ is the wind stress, calculated from the U_{10m} wind speed

f is the coriolis parameter, ρ is density of the water column

x is the width of the continental shelf (52 km)

W is the velocity of upwelling

as depicted in the schematic to the right.

In addition to this estimate of upwelling, upwelling velocities from the NOAA PFEL global upwelling index were used for the transect region. The upwelling index ($\text{m}^3 \text{s}^{-1} 100 \text{ m}$) describes \bar{u} over a width (L) of 100 m, therefore to convert the upwelling index into w (m d^{-1}), the index is divided by $L \cdot D$, and multiplied by the number of seconds in a day (86400). The NOAA upwelling model's source data is the US Navy Fleet Numerical Meteorology and Oceanography Centre (FNMOC) synoptic surface pressure analyses, a gridded wind velocity and surface pressure product at 1 degree resolution. The upwelling model uses the orientation of the coastline, average MLD densities, wind speeds and air pressure to calculate \bar{u} over a length (L) scale of 100 m. To calculate upwelling, w , requires the division of \bar{u} by ($L \cdot x$). Essentially, this is the same Ekman theory based calculation, but is based on FNMOC wind speed data, rather than ERA interrim data.

The size of $F_{\text{up}}(\text{O}_2)$ calculated using either Ekman parametrisation (equations 11-14), or the NOAA PFEL index is similar in size to the combined $F_{\text{g}}(\text{O}_2)$ and $F_{\text{bub}}(\text{O}_2)$ (figure 5.8 C, 5.9 D.) There was upwelling for a significant portion of the mission (figure 5.5 B), and the oxygen concentration was always lower at 85 m depth, compared to the mixed layer (figure 5.5 A), therefore the net flux was negative (a loss of oxygen from the watercolumn), as seen in figure 5.5 C.

Estimating productivity using a watercolumn inventory technique

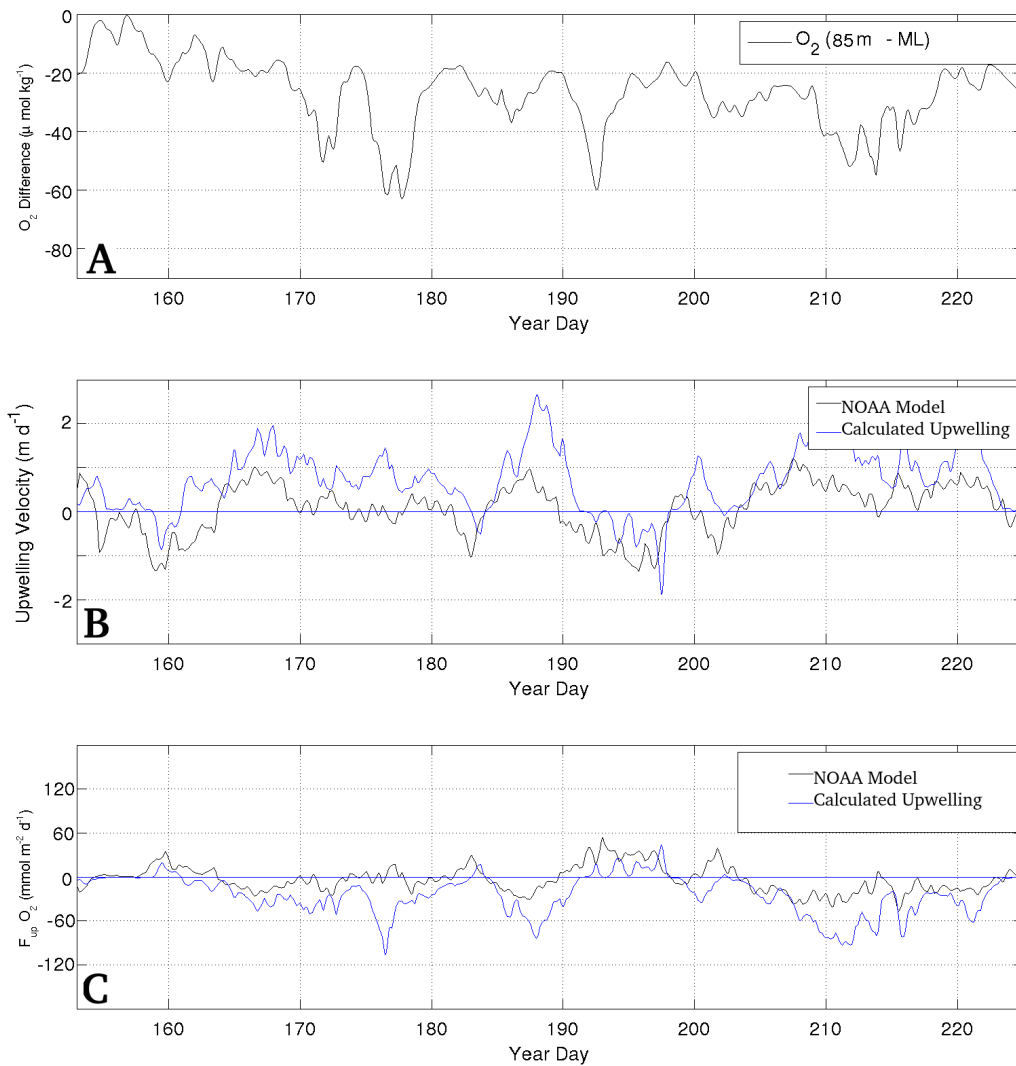


Figure 5.11

A: The oxygen difference between 85 m and the mixed layer. This is multiplied by the upwelling velocity to get watercolumn oxygen inventory dilution

B: Upwelling velocities calculated from each of the two models.

C: $F_{up}(O_2)$ calculated using the two descriptions of upwelling, my own Ekman calculated upwelling, and upwelling from the NOAA model (3) This has been calculated by $(O_2 \text{ ML} - O_2 \text{ 85 m}) \times \text{upwelling velocity}$.

Estimating productivity using a watercolumn inventory technique

Figure 5.11 indicates that there is little difference between the NOAA modelled upwelling data, and the upwelling calculated using ERA wind speed data. There is considerable confidence in the community with the NOAA model, and as the NOAA model has been extensively used to describe upwelling in the region before (Barton et al. 2001, 2008, Teira et al. 2011), it has been used in all subsequent calculations.

NCP Conclusion: The final calculation of NCP

NCP can be calculated by:

$$[17] \quad NCP(mmolm^{-2}d^{-1}) = F_i - (F_g + F_{Bub} + F_{up})$$

To calculate NCP, the oxygen fluxes caused by physical processes ($F_g(O_2)$, $F_{up}(O_2)$ and $F_{bub}(O_2)$) need to be gridded onto the same longitudinal transect grid as the watercolumn oxygen inventory rate of change (figure 5.6 & 5.13 A). This is shown in figure 5.12 A,C,E. To ensure that this gridding technique does not result in aliasing or the production of anomalous data, the gridded data / gridded timestamp is plotted on top of the original data and timestamp in figure 12 B,D & F. Here, the strong agreement between gridded and original data show that this gridding technique works satisfactorily.

By combining the fluxes: $F_g(O_2)$, $F_{up}(O_2)$ and $F_{bub}(O_2)$ with the inventory rate of change ($\Delta I(O_2)/\Delta t$), as-per equation (17), NCP values for the longitudinal grid can be calculated (figure 5.14 A and B.) Finally, using the Matlab function `gridfit.m`, NCP can be displayed as a Hovmöller plot (figure 5.14 C.)

By completing this final calculation, it was found that average NCP over the mission was $15.34 \text{ mmol m}^{-2} \text{ d}^{-1}$, indicating that the region was net autotrophic. Of the four NCP components, the RMS size of each flux displayed in figure 5.6 A was:

$F_i [O_2] (52.2 \text{ mmol m}^{-2} \text{ d}^{-1}) > F_g [O_2] (-13.3 \text{ mmol m}^{-2} \text{ d}^{-1}) > F_{up} [O_2] (-8.3 \text{ mmol m}^{-2} \text{ d}^{-1}) > F_{bub} [O_2] (4.1 \text{ mmol m}^{-2} \text{ d}^{-1})$ with $\Delta I(O_2)/\Delta t$, and $F_{bub}(O_2)$ providing a net gain of oxygen into the watercolumn, and $F_g(O_2) - F_{up}(O_2)$ providing a net loss of oxygen into the watercolumn (figure 5.6 A and B). The combined equation shows that the water column inventory ($F_i(O_2)$) describes 55 % of the total net flux, and physical O_2 fluxes

Estimating productivity using a watercolumn inventory technique

($F_{\text{bub}}(\text{O}_2)$, $F_{\text{g}}(\text{O}_2)$, $F_{\text{up}}(\text{O}_2)$) calculated using the parametrizations above describe 45 % of the net flux.

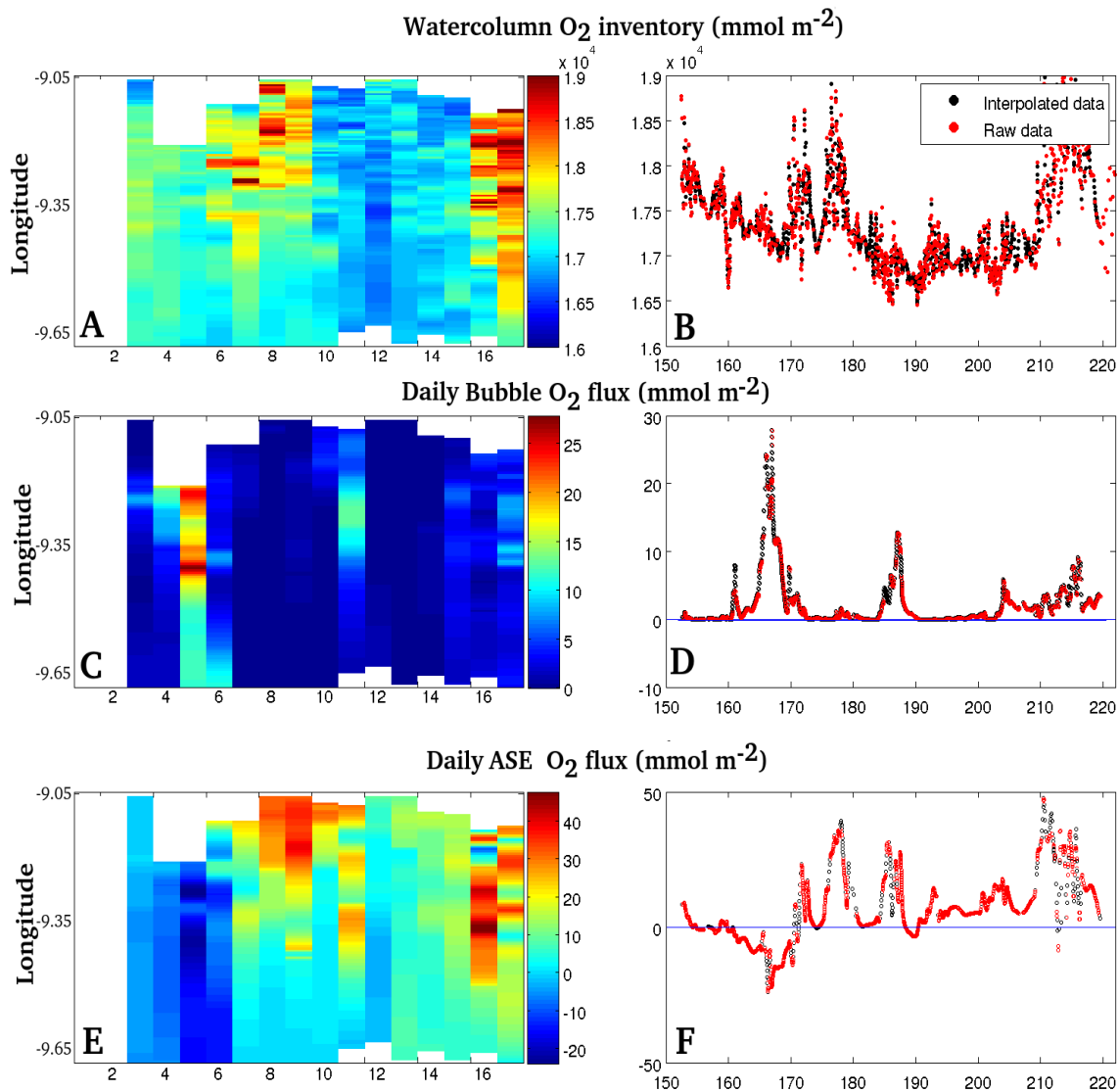


Figure 5.13A: watercolumn oxygen inventory, B: F_{bub} and C: F_{g} gridded onto the longitudinal transect grid used for the watercolumn oxygen inventory rate of change. To check that this longitudinal transect gridding technique didn't alter the data, the gridded data and gridded timestamp data is plotted with the original data (B,D,E).

Estimating productivity using a watercolumn inventory technique

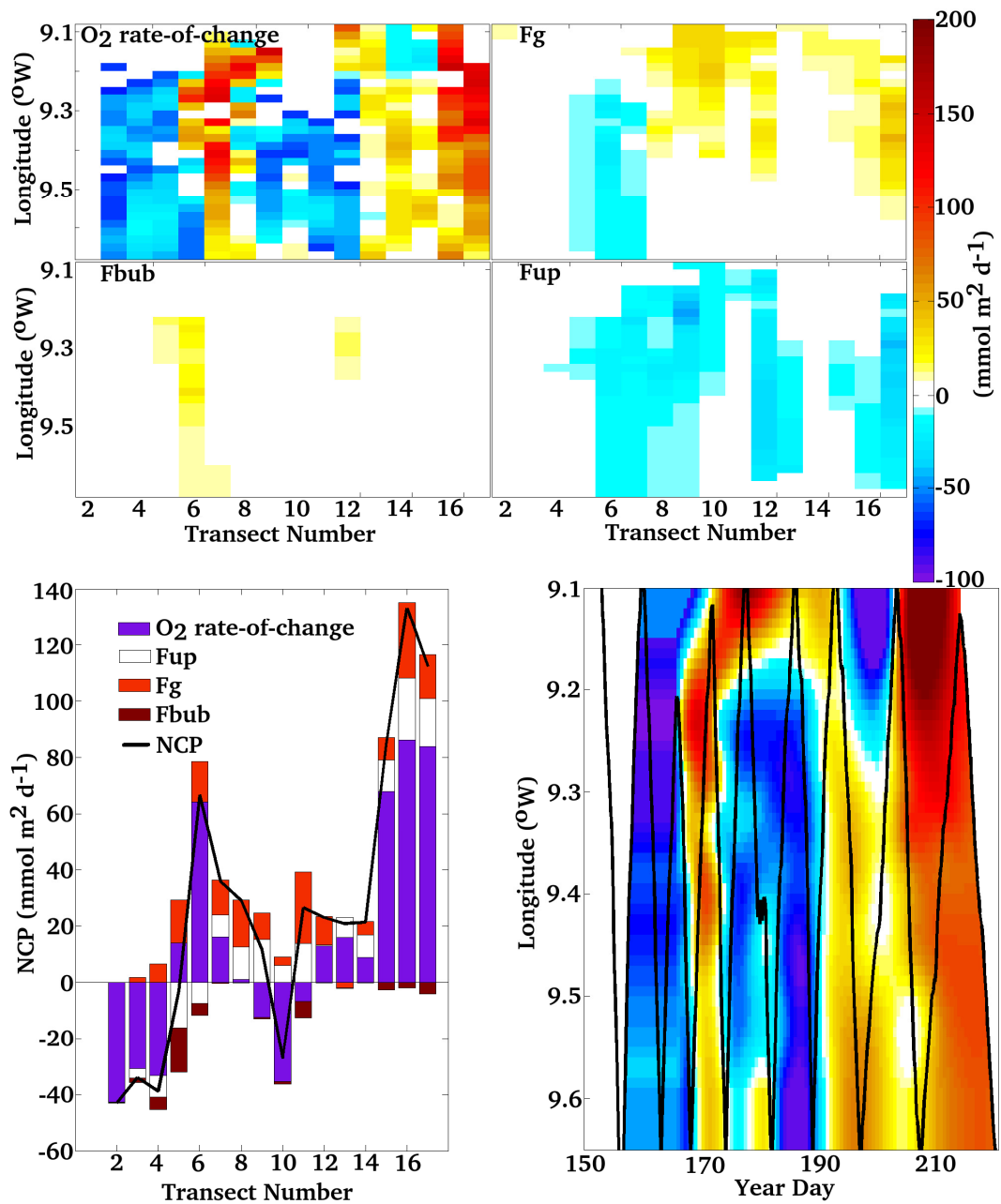


Figure 5.14: Oxygen rate of change, F_g, F_{bub} and F_{up} plotted with transect number. These four components are added together to produce an estimate of NCP, which can be plotted for the entire mission as a Hovmoller. The black lines on the Hovmoller indicate the Seagliders transect.

5.6 Conclusions

Observations of bloom dynamics from chapter four were seen in NCP values. There are two large bloom events featuring a highly autotrophic watercolumn (5.14 C), which are associated with the two main upwelling events observed over T4-6 and T15-17 (table 4.1). A smaller upwelling event at T11 is also observed in NCP data, however peak oxygen production was only 20-55 mmol m⁻² d⁻¹, compared with maximum NCP (O₂) rates of 117 and 102 mmol m⁻² d⁻¹ during the main bloom events. The average NCP for the summer season was 15.34 mmol m⁻² d⁻¹ over the 17 transects. Net heterotrophy (at a maximum of -67 mmol m⁻² d⁻¹ O₂) occurred twice, once for 11 days of particularly calm weather between year days 153 and 164, and then subsequently after the first bloom event. The change from maximum net autotrophy to heterotrophy and vice versa occurred over short timescales of three to six days, highlighting the impact of short timescale physical and biogeochemical processes on NCP. The strongest net heterotrophy or net autotrophy signals were east of the shelf break front, confirming the biogeochemical and physical observations from chapter four.

Estimating NCP through Seaglider-collected mass balance oxygen calculations has proved an effective technique in highly variable watercolumn conditions. Traditional monthly sampling cruises in the region (Barton et al. 2002) would not be at high enough temporal resolution to observe upwelling and bloom development, with the timescale from initial shoaling of isopycnals indicating upwelling to NCP collapse of only 14 days for the first upwelling event. However, as with all techniques for estimating NCP, there are some unaccounted processes, as discussed below.

Unaccounted processes

Essentially, processes that result in net loss of gain of oxygen within the watercolumn outside of F_{up} , F_{bub} and F_g are unaccounted for. These include:

Estimating productivity using a watercolumn inventory technique

F diapycnal (O₂)

Diapycnal mixing between the surface and base of the water column itself would not influence oxygen inventories, as the net oxygen inventory of the water remains the same (figure 5.1.) However, diapycnal mixing across the base of the water-column could alter oxygen values if the water-mass below the watercolumn had a different oxygen concentration to the water above. Oxygen concentrations below the oxycline decrease slowly in the study region, typically $< 0.5 \mu\text{mol kg m}^{-1}$ per meter of depth, therefore the resulting oxygen gradient between the watermasses being diapycnally mixed will be very low, so this flux should be almost negligible as long as the base of the watercolumn is far below the oxycline.

F surfactant (O₂)

Surfactants have been identified as able to retard $F_g(\text{O}_2)$, by increasing k_w (Stanley et al. 2009). Again, the instrumentation on the Seaglider was insufficient to make any estimate of surfactant concentration, and studies into the effects of surfactants are limited. The one study into the effects of surfactants found a strong inverse correlation with wind speed and wave height (Stanley et al. 2009). As the Seaglider transect region was in an exposed area of the North Atlantic, with strong winds and a long fetch, the surface conditions are likely to have been rough, thus inhibiting the effects of surfactants by mixing them through the watercolumn. It is for this reason, we can discount the surfactants effect on air-sea gas exchange.

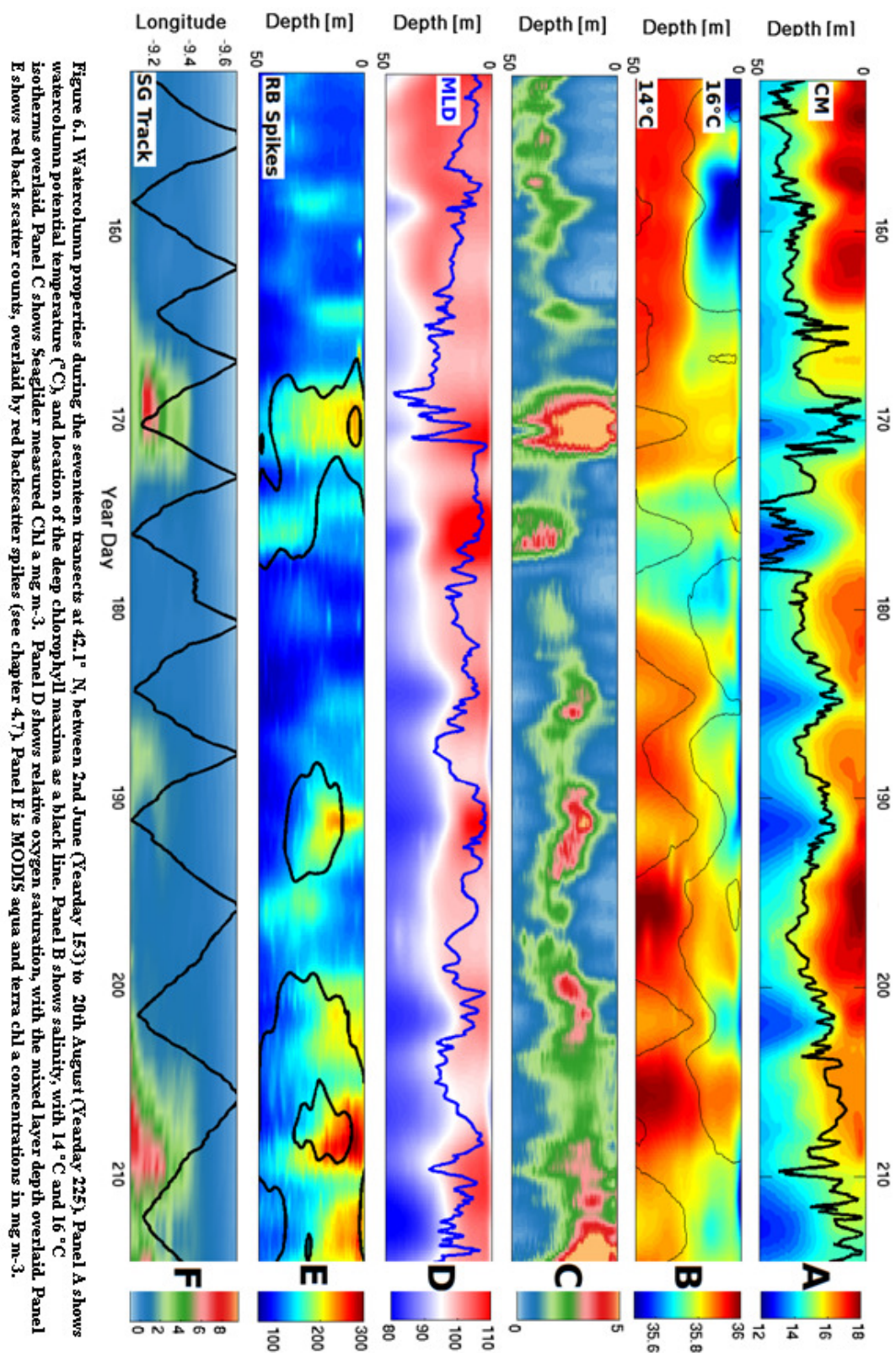
F Advection (O₂)

One of the major issues with an oxygen inventory technique, (compared to invitro incubations) is accounting for changes in oxygen resulting from the advection of watermasses with differing properties. We have attempted to minimize this, by maintaining a transect in a region that is not at a geographical boundary, or featuring any large variations in environmental conditions either to the North or the South (chapter one). Therefore, we assert that if any water is advected into the transect region, it is likely to have similar physical and biogeochemical properties to water advected out of the

Estimating productivity using a watercolumn inventory technique

transect region. As this is the first attempt to estimate NCP using a Eulerian seaglider technique, there is no precedence set in reducing this advection uncertainty. The NCP data appears to indicate that productivity east of the shelf break front is highly homogenous. If water advected from the east had a different oxygen concentration to the water displaced, a gradient would be observed across the shelf region, as the oxygen signal from advected water is mixed into the residential shelf water. No such gradient is observed in oxygen anomalies (figure 4.15), although anomalies caused by phytoplankton blooms are highlighted as strong positive anomalies. This suggests that phytoplankton bloom dynamics are the first order control on watercolumn oxygen inventories, and are sufficiently strong to mask any signal from the advection of water with differing biogeochemical properties.

Chapter 5 An overview of summer 2010 and final conclusions



6.1 Overview of summer 2010

Summer 2010 saw two major upwelling events occurring between YD 165 to 175/ T4-6 and YD 216/ T15 onwards (figure 6.1 B, table 4.1). This is shown by the presence of near surface colder water, caused by the advection of ENACWP towards the surface (figure 6.1 B). The biological effects of these upwelling events can be identified by rapidly increasing chl a and oxygen concentrations observed by both the Seaglider (YD 165-207 and 216 onwards- panel D and E, figure 5.14), and MODIS chl a for the transect region (panel G, figure 5.14.) Both upwelling events were preceded by an intensification of wind speed over the transect region, between YD 165 to 175/ T4-6 and 208/ T15 onwards (table 4.1).

Previous estimates suggest that the upwelling system responds within 1-2 days to a change in wind forcings (MacAyeal 1994). Seaglider observations confirm this fast response, where a change to along-shore wind stresses led to shoaling of isopycnals (within one day), and an upwelling of colder (than the surface) deep water at YD 166 and YD 209 (figure 6.1, B). In addition to upwelling, mixed layer depths, also increased during these wind intensification events, with the deepest MLD's occurring during both the fastest wind speeds and strongest phytoplankton blooms between YD 166-175 and YD 216 onwards (figure 5.14 C & 6.1 B). The correlation between Seaglider physical observations and MODIS/ ERA interim data are discussed in more detail in section 4.2-4.4.

The first 15 days of the Seaglider transect (YD151 -165) saw a strongly stratified watercolumn (seen in both temperature and salinity- panels B and C, figure 6.1), with a shallow mixed layer depth (<20 m), light westerly winds (<9 ms⁻¹) and warmer temperatures (17 °C) observed in the upper 20 m of the watercolumn. The high stability of the watercolumn was also indicated by the formation of a fresher water cap, seen from YD 153 to 156 extending from the surface to 8 m. The origin of this fresher water cap has been previously been assigned to low density riverine outflow from the Rias along the Galician coastline, and is associated with a stable, stratified watercolumn (Barton et al. 2001). The stratified watercolumn results in very low chl a concentrations observed in both Seaglider and MODIS products (figure 6.1, Panels G and E). Additionally, high CDOM concentrations may indicate that this water has remained on shelf for a substantial period of time and contains little 'fresh' ENACWP (section 4.3). Between YD 160 -168 of the Seaglider transect

Estimating productivity using a watercolumn inventory technique

shows net heterotrophy (figure 5.14 C), and a -1 to -4 % oxygen undersaturation within the mixed layer (figure 5.4 C). During this time period, there was a net air to sea flux via both $F_g(O_2)$ and $F_{bub}(O_2)$ (figure 5.13). The heating of the near surface watercolumn would act to increase the relative O_2 saturation of this water, and result in some of the oxygen undersaturation observed.

NCP between YD 169 and 179/ T5-8 was strongly autotrophic. This change in NCP regime was initiated by the first upwelling event between YD 165 and 170, and the resulting phytoplankton bloom (figure 6.1). The delay between the onset of the intensified wind, upwelling and subsequent net autotrophy was four days. Directly following this bloom event, there was a substantial reduction in chl a, and indication of particulate export and remineralisation in the aphotic zone (section 4.6). This post bloom period also saw the net heterotrophy. A second, smaller upwelling event occurred during YD 191/ T11. However, the resulting bloom (in terms of chl a concentrations, and NCP values) was substantially smaller than the first bloom event, and the watercolumn returned to near metabolic balance between YD 195-208/ T12-15.

The final upwelling event was the largest observed during summer 2010.

1. A second, smaller upwelling event occurred between YD 199 to 202. Again, this resulted in net autotrophy four days later, between YD 203 to 206.
2. The second large bloom occurred from 212 onwards, six days after the initiation of the upwelling.
3. All periods with the exception YD 160 -168 and 209 and 214, see a net loss of oxygen from the supersaturated upper ocean to the atmosphere- with the height of oxygen production occurring on YD 170, 6 days after peak wind speed, featuring with NCP values up to $132 \text{ mmol m}^{-2} \text{ day}^{-1} O_2$ (figure 5.7).
4. Of the two upwelling/bloom events, the first period (YD 169 to 191) yielded higher primary productivity than the second period (YD 215).

Previous NCP observations and P_p estimates

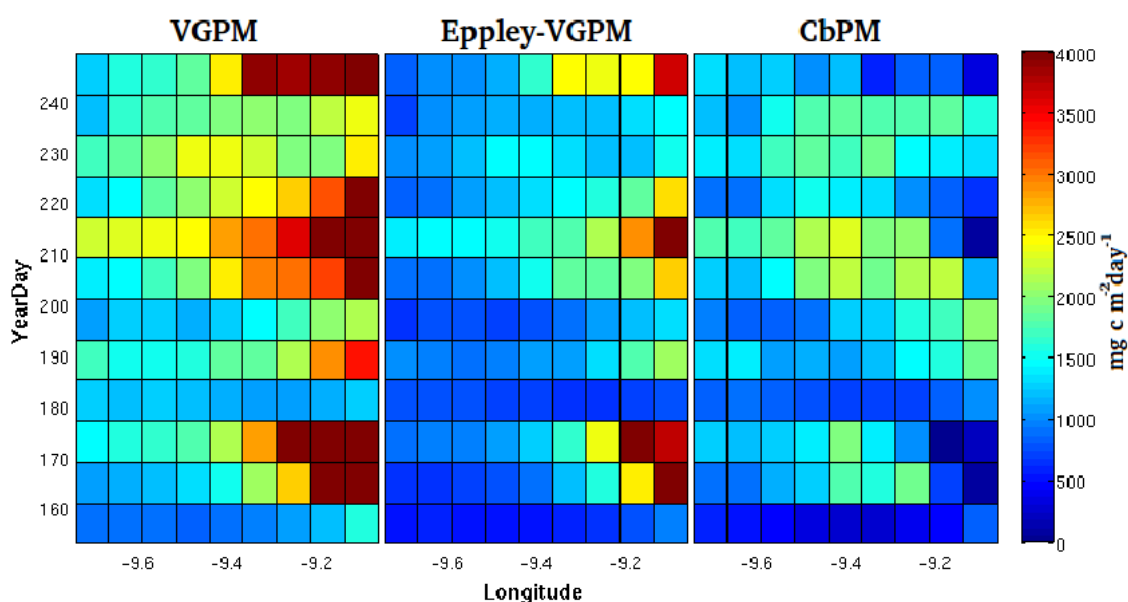
Two studies in adjoining regions estimate NCP at $81.25 \text{ mmol m}^{-2} \text{ d}^{-1} O_2$ in the Mauritanian upwelling, and $32 \text{ mmol m}^{-2} \text{ d}^{-1} O_2$ at 42° N , but in an open ocean setting (Serret et al. 2009,

Estimating productivity using a watercolumn inventory technique

Maixandeu et al. 2004). A comparable study was completed by Serret in 1999, on three sites in the southern Bay of Biscay, sampling the near shore, shelf edge and open ocean. For the nearshore sample site spring-bloom NCP was measured at $220 \text{ mmol O}_2 \text{ day}^{-1}$, decreasing through the summer as the region became a net oxygen sink from the atmosphere of $-89 \text{ mmol m}^{-2} \text{ d}^{-1} \text{ O}_2$. Our estimates for both seasonal averages and minimum and maximum NCP estimates fall within these ranges.

One source of primary productivity (N_p) data is NASA/ University of Oregon's vertically generalized productivity model (VGPM). This model uses SST and ocean-color data from MODIS to estimate N_p (figure 5.16). The removal of the DCM and mixing of phytoplankton through the surface waters for both upwelling events coincided with the peak VGPM P_p observed, but preceded peak NCP by 6 and 4 days respectively (panel C fig 3), highlighting the previously observed lag between peak P_p and peak NCP (eg Alvarez-Salgado et al. 2001.)

Water column relaxation after the first upwelling event on YD174 was mirrored by a four-fold decline in VGPM P_p from >400 to $<100 \text{ mg C m}^{-2} \text{ day}^{-1}$ over eight days (panel C, fig 6.1), and lower surface- 10m oxygen and chlorophyll a concentrations (panels D and E, fig.6.1). This relaxation was also observed in the shallowing of the MLD and rapid re-stratification of the top 20m (panel c, fig.2). However, NCP remained strongly autotrophic for this period (panel a, fig 6.1), with a NCP peak from YD172 to 178.



Water column spatial patchiness

The patchiness of the water-column can be seen at YD 166, where a change to along-shore wind stresses led to an almost immediate shoaling of isopycnals. However, the highest watercolumn NCP, lowest sea surface temperatures, and the smallest density variations between 0m-100m depths were observed at YD171, at a point where the initial shoaling isopycnal structure of the watercolumn was rapidly homogenised by a deepening MLD. This two step process of initial shoaling followed by MLD homogenisation is seen in the second upwelling, with shoaling isopycnals occurring at YD203, and water-column homogenisation 6 days later corresponding with a larger NCP and P_p peak. The difference between the first stage shoaling watercolumn and the second stage mixed watercolumn in terms of P_p is substantial at 56% increased production. Qualitatively mirroring P_p , chl a measurements also show initial increase during isopycnal shoaling, followed by a strong bloom during the later MLD homogenised watercolumn stage (figure 5.14, YD171 and 208).

A smaller upwelling period occurred at YD 188- 192, observable in increased NCP and sea surface temperatures. However, although step one, the shoaling of isopycnals occurred, the upwelling did not persist long enough to allow for MLD homogenisation of the upper watercolumn, with the result that NCP and P_p failed to match either of the other two larger upwelling events.

A ML shallowing event, initiated by a 90° change in wind direction occurred during YD172. This event resulted in the rapid re-stratification of the water-column, and effectively started the demise of the first bloom, with this re-stratification corresponding with a large decrease in P_p (fig 6.1). NCP remained autotrophic for a further 8 days post event, before becoming heterotrophic at YD180. Peak chl a and oxygen levels between YD172 and 180 can also be seen retreating to deeper depths, suggesting the rapid depletion of nutrients in the near surface watercolumn.

6.2 Context

Estimating productivity using a watercolumn inventory technique

The Seaglider provides a useful alternative to traditional (research vessel based) biogeochemical sampling campaigns. Over 500,000 individual point measurements of temperature, salinity, pressure, oxygen, chl a, backscatter and CDOM were made over summer 2012, at a total cost of less than £25,000 (excluding the initial purchase price of the Seaglider). Although not experienced during this mission, the Seaglider is able to work in inhospitable conditions that prevent research vessel based studies being completed, providing an option to sample remote and/or hostile regions of the world's oceans at reasonable cost (Eriksen et al. 2001). Is the Seaglider a replacement for these traditional methods? Although on first appearances, the Seaglider appears to solve many of the problems with ship based oceanography sampling, namely the expense and endurance issues, the platform is not a direct replacement, nor, in current configuration, ever can be in. Collected data is in the form of a series of v-shaped dives, at spatiality unequal sampling rates. This poses problems when interpolating the data, and requires more complex gridding techniques than a comparable CTD transect with equal spatial sampling (chapter 2). The instrument package fitted to the Seaglider is a compromise between size, power consumption, reliability and accuracy. The instruments are relatively new and untested, and data have required extensive post processing (calibration and lag correction) to use the data for scientific analysis. Even when processed, the data from these instruments is not as accurate as traditional methods (such as Winkler titrations) used on a research ship (Martini et al. 2007).

It is perhaps incorrect to compare the data product from the Seaglider with research vessels; the Seaglider provides a subtly different type of data set. Essentially, Seagliders trade precision and accuracy for temporal resolution when compared to data borne of research vessels. Due to the endurance of the Seaglider, unique features of the watercolumn can be tracked continuously as they evolve over a season. For example, on this mission the development of upwelling was tracked through temperature and salinity data, and it's delayed effects on the phytoplankton bloom dynamics was seen in chl a and oxygen, and eventually backscatter in the aphotic zone. The development of upwelling, the phytoplankton bloom and particulate export occurred over a period of a couple of weeks (chapter 4). This progression of biogeochemical processes within the watercolumn may be missed in a typical cruise transect, as this data provides a 'snapshot' of the watercolumn at a single point in time. This snapshot is at a higher level of accuracy and precision than a Seaglider transect, however it provides no information on the watercolumn dynamics immediately before and after the sampling. Although this can be solved by repeat cruise transects, money and time restraints often preclude this.

Estimating productivity using a watercolumn inventory technique

Other sampling techniques, such as mooring and Argos floats can match the endurance of the Seaglider. Moorings have been used to good effect in the region before, and are useful for observing the progression of watercolumn processes (Torres & Barton 2007). However, these moorings are vulnerable to collision with the considerable shipping activity using the Port of Vigo (Lopes et al. 2013). Moorings can also be targeted by thieves, as was unfortunately demonstrated by a mooring deployed by Des Barton east of the Seaglider transect over summer 2010, which was extensively damaged by the theft of its solar panels. The Seaglider is not immune to either theft, or collision with shipping, however the relatively short amount of time it spends on the surface considerably reduces this risk.

Argos floats are considerably cheaper than gliders, at £15,000-20,000 (Graver 2005), and can carry similar sensor packages as gliders (Emerson et al. 2008; Alkire et al. 2011). The choice between using Seaglider and Argo floats is essentially a choice between Lagrangian and Eulerian sampling techniques. In a subtropical gyre system, an Argo float based Lagrangian study has been shown to be possible, as the horizontal advection of the watercolumn is minimal and can be discounted (Riser & Johnson 2008b). However, our Seaglider observations of the Iberian upwelling system have indicated that in addition to the southerly Portugal current, there is a westward advection of water within the Ekman layer, an eastward movement of water on-shelf at depth during upwelling, and a northwards countercurrent transporting Mediterranean outflow water polewards. To deploy a profiling argo float within this system would not constitute a true Lagrangian study, as the horizontal advection of the Argo float will result from a component of all of these currents.

The Iberian upwelling system is a comparatively productive region in the context of the greater North Atlantic (Cermeño et al. 2006; Relvas et al. 2007; Torres & Barton 2007). However, regions of high productivity do not necessarily result in strongly autotrophic NCP, as POC transported into the region from terrestrial or fluvial sources can result in very high levels of respiration, often outstripping the high levels of NPP found in these regions (Smith & Hollibaugh 1993). Deriving a net metabolic balance for a region that is famed for its high variability is challenging. Many previous attempts at calculating NCP using the watercolumn oxygen inventory technique have been in regions with limited horizontal advection, such as within the cores of subtropical gyres (Nicholson et al. 2008). In-vitro techniques to calculate NCP are difficult to apply in the Iberian upwelling system, as phytoplankton blooms (as identified using chl a and total oxygen concentration as a proxy- chapter 4) are very patchy. Therefore, in-vitro derived estimates of NCP are likely to be highly influenced by the bloom

Estimating productivity using a watercolumn inventory technique

dynamics of the sample region, the community structure, the depth of the water sample, and the physics of the watercolumn at the time of sampling. This does not preclude the use of in-vitro sampling of the watercolumn to estimate NCP, and studies have been completed using this technique in the Ria de Vigo. However, to measure the net metabolism of the Iberian upwelling system over the course of an entire summer season requires a huge number of incubations, taken at considerable expense in terms of time and cost. For this reason, developing a technique to measure NCP using a Seaglider appears to have merit.

One of the unique features of the Seaglider dataset is the capability to have multiple biogeochemical and physical measurements made at the same point within the watercolumn. This enables oxygen, T, S and optical output to be compared directly with one-another, and derived ratio products calculated, such as the oxygen anomalies and backscatter products in chapter 4.

6.3 Future research

One of the major processes in the region is the horizontal advection of water, whether through Ekman transport, or as part of the greater Portugal current (Relvas et al. 2007). We have observed this through the variations in T and S, and noted the subtle difference in the water advected onto the continental shelf, and the water advected offshelf, and the effect this has on phytoplankton blooms dynamics observed in the two areas. Tracking the advection of water via satellite is difficult, due to the imperfect relationship between SST and the lower watercolumn caused by solar heating and mixing (chapter 4). Therefore, direct measurements of current velocities would improve this study. By siting two sea floor mounted ADCPs (one on the shelf break, and the other mid shelf), current velocities in the offshelf and on shelf regions could be used to calculate the origin of the advected water. By deploying two additional Seagliders, one 0.5 degrees north of the transect region, and the other 0.5 degrees south of the region, the watercolumn properties of any advected watermasses could be ascertained, hence adding confidence to our rate of change calculations.

With respect to the Williams (2013) and Duarte (2013) paper's discussion on the variation between NCP methods, it would be useful to complete concurrent in-vitro NCP experiments, during both fully developed upwelling and relaxation, in order to compare the differences between in-vitro and the watercolumn inventory technique.

Estimating productivity using a watercolumn inventory technique

Finally, although this thesis is focused on the biogeochemical variability of the region, I have completed further work on the physical processes that can be observed within the Seaglider dataset. Glider observations of small scale (1- 10 m) T and S changes, coupled with Seaglider observations of watercolumn upwelling (calculated as the difference between the vertical velocity predicted by the Seaglider hydrodynamic model, and actual vertical velocity derived from Seaglider depth measurements, Frajka-Williams et al. 2009). appears to be useful to examine internal wave dynamics within the watercolumn ((Rudnick et al. 2013).

References

- Alkire et al., 2011. Estimates of net community production and export using high-resolution, lagrangian measurements of O₂, NO₃ and POC through the evolution of a spring bloom in the North Atlantic. *Deep Sea Research Part I: Oceanographic Research Papers*.
- Alvarez-Salgado, Miguez, B.M. & Pegrez, F.F., 2011. Net ecosystem of dissolved organic carbon in a coastal upwelling production system: of the North the Ria de Vigo , Iberian margin Atlantic. *Limnology*, 46(1), pp.135–147.
- Álvarez-Salgado, X. et al., 2001. Off-shelf fluxes of labile materials by an upwelling filament in the NW Iberian Upwelling System. *Progress in Oceanography*, 51(2), pp.321–337.
- Anthony Vodacek, Neil V. Blough, Michael D. DeGrandpre, E.T.P. and R.K.N., 1997. Seasonal Variation of CDOM and DOC in the Middle Atlantic Bight: Terrestrial Inputs and Photooxidation. *Limnology and Oceanography*, 42(4), pp.674–686.
- Bakun, A. & Nelson, C.S., 1991. The Seasonal Cycle of Wind-Stress Curl in Subtropical Eastern Boundary Current Regions. *Journal of Physical Oceanography*, 21(12), pp.1815–1834.
- Barton, E.D., 2001. Canary and portugal currents canary and portugal currents. , pp.380–389.
- Behrenfeld, M. & Falkowski, P.G., 1997. A consumer's guide to phytoplankton primary productivity models. *Limnology and Oceanography*, 42(7), pp.1479–1491.
- Behrenfeld, M.J. et al., 2006. Climate-driven trends in contemporary ocean productivity. *Nature*, 444(7120), pp.752–5.
- Bender, M. et al., 1987. A comparison of four methods for determining planktonic community production. *Limnology and Oceanography*, 32(5), pp.1085–1098. Berntsson, M. et al., 1997. Multivariate experimental methodology applied to the calibration of a Clark type oxygen sensor. *Analytica Chimica Acta*, 355(1), pp.43–53.
- Bode, A. & Varela, M., 1998. Mesoscale estimations of primary production in shelf waters: a case study in the Golfo Artabro (NW Spain). *Journal of Experimental Marine Biology and Ecology*, 229(1), pp.111–131.
- Borges, A.V. et al., 2006. Carbon dioxide in European coastal waters. *Estuarine, Coastal and Shelf Science*, 70(3), pp.375–387.
- Boyd, P. et al., 2000. A mesoscale phytoplankton bloom in the polar Southern Ocean stimulated by iron fertilization. *Nature: International Weekly Journal of Science*, 407, pp.695–702.

- De Boyer Montégut, C., 2004. Mixed layer depth over the global ocean: An examination of profile data and a profile-based climatology. *Journal of Geophysical Research*, 109(C12), p.C12003.
- Briggs, N. et al., 2011. High-resolution observations of aggregate flux during a sub-polar North Atlantic spring bloom. *Deep Sea Research Part I: Oceanographic Research Papers*, 58(10), pp.1031–1039.
- Castro, C.G., Pe, F.F. & Fraga, F., 2000. Coupling between the thermohaline , chemical and biological " elds during two contrasting upwelling events in the NW Iberian Peninsula. , 20, pp.189–210.
- Castro-Morales, K. & Kaiser, J., 2011. Using dissolved oxygen concentrations to determine mixed layer depths in the Bellingshausen Sea. *Ocean Science Discussions*, 8(3), pp.1505–1533.
- Cermeño, P. et al., 2006. Phytoplankton size structure and primary production in a highly dynamic coastal ecosystem (Ría de Vigo, NW-Spain): Seasonal and short-time scale variability. *Estuarine, Coastal and Shelf Science*, 67(1-2), pp.251–266.
- Cetinić, I. et al., 2012. Particulate organic carbon and inherent optical properties during 2008 North Atlantic Bloom Experiment. *Journal of Geophysical Research*, 117(C6), p.C06028.
- Chavez, F.P. & Messié, M., 2009. A comparison of Eastern Boundary Upwelling Ecosystems. *Progress in Oceanography*, 83(1-4), pp.80–96.
- Cullen, J.J., 1982. The Deep Chlorophyll Maximum: Comparing Vertical Profiles of Chlorophyll a. *Canadian Journal of Fisheries and Aquatic Sciences*, 39(5), pp.791–803.
- Emerson, S. et al., 1997. Experimental determination of the organic carbon flux from open-ocean surface waters. , 389(6654), pp.951–954.
- Emerson, S., Stump, C. & Nicholson, D., 2008. Net biological oxygen production in the ocean: Remote in situ measurements of O₂ and N₂ in surface waters. *Global Biogeochemical Cycles*, 22(3)
- Eppley, R.W., Holmes, R.W. & Strickland, J.D.H., 1967. Sinking rates of marine phytoplankton measured with a fluorometer. *Journal of Experimental Marine Biology and Ecology*, 1(2), pp.191–208. Available at: <http://www.sciencedirect.com/science/article/pii/0022098167900147>
- Eriksen, C.C. et al., 2001. Seaglider: a long-range autonomous underwater vehicle for oceanographic research. *IEEE Journal of Oceanic Engineering*, 26(4), pp.424–436.
- Falkowski, P., 2000. The Global Carbon Cycle: A Test of Our Knowledge of Earth as a System. *Science*, 290(5490), pp.291–296.

- Falkowski, P.G. et al., 1988. The fate of a spring phytoplankton bloom: export or oxidation? *Continental Shelf Research*, 8(5-7), pp.457–484. Available at: <http://adsabs.harvard.edu/abs/1988CSR.....8..457F> [Accessed September 20, 2013].
- Faure, V. et al., 2006. Relevance of various formulations of phytoplankton chlorophyll a:carbon ratio in a 3D marine ecosystem model. *Comptes rendus biologiques*, 329(10), pp.813–22. Available at: <http://www.ncbi.nlm.nih.gov/pubmed/17027642> [Accessed September 16, 2013].
- Feistel, R., 2010. TEOS-10: A New International Oceanographic Standard for Seawater, Ice, Fluid Water, and Humid Air. *International Journal of Thermophysics*, 33(8-9), pp.1335–1351. Available at: <http://link.springer.com/10.1007/s10765-010-0901-y> [Accessed September 11, 2013].
- Frajka-williams, E., 2009. The spring phytoplankton bloom and vertical velocities in the stratified and deep convecting Labrador Sea, as observed by Seagliders.
- Gago, J., Miguez, B.M. & Pegrez, F.F., 2011. Net ecosystem of dissolved organic carbon in a coastal upwelling production system □: of the North the Ria de Vigo , Iberian margin Atlantic. , 46(1), pp.135–147.
- Gawarkiewicz, G. & Chapman, D.C., 1992. The Role of Stratification in the Formation and Maintenance of Shelf-Break Fronts. *Journal of Physical Oceanography*, 22(7), pp.753–772. Available at: [http://journals.ametsoc.org/doi/abs/10.1175/1520-0485\(1992\)022<0753:TROSIT>2.0.CO;2](http://journals.ametsoc.org/doi/abs/10.1175/1520-0485(1992)022<0753:TROSIT>2.0.CO;2) [Accessed September 20, 2013].
- Gieskes, W.W.C., Kraay, G.W. & Baars, M.A., 1979. Current 14C methods for measuring primary production: Gross underestimates in oceanic waters. *Netherlands Journal of Sea Research*, 13(1), pp.58–78. Available at: [http://dx.doi.org/10.1016/0077-7579\(79\)90033-4](http://dx.doi.org/10.1016/0077-7579(79)90033-4) [Accessed September 10, 2013].
- Gist, N. et al., 2009. Seasonal and spatial variability in plankton production and respiration in the Subtropical Gyres of the Atlantic Ocean. *Deep Sea Research Part II: Topical Studies in Oceanography*, 56(15), pp.931–940. Available at: <http://dx.doi.org/10.1016/j.dsr2.2008.10.035> [Accessed August 30, 2013].
- Graver, J., 2005. *Underwater glider: Dynamics, control and design*. Thesis, University of Princeton.
- Hoag, K.J., 2005. Triple oxygen isotope composition of tropospheric carbon dioxide as a tracer of terrestrial gross carbon fluxes. *Geophysical Research Letters*, 32(2), p.L02802. Available at: <http://doi.wiley.com/10.1029/2004GL021011> [Accessed September 10, 2013].
- J. Arístegui, X. Álvarez-Salgado, E. Barton, F. Figueiras, S. Hernández-León, C. Roy, A.S., 2006. *Oceanography and fisheries of the Canary Current/Iberian region of the eastern North Atlantic*, Available at: http://www.iim.csic.es/~barton/Aristegui_The_Sea_2006.pdf [Accessed July 19, 2013].

- Jenkins, W.J. & Goldman, J.C., 1985. Seasonal oxygen cycling and primary production in the Sargasso Sea. *Journal of Marine Research*, 43(2), pp.465–491. Available at: <http://www.ingentaconnect.com/content/jmr/jmr/1985/00000043/00000002/art00010>
- Jiao, N. et al., 2010. Microbial production of recalcitrant dissolved organic matter: long-term carbon storage in the global ocean. *Nature reviews. Microbiology*, 8(8), pp.593–9.
- Joint, I., Rees, A.P. & Woodward, E.M.S., 2001. Primary production and nutrient assimilation in the Iberian upwelling in August 1998. *Progress in Oceanography*, 51(2-4), pp.303–320.
- Kahru, M. et al., 2009. Trends in primary production in the California Current detected with satellite data. *Journal of Geophysical Research*, 114(C2), pp.1–7.
- Kowalczyk, P. et al., 2003. Characterization of CDOM in an organic-rich river and surrounding coastal ocean in the South Atlantic Bight. *Aquatic Sciences - Research Across Boundaries*, 65(4), pp.384–401.
- Laws, E.A., 1991. Photosynthetic quotients, new production and net community production in the open ocean. *Deep Sea Research Part A. Oceanographic Research Papers*, 38(1), pp.143–167.
- Lopes, C. et al., 2013. Sustainability of port activities within the framework of the fisheries sector: Port of Vigo (NW Spain). *Ecological Indicators*, 30(null), pp.45–51.
- López-Jamar, E. et al., 1992. Upwelling and outwelling effects on the benthic regime of the continental shelf off Galicia, NW Spain. *Journal of Marine Research*, 50(3), pp.465–488.
- Lorenzo, L.M. et al., 2005. Across-shelf variability of phytoplankton composition, photosynthetic parameters and primary production in the NW Iberian upwelling system. *Journal of Marine Systems*, 54(1-4), pp.157–173.
- Lutz, V. Sathyendranath, S. Head, S., 2003. Variability in pigment composition and optical characteristics of phytoplankton in the Labrador Sea and Central North Atlantic. *Marine Ecology Progress*, 260, pp.1–18.
- Marra, J., 2009. Net and gross productivity: weighing in with ¹⁴C. *Aquatic Microbiology and Ecology*, pp.123–131.
- Martini, M., Butman, B. & Mickelson, M.J., 2007. Long-Term Performance of Aanderaa Optodes and Sea-Bird SBE-43 Dissolved-Oxygen Sensors Bottom Mounted at 32 m in Massachusetts Bay. *Journal of Atmospheric and Oceanic Technology*, 24(11), pp.1924–1935.
- Maxwell, K., 2000. Chlorophyll fluorescence--a practical guide. *Journal of Experimental Botany*, 51(345), pp.659–668. Available at: <http://jxb.oxfordjournals.org/content/51/345/659.full> [Accessed September 3, 2013].

- Morán, X.A.G., Fernández, E. & Pérez, V., 2004. Size-fractionated primary production , bacterial production and net community production in subtropical and tropical domains of the oligotrophic NE Atlantic in autumn. , 274, pp.17–29.
- Morgan-Smith, D. et al., 2013. Diversity and distribution of microbial eukaryotes in the deep tropical and subtropical North Atlantic Ocean. *Deep Sea Research Part I: Oceanographic Research Papers*, 78(null), pp.58–69.
- Mouriño-Carballido, B. & Anderson, L. a., 2009. Net community production of oxygen derived from in vitro and in situ 1-D modeling techniques in a cyclonic mesoscale eddy in the Sargasso Sea. *Biogeosciences*, 6(8), pp.1799–1810.
- Nicholson, D., Emerson, S. & Eriksen, C.C., 2008. Net community production in the deep euphotic zone of the subtropical North Pacific gyre from glider surveys. *Limnology and Oceanography*, 53(5_part_2), pp.2226–2236.
- Nightingale, P.D. et al., 2000. In situ evaluation of air-sea gas exchange parameterizations using novel conservative and volatile tracers. *Global Biogeochemical Cycles*, 14(1), pp.373–387.
- Nowald, N. et al., 2006. Distribution and transport processes of marine particulate matter off Cape Blanc (NW-Africa): results from vertical camera profiles. *Ocean Science Discussions*, 3(4), pp.903–938. Available at: <http://hal.archives-ouvertes.fr/hal-00298401> [Accessed September 25, 2013].
- Pacala, S.W. et al., 2001. Consistent land- and atmosphere-based U.S. carbon sink estimates. *Science (New York, N.Y.)*, 292(5525), pp.2316–20.
- Pai, S.-C., Gong, G.-C. & Liu, K.-K., 1993. Determination of dissolved oxygen in seawater by direct spectrophotometry of total iodine. *Marine Chemistry*, 41(4), pp.343–351.
- Peliz, Á. et al., 2002. Fronts, jets, and counter-flows in the Western Iberian upwelling system. *Journal of Marine Systems*, 35(1-2), pp.61–77.
- Peng, T.-H. et al., 1987. Seasonal variability of carbon dioxide, nutrients and oxygen in the northern North Atlantic surface water: observations and a model. *Tellus B*, 39B(5), pp.439–458.
- Le Quéré, C. et al., 2009. Trends in the sources and sinks of carbon dioxide. *Nature Geoscience*, 2(12), pp.831–836.
- Queste, B.Y. et al., 2012. Deployments in extreme conditions: Pushing the boundaries of Seaglider capabilities. In *2012 IEEE/OES Autonomous Underwater Vehicles (AUV)*. IEEE, pp. 1–7.
- Relvas, P., 2002. Mesoscale patterns in the Cape São Vicente (Iberian Peninsula) upwelling region. *Journal of Geophysical Research*, 107(C10), p.3164.
- Relvas, P. et al., 2007. Physical oceanography of the western Iberia ecosystem: Latest views and challenges. *Progress in Oceanography*, 74(2-3), pp.149–173.

- Reuer, M.K. et al., 2007. New estimates of Southern Ocean biological production rates from O₂/Ar ratios and the triple isotope composition of O₂. *Deep Sea Research Part I: Oceanographic Research Papers*, 54(6), pp.951–974.
- Riser, S.C. & Johnson, K.S., 2008a. Net production of oxygen in the subtropical ocean. *Nature*, 451(7176), pp.323–5.
- Riser, S.C. & Johnson, K.S., 2008b. Net production of oxygen in the subtropical ocean. *Nature*, 451(7176), pp.323–5.
- Robinson, C. et al., 2002. Plankton respiration in the Eastern Atlantic Ocean. *Deep Sea Research Part I: Oceanographic Research Papers*, 49(5), pp.787–813.
- Rudnick, D.L., Johnston, T.M.S. & Sherman, J.T., 2013. High-frequency internal waves near the Luzon Strait observed by underwater gliders. *Journal of Geophysical Research: Oceans*, 118(2), pp.774–784.
- Sarmiento, Jorge L. Gruber, N., 2006. *Ocean biogeochemical dynamics*. Princeton University Press.,
- Sarnthein, M. et al., 1988. Global variations of surface ocean productivity in low and mid latitudes: Influence on CO₂ reservoirs of the deep ocean and atmosphere during the last 21,000 years. *Paleoceanography*, 3(3), pp.361–399.
- Serret, P. et al., 2009. Predicting plankton net community production in the Atlantic Ocean. *Deep Sea Research Part II: Topical Studies in Oceanography*, 56(15), pp.941–953.
- Serret, P. & Robinson, C., 2001. Latitudinal variation of the balance between plankton photosynthesis and respiration in the E Atlantic Ocean. *Limnology and oceanography*, 46(7).
- Smith, S. V. & Hollibaugh, J.T., 1993. Coastal metabolism and the oceanic organic carbon balance. *Reviews of Geophysics*, 31(1), p.75. Available at: <http://doi.wiley.com/10.1029/92RG02584> [Accessed September 10, 2013].
- Stanley, R.H.R. et al., 2010. Net community production and gross primary production rates in the western equatorial Pacific. *Global Biogeochemical Cycles*, 24(4), p.n/a–n/a. Available at: <http://doi.wiley.com/10.1029/2009GB003651> [Accessed May 23, 2013].
- Stanley, R.H.R. et al., 2009. Noble gas constraints on air-sea gas exchange and bubble fluxes. *Journal of Geophysical Research*, 114(C11), p.C11020.
- Stommel, H., 1989. The Slocum mission. *Oceanography*, 2.1, pp.22–25.
- Takahashi, T. et al., 2002. Global sea–air CO₂ flux based on climatological surface ocean pCO₂, and seasonal biological and temperature effects. *Deep Sea Research Part II: Topical Studies in Oceanography*, 49(9-10), pp.1601–1622.
- Tengberg, A. et al., 2006. OCEANOGRAPHY: METHODS Evaluation of a lifetime-based optode to measure oxygen in aquatic systems. *East*, (1964), pp.7–17.

References and appendix

- Tilstone, G. et al., 1999. Significance of nanophytoplankton photosynthesis and primary production in a coastal upwelling system (Ría de Vigo, NW Spain). *Marine Ecology Progress Series*, 183, pp.13–27.
- Torres, R. & Barton, E.D., 2007. Onset of the Iberian upwelling along the Galician coast. *Continental Shelf Research*, 27(13), pp.1759–1778.
- Vilas, F., Bernabeu, A.M. & Méndez, G., 2005. Sediment distribution pattern in the Rias Baixas (NW Spain): main facies and hydrodynamic dependence. *Journal of Marine Systems*, 54(1-4), pp.261–276.
- Van Weering, T.C.. et al., 2002. Recent sediment transport and accumulation on the NW Iberian margin. *Progress in Oceanography*, 52(2), pp.349–371.
- Williams, P.J. le B. et al., 2013. The Oligotrophic Ocean Is Autotrophic*. Available at: <http://www.annualreviews.org/doi/abs/10.1146/annurev-marine-121211-172335>

Assessing the performance of Argos tags using an autonomous underwater glider.

Abstract

Technological advancements have broadened the scope of animal tracking tags from purely zoological research towards oceanography data collection. The quality of this data is difficult to quantify, due to the inherent lack of calibration opportunities available. Here, we demonstrate a calibration solution, using four autonomous underwater vehicles (iRobot Seagliders) as a test bed for the assessment of these tags under conditions that approximate their usual operating environment.

The general reliability of the tags (Wildlife computers Spot-5 Argos tag) was found to be faultless, with no degradation of tag functionality over the course of the missions. An inter-comparison between tag and Seagliders data showed that temperature and surfacing statistics closely matched, with the tags identifying every Seaglider surfacing, and producing time-at-temperature statistics within 0.5 °C of Seaglider CTD data. The Geolocation functioning of the tags varied, with the elliptical error definitions accurate within specification. Isotropic tag geolocation accuracy were worse than the manufacturer specifications, at approximately double CLS ARGOS location class (LC) estimates. Average 63th percentile isotropic errors for this study: LC-3 950 m, LC-2 1128 m, LC1 1845 m, LC-0 4.3 Km, LC-A 4.8 km and LC-B 10.6km. The geolocation accuracy of the tags was adversely affected by movement. Transporting an activated tag at a constant velocity of 5.1 m s⁻¹ resulted in a halving of geolocation accuracy (2263 m average for LC-1,2 & 3) when compared to stationary geolocation accuracy (853 m average for LC-1,2 & 3).

Introduction

Small, disposable, animal-tracking tags have been extensively used in both marine biology, zoology and physical oceanography, providing insight into a wide range of research topics from the migration patterns of large marine mammals to collecting temperature and salinity profiles of ice covered oceans. As the use of such technology increases, so does the requirement to find a suitable method of assessing the reliability, and long-term stability of the data from these tags. Tracking large marine animals from surface observations is difficult and often inaccurate, due to their mobility and amount of time spent underwater. This aspect of monitoring has been revolutionised with the development of compact, geolocating tags, such as the Wildlife Computers Spot-5 tag [Hammerschlag *et al.*, 2011]. As electronic engineering and the miniaturisation of sensors has progressed, the basic geolocating function of the tags has been augmented with other functions useful to animal monitoring or physical oceanography, such as the measurements of temperature, pressure, salinity or light levels [Costa *et al.*, 2008; Hooker and Boyd, 2003]. The Spot-5 tag by Wildlife Computers is such an example of an augmented tag, with the tag able to provide geolocations, haul-out (time spent above water), and water temperature statistics. Designing a tag to be attached to a marine animal results in many engineering compromises. The tag must be as small and unobtrusive to the lifestyle of the host organism as possible, yet also combine aspects such as long battery life, robustness and water resistance. The result of this miniaturisation is the use of sensors that have not had the decades of incremental improvements that the CTD (conductivity, temperature, depth) packages typically used in physical oceanography have undergone, reducing confidence in tag collected data.

In-situ assessment of marine wildlife tags is challenging, as it is impractical to fit additional redundant instrumentation (with the purpose to provide calibration data) on tracked animals. The reliability of the tag is also difficult to gauge, as the tags are prone to fail off, or be lost with the death of the tagged organism. To date, only inter-comparisons between Argos

and GPS geolocation have been completed, with no available literature on the *in-situ* performance of tag haul-out and temperature statistics. To test the *in-situ* performance of all functions on the Spot-5 tag, we attached tags to four iRobot Seagliders, deployed in the Indian Ocean and Weddell Sea during early 2012 (figure 1). The Seaglider is a high endurance, buoyancy driven autonomous underwater vehicle, profiling in a sawtooth trajectory to a maximum depth of 1000 m for missions that can extend to many months in duration [figure 1 b, *Eriksen et al.*, 2001]. With user specifiable instrumentation, the four Seagliders used for this study were fitted with a CTD and GPS receiver. Typically programmed to surface at the end of each dive, the Seaglider remains buoyant, until two GPS coordinates and an iridium satellite data upload are completed, a process that can take from 5 minutes to a few hours depending on the volume of data transmitted and quality of connection (*Eriksen et al.*, 2001). Here, we compare the *in-situ* performance of Spot-5 tags against the GPS geolocation recorded by Seagliders (Seagliders 546, 539 and 522), and the Indian Ocean (Seaglider 537. Figure 1 a). The tags on Seagliders 522 and 539 were also programmed to collect haulout and temperature statistics, which was compared with the *in-situ* data collected by the Seagliders CTD.

2. Methods

2.1. Wildlife Computers Spot-5 tag

The Spot-5 tag was affixed midway along the upward facing aerial shaft of the Seaglider (figure 1 b). After each Seaglider dive, the Seaglider breaches the water's surface, and manoeuvres so it's aerial (and attached tag) are above the water's surface and able to commence communication. The tag was set to collect data and attempt to broadcast data at every available opportunity, 24 hours a day. Tag data including Argos geolocations and timestamps, haul-out statistics and temperature statistics were initially processed using Wildlife Computers data analysis program (WC-DAP3), then analysed and compared against the Seaglider dataset using Matlab. The tag itself was not subject to any further post

manufacturer calibration, as typical in other tag deployments [*Hammerschlag et al.*, 2011; *Hooker and Boyd*, 2003]. Geolocations were processed at CLS ARGOS using the latest Kalman filtering method, a technique that removes erroneous geolocations according to estimates of average velocities observed by the tag between previous geolocations [*Know*, 2012]. The limited bandwidth available through the Argos system is a major restriction on tag data transmission. Hence, discrete tag measurements of the watercolumn temperature and times of haul-out are binned internally within the tag, with the resulting (smaller file-sized) data transmitted via Argos [*Un*, 2011]. Haul-out is measured as a percentage of each hour that the tag was out of the water. Temperature data transmitted are the percentage of each 6-hours that the tag measured temperatures in twelve temperature bins [*Un*, 2011]. To compare the haul-out statistics and temperature statistics from the Argos tag against the Seaglider, we binned the Seagliders surfacing and temperature measurements into the same structure as used by the Spot-5 tag, allowing direct comparison between the two datasets.

CLS ARGOS provides each Argos geolocation with two error definitions. The first is an isotropic definition, providing a circular radius around the geolocation within which there is a 63% likelihood of the actual geolocation of the tag. The second, less commonly used error defines an ellipse, within which there is again a 63% likelihood of the tag being (figure 3 c, [*Know*, 2012]). Using the Seaglider GPS geolocation as the central point of this geolocation error radius, the Argos tag geolocation can be assessed to be contained within the bounds or lie outside the error radii (figure 3 c).

To assess the effects motion have on the geolocation accuracy of the Argos tag, one tag was set to transmit during a transit of the RRS James Clark Ross (JCR) from the Falkland Islands to South Georgia (Figure 1). Here, the Seaglider aerial and tag assembly was attached to the upper deck of the ship, and the tag activated. The ship cruised directly from Port Stanley, Falkland Islands to Bird Island, South Georgia at 11 knots (5.1 m s^{-1}), before remaining at anchor for a further couple of days. During the transit and stationary period, geolocations from the tag were compared against GPS based location from the ships navigational system.

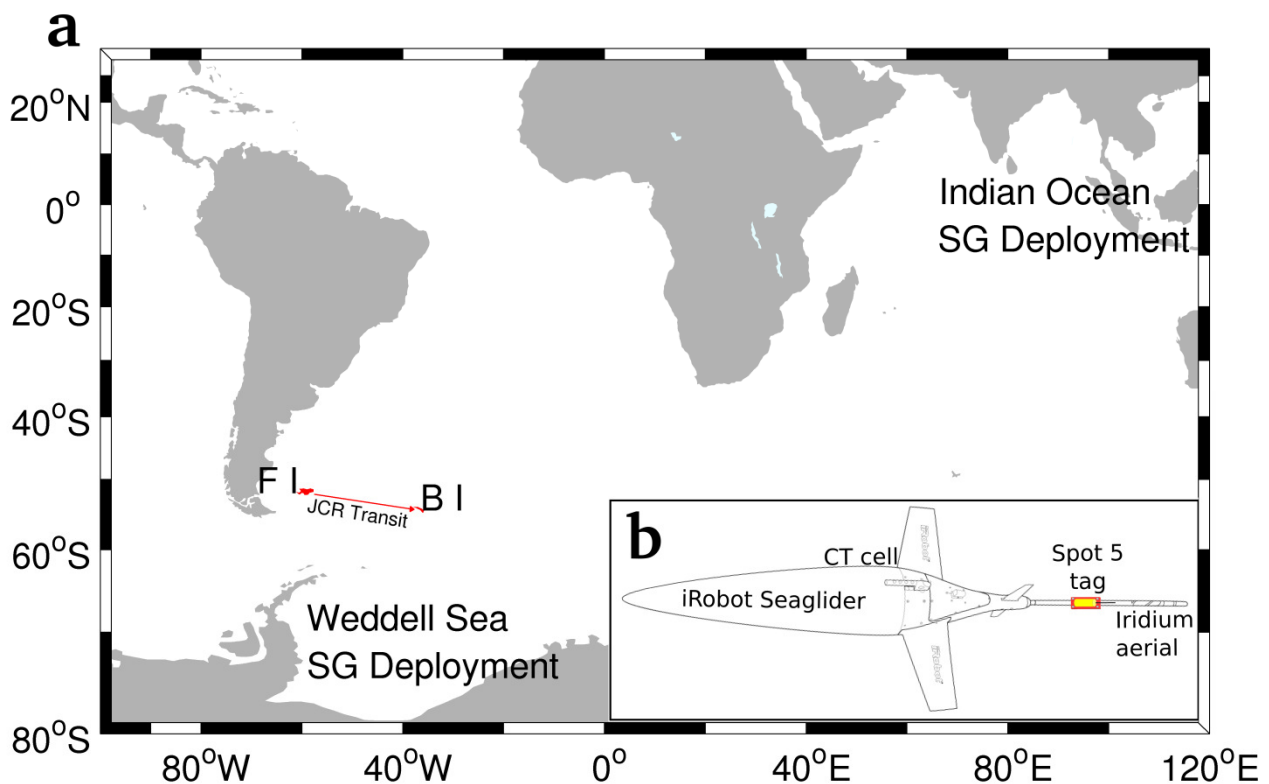


Figure 1

- a. The location of the four Seaglider based Spot-5 Argos tag deployments, and the Jame Clark Ross transit.**
b. The mounting position of the Wildlife computers Spot5 tag on the iRobot seaglider.

2.2. iRobot Seaglider

The CTD on the Seaglider was calibrated by Sea-bird/ Paine Electronics pre mission, and periodically checked and confirmed for correct readings *in-situ* during the mission using bottle sample calibrated CTD/ rosette data and GPS coordinates from the deployment ships (RRS James Clark Ross for Weddell Sea deployments, RV Roger Revelle for the Indian Ocean deployment) at any time the Seaglider was in close proximity to the ship. Unlike the

Spot-5 tag, the Seaglider has a high-speed Iridium data transfer system [Eriksen *et al.*, 2001], allowing all temperature measurements and timestamps to be transmitted. With user definable sampling frequency, the Seagliders were programmed to sample depth and time measurement every 4-12 seconds for the missions.

We binned the Seaglider temperature data using the same bin definitions as the Spot-5 tag bins to aid inter-comparison. Haul-out statistics were assessed as being the time the Seaglider spent on the surface transmitting data with the aerial above the water's surface, and hence 'dry' (fig 1, positions A and B). The Seaglider attempts to gain a GPS coordinate at the start and end of each of these transmission surfacings. After the second GPS coordinate is received, the Seaglider starts its next dive. Hence, we use the time between these two GPS geolocations to define the periods during which the aerial (along with the Spot-5) is 'dry' and above the water.

The surface drift experienced by the Seaglider between surfacing and diving again (i.e. the distance travelled between the first and second Seaglider GPS fixes) was approximated to a linear path. We interpolate between these start and end geolocations to provide an estimate of the Seaglider's position-at-time between the GPS fixes, and it is this interpolated field that is compared with the Argos tag geolocation. To calculate the Argos tag error distance, the distance between the coordinates from the Argos tag and the temporally matching interpolated Seaglider coordinates are processed using Vincenty's inverse geodesics formula (Vincenty 1975).

3 Results & Discussion

3.1. Geolocation and locational errors

The Argos system, through the use of the Doppler shift, is able to locate a tag anywhere on Earth's surface [Lopez and Malarde 2011]. The tag transmits at a fixed

frequency (f_{tag}) between 401.620 to 401.680 MHz, with the precise transmission frequency registered with CLS Argos upon tag activation. This transmission is received by the polar-orbiting satellites of the NOAA and EUMETSTAT Argos missions at frequency $f_{received}$ (Lopez and Marlarde 2011). The change in frequency (Doppler shift) between the transmission and the received messages is a function of the velocity of the satellite (V_{sat}), tag (V_{tag}), and the location and pathway of the satellite (S) and tag (B) with respect to the earth's surface. As the Doppler shift on tag frequency is a 2D problem (with both longitudinal and latitudinal components), the unitary vector between transmission from the tag to the satellite (S-B) and the Euclidean norm of this vector ($\|S-B\|$) needs to be considered, with this represented as term u in the equation below [Lopez and Lalarde 2011]. As neither the frequency of the tag transmission, or the timing and location accuracy of the satellite are perfect, a term (v) is needed to account for random noise, with this error featuring a mean of zero, and a normal Gaussian distribution. Considering all of the above, the Doppler shift relationship writes as:

$$f_{received} = \left(1 - \frac{(V_{sat} V_{tag}) \cdot u}{c}\right) f_{transmitted} \quad \text{where} \quad u = \frac{\|S - B\|}{\|S - B\|}$$

and

$$f_{received} = h(f_{transmitted}, B, S, V_{tag}, V_{sat}) + v$$

Where c is the speed of light, and with the assumption that $V_{sat} \gg V_{tag}$, allowing V_{tag} to be neglected in CLS ARGOS's computations [Lopez and Marlarde 2011].

Using this relationship, estimates of B can be completed by recording the frequency of two or more received transmissions ($f_{received}$), and triangulating the position B based on satellite ephemeris and tag transmission frequency [Lopez and Marlarde 2011]. This triangulation technique results in two estimates of B, the correct geolocation, and a mirror image geolocation on the opposite side of the satellite track. Choosing between the two geolocations is completed at CLS ARGOS using either a least-square or Kalman filtering technique, with

both techniques designed to find the most likely geolocation using information from previous geolocations and velocities data [Lopez and Marlarde 2011]. We elected to use the Kalman filter processing technique for all data, as the technique has been shown to be superior to the least squares method at identifying the correct geolocation processing [Lopez and Marlarde 2011].

The CLS ARGOS service provided us with Kalman filtered geolocations and isotropic (circular) and elliptical error definitions for each of the geolocations (figure 3 c). Argos tag's actual geolocation should fall inside the boundaries of the isotropic and elliptical areas for approximately 63 % of all Argos derived geolocations [Yann Bernard CLS Argos, personal communication]. We find that of the two error definitions, the elliptical definition is most accurate at constraining the true geolocation of the tag, with 59% and 64% of geolocation accurate (and thus falling within the error boundaries) for the Indian Ocean and Weddell Sea. The isotropic error definition performs less well, constraining the error only 46% and 39% for the Indian Ocean and Weddell Sea respectively. This difference is not attributable to a difference in area covered by the two error definitions (fig 3 c), with the mission average difference between areas covered by the isotropic and elliptical error definitions within 4 % for SG522, 537 and 539. There was no degradation of geolocation accuracy with time, highlighting that the tag transmission frequency ($f_{\text{transmitted}}$) remained stable during the missions as this is the only component in geolocation that relates exclusively to the tag.

Comparing our results for the isotropic error definition with other geolocation accuracy studies, all studies except Vincent et al., (2002) found that the CLS location class error bands underestimate the true error radius. The average errors from this study indicated that observed error is approximately double for each of the error classes (Table 2) at LC-3 950 m, LC-2 1128 m, LC1 1845 m, LC-0 4300 m versus CLS estimates of LC-3 <250 m, LC-2 <500 m, LC-1 500-1500 m, LC-0 >1500 m. The most accurate Argos tag geolocations came from the tag aboard the RRS James Clark Ross, whilst the ship was stationary and at anchor in Bird Island ($V_{\text{tag}} = 0 \text{ m s}^{-1}$), South Georgia (table 2). Seaglider mounted tag geolocations were slightly less accurate, possibly in part due to the oversimplification of

Seaglider drift as a linear path between the first and second GPS coordinates. (However, surface drift velocities from the Seaglider were small with V_{tag} typically less than 0.2 m s^{-1} , and with no intermediary GPS coordinates it would be capricious to make any other prediction of drift pathway). The largest geolocation errors came from the tag mounted to the RRS JCR during the Stanley- Bird Island transit (table 2). The GPS location of the ship was known at all times during this transit, so the error in geolocation is entirely due to Argos geolocation error. The error is also not due to tag malfunctioning, as proven by the accuracy of the geolocations made whilst the ship was stationary where the same tag was used. The ship steamed in a straight line from Stanley to Bird Island (an easterly bearing, figure 1) at 11 knots ($V_{tag} = 5.1 \text{ m s}^{-1}$).

Table 2

Argos tag geolocation errors from GPS coordinates for our data (Indian Ocean and Weddell Sea) and 8 comparable studies for the 5 different grades of location class (LC). All errors at the 63th percentile, except Soutullo et al., 2008 which is the median error, as 63th percentile errors were unavailable for all LC's. CLS claimed accuracy uses error definition 1, a circular error radius as depicted in figure 3.

Study	LC-3	LC-2	LC-1	LC-0	LC-A	LC-B
CLS location class accuracy	<250 m	250 m- 500 m	500m- 1500m	>1500m	Not quoted	Not quoted
Indian Ocean SG (this study)	453 m	989 m	1780 m	4300 m	6700 m	12900 m
Weddell SG (this study)	430 m	1021 m	1670 m	4100 m	7200 m	11500 m
Weddell Ship (this study)	2469 m	1735 m	2586 m	5247 m	3519 m	14771 m
Bird Island Ship (this study)	449 m	765 m	1344 m	3778 m	1784 m	3215 m
Costa et al., 2010	490 m	1010 m	1200 m	4180 m	6190 m	10280 m
Keating et al.,1991	361 m	903 m	1188 m	N/A	N/A	N/A
Vincent et al., 2002	226 m	372 m	757 m	N/A	N/A	N/A
White and Sjoberg., 2002	N/A	1022 m	2238 m	3792 m	N/A	N/A
McKeown and Westcott 2012	1001 m	847 m	1950 m	2467 m	1722 m	13120 m
Soutullo et al., 2008	300 m	1300 m	900 m	7400 m	12700 m	35000 m
Dubin et al., 2009	500 m	700 m	1500 m	4600 m	2100 m	18300 m
Witt and Hawkes., 2008	400 m	700 m	800 m	2300 m	1400 m	18000 m
Average (this study)	950 m	1128 m	1845 m	4356 m	4801 m	10597 m

Analysis of all geolocation data shows that the errors were not randomly distributed, instead having a larger longitudinal than latitudinal error component (figure 3 a). There was an equal east- west distribution in the error data, except for $V_{tag} = 5.1 \text{ m s}^{-1}$ tag data, where most of the errors were offset towards the west, or opposite the direction of travel (figure 3 b). There was an average difference of 1425 m between $V_{tag} = 0 \text{ m s}^{-1}$ and 5.1 m s^{-1} for LC3, 2 and 1 (table 2). All CLS Argos geolocations are given a single timestamp that falls within the range between the timestamp of the first received transmission ($t_{received}$) and the last received transmission, a difference of 0 - 420 seconds for the RRS JCR deployed tag, suggesting that the decreased accuracy of geolocations are of a similar magnitude to the distance travelled by the RRS JCR mounted tag between the first and last messages (and hence estimates of B). It is for this reason that we hypothesize that this inaccuracy is due to CLS Argos not considering V_{tag} in geolocation calculations for their kalman filtering techniques. Further to this, we would recommend the use of other post-processing techniques to improve geolocations for tags mounted on fast moving animals. An example of such a technique uses knowledge of both the species migratory patterns, and maximum velocities to judiciously filter outliers in Argos geolocation (Nicholls and Robertson 2007). Essentially, if an animal was on a northerly migratory route, with a maximum velocity of $X \text{ m s}^{-1}$, and then all subsequent geolocations either to the south, or outside the possible range ($X \text{ m s}^{-1}$ multiplied by the time difference between geolocation 2 and geolocation 1) of the animal can be flagged as inaccurate. The technique can be further enhanced through the use of elliptical error definitions as the bisection between the ellipse radius of the starting point, the ellipse error radius of the following geolocation, and the radius of the maximum possible distance travelled by the animal will yield a decreasing area with increasing eccentricity of the two ellipses, thus further increasing locational accuracy.

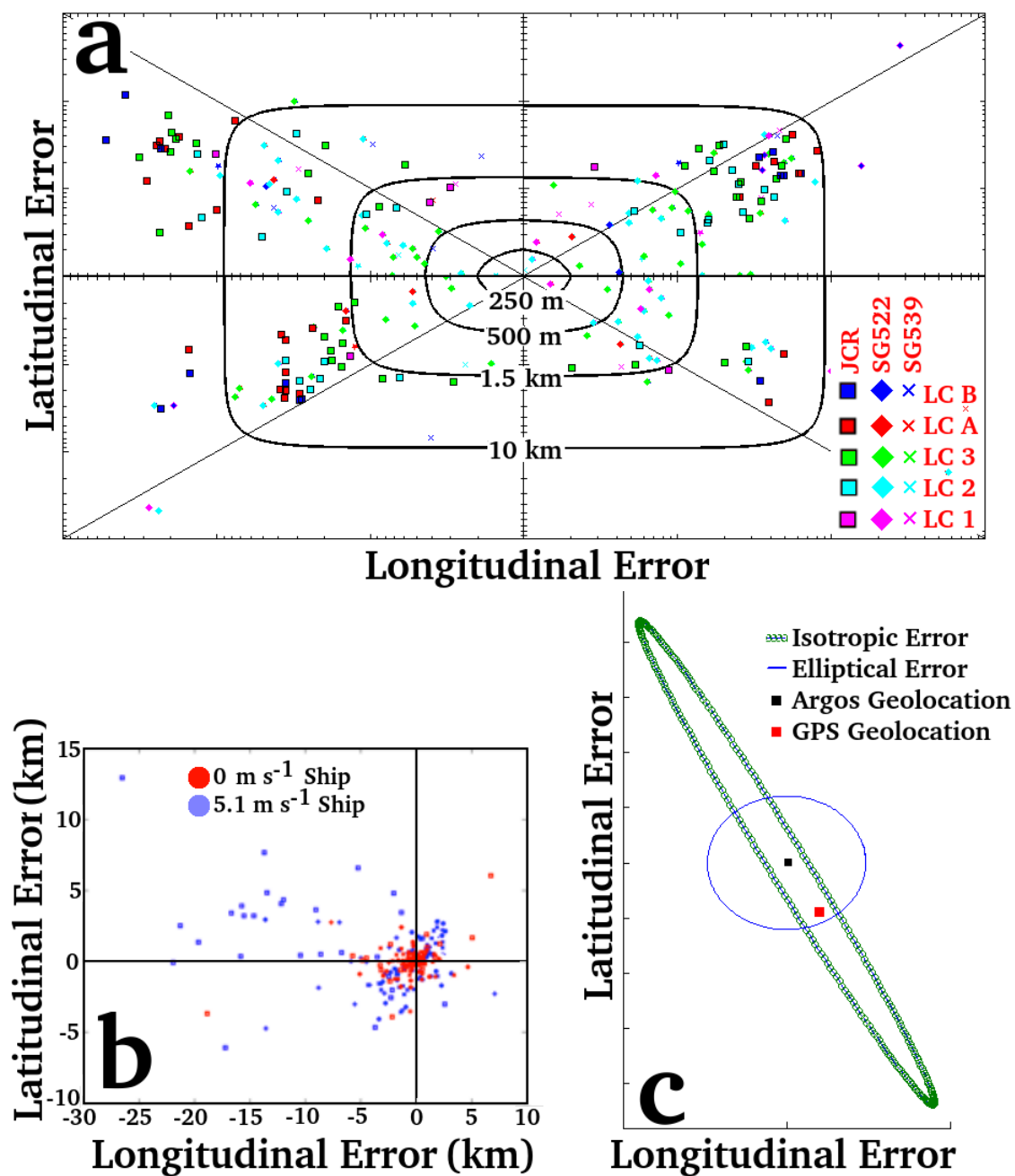


Figure 3

a Log-log plot of all geolocation errors (Argos geolocation- GPS geolocation) for the three seagliders and the JCR mounted tag

b Geolocational errors for $V_{tag} = 0$ and $V_{tag} = 5.1 \text{ m s}^{-1}$ JCR tag data

c An example of elliptical and isotropic (circular radii) geolocation error estimates, as provided by CLS Argos for a typical surfacing of the Seaglider (dive 120, SG522).

3.2. Haul-out and temperature statistics

The Spot-5's onboard thermocouple was accurately calibrated for both SG522 and SG539 with good agreement between the tag temperature data and the Seaglider CTD (figure 4 a and b). Watercolumn temperature features, such as a core of 0 to 0.5 °C water observed by SG522, were apparent in both Seaglider and tag datasets (figure 4 a and b). The tag temperature statistics overestimated the time the tags spent in warmer (1- 2.5 °C) water by up to 6% (figure 4 c). These warm temperature overestimates appear to be diurnal, being most prevalent between local noon – 6pm, suggesting that the cause of this overestimate is solar heating of the tag, whilst at or near the surface.

The Spot 5 tag has no inbuilt pressure sensor, therefore haul-out statistics estimated by the tag rely on the wet-dry sensor registering as being 'dry'. The two datasets shows that the Spot-5 tag performed well, identifying all Seaglider surfacing manoeuvres for both SG522 and SG539. Additionally, there were no surfacings recorded by the tag whilst the Seaglider was programmed to remain underwater (Figure 4 d and e, yeardays 38 -41). Using the statistics from both the tag and the Seaglider to estimate the percentage of time spent on the surface over the course of the mission, we found that the tags fitted to Seaglider 522 and 537 recorded a haulout of only 9.6 and 9.7 %, compared to the true Seaglider recorded values of 15.1 and 15.6% (Figure 4 f). Therefore, the wet/dry sensor system appears to worked well in the identification of Seaglider surfacings, but consistently underestimated the amount of time spent on the surface by the Seaglider. This underestimation can be large, with the maximum daily discrepancy between the haul-out statistics from the SG and the Spot-5 tag 11.4% (fig 4 d, yearday 35). During this time, we hypothesis that the Seaglider remained on the surface, but the tags wet/dry sensor registered as being wet. We suggest two probable scenarios that would result in this; the first being heavy rainfall, soaking the wet-dry sensor whilst it was above the sea surface. The second may be caused by the splashing of the wet-dry sensor by waves. The low ambient temperatures in the Weddell Sea would retard any evaporation of water from the sensor, hence increasing this error. False 'wet' readings will not only result in an overestimation of the time that the tag spends underwater, but also alter the temperature statistics. When the wet-dry sensor on the tag is wet whilst tag is on the sea

surface, temperature statistics are collected, resulting in the erroneous recording of air temperature. The data appear to support this conclusion, with a clear diurnal cycle visible in the anomalies- high temperature outliers tending to occur during noon- 6pm, and warm temperature outliers during the daytime (fig.4 c). This suggests that the siting of the Argos tag with respect to the water during surfacing affects the quality of the data collected. Essentially, the further away from the water's surface, and the more sheltered the tag, the more accurate temperature and haulout statistics are. On the Seaglider, the tag was approximately 20cm from the water's surface, during Seaglider communications in a flat sea state (figure 1 a).

3.3. General Reliability

The four Seaglider missions described in this paper each lasted for more than two months, and maximum depths of 1000m were frequently attained. Over this time period, no tag has been proven to have failed, and temperature and haul-out statistics (when activated) remained functional over the entire mission. The tag mounted on the RRS James Clark Ross also functioned without failure for the shorter duration (7 days) of that mission.

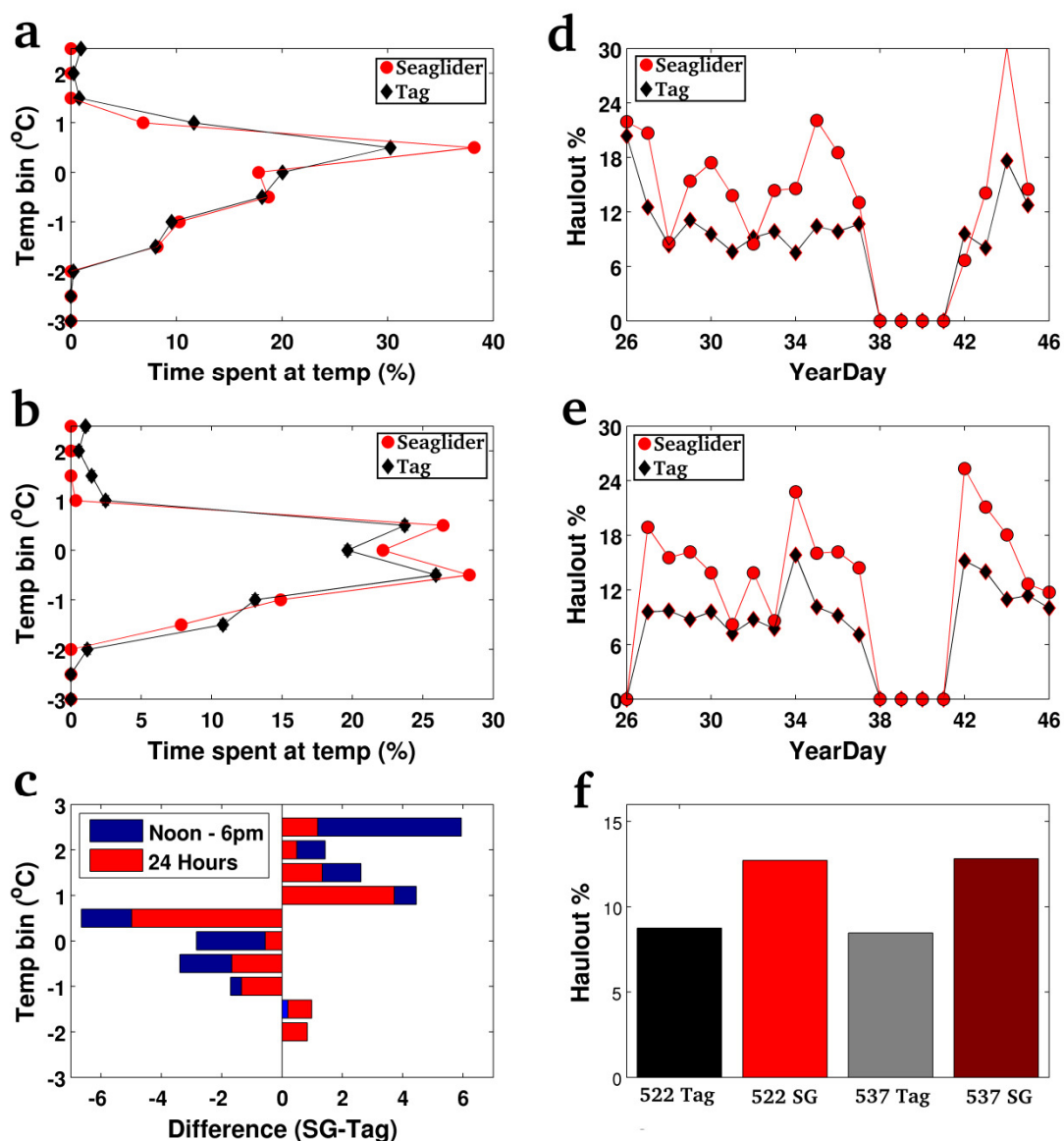


Figure 4

a & b The percentage time spent within each temperature bin for the Seaglider and Argos tag on SG 522's deployment (panel a). Panel b represents 539's deployment.

c. The difference (in percentage) between the Argos tag data and the Seaglider data for data collected over all 24 hours of each day ('24 hours'), and solely noon – 6pm local time.

d. & e. The percentage of each day that the Seaglider was at the surface, with the aerial assembly out of the water as recorded by the Seaglider, and the Argos tag. Panel d represents 522's deployment, panel e represents 539's deployment

f. The mission average haulout time (as a percentage), recorded by the Argos tag and Seaglider.

4. Conclusion

Using a Seaglider as a platform for the assessment of the Wildlife computers Spot-5 Argos tag has proved highly successful. Basic tag reliability such as battery life and water resistance were tested and found satisfactory. For future wildlife tag research and development, gliders provide a useful combination of user specifiable instrumentation, low (compared to a research ship) mission costs, and a dive-climb routine that simulates the marine mammals that the tags are frequently deployed on.

Focusing on the tag itself, the vast majority of previous studies using Argos geolocations favour the isotropic error definition. However, we find that these isotropic error definitions provided poor accuracy compared with the specifications provided by CLS ARGOS, confirming previous work on assessing the accuracy of Argos isotropic errors. The elliptical error definition performed significantly better than the isotropic error definition for both regions, and there were no significant difference between tag accuracies in polar or tropic regions. The largest inaccuracies in tag geolocation were seen on the moving RRS JCR mounted tag, whilst the smallest inaccuracies were seen from the same tag, whilst the James Clark Ross was stationary. This suggest that the tag's geolocation function is more suited to applications where the organism is relatively sessile whilst on the water's surface.

The haul-out and tag temperature statistics were broadly accurate, but appeared to suffer from the false triggering (possibly by waves and/or rain) of the wet-dry sensor whilst the Seaglider was at the surface, with these errors identified by diurnal cycles in this data, the pressure sensor, rather than a wet-dry sensor would potentially remove this source of error.

References

- Costa, D. P. et al. (2010), Accuracy of ARGOS locations of Pinnipeds at-sea estimated using Fastloc GPS., edited by Y. Ropert-Coudert, *PloS one*, 5(1), e8677, doi:10.1371/journal.pone.0008677.
- Costa, D. P., J. M. Klinck, E. E. Hofmann, M. S. Dinniman, and J. M. Burns (2008), Upper ocean variability in west Antarctic Peninsula continental shelf waters as measured using instrumented seals, *Deep Sea Research Part II: Topical Studies in Oceanography*, 55(3-4), 323-337, doi:10.1016/j.dsr2.2007.11.003.
- Cristina Tobler de Sousa, Helio Koiti Kuga, A. W. S. (2003), Geo-location of transmitters using real data, doppler shifts and least squares, *antartica.cptec.inpe.br*, 52, 915-922. [online]
- Eriksen, C. C., T. J. Osse, R. D. Light, T. Wen, T. W. Lehman, P. L. Sabin, J. W. Ballard, and A. M. Chiodi (2001), Seaglider: a long-range autonomous underwater vehicle for oceanographic research, *IEEE Journal of Oceanic Engineering*, 26(4), 424-436, doi:10.1109/48.972073.
- Hammerschlag, N., A. J. Gallagher, and D. M. Lazarre (2011), A review of shark satellite tagging studies, *Journal of Experimental Marine Biology and Ecology*, 398(1-2), 1-8, doi:10.1016/j.jembe.2010.12.012.
- Hays, G. C., C. J. a. Bradshaw, M. C. James, P. Lovell, and D. W. Sims (2007), Why do Argos satellite tags deployed on marine animals stop transmitting?, *Journal of Experimental Marine Biology and Ecology*, 349(1), 52-60, doi:10.1016/j.jembe.2007.04.016
- Ho, K. (1993), Solution and performance analysis of geolocation by TDOA, *Aerospace and Electronic Systems, IEEE*, 29(4), 1311-1322.
- Hooker, S. K., and I. L. Boyd (2003), Salinity sensors on seals: use of marine predators to carry CTD data loggers, *Deep Sea Research Part I: Oceanographic Research Papers*, 50(7), 927-939, doi:10.1016/S0967-0637(03)00055-4.
- Know, A. (2012), *CLS ARGOS user manual*.
- Nicholls, D. G. (2007a), Measuring accuracy and precision for CLS: Argos satellite telemetry locations, , 54.
- Nicholls, D. G. (2007b), Validating locations from CLS: Argos satellite telemetry, , 54, 121-136.
- Richharia, M., and L. D. Westbrook (2010), *Satellite Systems for Personal Applications Concepts and Technology*, Wiley. [